Diffusion Processes of Atoms and Small Molecules Studied by High-Speed Variable Temperature Scanning Tunneling Microscopy

Hannah Katharina Illner

aus

Dachau, Deutschland

2025

Erklärung

Diese Dissertation wurde im Sinne von §7 der Promotionsordnung vom 28. November 2011 von Herrn Prof. Dr. Joost Wintterlin betreut.

Eidesstattliche Versicherung

Diese Dissertation wurde eigenständig und ohne unerlaubte Hilfe erarbeitet.

München, 30.10.2025

<div style="text-align:right">

_____

Hannah Illner

</div>

Dissertation eingereicht am:	26.08.2025
1. Gutachter:	Prof. Dr. Joost Wintterlin
2. Gutachter:	Prof. Dr. Sebastian Günther
Mündliche Prüfung am:	27.10.2025

für Uta

Table of Contents

1. Introduction

Surface science is the study of solid surfaces, and with the development of ultra-high vacuum techniques, this research field has expanded remarkably over the last half century. The variety of experimental methods is broad and ranges from spectroscopy techniques, which deliver an average signal over the whole sample, to focused techniques like scanning tunneling microscopy, which provide microscopic information down to single-atom resolution. The aim of surface science is the fundamental understanding of structures, and processes that take place on surfaces. A very large number of industrial processes are based on heterogeneous catalysis, i.e., on reactions of molecules on solid surfaces. The catalytic surfaces make the processes effective by lowering the activation barriers. Consequently, surfaces play a crucial role in converting molecules into desired products by providing active sites. A surface reaction can be divided into four basic steps: adsorption onto the surface, diffusion of the adsorbed reactants to active sites or towards a reaction partner, reaction itself (usually across several transition states), and desorption of the products.

In this work, the focus will be set on the diffusion of adsorbed atoms and small molecules on surfaces. In general, diffusion of adsorbates on surfaces can be divided into two separate phenomena: mass transfer along a concentration gradient, and self-diffusion, i.e. the intrinsic diffusion driven by the thermal mobility at a given temperature. The latter also persists at thermodynamic equilibrium when adsorbates are evenly distributed on a surface. Surface diffusion can, in general, be described as a stochastic hopping between the energy minima on the potential energy landscape of the surface.[1]

The diffusion energy barrier E_d is defined as the minimum energy an adsorbate must overcome to move from one stable adsorption site to another equivalent one. The rate of the process increases with temperature and is described by the Arrhenius law (eq. 1.1):

$$D = D_0 \, e^{\left(\frac{-E_d}{k_\mathrm{B}T}\right)} \tag{1.1}$$

The diffusion coefficient D quantifies the rate of the process with respect to the displacement distribution of the adsorbate. The Boltzmann term contains the Boltzmann constant k_B and the absolute temperature T, and it determines the probability

that an adsorbate has the required energy to overcome the activation barrier. The preexponential factor D_0 is, in surface diffusion processes, often related to the vibrational frequencies of the adsorbates, which is then called the attempt frequency. The diffusion constant and the jump frequency are connected by the following equation 1.2:

$$D = \frac{\langle r^2 \rangle}{4t} = \frac{a^2}{4}\,\Gamma \tag{1.2}$$

with 4 for an isotropic surface, i.e., hexagonal or quadratic; r is the displacement in the time t, a is the lattice constant, and Γ the jump frequency.

In addition to the quantitative description of diffusion processes, a mechanistic description of these processes is also of great interest. However, special experimental setups and methods are necessary to perform measurements of diffusion processes.

The beginning of the quantitative analysis of surface diffusion was set by the field emission microscopy (FEM) that was established in the 1930s.[2] In this setup, a high negative electric potential is applied to a metal tip under UHV conditions, and the emitted electrons are observed on a fluorescent screen. The current is sensitive to the local work function which makes it possible to detect adsorbates on the metal surface and also to observe diffusion by monitoring the distribution of the adsorbates on a partly covered sample. The method is restricted to only a few metals with high melting points (such as W, Mo, Re, and Ta) and to the area of the tip apex. Furthermore, it has to be assured that the applied high electric field does not influence the mobility of the adsorbates. However, important aspects of surface diffusion were provided by FEM.[3–5]

Field ion microscopy (FIM), which was established roughly two decades later, specializes in the diffusion of metal atoms or clusters adsorbed on metal tips.[6] The setup is very similar to FEM, but a positive potential is applied to the tip, and gas atoms (He or Ne) near the surface are ionized by the strong electric field. During imaging, the tip is cooled to temperatures below 100 K, which provides atomic resolution. Between the measurements, the field is switched off and the sample is heated to a temperature at which the diffusion takes place. This method is, however, also very limited to only a few metals and the small area of the elaborately prepared sharp tips.

As ultra-high vacuum (UHV) based techniques for sample preparation and surface analysis improved significantly in the following years, this coincided with the development of investigation techniques for diffusion processes. Laser-induced thermal desorption (LITD) is used for the analysis of the diffusion of a large number of different adsorbates. In the experiment, a single crystal surface of a metal is covered

with an adsorbate, and a small area of the surface is illuminated by a laser pulse so that the adsorbates desorb thermally from this area. The depleted area fills again with adsorbates diffusing from the surrounding area so that thermal equilibrium is recovered. A second laser pulse is applied on the same surface area, and the desorbing molecules are quantitatively analyzed. The time evolution of this signal is used to evaluate the diffusion constant.[7,8] The only requirements are that the adsorbate desorbs thermally and is detectable by mass spectrometry. A downside with this technique is that it lacks spatial information about the sample surface. The investigated surface areas are typically in the 100 μm range, which necessarily includes steps or other surface defects that influence the diffusion behavior of the adsorbates.

Another macroscopic method to study surface diffusion is the photoelectron energy microscope (PEEM), combined with LITD to introduce a concentration gradient in the adsorbate layer. With PEEM, which records images with a CCD camera, the surface can be imaged with a temporal resolution of 20 ms. (CCD is the abbreviation for charge-coupled device, which is a light-sensitive electronic sensor that collects two-dimensional data.) The photoelectrons are created by illuminating the sample with UV light from either a laboratory or synchrotron source.[9,10] Diffusion constants can be measured, e.g., by creating a grating in the adsorbate layer (by means of an interference pattern of two lasers) and measuring the decay of the grating to a homogeneous distribution.[11] The diffusion is measured either by a second-harmonic diffraction (SHD) or a linear optic diffraction (LOD) technique. A major issue, however, of macroscopic studies is the averaging over larger (macroscopic) areas and variable coverages θ. In most cases, diffusion in the sense of mass transport caused by a concentration gradient of the adsorbates is investigated. Moreover, at high coverages, attractive or repulsive interactions among the adsorbates have to be taken into consideration.

Another method is quasielastic helium atom scattering (QHAS). In this technique, diffusion in the adsorbate layer is investigated by the broadening effect of the reflected helium beam that undergoes a characteristic energy exchange with the atoms on the surface.[12,13] From the fact that high diffusion constants are required, this technique has a rather limited application spectrum, for example, to weakly bound gases on metal surfaces or high temperatures.

With the development of the scanning tunneling microscopy (STM) technique, the options of studying surface phenomena reached a new level.[14,15] In the STM, a metallic tip is positioned over a conducting surface at a distance of $\approx$ 1 nm, and as a voltage is applied between the tip and the sample, a small tunneling current can be

measured. Images are recorded by scanning the tip over the sample. These images represent a combination of the local density of states (LDOS) and the topography of the sample. In that way, a three-dimensional map of the surface is drawn with atomic resolution. Besides investigations on structural information, STM opens up a variety of options to study surface diffusion.

Local fluctuations in the coverage of adsorbates can be measured by recording the tunneling current without moving the tip.[16,17] Adsorbates that cross the tunneling region cause a change in the current, from which diffusion parameters can be extracted. However, no images are recorded in this mode, so that any spatial effects, such as particle-particle interactions, do not become directly visible.

More sophisticated is the method of tracer diffusion, where the diffusion of single atoms or molecules is directly followed on an atomic resolution level. This can be done in two ways: First, the movement of the adsorbate is followed by the tip, which is realized with a two-dimensional lateral feedback that locks the position of the tip directly above the adsorbate. Again no images are recorded.[18,19] Second, the diffusion of individual adsorbates is tracked through their position in consecutive images.[20,21] In this case, the accessible jump frequency of the investigated surface species is limited by the acquisition time of the STM images. However, this method opens up the possibility to study a large variety of different systems of adatoms and adsorbates of various kinds.

However, in STM, special care has to be taken as interactions of the tip with the adsorbates can influence the diffusion behavior. The method has been constantly developing further, especially by enhancing the scanning rate, which enables recording images at video rates of up to 50 Hz.[22] The range of hopping rates that are accessible is extended as the scanning rates become higher. Moreover, by increasing the number of recorded images, a better statistical evaluation of the diffusion processes is possible. In this regard, computer techniques become inevitable for analyzing and evaluating the diffusion parameters from the large amount of recorded data.

STM is the method that is chosen in the present work to analyze diffusion processes and the diffusion mechanisms of atoms and small molecules on surfaces at the atomic level. The STM setup combines high-speed scanning and high image acquisition rates with variable temperature measurements. This combination makes it a powerful tool to analyze diffusion of adsorbates on single-crystalline metal surfaces and evaluate diffusion mechanisms and kinetic parameters. The high-speed mode allows one to follow adsorbate motions with jump frequencies that range over two

to three orders of magnitude. Movies with frame rates up to 50 frames per second (fps) can be reached, with usually applied frame rates of 10-12 fps. At the same time, atomic resolution is maintained during data acquisition. The large number of recorded images makes it possible to compile reliable statistics. From the fact that the temperature is variable and measurements are conducted over a large temperature range, kinetic parameters, which are an important characteristic of diffusion, can be extracted. From the recorded STM images and the tracking of individual particles, experimental jump distributions are obtained. In the evaluation process the jump frequencies are determined and from the temperature dependence of these values, given in the Arrhenius law (equation 1.1), the energy barrier and the preexponential factor of the diffusion process are accessed.

The STM setup is specialized to measure diffusion of single particles at low coverage so that interactions (both attractive and repulsive) between adsorbates are excluded, and solely thermal mobility is examined. However, in some cases, the influence of a coadsorbate might be of special interest, and these systems can be investigated with high-speed variable temperature STM as well. Essential for the analysis is the evaluation with a tracking tool. This tool is especially designed for identifying and tracking individual particles in high-speed STM data, which is realized with a multiscale wavelet algorithm.[23] The tracking tool, as well as the high-speed scanning feature of the STM set-up, was established and implemented in the work of Ann-Kathrin Kügler (Henß).[24] This combination makes it possible to track multiple particles in a large number of STM frames and extract experimental jump distributions. These distributions provide a statistical pattern of the thermally activated diffusion. They describe the distances and the directions of the jumps and how often a hopping event between neighboring adsorption sites occurs. The temperature dependence of the jump frequencies provides information on the energy barrier and attempt frequency according to the Arrhenius law.

The following is an overview of the results that will be presented in this thesis.
The diffusion studies were performed with adsorbed oxygen, hydrogen, carbon atoms, ethylene and CO molecules on Au(111) and Ru(0001) single crystal surfaces. These systems were chosen because the adsorbates play central roles in several large-scale industrial catalytic processes. Reactions such as the Fischer-Tropsch (synthesis of hydrocarbons), the methanol synthesis, steam reforming, the water gas shift reaction, and the oxidation of CO, to name only a few, are all connected by the fact that carbon-containing species – such as CO or CH_x – are present on the surface during the reaction. The syngas mixture, containing both CO and H_2, produced by steam reforming (from methane and water) and the water gas shift reaction, plays

a role in many processes. The mentioned reactions have in common that carbon monoxide is present on the surface, and that carbon is an active species. In surface science, the mechanistic understanding on an atomic level is targeted to gain more insights into the surface processes, like the diffusion of the adsorbates. The behavior of intermediates on surfaces is an essential factor for the activity and selectivity of reaction pathways.

The present work can be divided into two main projects. The first project studies single oxygen atoms embedded in an adlayer of CO on Ru(0001). This system is of interest as it reflects a crowded situation of coadsorbates on a surface and targets the influence on the mobility of the components. The mobility of single oxygen atoms is investigated, and the CO molecules form an adlayer environment. This rather simple system is ideally suited for the above described technique of high-speed variable temperature STM (VT-STM). After successful tracking of the oxygen atoms and the identification of a new diffusion mechanism, the so-called door-opening mechanism, in studies performed by Ann-Kathrin Kügler (Henß)[24,25] on the same system, further research questions on that well-defined system were investigated. In chapter 5 the new results are presented. They are divided into three parts: the diffusion of oxygen atoms along domain boundaries of the ordered CO structure, the solution of the saturation coverage structure of CO, and the diffusion of oxygen atoms at CO saturation coverage on Ru(0001). A summary of the key results of the respective publications are given, as well as the actual publications.

The second project of this work originally aimed at single carbon atoms adsorbed on the Ru(0001) surface, to observe their diffusion behavior on the surface, and, in the best case, to be able to follow a reaction of the carbon atoms with hydrogen by means of the high-speed STM setup. This project required preparation of adsorbed carbon atoms on the surface. For this purpose, a carbon evaporator was installed and put into operation. Chapter 3 deals with the characterization of the carbon species that are emitted from the evaporator. Experiments on a Au(111) and a Ru(0001) single crystal sample were conducted. However, as it turned out, no single carbon atoms were obtained on the Ru(0001) surface. A different carbon species was discovered that exhibits an intriguing diffusion behavior. Chapter 4 focuses on the investigations of this carbon species, which can either be prepared by carbon evaporation or ethylene dosing. STM data of this species and the experiments performed to identify its atomic composition are presented as well as the investigations of its diffusional behavior. Two cooperations, one with Simon Wanninger from the group of Professor Don C. Lamb at the Ludwig-Maximilians-Universität (LMU)

Munich and another with Sung Sakong and Axel Groß from the University of Ulm were established. The chapter ends with a discussion on the compensation effect, as this phenomenon is observed in the diffusion process of the studied molecule.

Before the results are presented, the experimental set-up and the applied methods are shortly described in the following chapter 2. The sample preparations of both crystal surfaces, Au(111) and Ru(0001), are also described.

2. Experimental Setup and Methods

The experiments were all performed in an ultrahigh vacuum (UHV) chamber of the Wintterlin group at the Ludwig-Maximilians-Universität München (LMU Munich). The UHV chamber was designed by T. Gritsch at the Fritz-Haber Institute in Berlin and was moved to Munich in 2002.[26] Since then, it has been modified several times. In particular, the built-in STM setup has been changed in previous PhD studies. In the following, the UHV chamber, the available and used analytic methods, as well as the samples are described.

2.1. Ultrahigh vacuum chamber and its components

The UHV chamber is equipped with a turbo molecular pump (*Pfeiffer vacuum TMU521*) with a rotary pump to generate the forevacuum, and an ion getter pump. The pressure is measured by a *Bayard-Alpert* ion gauge by *Arun Microelectronics Limited (AML)*. The UHV system provides a base pressure of $< 1 \times 10^{-10}$ Torr. In the period of this work, some modification works in the chamber setting were made. The titanium sublimation pump and the low energy electron diffraction optics were replaced by a thermal desorption spectroscopy (TDS) setup with a bypass that is separately pumped by a small turbo molecular pump (*HiPace 80*) with a rotary pump for the forevacuum. The quadrupole mass analyzer (*QMS/QMA 200, Pfeiffer Vacuum*) is in addition to that used for analyzing the residual gas phase.

The following gases were available for dosages via background dosing through leak valves: Ar (purity: 99.999 Vol.%, *Linde Minican*), O_2 (purity: 99.995 Vol.%, *Linde Minican*), CO (purity: unknown, *Linde* glass container), H_2 (purity: 99.999 Vol.%, *Linde Minican*), ethylene (purity: 99.95 Vol.%, *Air Liquide Minican*), acetylene (purity: 99.6 Vol.%, 1 Vol.% in nitrogen gas (purity: 99.999 Vol.%), *Messer Minican*).

The chamber is equipped with a manipulator that holds the sample, for preparation and surface analysis by Auger electron spectroscopy (AES), low-energy electron diffraction (LEED), and thermal desorption spectroscopy (TDS). The chamber

also houses a home-built variable temperature scanning tunneling microscope (VT-STM), the main equipment used in this work.

For preparation, the sample is hold in the manipulator, which is equipped with a tungsten filament mounted on the backside of the sample. By radiative heating form the hot filament, sample temperatures up to 600 °C can be reached. To reach higher temperatures, a high-voltage (up to 2 kV) is applied between the filament and the sample. By electron bombardment, temperatures above 1500 °C can be reached. Further, the manipulator is equipped with a cooling system. Liquid nitrogen is pumped by a rotary pump through a tube that leads to a copper block at the front end of the manipulator, that serves as a cooling reservoir. From there copper braids lead to the sample holder. The sample can be cooled to temperatures of approximately -165 °C in that way.

A further facility for the sample preparation is the sputter gun (*Leybold-Heraeus*). Argon atoms are ionized in the gun and are accelerated to an energy of 1 keV to the sample. Bombardment by the Ar^+-ions removes the topmost atom layer of the sample. The usually applied Argon pressure for the cleaning procedure was 5×10^{-5} Torr, with a resulting iron current at the sample of 5 μA.

The UHV chamber is equipped with an Auger electron spectrometer (AES) for the analysis of the chemical composition of the sample surface. The AES system from *Perkin-Elmer* is composed of an electron gun (usual acceleration voltage of 3 kV), a single-pass cylindrical mirror analyzer for energy-separation, and a Channeltron detector for Auger electrons. In the lock-in amplifier (*Model 5209, EG&G*), the signal is amplified and differentiated with respect to the electron energy. The parameters are set individually for the spectrum type (overview or detail). The signal is converted by an analog-to-digital converter (± 10 V, 12 bit, *PS-2115*, *Pasco*) and then recorded with the program *Data-Studio* (*Pasco*).

A thermal desorption spectroscopy (TDS) setup was implemented in the scope of this work. Because of the space restrictions, the LEED optics and the titanium sublimation pump were detached. A cylinder with a small circular opening in the center was installed in the chamber that contains the head of the quadrupole mass spectrometer (QMS) (*QMS/QMA 200, Pfeiffer Vacuum*). A bypass provides a connection to the main UHV chamber and is equipped with a separate turbo molecular pump (*HiPace 80*) with a rotary pump providing the forevacuum to pump the inside of the cylinder. Two manual gate valves were added, with which differential pumping can be enabled or disabled.

A further facility that was added to the UHV chamber in the scope of this work is an electron beam evaporator *EFM 3* from *Focus GmbH* (Germany), equipped with a carbon target (*Goodfellows*). The evaporator is connected to the chamber via a CF 35 flange, and is equipped with connections for cooling water and fedthroughs for the high voltage and for the control unit. The working principle of the evaporator is explained in chapter 3.

As the central element, the UHV chamber houses a high-speed variable temperature STM (VT-STM). The variable temperature function is realized by simultaneous heating and cooling. The sample is mounted to a copper block that is connected via copper braids to a liquid helium cryostat. Sample temperatures down to -223 °C are realized. By counterheating with a tungsten filament mounted beneath the sample the temperature can be continuously adjusted and raised up to 200 °C. In the (quasi) constant height mode, videos with image rates up to 50 frames per second (fps) can be recorded. The video-rate function was implemented by Ann-Kathrin Kügler (Henß), and the details are described in her dissertation.[24]

The chamber is mounted on four pneumatic vibration isolators (*Newport XL-A*), which are inflated with nitrogen at a pressure of approximately 5 bar during the STM measurements. In addition, the turbopumps and rotary pumps are shut down, and the vacuum is maintained by the ion getter pump. In this way, stable conditions without mechanical noise for STM experiments are obtained.

2.2. Auger electron spectroscopy

Auger electron spectroscopy (AES) is a surface-sensitive analytical method to characterize the elemental composition of the top few atomic layers of a sample. The technique can detect all elements except hydrogen and helium, has a low detection limit, and is relatively cost-effective compared to other surface analysis methods. In this work, AES has been used to check the sample surfaces for residual contaminations during the preparation cycles and to verify the cleanliness before an experiment. Additionally, the adsorption of carbon from the evaporator or from the dosing with hydrocarbon molecules has been monitored.

This analysis method is based on the Auger effect that is schematically illustrated in figure 2.1.[27] Free electrons are thermally generated at a heated filament and then accelerated by the anode voltage to the sample surface with a kinetic energy in the range from 3 to 30 kV. In this work, the energy was set to 3 keV. The incident

electrons eject electrons from the inner shell of a sample atom; in the scheme shown in figure 2.1, it is an electron from the K shell. An electron from a higher shell, here the L_1 shell, fills up the resulting electron hole. The energy difference $E_K - E_{L_1}^*$ that is released in this process is either leaving the sample as characteristic radiatively emitted x-ray fluorescence $h\nu$ or is transferred to a third electron of the same or a higher electron shell. This third electron is then leaving the sample and is called the Auger electron. The kinetic energy of the Auger electron is described by the following equation:

$$E_{\text{kin}}^{\text{Auger}} = E_K - E_{L_1}^* - E_{L_{2,3}}^* - \Phi_{\text{sample}} \tag{2.1}$$

E_i is the binding energy of an electron in shell i and E_i^* is the binding energy in shell i in the presence of an electron hole. The energies refer to the Fermi level of the sample and Φ_{sample} is the work function of the sample.

The kinetic energy of the Auger electron is independent of the energy of the incident electron and is solely dependent on the energy levels involved in the process. Thus, it is an element-specific energy. Due to the low intensity of the Auger transitions, in the spectra, not the intensity but the derivative of the intensity is plotted against
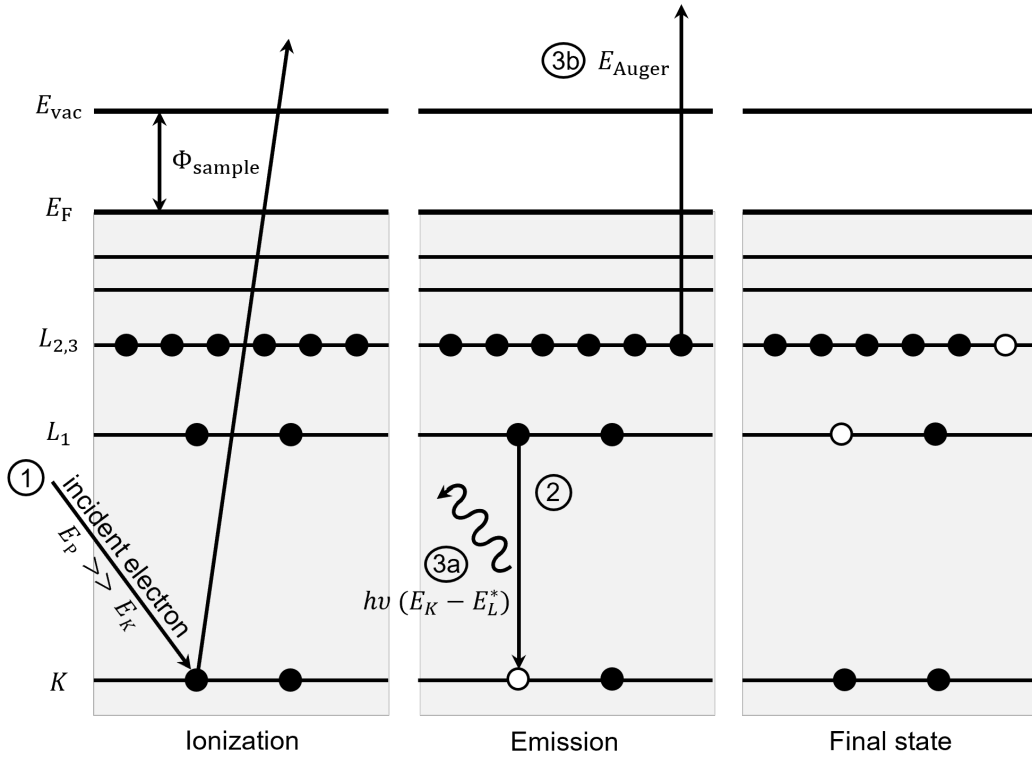
Figure 2.1 : Energy scheme of the Auger effect in which an incident electron (1) that ejects an electron from the inner shell (2) can either cause the emission of $h\nu$ (3a) or the emission of an Auger electron (3b).

the energy. The surface sensitivity of the Auger electron spectroscopy is given by the mean free pathway of electrons in solids that depends on their energy. In the energy range from 10 to 1000 eV, the electrons' mean free pathway is at a minimum.[28] The typical energies for Auger electrons are in this range, which means that these electrons come from the first ten monolayers of the sample.

2.3. Low energy electron diffraction

Low-energy electron diffraction (LEED) is a surface-sensitive technique to analyze structures on single-crystalline surfaces by visualizing the 2D reciprocal lattice space. The sample surface is illuminated with electrons with a kinetic energy E_{kin} between 20 and 500 eV, which are diffracted at the sample surface. According to the de-Broglie relation (given in equation 2.2), the wavelength $\lambda_{\text{de-Broglie}}$ of these electrons is in the order of the lattice constant of the sample.

$$\lambda_{\text{de-Broglie}} = \frac{h}{p} = \frac{h}{\sqrt{2 m_e E_{kin}}} \tag{2.2}$$

with h: Planck constant, p: momentum, m_e: electron mass

In the experiment, electrons from a hot filament are accelerated by the anode voltage to the desired kinetic energy and focused with a lens system. The electrons pass through a drift tube and hit the sample surface perpendicularly. The diffracted electrons pass three grids, of which the first and the third are grounded to create a field-free space. A suppressor voltage is applied to the second grid, which prevents inelastically scattered electrons from passing through. A high voltage is applied to a fluorescent screen behind the grid system, accelerates the electrons and makes them visible. From the diffraction pattern, the real space lattice can be obtained by the analysis of the beam intensities. Surface reconstructions and ordered adsorbate layers that form periodic structures on the surfaces can be analyzed by LEED. In this work, LEED was especially used to investigate the superstructures of carbon monoxide on Ru(0001).

2.4. Thermal desorption spectroscopy

Thermal desorption spectroscopy (TDS) is a method to analyze the desorption characteristics of gases and other adsorbates on surfaces. To start the experiment, the investigated species are usually adsorbed on the cold sample surface. The temperature is then ramped up until desorption. The desorbing gases are detected by a quadrupole mass spectrometer. The thermal behavior, like the desorption temperature and kinetics, give insights into the thermal stability and the binding energies of the adsorbed species. The measurements can be performed either qualitatively by detecting a whole mass spectrum or quantitatively by monitoring selected masses over a temperature and time range.

To record a TDS, the sample is placed on the vacuum side of the small opening, a standard procedure to reduce the background signal from the hot parts of the manipulator. For measurements, the connection to the main chamber is closed with a manual gate valve, and the gas volume is pumped by a separate turbo molecular pump backed-up with a rotary pump. In the experiment, the sample is cooled by liquid nitrogen, and gases or other species are adsorbed on the cold surface. In a second step, the sample is heated by the filament beneath the sample holder, and the desorbing species are detected.

2.5. Scanning tunneling microscopy

Scanning Tunneling Microscopy (STM) is the main method used in the present work. STM can image surfaces with atomic resolution, and in addition, it is possible to investigate the dynamic behavior of adsorbates on the surface, as it is done in this work.

The STM method is based on the quantum mechanical tunnel effect. A thin metallic tip is moved over a conductive surface at a distance small enough so that electrons can pass the potential barrier by tunneling (about 1 nm). A voltage (tunneling voltage V_t) is applied between the tip and the sample surface, which generates a small current (tunneling current I_t) in the range of nA. The tunneling current I_t depends on the tunneling voltage V_t, as well as on the local density of states at the Fermi level $LDOS(E_F)$; and it depends exponentially on the distance s between the sample and the tip. κ is a transmission coefficient that is defined by the effective barrier Φ_{eff} (which is approximated by $\Phi_{\text{eff}} = \frac{1}{2}(\Phi_{\text{tip}} + \Phi_{\text{sample}})$), the mass of an elec-

tron m_e and the reduced Planck constant $\hbar$. Equation 2.3 describes the tunneling current I_t for the case of small tunneling voltages V_t ($eV_t << \Phi_{\text{eff}}$).[29,30]

$$I_t \propto LDOS(E_F) \cdot V_t \cdot e^{-2\kappa s} \tag{2.3}$$

with the decay length κ equal to:

$$\kappa = \sqrt{\frac{2m_e \Phi_{\text{eff}}}{\hbar^2}} \tag{2.4}$$

With a typical Φ_{eff} of 4 eV, a change in the distance s of 1 Å causes a one order of magnitude change in the tunneling current I_t. This means that a slight variation in the height of the sample surface has a huge impact on the tunneling current. As a result, the STM has a high spatial resolution in vertical and lateral directions. However, as the local density of states at the Fermi level $LDOS(E_F)$ also has an impact on the tunneling current I_t, the resulting STM images are a superposition of electronic structure and topography of the sample surface.

Figure 2.2 shows the potential barrier illustrated in an energy scheme. The two Fermi levels of the sample $E_F(\text{sample})$ and the tip $E_F(\text{tip})$ are shifted relative to each other by the value of the applied tunneling voltage eV_t. In the figure, a negative tunneling voltage is applied to the sample, which results in an upward shift of the Fermi energy of the sample with respect to the Fermi level of the tip. The tunneling current is given by the electrons in the energy window eV_t that tunnel from occupied states of the sample into empty states of the tip. In this way, a so-called *filled state* image is produced. The reverse process, in which a positive voltage is applied to the sample, leads to a so-called *empty state* image.

The STM can be operated in two different modes, in which the tip is scanning in a grid-like movement over the sample. In the constant current mode, the tunneling current is held constant by means of an electronic feedback loop, and the vertical position of the tip is regulated by piezo ceramics. By measuring the control signal of the z-coordinate as a function of the other two scan coordinates in x- and y-direction, a three-dimensional STM image is generated. This is the conventional mode for STM images, but because of the limited band width of the feedback it operates with rather low scanning rates of several Hz. Depending on the image size, it can take up to several minutes to scan an image.

The second mode is the (quasi) constant height mode. In this mode, the tip is scanned over the sample at a constant z-value. The recorded signal is the tunneling
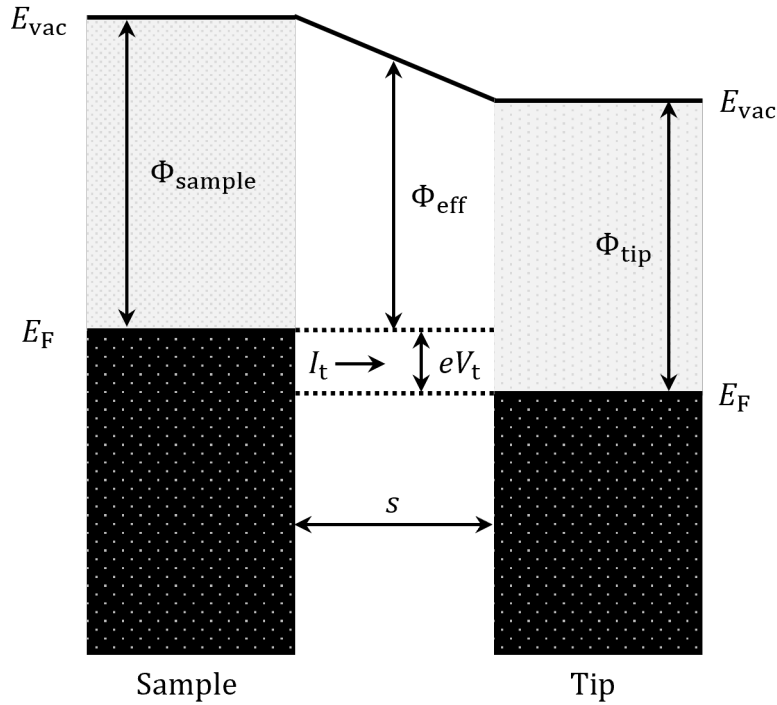
Figure 2.2 : Energy scheme that illustrates the relations of the tunneling parameters as the tunneling current I_t, the tunneling voltage V_t, and the distance s while the tunneling process.

current. In the experiments presented here, the images were recorded with a negative tunneling voltage, resulting in an inversion of the image contrast compared to the constant current mode. In the constant height mode the feedback is no longer limiting, so that the scan frequency can be increased to the low kHz regime, and frame rates of up to 50 fps are achievable. The usual scanning parameters for videos in this study were a scan frequency of 2000 Hz at an image size of 200×200 pixel, which gives an image rate of 10 fps. The electronic feedback loop of the vertical position of the tip is not switched off completely but operates at a very low frequency, in order to compensate for thermal drift or piezo creep.

The variable temperature beetle-type STM in the UHV chamber used for the experiments of this thesis was designed and constructed by Rolf Schuster and Joost Wintterlin. The video-rate mode was implemented in the scope of the dissertation of Ann-Kathrin Kügler (Henß), and the details can be found there.[24] In her dissertation, the digital scan control and the data acquisition was designed and a digital-analog converter with sufficient conversion rates was implemented. In addition, a home-built I/V-converter with a bandwidth of 300 kHz developed by Joachim Wiechers was installed. The basic concept of the beetle-type STM was developed by Besocke and Frohn et al.[31,32]

In figure 2.3, a photograph of the used VT-STM setup is shown. The sample holder with the sample is clamped to the central Cu block (2). The beetle-type STM (1) with its three piezo legs with stainless steel spheres is set on the three ramps on the sample holder by the vertical manipulator (4). The fourth piezo in the center holds the tip. When the beetle stands on the sample holder, it is mechanically decoupled from the manipulator. The copper plates of the stack on which the setup is mounted (5) are separated by elastic viton pieces that damp the STM from mechanical vibrations. However, a complete decoupling from the UHV chamber is not possible since a connection to the helium cryostat (3) is required. The approach of the tip towards the sample surface is realized by a consecutive rotational movement of the three outer piezo ceramics on the helical ramps on the sample holder (see figure 2.5). The rotation is stopped by an electrical feedback loop as soon as a tunneling current between the tip and the sample is measured. The scanning movement is performed by the inner piezo ceramic that holds the tip.
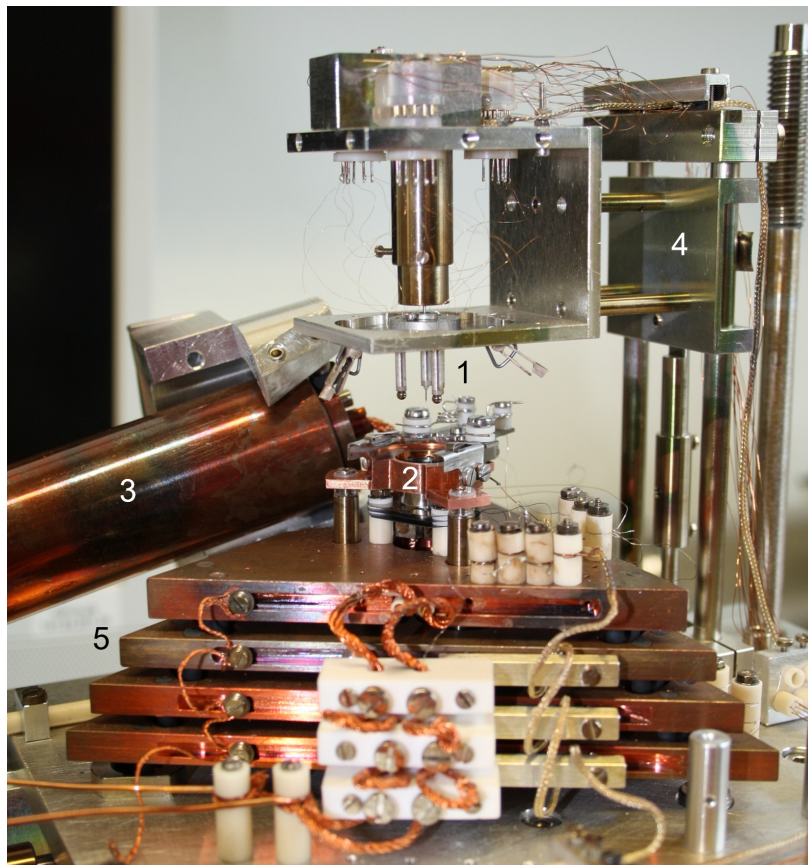
Figure 2.3 : Variable temperature STM setup with the beetle STM (1) in the center. The copper block (2) that can clamp the sample holder contains a heating filament and is connected by stranded copper wire to the helium cryostat (3). By means of the vertical manipulator (4) the beetle STM is put on the sample holder with its three piezo legs. The stack of copper plates (5) damps the setup from mechanical vibrations. (From Henß et al., ref [22]. Reprinted with permission from The Japan Society of Applied Physics.)

## 2.6. Sample preparation and temperature measurement

The experiments of this thesis were performed on three samples: two Au(111) single crystals and a Ru(0001) single crystal. All crystals are mounted on specially manufactured sample holders of stainless steel (Au(111)-1 crystal) or molybdenum (Au(111)-2 and Ru crystal) that fit the requirements for the experimental setup regarding the temperature measurement and the sample holding in the manipulator and the STM. In case of the Au crystals stainless steel screws are used to mount the crystal to the holder, for the Ru crystal molybdenum screws respectively. The holders are equipped with Pt/PtRh thermocouple contacts (type S) that make contact with corresponding fittings at the manipulator and the STM setup. The contacts consists of thick thermocouple wires (diameter 0.5 mm) that are mounted to Al_2O_3 insulation tubes fixed by screws to the sample holder. From the thicker thermowires, thin wires with a diameter of 0.05 mm are connected to the crystal (from the backside in the Au case and spotwelded to the surface in the Ru case, see figures 2.4 and 2.5). At the manipulator and at the STM, specially designed thermocouple clamps make contact when the sample holder is inserted into the corresponding mounting assemblies. Each sample holder contains a helical ramp segmented into three parts that act as platforms for the three legs of the beetle-type STM.

2.6.1. Au(111) crystals

The Au crystals have been used for pre-experiments to study the carbon evaporator installed in the UHV system; the results are presented and discussed in chapter 3. The first Au(111) crystal [Au(111)-1] had been used, before this work, for various experiments over a long time period. The second Au(111) crystal [Au(111)-2] was bought in the scope of this work and only used for the carbon evaporation experiments.

Both Au(111) crystals are hat-shaped, with 7 mm bottom diameter, 5 mm top diameter, and 1.8 mm height. The mounting of the crystals in the sample holders is shown in figure 2.4. The crytal is mounted at the rim of the "hat" to the sample holder such that its polished front side is accessible through the central opening of the holder. Rings of tantalum are placed between the crystal and the sample holder to adjust the distance between the sample surface and the STM tip. For temperature measurement, wires (PtRh (1) and Pt (2)) with a diameter of 0.05 mm are sandwiched between the crystal backside and a SiC platelet (3) from the backside of the sample (figure 2.4, right). The SiC platelet ensures more even heat distribution during the heating process. The wires are fed through small ceramic tubes to the

front side of the sample holder, where they are spot-welded to the corresponding Pt/PtRh wire pair around the Al_2O_3 insulation tubes. Ta washers (4) hold the crystal/SiC sandwich in place.
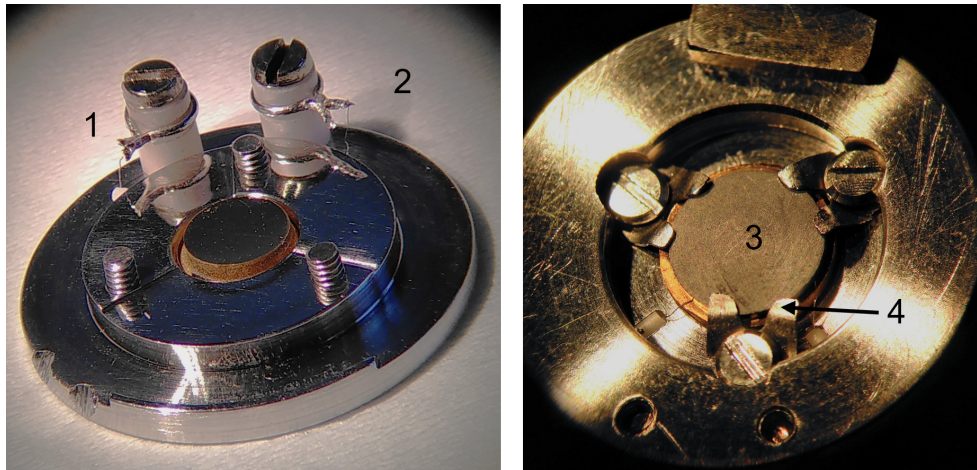
Figure 2.4 : Top and bottom view of the Au(111)-1 crystal in the stainless steel sample holder, PtRh (1) and Pt (2) thermowires, SiC platelet (3) and Ta washers (4).

The Au(111) crystals are prepared in UHV by alternating sputtering and annealing cycles. The sputter gun was operated at an Argon pressure of 5×10^{-5} Torr. The ion energy was set to 1 kV and a current of 5 µA was measured at the sample. Depending on the contamination on the sample surface, the sputter time was varied between 10 to 30 minutes. After Argon sputtering, the sample was annealed to a temperature of 600 °C to 770 °C for 10 to 60 minutes. A longer annealing step increased the size of the atomically flat terraces on the single crystal surface.

The main problem with the Au(111)-1 crystal were numerous stepped areas on the surface, despite long annealing times. The Au(111)-2 crystal permanently exhibited an unidentified species of foreign atoms in the STM images that could not be identified in the AE spectra.

2.6.2. Ru(0001) crystal

The Ru(0001) crystal was used in the study of the carbon species from the carbon evaporator (chapter 3) and for the diffusion studies of a specific carbon molecule (chapter 4). The Ru(0001) crystal is disc-shaped with a diameter of 5 mm. In this case no hat shape was chosen because the thermal contact at the rim to the sample holder is too good; preventing reaching the high temperature required for Ru. Instead the crystal was mounted to the holder by two special Ta clamps attached to slits at the sides of the crystal. A tantalum ring and three molybdenum screws

fix the crystal from the rear side of the sample holder. Figure 2.5 shows the Ru crystal mounted to the sample holder (left) and the holder together with the crystal held in the manipulator (right). (1 and 2 mark the thermowires, PtRh and Pt.) The contact of the thermowires on the sample holder with the counterparts at the manipulator are shown.
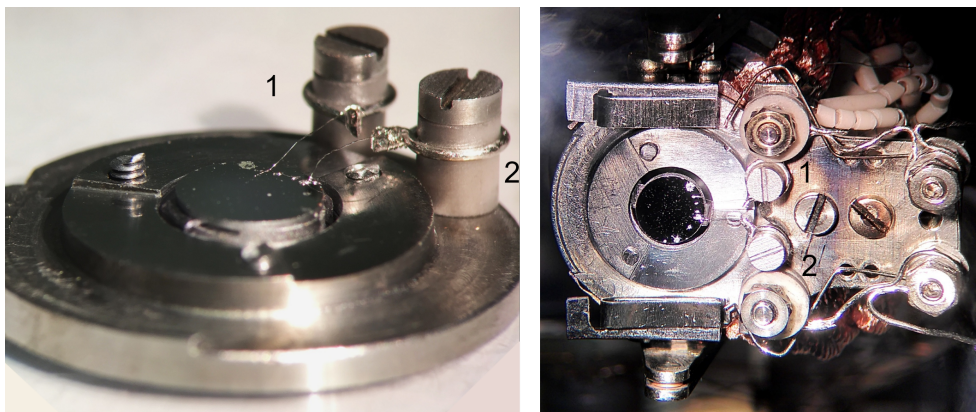
Figure 2.5 : Left: Ru(0001) crystal mounted to the molybdenum sample holder. Right: sample holder on the manipulator. Thermocouple contacts PtRh (1) and Pt (2) make contact to the corresponding fittings on the manipulator; the thin thermowires seen in the left figure are spot welded to the crystal surface.

In order to obtain a clean surface, the Ru(0001) surface was prepared in UHV in consecutive preparation cycles. Each cycle included 10 to 15 minutes of Argon sputtering. The ion energy was set to 1 kV, the Argon backpressure was set to 5×10^{-5} Torr, and the ion current measured at the sample was 5 μA. After sputtering, the Ruthenium crystal was annealed at 1200 °C for about 30 seconds. This temperature was reached by electron bombardment. It followed an oxygen treatment at a sample temperature of 500 °C to 550 °C for which the chamber was backfilled with oxygen at a pressure of 2×10^{-7} Torr for 10 to 15 minutes. This treatment removed carbon residuals from the surface. Afterwards, the crystal was heated to > 1400 °C for a few seconds (flash) to remove residual oxygen from the surface by desorption. A shorter preparation cycle was performed when the carbon contamination was low. In this case, the sample was not sputtered but heated to 350 °C to remove carbon monoxide. The oxygen treatment was adjusted. It was sufficient to dose 2 to 10 Langmuir (1 Langmuir (L) $= 1.33 \times 10^{-6}$ mbar s) of oxygen on the surface at approximately 150 °C, followed by a flash to 1400 °C. Right before each experiment, the crystal was heated to 350 °C to remove any CO that had adsorbed from the residual gas when the crystal cooled after the preparation cycle.

Usually, the sputtering-heating-oxidizing-heating cycle was performed several times. The surface composition was continuously monitored with AES. In figure 2.6, AE spectra of the Ru(0001) sample before and after cleaning cycles are shown. In the overview spectrum in figure 2.6 (a), the characteristic AE spectrum of Ru is displayed. The *MNN* transition peak of Ruthenium overlaps with the carbon *KLL* peak at 273 eV. However, the coverage of carbon can nevertheless be determined, using the fact that the C_{KLL} peak is strongly asymmetric whereas the Ru_{MNN} peak is symmetric. The asymmetry of the overlapping peaks at 273 eV can therefore be used as a measure of the carbon coverage.[33–35] The black spectra in fig. 2.6 were obtained from a carbon contaminated Ru sample, and the asymmetry ratio r is 1.35 (r is the intensity ratio of the upper to the lower half of the signal). The red spectra were recorded after three preparation cycles. The asymmetry ratio has decreases to 1.27, which is in the expected range from 1.26 to 1.29 for a clean Ruthenium surface.[35,36] Besides carbon, oxygen and nitrogen are detected on the contaminated sample which are removed by the preparation cycles, as it is shown in the detail spectra in figure 2.6 (c) and (d).
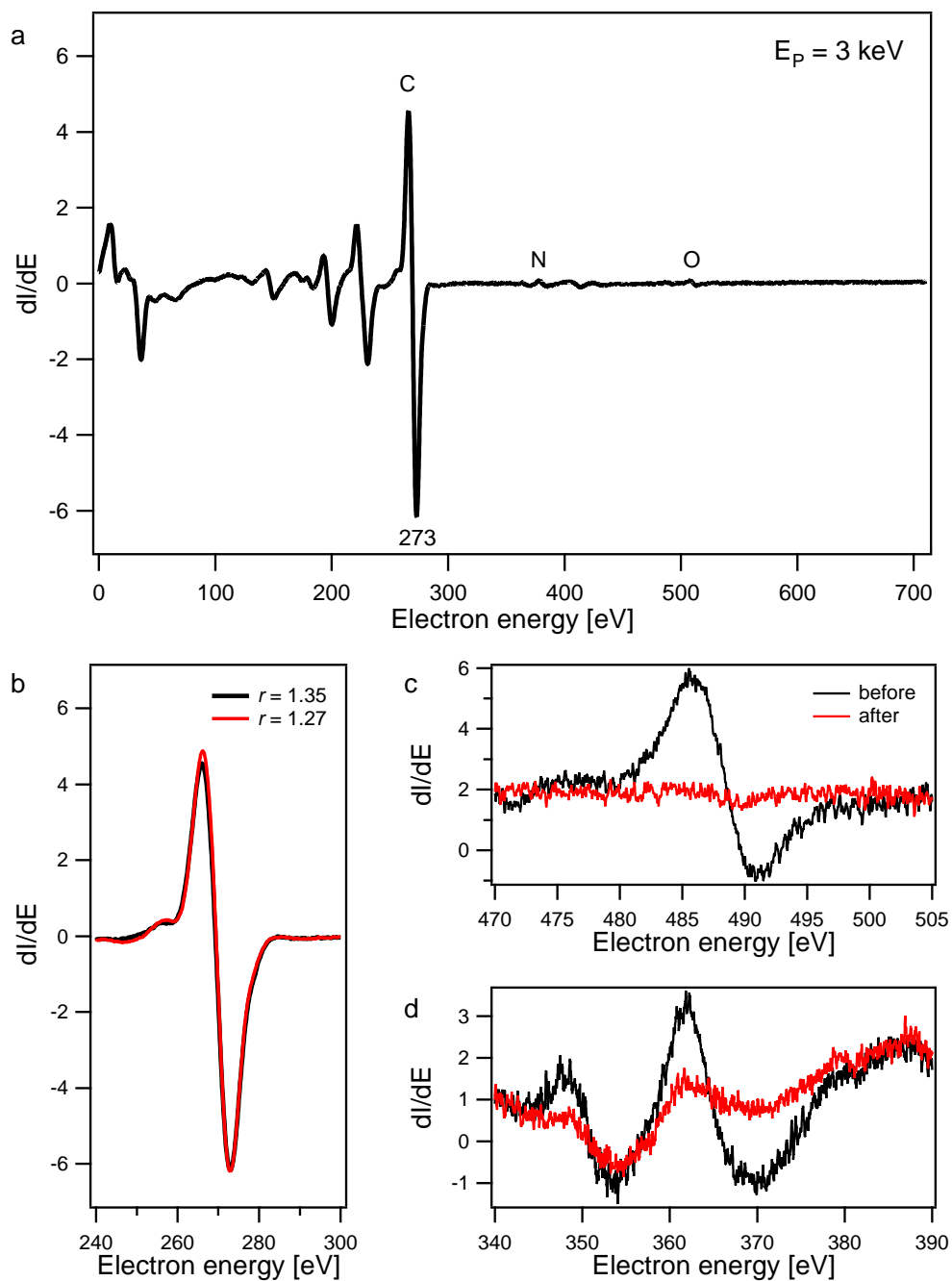
Figure 2.6 : AE spectra of the Ru(0001) sample, contaminated (black) and after three preparation cycles (red), a) overview spectrum, b) peak at 273 eV before and after the preparation, with asymmetry ration r, c) oxygen signal, d) nitrogen signal; kinetic energy of the incident electrons was 3 kV in all spectra.

3. Investigation of Carbon Species from Carbon Evaporation

There are three methods for preparing carbon species on surfaces described in the literature. A first method is the dosing of hydrocarbon molecules, like ethylene, methane, or ethane, on the surface and dehydrogenating the molecules at elevated temperatures. In this way, carbidic carbon structures[37,38] or graphene have been prepared on several metallic surfaces like Pt, Co, and Ru.[39–41] A second approach is the segregation of carbon from the bulk. In a low temperature STM study, Shimizu et al. investigated single carbon atoms on the Ru(0001) surface segregated from the bulk.[42] The segregation method can also be used for the growth of graphene on Ru(0001).[35,43] The third method is carbon evaporation. This technique makes it possible to grow carbon films of various thicknesses.[44] In a low energy electron microscopy (LEEM) study, Loginova et al. using the the evaporation method showed that graphene grows by attachment of carbon clusters to the edges of the growing graphene layer.[45] However, the nature of the carbon species that impinge on the surface from the evaporator, i.e., C atoms or cluster of several C atoms, is still an open question. Moreover, in order to study diffusion processes, very low concentrations of surface carbon are needed. It is, therefore, necessary to be able to control the amount of surface carbon created by a given method. In the present work, the preparation of carbon by evaporation has been investigated.

Figure 3.1 (a) shows a drawing of the installed electron beam evaporator *EFM 3* from *Focus GmbH*. (2) is a Cu cooling shroud in the center of which the carbon target is held (1). The evaporator has feedthroughs for the filament/thermocouple control (4), the high voltage (6), the flux monitor (5), and cooling water (3). It also has a linear motion drive (7) that moves the target inside the cooling shroud, and a shutter actuator (8); both are operated by hand. Figure 3.1 (b) is a sectional drawing that shows the inside of the cooling shroud. Under working conditions, a current I_{fil} [A] is applied to the filament, and a high voltage is set between the filament and the carbon rod that accelerates electrons onto it. The emission current I_{emis} [mA] serves as a parameter of the heating rate of the target. The evaporation rate is measured by the flux current I_{flux} [nA]. A certain fraction of the evaporated material is ionized by the electrons used for the heating. At the outlet opening of

the evaporator, these ionized atoms recombine with the current-carrying wire. I_{flux} is proportional to the amount of evaporated material. The sample is positioned perpendicular to the outlet of the evaporator at a distance of 2 cm.
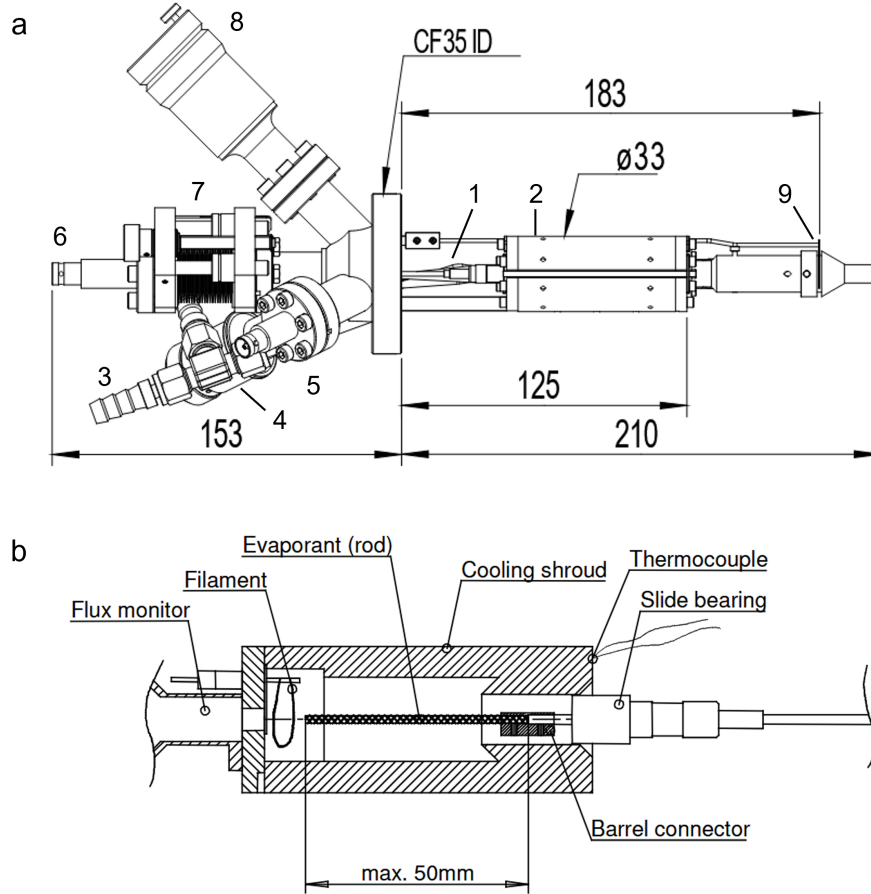
Figure 3.1 : Electron beam evaporator *EFM 3*, a) drawing of the electron beam evaporator with its components. 1: target holder, 2: copper cooling shroud, 3: cooling water, 4: filament/thermocouple feedthrough, 5: flux monitor, 6: high-voltage feedthrough, 7: linear transfer, 8: shutter actuator, 9: shutter.[46] b) sectional drawing showing the inside of the evaporator with evaporant (carbon rod), the heating filament and the flux monitor.[47]

In a research internship by Luca Camuti, the carbon target was installed in the evaporator and the amount of evaporated carbon was monitored with an X-ray photoelectron spectrometer (XPS). The experiments were performed in another UHV chamber equipped with XPS and sample preparation techniques for sputtering, oxidizing and heating. The sample was an polycrystalline Ag foil. The evaporation parameters, the filament current I_{fil}, the emission current I_{emis}, the flux current I_{flux}, and the evaporation time t_{evap}, were tested with respect to the observed carbon coverage on a Ag sample. A linear correlation of the carbon coverage and the product $I_{\text{flux}} \times t_{\text{evap}}$ was determined. The XPS measurements (with a non-monochromatic

x-ray source) revealed a single carbon peak with its maximum at 283.7 ± 0.3 eV, which lies in the range of atomic carbon.[40,48,49] However, aliphatic carbon species (C-C, C-H) cannot entirely ruled out. Still, it was concluded that atomic carbon is the most probable species ejected from the evaporator.

The carbon evaporator was then mounted to the UHV chamber equipped with the VT-STM setup, and the carbon species were investigated by scanning tunneling microscopy (STM). The carbon amount was monitored with AES. The experiments were performed with Au(111) and Ru(0001) single crystals as described in chapter 2.6. The initial aim of the carbon evaporating experiments was to produce single carbon atoms on the metal surfaces.
In the following chapter, the results on the carbon evaporation on Au(111) are presented and discussed, followed by the results on Ru(0001).

3.1. Carbon evaporation on the Au(111) surface

3.1.1. Carbon evaporation at room temperature

The Au(111) surface is known to form the so-called herringbone reconstruction. The topmost layer is contracted in one dimension, leading to a mismathch with the second layer. The atoms of the first layer alternating shift from fcc to bridge to hcp to bridge to fcc sites again with a regular periodicity of 22 unit cells. A $(\sqrt{3} \times 22)$rect superlattice results. The atoms close to the bridge sites are slightly higher than the atoms close to the fcc and hcp sites, which gives rise to two parallel, bright lines in the STM images. Figure 3.2 displays two STM images of the clean Au(111) surface; the left image shows the herringbone reconstruction on a larger scale over several terraces. In the top left corner of the image there are two screw dislocations. The saw tooth pattern of the atomic steps has the periodicity of the reconstruction which obviously has a certain restructering effect on the steps. The right image displays a smaller area of the surface and is recorded with atomic resolution. The stripes are the herringbone reconstruction, and the fine structure represents the gold atoms of the first surface layer. One can also see a bending in the stripe directions; these bends ("elbows") represent domain boundaries between rotational domains of the reconstruction. A detailed description of the reconstruction can be found, for example, in the dissertation of J. V. Barth.[50]

In this work, two Au(111) single crystals were used [Au(111)-1 and Au(111)-2]. If no specific temperature is noted, the images were recorded at room temperature.

The preparation method for a contamination free surface with large terraces has already been described in chapter 2.6.
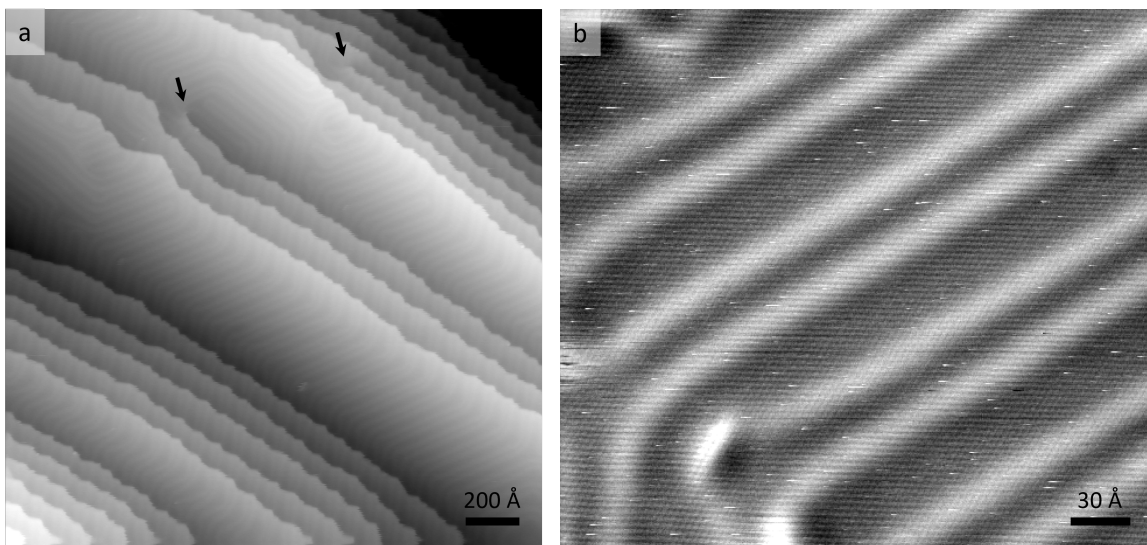

Figure 3.2 : The clean Au(111) surface (Au(111)-1 crystal). a) large overview with steps, terraces and screw dislocations (black arrows), $V_t = -1.0$ V, $I_t = 1$ nA, b) image of the Au(111) surface with atomic resolution, $V_t = -1.0$ V, $I_t = 1$ nA.

The first experiments to test the performance of the carbon evaporator were executed with Au(111) samples which are easy to clean and the reconstructed Au(111) surface is well known and usually well resolved in the STM measurements. The parameters of the evaporator, especially I_{flux}, which is proportional to the amount of evaporated carbon, were monitored. AES showed a peak at 262 eV caused by the KLL transition of carbon. (The peak position is shifted by 10 eV with respect to the literature value of 272 eV.[36] This offset is caused by an insufficient calibration of the AES instrument.)

In figure 3.3 (a), a series of AE spectra is shown after evaporation at a constant I_{flux} between 1.77-1.88 nA and evaporation times between 20 and 50 s. Carbon was evaporated cumulatively and AE spectra were measured after every run. The amplitude of the carbon peak (indicated in the figure with black lines) is taken as a measure of the carbon amount on the surface. (Note that the AE spectra are recorded in a derivative mode.) As expected, a rise in the carbon signal with evaporation time is observed.

In figure 3.3 (b), the measured peak intensities are plotted against the evaporation time t_{evap}. The blue series refers to the AE spectra in figure 3.3 (a). The data of the red series were acquired at a higher flux rate of 2.10-2.20 nA. Both data sets reveal a rather linear behavior of the carbon peak and evaporation time. At lower carbon coverage, the slope is somewhat lower, and at evaporation times above 100 s
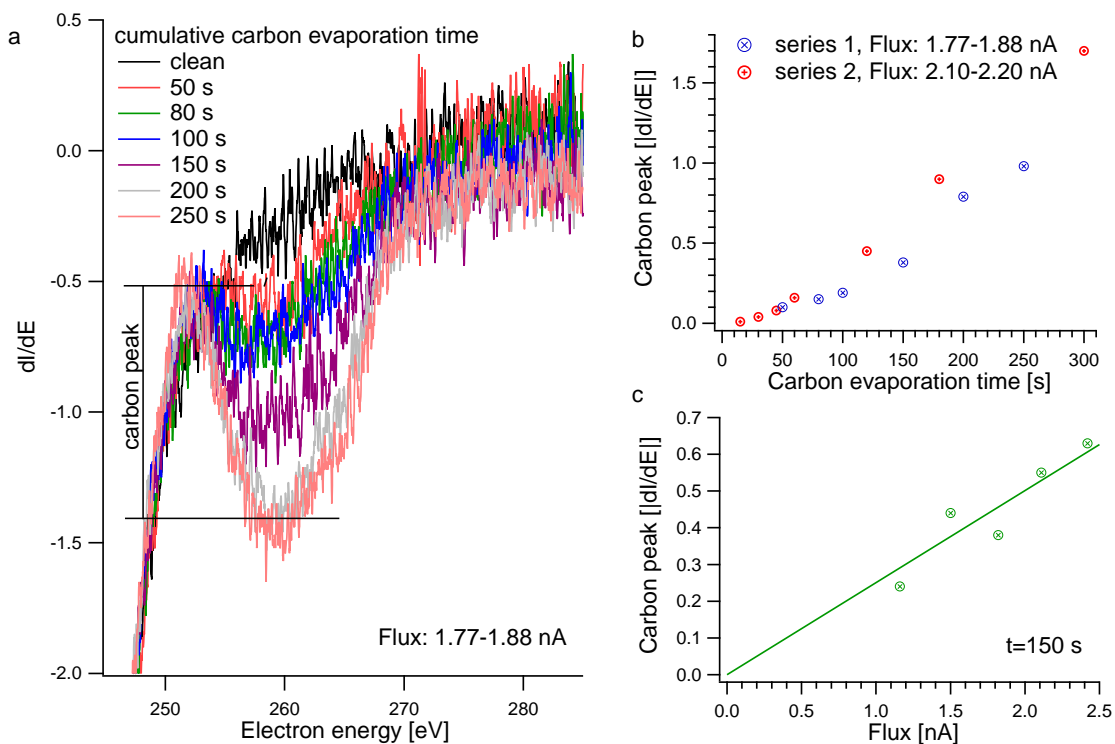
Figure 3.3 : Cumulative carbon evaporating series on Au(111) measuring the increase of the carbon peak in the AE spectra. a) AE spectra (series 1) for different carbon evaporation times, for the pink spectra the measurement of the carbon peak is marked, b) graph of two cumulative carbon evaporating series at different flux rates, c) graph of carbon peaks at different flux rates at constant evaporation time.

it becomes steeper. This is probably caused by the fact that the measurement of the carbon peak at low values is not precise. Further, it is noticed that the slope is higher at a higher flux value, i.e., a higher flux leads to a higher amount of carbon. This relation was further analyzed in another series of experiments.

In figure 3.3 (c), the intensity of the carbon peak is plotted versus I_{flux} while t_{evap} is held at 150 s. A linear relationship of I_{flux} and the amount of carbon on the Au(111) surface is detected. Hence, in the experiments described in the following, the product $C_{evap} = I_{flux} \cdot t_{evap}$ is chosen to describe how much carbon has been evaporated onto the sample surface.

The STM measurements presented in the following were performed after carbon evaporation at sample temperatures of room temperature or slightly above (≤ 50 °C). The STM image in figure 3.4 (a) shows a large area of the Au(111) surface. The characteristic herringbone reconstruction is clearly visible. The adsorbed carbon species are imaged as protrusions and are observed to accumulate at the elbows of the reconstruction. The features from short chains and consist of smaller spherical units (see figure3.4 (b)). The chains are mainly one unit wide and have

different lengths. It is also observed that several of the small units form clusters. Figure 3.4 (b) and (c) show more detailed STM images. One can see that the step edges are decorated by chains of the same spherical units. It is evident that the agglomerates consist of the uniform units. The average distance between the maxima in the chains is about 5.3-5.6 Å, which is too large for a carbon-carbon bond. The distance corresponds to approximately twice the Au lattice constant ($a_{\text{Au}} = 2.8$ Å). Further, the angles between the maxima in the chains are not uniform, which also indicates that the geometry is not defined by chemical bonds between the units.
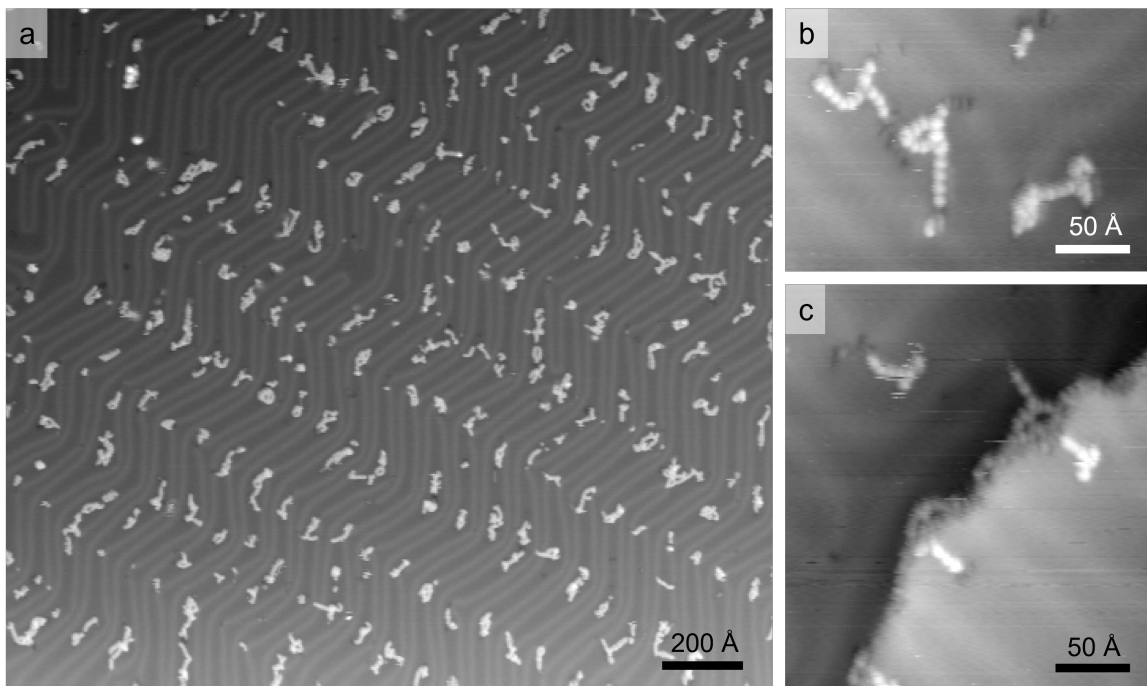
Figure 3.4 : Carbon evaporated on Au(111)-1. a) Large scale image of evaporated carbon, $V_{\text{t}} = -1.0$ V, $I_{\text{t}} = 1$ nA, $C_{\text{evap}} = 173$ nAs, b) and c) detailed images of carbon agglomerates on a terrace and at a step, $V_{\text{t}} = -0.2$ V, $I_{\text{t}} = 1$ nA, $C_{\text{evap}} = 143$ nAs.

The fact that the carbon species accumulate at the elbows of the gold reconstruction and at step edges indicates that the carbon species that hit the sample surface are mobile. A probable scenario is that carbon atoms or clusters impinge on the surface, and then move to the energetically most stable adsorption sites and agglomerate there, forming longer chains. Whether the mobile species are single atoms or clusters of several carbon atoms cannot easily be determined.

3.1.2. Carbon evaporation at low temperature

By evaporating carbon onto a cooled sample surface, the fast thermal diffusion processes of the impinging species can be slowed down or even prevented. In this

section, the species produced by the carbon source is further characterized at sample temperatures between −155 °C and −20 °C.

In these experiments, the Au(111) sample was cooled in the manipulator to −145 °C and carbon was evaporated onto the cold surface. The cold and carbon-covered sample was then transferred to the already cold mounting stage of the STM. During transfer, the sample temperature might have increased by a few degrees. The STM image in figure 3.5 shows the sample surface at −155 °C. Several aspects are noticeable when one compares the features with those in the room temperature experiments (figure 3.4). Firstly, the bright features are smaller, and no chains have been formed on the surface. Secondly, the features are not exclusively adsorbed in the elbow regions of the herringbone reconstruction, but they are more or less statistically distributed over the surface. Third, the features are not uniform, and there are still several species of different sizes. The rather large white feature in the middle of figure 3.5 is probably caused by the scanning motion of the tip that accumulated the smaller features in a pile. In other regions more of these features are observed.
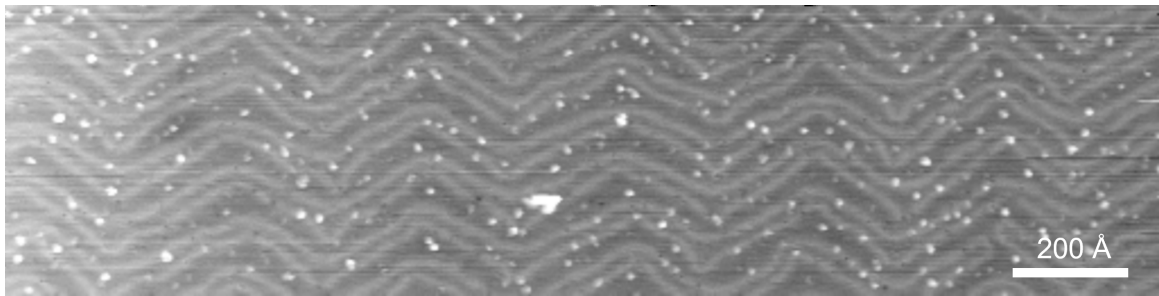
Figure 3.5 : Carbon evaporated on the cold Au(111)-1 surface. STM image recorded at −155 °C, $V_t = -1.0$ V, $I_t = 1$ nA, $C_{evap} = 75$ nAs at −140 °C.

It is not possible to assign a defined species to each feature in the STM images. However, the smallest round features might be assigned to single carbon atoms.

Figure 3.6 shows the sample surface at −20 °C. The carbon features are slightly larger, and only a few longer chains are observed. The distribution of the features has changed as more of the features are positioned in the low-energy adsorption sites of the herringbone reconstruction. One can conclude that the smaller species are mobile even at relative low temperatures, diffuse to low-energy sites, and aggregate to form larger features. It can be concluded that evaporation at a sample temperature of ≤ -140 °C at least partially produces atomic carbon.

Further, it can be said that on the Au(111) surface, the single carbon atoms (or even small clusters of undefined size) are mobile within a temperature range of −155 °C
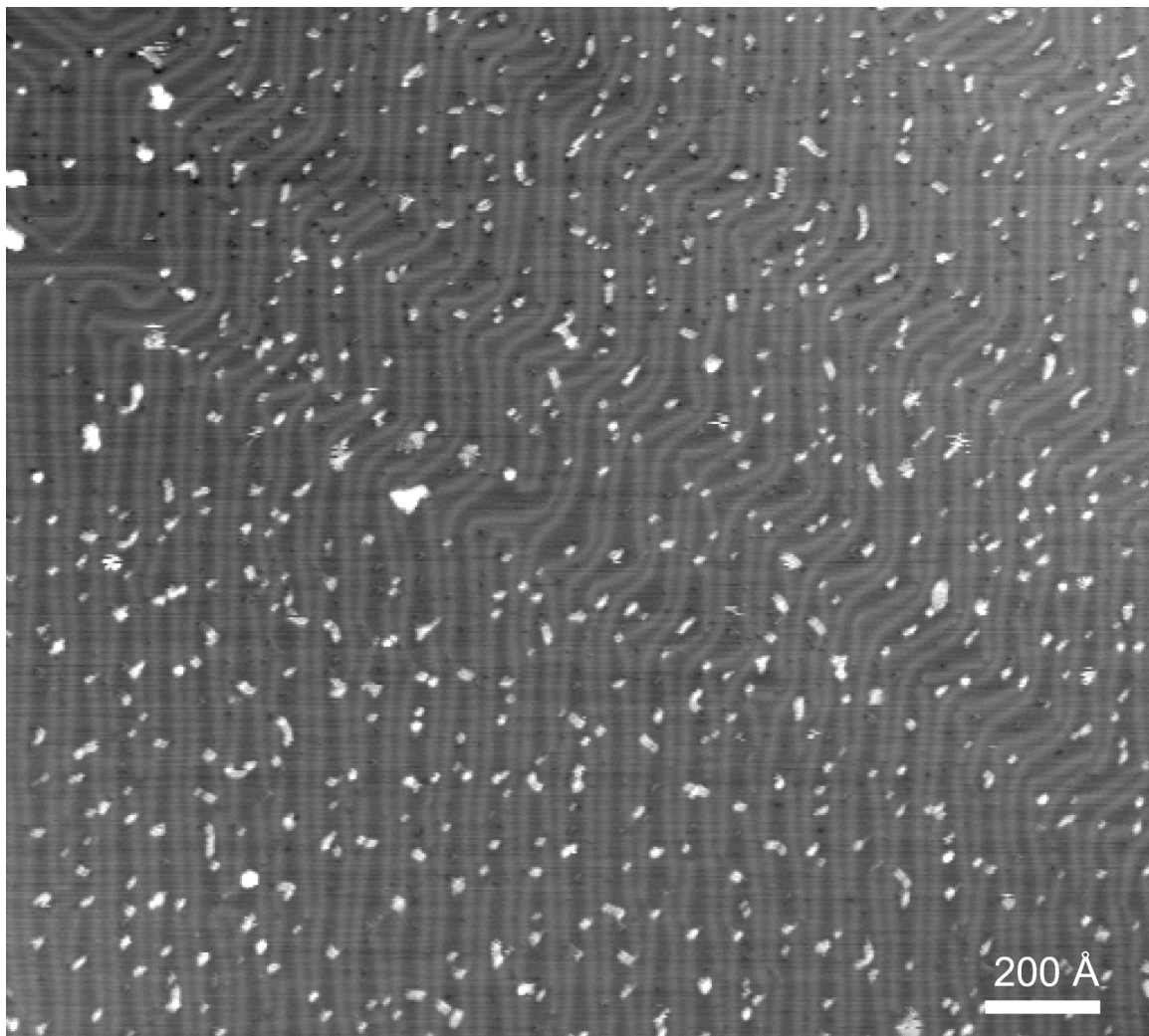
Figure 3.6 : Carbon evaporated on the cold Au(111)-1 surface and then heated
to the recording temperature of -20 °C, $V_t = -1.0$ V, $I_t = 1$ nA, $C_{evap} = 75$ nAs
at -140 °C.

to room temperature. At room temperature, the carbon is already accumulated
into clusters, and chains of aggregates have formed at the elbows of the herringbone
reconstruction where they are no longer mobile.

3.1.3. TDS of the clean and carbon covered Au(111) surface

In this subsection, the thermal desorption experiments of the clean and the carbon-
covered Au(111) surface (Au(111)-2 crystal) will be described and discussed.

In these experiments, the Au(111) sample was cooled by liquid nitrogen in the ma-
nipulator, and carbon was evaporated on the cold surface. In the TDS measurement,
the masses (m/z) 2, 12, 16, 18, 28, 32, and 44 were monitored. These m/z ratios
cover hydrogen, water, CO, O_2, N_2, CO_2. The temperature was ramped manually
from -158 °C to 726 °C. In figure 3.7, TD spectra of a clean (a) and a carbon-

covered Au(111) surface (Au(111)-2 crystal) (b) are displayed. The initial peaks of the masses 2, 18, and 28 (hydrogen, water, and carbon monoxide) are background-related and most likely come from the heating filament. These peaks are followed by a slightly wider second peak (between 200 °C and 400 °C) that is assigned to molecules that desorb from parts of the manipulator or sample holder that get also warm.
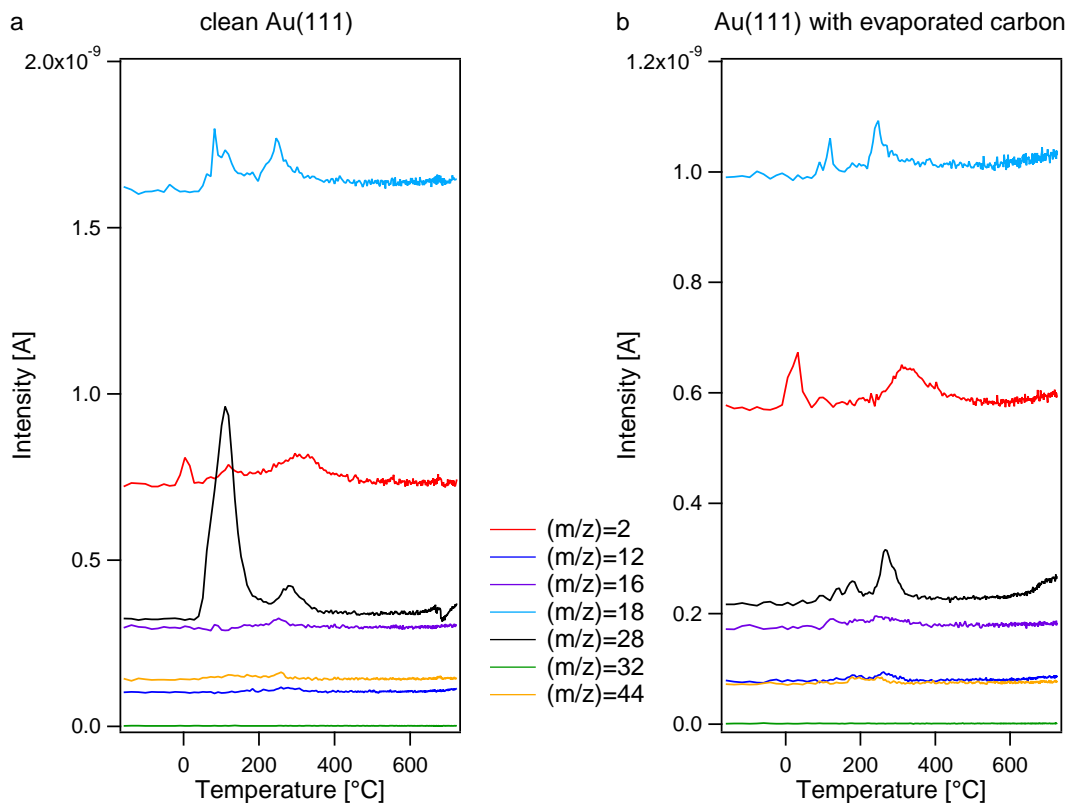
Figure 3.7 : TD spectra from the clean Au(111) surface and the Au(111) surface with evaporated carbon, $C_{evap} = 400$ nAs at -160 °C.

The desorption spectra of the clean and the carbon-covered surface show the same characteristics; the peaks have the same size and arise at the same temperatures. The shapes of the first peaks, when the heating filament is turned on, varies somewhat between the two measurements, and there is also a small difference in the intensities due to the different background pressures at the two measurements. However, no extra peaks can be recognized in the spectra that would be caused by the evaporated carbon.

Since no difference in the spectra and especially no additional hydrogen signal is observed in the TD spectra of the carbon-covered Au(111) surface, the evaporator does not produce any (desorbing) impurities.

3.2. Carbon evaporation on the Ru(0001) surface

3.2.1. Carbon evaporation at room temperature

In this section, the observed carbon species on the Ru(0001) surface are analyzed, and in the following chapter 4, the focus is on one special species and its surface diffusion.

As expected from the previous experiments on Au(111), after evaporation on the Ru(0001) surface in the AE spectra carbon is detected. Because, as discussed in chapter 2.6, the Ru and carbon Auger peaks overlap the carbon amount was estimated by the asymmetry of the peak. The oxidation state of the carbon cannot be determined by AES. Also, the amount of carbon cannot be quantified exactly. The AE spectra of the Au(111) sample showed a linear behavior between carbon evaporation time and the carbon signal (figure 3.3). The data from higher carbon doses were extrapolated to find parameters at which low carbon coverages can be generated. For the evaporation of carbon on the Ru(0001) surface, dosages of 10 to 100 nAs were chosen, at sample temperatures $\leqq$ 50 °C.

In figure 3.8, two STM images of the carbon-covered Ru(0001) sample with different amount of evaporated carbon (76 nAs and 20 nAs) are displayed. As already observed in the case of Au(111), the step edges are decorated with bright features (figure 3.8(a)), but also on the terraces, bright features are observed. The bright features are assigned to carbon, as carbon is also imaged bright on the Au(111) surface. Some dark dots are assigned to nitrogen atoms. In all experiments with the Ru(0001) sample, a small amount of N atoms was detected, the origin of which could not be clarified. From other experiments, it is known that also a small amount of oxygen atoms is on the surface, which in the slow constant current mode of the STM, are imaged as black stripes due to their high mobility. Besides these minor contaminations with N and O, the surface is covered with at least three different bright species that originate from the carbon evaporation procedure.

The smallest detected units are elliptic with average lengths between 2.3 Å and 5.7 Å depending on the condition of the STM tip; two of these particles is marked with a red arrows in figure 3.8. Under certain conditions, the particles show two maxima (detailed figure 4.2 in chapter 4.1.2). There are three distinct orientations of the elliptic particles corresponding to the equivalent directions of the hexagonal Ru lattice. Further, some of these particles arrange in longer straight chains in which the single units are still distinguishable, marked by black arrows in figure 3.8.
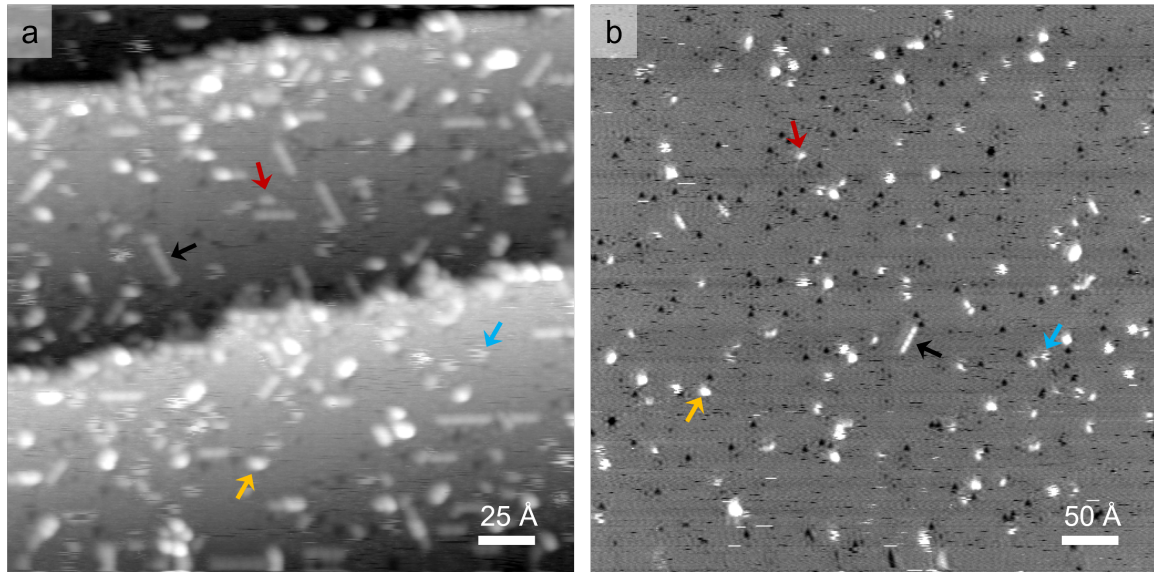
Figure 3.8 : Carbon evaporated on the Ru(0001) surface, a) area with atomic steps, $V_t = -1.0$ V, $I_t = 1$ nA, $C_{evap} = 76$ nAs at $T_{sample} = 50$ °C, b) on a terrace with a lower amount of evaporated carbon, $V_t = -0.4$ V, $I_t = 1$ nA, $C_{evap} = 20$ nAs at $T_{sample} = 35$ °C; one of each carbon species is marked with an arrow: an elliptic particles in red (a chain of elliptic particles in black), a larger particle in yellow and a dynamic particle in blue.

In addition, there are larger features which have mostly spherical shapes and an increased height (brighter in the STM image), yellow arrows in figure 3.8. A third species forms stripes with fuzzy borders (blue arrows), indicating that these species are dynamic and change their configuration in the time the tip takes to scan over the particle.

In TDS measurements of the clean Ru(0001) sample, the desorption of adsorbates from the surface was investigated. The TDS shown in figure 3.9 was recorded after a complete preparation cycle (containing sputtering, annealing, an oxidation step, and a high temperature flash - detailed description can be found in subsection 2.6.2). The spectra reveal hydrogen, although no hydrogen has been dosed. In addition, there is a rather large peak of mass 28 assigned to carbon monoxide, and the mass 12 belongs to the fragmentation of CO. Also, a small amount of mass 18 is detected that can be assigned to water.

It is concluded that the hydrogen and carbon monoxide adsorb on the sample surface from the background pressure of the UHV chamber despite a base pressure of $< 1 \times 10^{-10}$ Torr. This could not be prevented. As a consequence, from the fact that there is a significant amount of hydrogen on the Ru(0001) surface, one has to expect chemical reactions with the evaporated carbon.
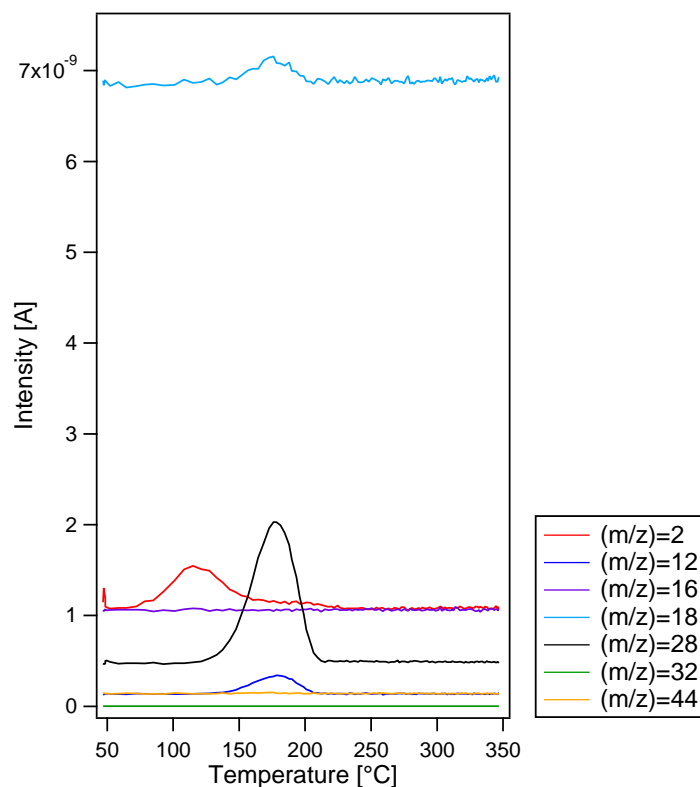
Figure 3.9 : TDS from the clean Ru(0001) surface. Recorded after a full preparation cycle and cooling the sample to 50 °C.

The STM images of the Ru(0001) surface with evaporated carbon reveal no features that can be attributed to carbon in atomic form. Single carbon atoms are expected to be visualized by STM as small, round (not elliptical) particles. In STM work by Shimizu et al., carbon atoms were prepared on a Ru(0001) surface by segregation from the bulk, and the measurements were performed at a low temperature (−267 °C).[42,51] The C atoms appeared as black features, i.e. as depressions. This finding stands in contrast to the protrusions observed in the STM images of carbon on Au(111) and to the bright features on the Ru(0001) surface. However, in the study by Shimizu et al., the surface species CH was imaged as a depression with a central bright maximum.[42] Consequently, the bright features in the STM images of the Ru(0001) sample (figure 3.8) are probably hydrogenated carbon species. Whereas the bright appearance of the carbon species on the Au(111) surface is more difficult to explain, since the TD spectra show no desorption of hydrogen.

In the room temperature experiments on the Au(111) surface, the impinging carbon species were concluded to be mobile, and this is probably also the case for the Ru(0001) surface. This could mean that the images recorded at room temperature no longer show atomic carbon but a modified state that is energetically more stable.

3.2.2. Carbon evaporation at low temperatures

In order to analyze whether the carbon species are formed by smaller units produced by the carbon evaporator, low-temperature evaporation experiments were performed on the Ru(0001) surface, like on the Au(111) surface. By evaporating carbon on the cold sample surface, thermally activated reactions (like a possible reaction of carbon and hydrogen) might be prevented or at least slowed down.

In these experimental, the clean Ru(0001) sample was cooled by liquid nitrogen in the manipulator to temperatures between -150 °C to -170 °C, and then carbon was evaporated onto the surface. Subsequently, the sample was transferred to the cold sample stage of the STM. (As the sample holder sometimes got stuck in the manipulator, the sample was first thawed to temperatures between -130 °C and -120 °C before it was transferred).

Figure 3.10 shows the Ru(0001) surface after the sample had cooled to -203 °C, and a large number of different features is observed. An assignment of all the features to specific molecules or atoms is not possible. However, some of the features are known from earlier experiments and can be assigned. There are dark small round particles that can be assigned to nitrogen or oxygen atoms, as mentioned above. Further, there are a few areas in the left and beneath the center of the image, where an ordered $(\sqrt{3} \times \sqrt{3})R30°$ superstructure can be identified that, based on the detection of CO in the TDS, can be assigned to CO. Besides these known features, there are small bright particles and larger bright features with rather undefined shapes. The bright imaging of these features indicates that they might be assigned to hydrogenated carbon species. The small particles seem to be immobile, while the larger features display somewhat fringed edges, which indicates that they might be mobile at the recording temperature of -203 °C.

The four STM images in figure 3.11 are single frames from STM movies recorded in the fast scanning mode. Because these images were recorded with negative tunneling current in the constant height mode, the image contrast is inverted with respect to the constant current images. Bright particles correspond to the dark features in the slow images and are assigned to oxygen or nitrogen atoms. The bright carbon-containing features are imaged dark in the constant height mode. As in the STM images above, the $(\sqrt{3} \times \sqrt{3})R30°$ superstructure of CO is detected in some areas (figure 3.11 (a)). The CO molecules are imaged dark grey. Even at -203 °C, mobile CO molecules are observed that attach and detach from the $(\sqrt{3} \times \sqrt{3})R30°$ islands. In the STM movies, it is further noticed that the applied tunneling voltage
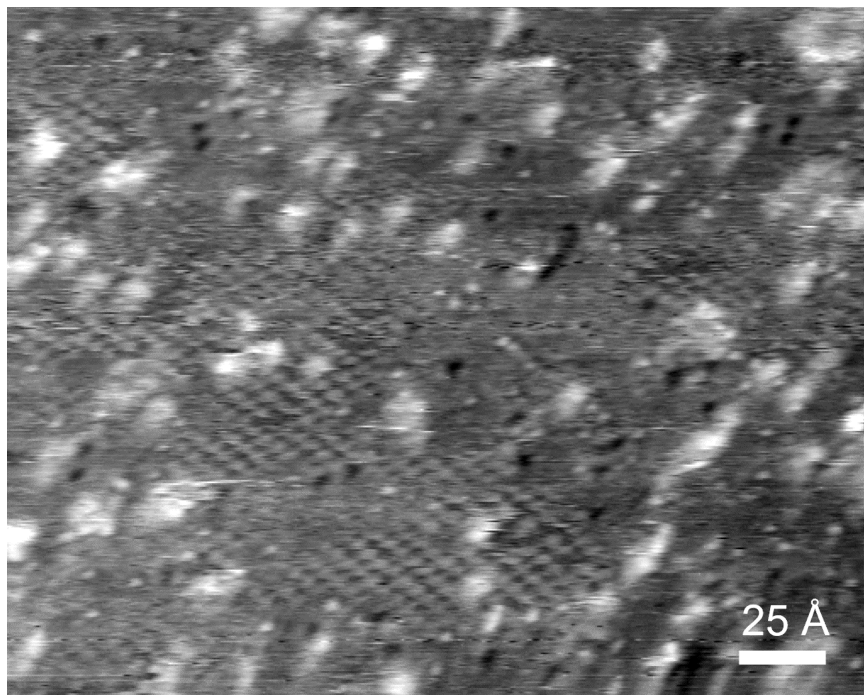
Figure 3.10 : STM image of the Ru(0001) surface with evaporated carbon on the cooled sample surface, recorded at $T = -203$ °C, $V_t = -1.0$ V, $I_t = 1$ nA, $C_{evap} = 20$ nAs at $T_{sample} = -170$ °C.

influences the mobility of the CO molecules on the surface, as a change in V_t can induce a change in the velocity of the CO molecules.

The main features, besides the CO molecules and some bright nitrogen or oxygen atoms, are small black particles that are immobile at a temperature of -203 °C (figure 3.11 (a) and (b)). In the images of figures 3.11 (c) and (d), the temperature has been increased to -77 °C. Figure 3.11 (c) was recorded with a somewhat unusual state of the tip in which the dark features in (a) and (b) appear bright with a dark rim. At this temperature, the particles are mobile but they clearly behave differently than the CO molecules that form a $(\sqrt{3} \times \sqrt{3})R30°$ superstructure and attract each other; these particles do not interact with each other. Figure 3.11 (d) shows a change in the state of the tip (the dark horizontal line in the upper half) after which the bright features changed to the more usual dark appearance. The exact configuration and state of the tip are never known in STM experiments. A metallic tip and a tip with an adsorbed molecule, can lead to very different images. Moreover, the tip state is often dynamically changing during the scanning procedure. The larger immobile features with different round shapes cannot be attributed to any specific adsorbates, but these particles most probably consist of several C atoms since they are imaged large, and hydrogen as a component is also possible.
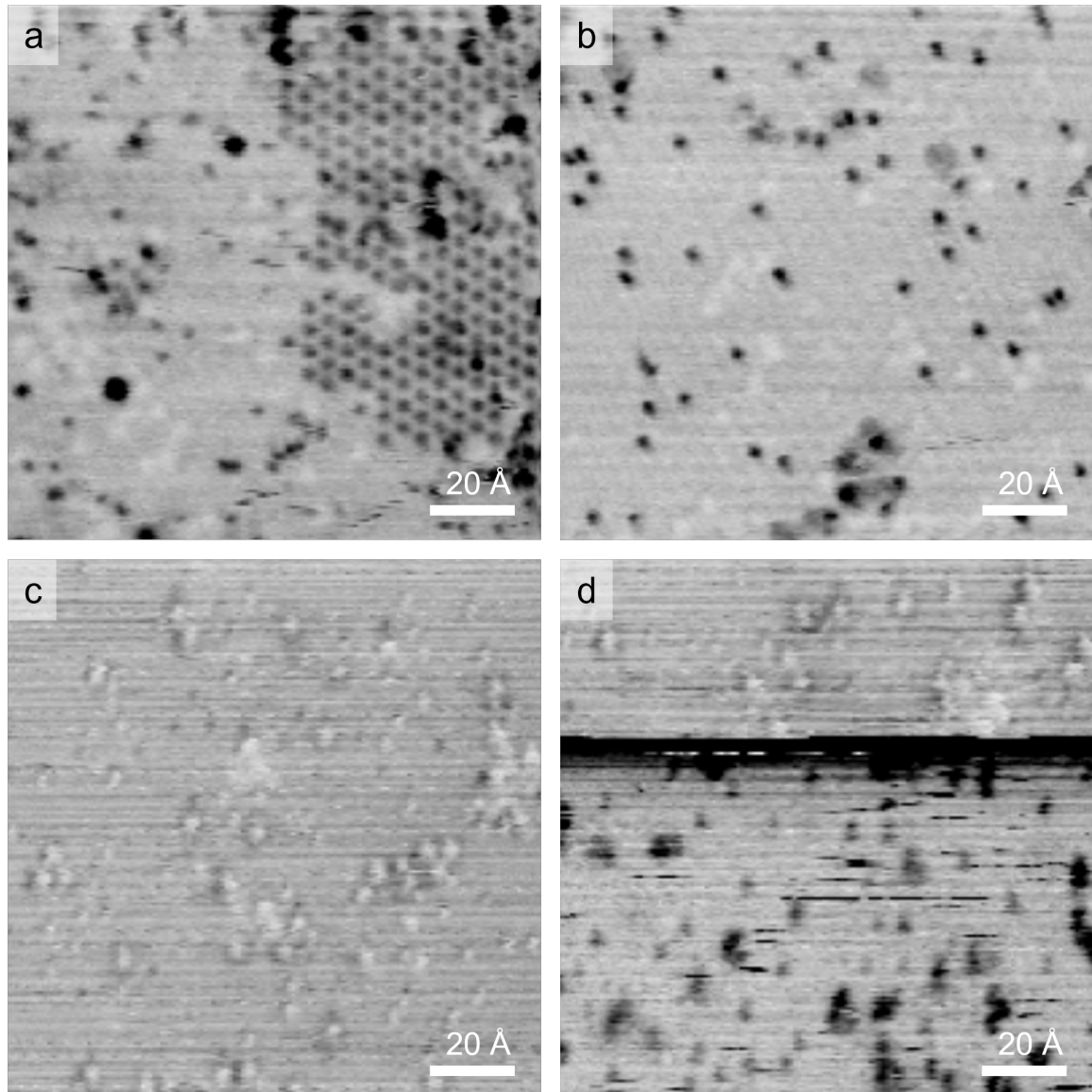
Figure 3.11 : Single frames from STM movies of the Ru(0001) surface with evaporated carbon on the cold sample surface, $C_{evap} = 20$ nAs at $T_{sample} = -170$ °C. a) and b) recorded at $T = -203$ °C with $V_t = -1.0$ V, $I_t = 3$ nAs, 10 fps c) and d) recorded at $T = -77$ °C with $V_t = -0.2$ V, $I_t = 3$ nA, 10 fps.

The elliptic particles that are observed at room temperature are not detected in the low-temperature evaporation experiments at -203 °C and -77 °C. This means that the formation of these particles is thermally activated. In a further experiment, carbon has been evaporated onto the cold Ru(0001) surface ($T = -170$ °C), and after T has increased to room temperature, STM measurements were performed. In the STM images in figure 3.12, the elliptic particles are present and observed as small bright particles in the constant current images (figure 3.12 (a)) and as black elliptic particles in the STM videos (figure 3.12 (b)) in the three different orientations defined by the Ru(0001) surface (red arrows). In addition, the surface is covered with CO molecules ordered in the $(\sqrt{3} \times \sqrt{3})R30°$ superstructure and some small islands of the (2×2) superstructure of oxygen atoms are observed (the high temperature flash in the preceding preparation cycle after the oxidation step was probably not sufficiently high enough).
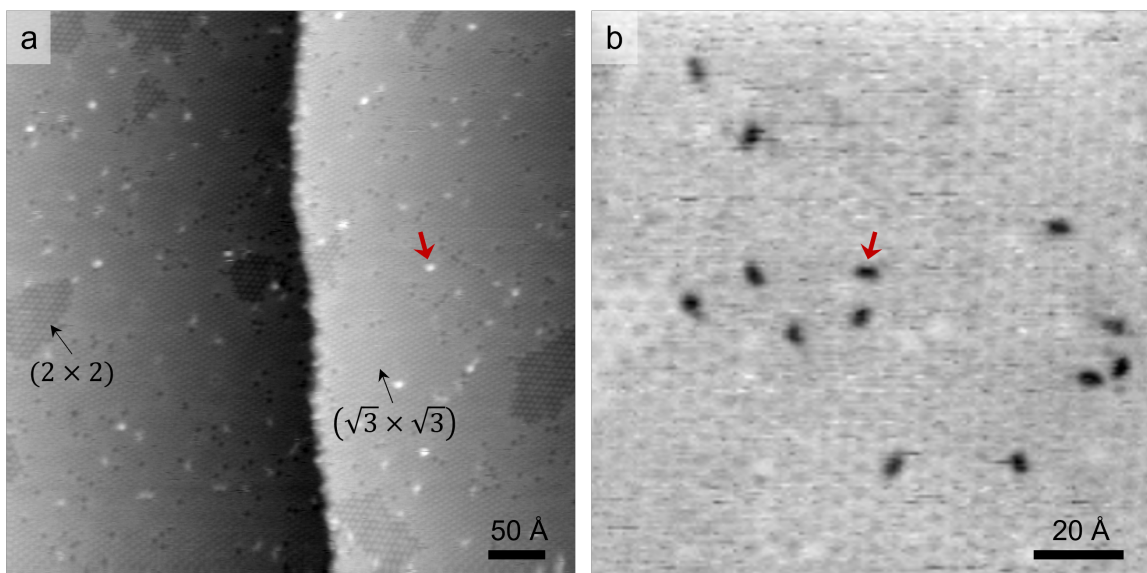
Figure 3.12 : STM images of Ru(0001) with carbon evaporated on the cold surface, $C_{evap} = 13$ nAs at $T_{sample} = -170$ °C, recorded at room temperature after the sample has thawed to room temperature a) STM image in slow constant current mode with $V_t = -0.2$ V, $I_t = 1$ nAs, b) STM frame from movie recorded in the fast scanning constant height mode with $V_t = -1.0$ V, $I_t = 3$ nA, 10 fps.

In the movies recorded at room temperature, it was observed that the elliptic particles change between the three orientations on the hexagonal surface, but do not diffuse laterally. This rotational motion and further diffusion processes, as well as the atomic composition of the molecule, are the subject of chapter 4.

3.3. Conclusion from the investigations of evaporated carbon

The original plan was to prepare carbon in atomic from on a metal surface. For this purpose a carbon evaporator was installed at the UHV chamber, and the species that resulted on the surfaces were analyzed. In the first set of experiments, carbon was evaporated on Au(111) samples. The amount of carbon was determined by AES, and the surface species were imaged by STM. In a second set, carbon was evaporated on a Ru(0001) sample, and the resulting species were also investigated by STM.

A first characteristic of the carbon species is that the adsorbed particles on the Au(111) surface are imaged as protrusions. The features consist of small (probably atomic) units that agglomerate at the elbows of the herringbone reconstruction of the Au(111) surface, and at the atomic step edges. In low-temperature experiments, the formation of agglomerates was not observed. Instead, smaller features were present on the surface that could be interpreted as single carbon atoms. When the surface was heated, similar agglomerates than those obtained by room temperature evaporation were observed. It is concluded that the species most probably emitted by the evaporator is atomic carbon, that is mobile on the Au(111) surface.

In the carbon evaporation experiments on the Ru(0001) surface, the observed surface species also appear as protrusions. Up to three different features can be distinguished, the smallest one is an elliptical particle that adsorbs in the three crystallographic directions on the hexagonal Ru(0001) surface. The two other species are larger. One is immobile, and the other one is imaged with fuzzy borders but shows no lateral mobility. Both species probably consist of several C atoms plus, possibly, hydrogen and display ill-defines shapes. The exact nature of these species could not be identified, and the further project focused on the elliptic particles.

In experiments in which carbon was evaporated on the cold Ru(0001) sample, the features assigned to carbon were smaller, and possibly one of the species is atomic carbon. However, this could not finally be concluded. TDS measurements revealed that hydrogen is present on the freshly prepared Ru(0001) sample, and therefore, a possible reaction of carbon with hydrogen to give hydrocarbon molecules cannot be excluded. Even in the low-temperature measurements, the imaging contrast of the detected particles indicates that the carbon is already hydrogenated. From the literature, CH fragments are expected to be displayed as protrusions with a dark

rim. Since the carbon species were (mostly) imaged as protrusions in the present work, it is concluded that the carbon is in some way hydrogenated.

The formation of the elliptic particle is thermally activated. However, the exact molecular nature of these particles is not known and is the subject of the following chapter 4.

Altogether, from this chapter 3, it can be concluded that the carbon source at least partially produces atomic carbon. However, at room temperature atomic carbon is no longer present on the surface, as it immediately forms agglomerates on Au(111) or stable hydrocarbon molecules on Ru(0001).

In contrast to the other carbon features, the elliptic species on the Ru(0001) surface, are well-defined and display an interesting dynamic behavior. For this reason, they were investigated in quite some detail; the results are presented in chapter 4. As the ellipses often displace a fine structure consisting of two minima, we will call them *dimers*. This does not suggest that they consist of two C atoms (or CH_x fragments). As we will show, they are most likely larger.

4. Diffusion of a Small Hydrocarbon Molecule

In catalytic surface reactions, the reactants, their decomposition products, intermediates, and reaction products are adsorbed in atomic or molecular form on the catalyst surface. During a reaction, these particles must inevitably move across the surface to find their reaction partners or special (active) sites on the surface at which a critical reaction step takes place. Surface diffusion, the random walk of the adsorbed particles between adsorption sites, is, therefore, an important component in all catalytic reactions. For adsorbed atoms, a single jump event is usually a relatively simple process. On metallic surfaces, adsorbed atoms are mostly bound to a high-symmetry site such as a hollow or bridge site, and when an atoms jumps, the bonding configurations along the path across the transition state do not change fundamentally. The situation is more complicated for a molecule, since one or more bonds to the atoms on the surface can exist. In the transition state of a jump to a neighboring adsorption site, the bonding situation can differ from the molecule's ground state. Furthermore, rotational motions are possible. Very little is known about the complex processes that underlie surface diffusion of polyatomic particles. In the present work, surface diffusion of a hydrocarbon fragment on a Ru(0001) surface was studied. Using high-speed STM, the dynamics of the process could be investigated and by temperature-dependent measurements Arrhenius parameters could be determined.

In macroscopic diffusion studies, mostly the diffusion of atoms and of CO has been investigated. Examples are the diffusion of hydrogen atoms on a carbon- or sulfur-covered Ru(0001) surface[52,53], the diffusion of potassium atoms coadsorbed with CO[54,55], the diffusion of CO on Mo(110)[56], and the diffusion of CO coadsorbed with sulfur on a Ni(110) surface[57] and with hydrogen atoms on a Ru(0001) surface[58]. CO has a rather simple bonding geometry as it binds in most cases perpendicular to the surface, making rotations irrelevant. These macroscopic studies show that lateral interactions between the adsorbates play a dominating factor in the diffusion motion. This makes extracting of atomic processes difficult, especially at high coverages. In addition, since the measurements average over a large area, surface defects, i.e., atomic steps, can have a significant impact.

For surface diffusion on a microscopic level, STM is the most suitable tool.[25,59–61] However, STM is typically slow compared to dynamic processes occurring on surfaces. Only a few studies investigated thermal processes of adsorbed molecules on surfaces. Examples are the rotation of individual naphthalene molecules on Pt(111) studied at temperatures between −10 °C to 28 °C[62], and the diffusion of the large molecule PVBA ((4-trans-2-(pyrid-4-yl-vinyl) benzoic acid) on Pd(110) for which a strictly one-dimensional diffusion along the close-packed direction of the surface was found.[63]

Many STM studies on molecular dynamics have focused on non-thermal processes. The measurements were performed at low, mostly liquid helium, temperatures, and, processes were induced with the tunneling tip, usually by increasing the tunneling current or the tunneling voltage (and thus the energy of the electrons). For example, the surface dynamics of acetylene, a representative small hydrocarbon molecule, was studied on metal surfaces like Cu(100)[64] and Pd(111)[65] by low-temperature STM, at −265 °C and −268.45 °C respectively. The rotations of acetylene has been induced by tunneling electrons that excite vibration modes of the molecule.[66,67]

The literature regarding surface mobility is more pronounced for large organic molecules. The properties of these molecules can be tuned by changing the molecular composition, so that the binding geometry, the interaction with the surface, and the molecular motion can be studied by STM at cryogenic temperatures. The STM tip has not only been used for imaging, but also as a manipulating tool to induce lateral/vertical displacement or even to form or break bonds.[68] The rotation movement of a propeller-shaped molecule, HB-DC (hexa-tert-butyl decacyclene), on Cu(001) has been studied by Gimzewski et al.[69] In the group of C. H. Sykes, molecular rotors of the thioether family have been extensively studied. In these studies the tunneling electrons have been used to excite vibrations that drive the rotational motion of a specific molecule.[70–73] The STM experiments in these studies were all performed at temperatures below −173 °C. The ability to manipulate molecules and induce controlled lateral motion has been applied in a particularly sophisticated way by inducing the motion of the anthracene-based so-called nanocar.[74]

All these processes that have been studied at cryogenic temperatures by tip manipulation are no thermal processes, whereas the surface processes in catalytic reactions are thermally induced. Such processes are not accessible with these methods.

The STM setup used in the present work differs from the setups used in previous diffusion studies. The high-speed variable temperature STM works at two to three orders of magnitude higher rates than standard STMs, and it can operate over a

broad range of temperatures, between −223 °C and 227 °C. In the high-speed mode, movies consisting of several thousand images are recorded, making statistical evaluations possible. Kinetic parameters, i.e., activation energies and preexponential factors, can be determined as first demonstrated by Ann-Kathrin Kügler (Henß) for the diffusion of O atoms embedded in a CO layer on Ru(0001).[25]

In the present study, this method has been applied to a hydrocarbon molecule adsorbed on the Ru(0001) surface. It was found that the dynamic behavior of this polyatomic molecule is complex. The molecule does not move by lateral jumps, as in a classical translation diffusion, but by a combination of two rotational motions. In table 4.1, an overview of the applied STM settings is given.

Table 4.1 : Parameters applied in the diffusion study of the small hydrocarbon molecule on Ru(0001).

parameter	setting
scan frequency	2000 Hz
image size in pixels	(200×200) px
image size in Å	(150×150) Å
frame rate	10 Hz (10 fps)
temperature range	−13 °C to 124 °C

Several problems had to be solved in this study. One difficulty was separating the different orientations of the particles during their rotations in the automatic evaluation procedure. This was achieved by means of a detailed statistical analysis. Additional efforts were made to eliminate any influence of the tip (i.e., of I_t and V_t) on the thermal behavior of the molecules. The main challenge was determining the exact chemical composition of the molecule. It is a small hydrocarbon fragment, but the exact number of C atoms was unclear. By extensive investigations, it was possible to narrow down the possible size, but a definitive result has not been reached yet. The two rotational movements of the molecule displayed a clear compensation effect, a phenomenon known from various other processes in heterogeneous catalysis, but previously not observed in surface diffusion of adsorbed atoms or molecules.

4.1. Findings on the molecule from STM movies

### 4.1.1. Preparation by ethylene dosing on Ru(0001)

The molecule that is the object of this study, referred to as *dimer* particle, has been prepared in two different ways: by carbon evaporation and by ethylene dosing (table 4.2). In the carbon evaporation experiments, a small amount of carbon $(10 - 100 \text{ nAs})$ was dosed onto the freshly prepared Ru(0001) surface as described in detail in chapter 3.2. In the other set of experiments, which are described below, 0.25 L to 2 L ethylene were dosed onto the clean Ru(0001) surface. In both preparation methods, an increase in the asymmetry of the Ru *MNN* peak in the AE spectra indicated an increasing amount of surface carbon. The method of ethylene dosing could be controlled more precisely than carbon evaporation and was less time-consuming.

Table 4.2 : Overview of the applied parameters for the preparation of the *dimer* particles on the Ru(0001) surface.

	carbon evaporation	ethylene dosing
preparation parameters	$C_{evap} = 10 - 100 \text{ nAs}$	$0.25 - 2$ L ethylene
sample temperature	≈ 50 °C	≈ 50 °C
advantages	no hydrogen	fast, more precise
disadvantages	time-consuming,	several surface species
	several surface species	

Figure 4.1 shows two STM images of a freshly prepared Ru(0001) surface on which, after a final temperature flash to 350 °C, 2 L ethylene had been dosed at around 50 °C. The STM image in figure 4.1 (a) was recorded in the slow scanning constant current mode, and the STM image in figure 4.1 (b) in the fast scanning constant height mode. As already mentioned, the image contrast is inverted because of the negative tunneling voltage. The STM images show a high coverage of the elliptic (*dimer*) particles (red arrows) that are oriented in the three crystallographic directions of the Ru lattice (indicated by arrows in the lower left corner). Some of the *dimer* particles are arranged in rows of two to five particles, in which the particles are oriented with their long axes along the rows. In addition to the *dimers*, two other species are observed on the surface. There are somewhat larger round particles (yellow arrows) that are imaged brighter or darker than the *dimers*, according to the scanning mode. Some of these larger particles are also elliptic, which may be

interpreted as two particles on neighboring sites. The third species is better visible in the slow scanning mode (figure 4.1 (a)) (blue arrows). This species is imaged with fuzzy borders, indicating site exchanges on the timescale of the image. Two such particles are marked in figure 4.1 (b). However, the coverage of this species was much lower than the other two. It was, therefore, not included in the analysis of the carbon coverage (chap. 4.2.4). All three surface species have also been observed in STM images when carbon was evaporated on the Ru(0001) surface (see fig. 3.8 in chap. 3.2.1).
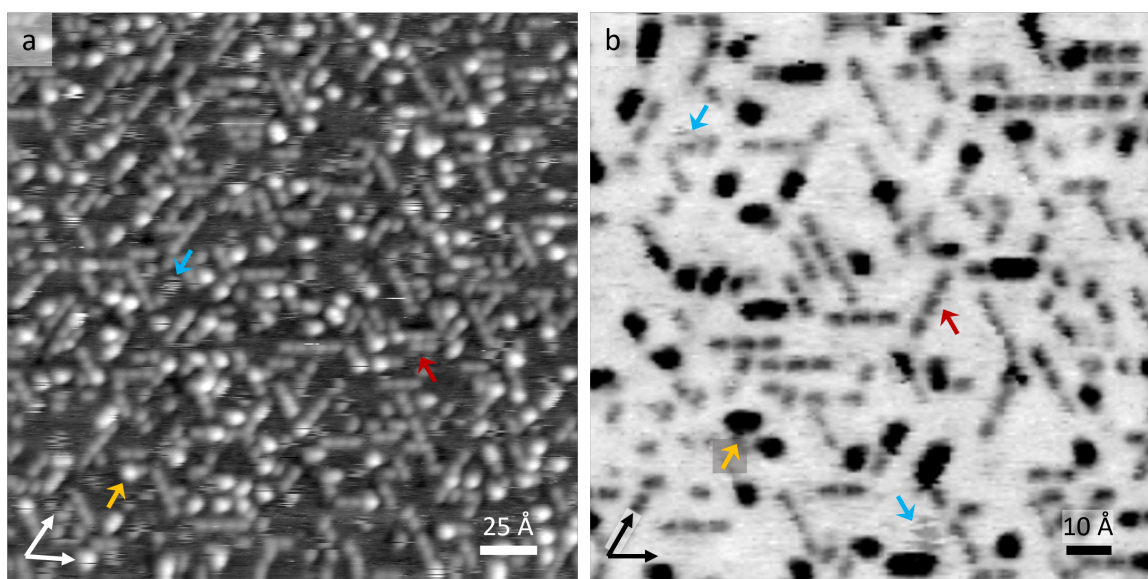
Figure 4.1 : STM images of Ru(0001) after dosing of 2 L ethylene at $T_{sample} = 50\,°C$, recorded at room temperature. a) STM image recorded in the slow constant current mode with $V_t = -0.2$ V, $I_t = 1$ nAs, b) STM frame from a movie recorded in the fast scanning constant height mode with $V_t = -0.2$ V, $I_t = 3$ nA, 10 fps. One of the three different species is marked with an arrow: elliptic particle in red, larger particle in yellow, and dynamic particle in blue (same color code as in figure 3.8); the orientation of the Ru(0001) surface is indicated by the arrows in the lower left corner.

In the carbon evaporation experiments, the presence of hydrogen on the surface led to the conclusion that the *dimer* particles are some hydrocarbon molecules. That the same features were observed after dosing of ethylene, which at this temperature is known to lead to a partial decomposition only, supports this conclusion.

4.1.2. Adsorption site of the molecule

The first piece of information contained in the STM data is the adsorption site of the molecule. The particles are found in three different orientations on the surface, and the STM shows that the particles jump between these three orientations. Figure 4.2 displays three STM frames that are one or two frames apart (corresponding to 0.1 s

or 0.2 s), which show the rotation. The central *dimer* particle jumps between the three orientations with respect to the red open circle that marks a fixed position in each frame. The red open circle is the center of rotation for that particle. When the molecule rotates, the centers of mass of the ellipse form the corners of an equilateral triangle (see model in figure 4.2 (d)). On a given terrace, all triangles point into the same direction (one corner up or down) and into the opposite direction on the next terrace. Figure 4.2 (d) shows a model of the Ru(0001) surface with two atomic steps. The threefold rotational symmetry of the Ru(0001) surface together with the A-B-A-B stacking of the lattice planes leads to the conclusion that the adsorption site of the *dimer* particles must be one of the threefold adsorption sites (hcp or fcc). In the displayed model, hcp was chosen arbitrarily, but the fcc counterpart is equally possible.
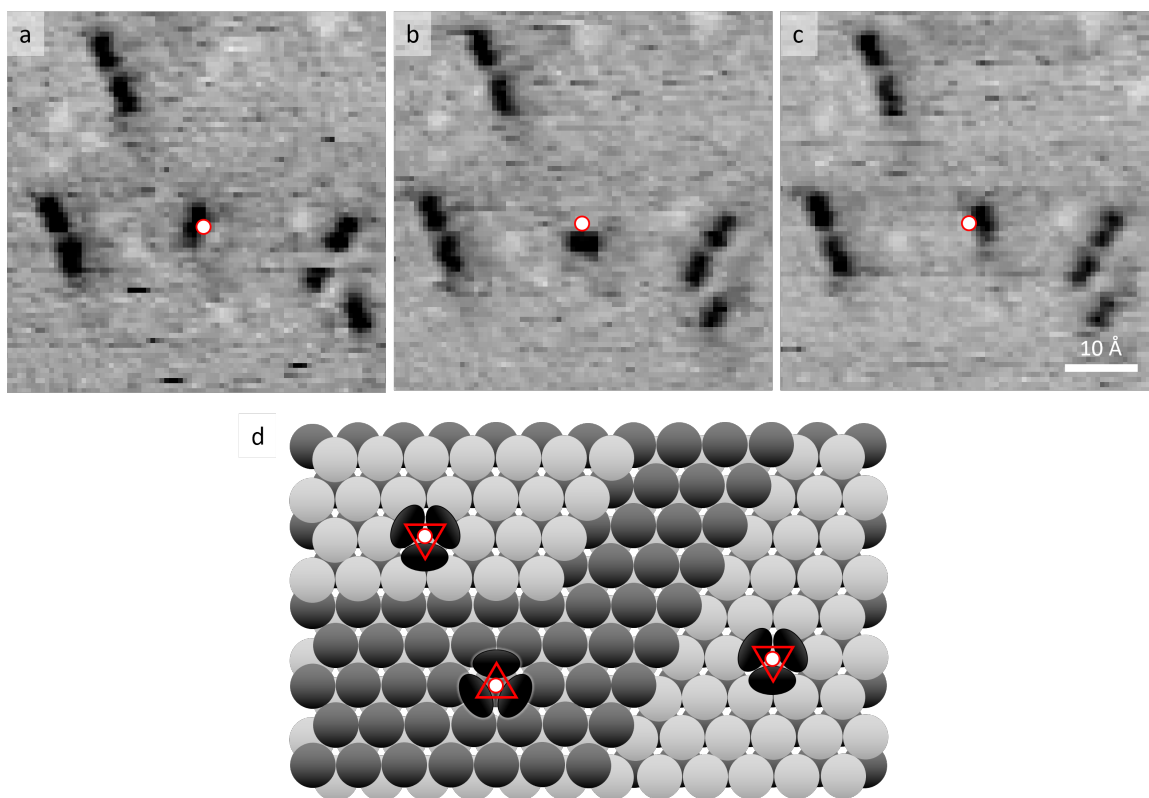
Figure 4.2 : a) to c) Three STM frames of the same area with eight *dimer* particles on the Ru(0001) surface, prepared by carbon evaporation, $C_{evap} = 40$ nAs. The central particle jumps between three positions with different orientation. The red open circle marks the same position in every frame, $V_t = -0.22$ V, $I_t = 3$ nA, 10 fps, $T = 30$ °C. d) Model of a stepped part of the Ru(0001) surface with a triangle of *dimer* positions on each terrace.

In order to gain more information on the adsorption site of the *dimer* particles, CO was additionally dosed on the surface. Dosing of 1-2 L CO leads to an ordered $(\sqrt{3} \times \sqrt{3})R30°$ superstructure on the Ru(0001) surface, in which all CO molecules adsorb on on-top sites. In some experiments, the CO superstructure was also observed

without CO dosing, as CO is a major component of the residual gas. Using the ordered structure of CO molecules around the *dimer* particles, one can determine their adsorption sites with higher precision than by the above analysis.

In figure 4.3, two different cases can be distinguished. In figures 4.3 (a)-(c), the center of rotation of the marked *dimer* particle is a lattice site of the $(\sqrt{3} \times \sqrt{3})R30°$ superstructure, which, as shown in the models (fig. 4.3 (d)-(f)), is a Ru on-top site. In figures 4.3 (g)-(i), the center of rotation is an interstitial site of the CO lattice, which, as shown in figures 4.3 (j)-(l), is also a Ru on-top site. Hence, in both cases, the *dimer* rotates around one Ru atom. The CO molecules are indicated in blue in figure 4.3. The red open circle marks the center of rotation, and the corners of the red triangle mark the positions of the centers of mass of the molecule. Next to the *dimer* molecule, not all positions are actually occupied by CO; in the models, these CO-free positions are colored in brighter blue. In the first case, the center of rotation of the *dimer* is assumed to be CO-free because configurations with more than one particle bound to the same metal atom are usually repulsive. In the STM images, this position often appears somewhat brighter than the CO molecules. In the second case, the $(\sqrt{3} \times \sqrt{3})R30°$ site closest to the *dimer* is assumed to be CO-free for the same reason. As a consequence, in this configuration, CO molecules have to move in order to enable a rotational movement of the particle. From DFT calculations, it is known that CO molecules highly fluctuate in the $(\sqrt{3} \times \sqrt{3})R30°$ structure.[25] A high coverage of CO does, therefore, not mean that the rotation of the *dimer* particles is hindered.

The center of rotation of the *dimer* particles is thus identified as an on-top Ru site. The molecule occupies a threefold site, but which one, fcc or hcp, is not clear.
In the STM movies recorded at room temperature, each particle only rotates around one Ru atom, and no lateral diffusion is detected. However, when the sample was heated to 80 °C and above, an additional motion, an on-site rotation, was observed. As will be shown in chapter 4.3, the combination of these two rotations leads to a translation, i.e., to surface diffusion.
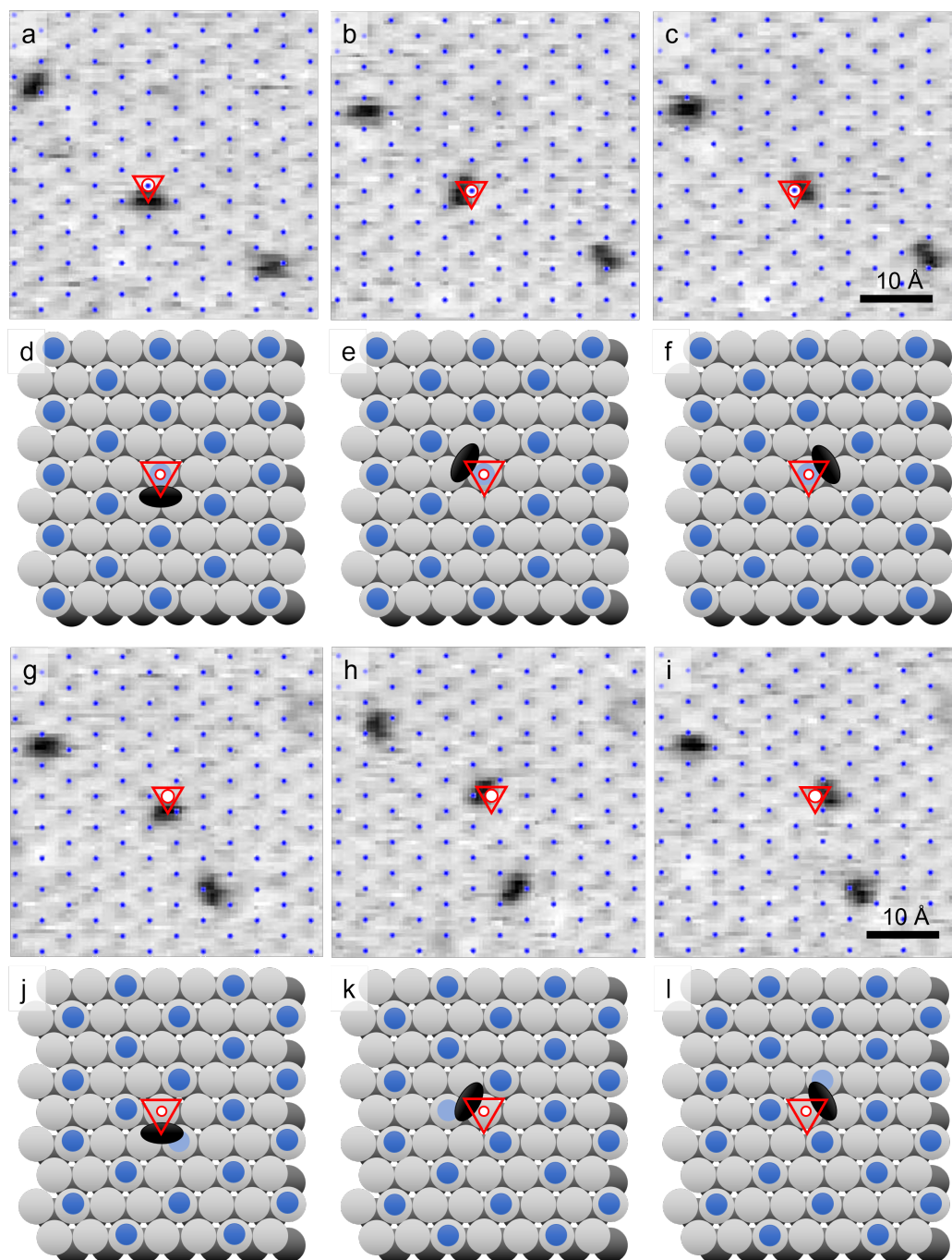
Figure 4.3 : STM images of *dimer* particles on the Ru(0001) surface, prepared by dosing 0.25 L ethylene, and an additional dosing of 1 L CO to form the $(\sqrt{3} \times \sqrt{3})R30°$ superstructure, with corresponding models. In a) to f), the particle rotates around a $(\sqrt{3} \times \sqrt{3})R30°$ lattice site, and in g) to l), the particle rotates around a $(\sqrt{3} \times \sqrt{3})R30°$ interstitial site. The center of rotation is marked with an open red circle, and a red triangle connects the centers of mass. CO molecules are marked by blue dots in the STM images and blue full circles in the models. Ruthenium atoms are indicated in grey and the *dimer* particle in black. Recording conditions of the STM movie: $V_t = -1.5$ V, $I_t = 3$ nA, 10 fps, $T = 30$ °C.

4.2. Attempts to identify the molecule

This subchapter presents the experiments that aimed at determining the atomic composition of the *dimer* particle. At the end, a list of the collected characteristics of the *dimer* particles is given.

4.2.1. Experiments with hydrogen

Starting from the initial idea of preparing atomic carbon and letting it react with hydrogen, the obtained *dimer* particles were treated with hydrogen. In these experiments, the *dimer* particles were prepared by carbon evaporation. At a sample temperature of 100 °C, the chamber was backfilled with hydrogen, and STM movies were recorded. The hydrogen pressure was held between $p_{H_2} = 2 \times 10^{-9}$ Torr and $p_{H_2} = 1.6 \times 10^{-7}$ Torr. During the treatment with hydrogen, *dimer* particles disappeared from the images. Figure 4.4 (a) shows two consecutive frames (0.1 s apart) from an STM movie, in which one *dimer* particle (red circle) disappeared. It was also observed that new *dimers* appeared (figure 4.4 (b)), but this happened less often than the disappearance of particles.

All four STM frames are taken from the same STM movie, which in total is 3731 frames long (recorded with 10 fps, corresponding to a length of 6 min), and in this time period, 13 molecules were observed to disappear, and 6 molecules to appear. Table 4.3 lists the number of events from several STM movies. For comparison, measurements without hydrogen treatment are listed as well.

In the hydrogen atmosphere, events in which *dimers* disappeared were about 2.5 times more often than events in which *dimers* appeared. Without hydrogen, about one order of magnitude fewer events were detected, and the ratio of disappearing and appearing events was 1:1. Over the entire period of the hydrogen treatment (about 1.7 hours), the average coverage of *dimer* particles did not decrease significantly.

Figure 4.5 shows six frames from an STM movie taken over a time period of 15.6 s (the red circle marks the same position and particle). At $t = 0.0$ s the particle appears as an elliptic *dimer* particle. In the following frame at $t = 0.1$ s, the particle appears larger and round, similar to the larger immobile features observed after preparation. The particle shows this shape for about 15 s before it changes back to the *dimer* shape ($t = 15.6$ s). Before and after the displayed sequence the particle was imaged as a usual *dimer* particle and showed the characteristic diffusion behavior as the other *dimer* particles.
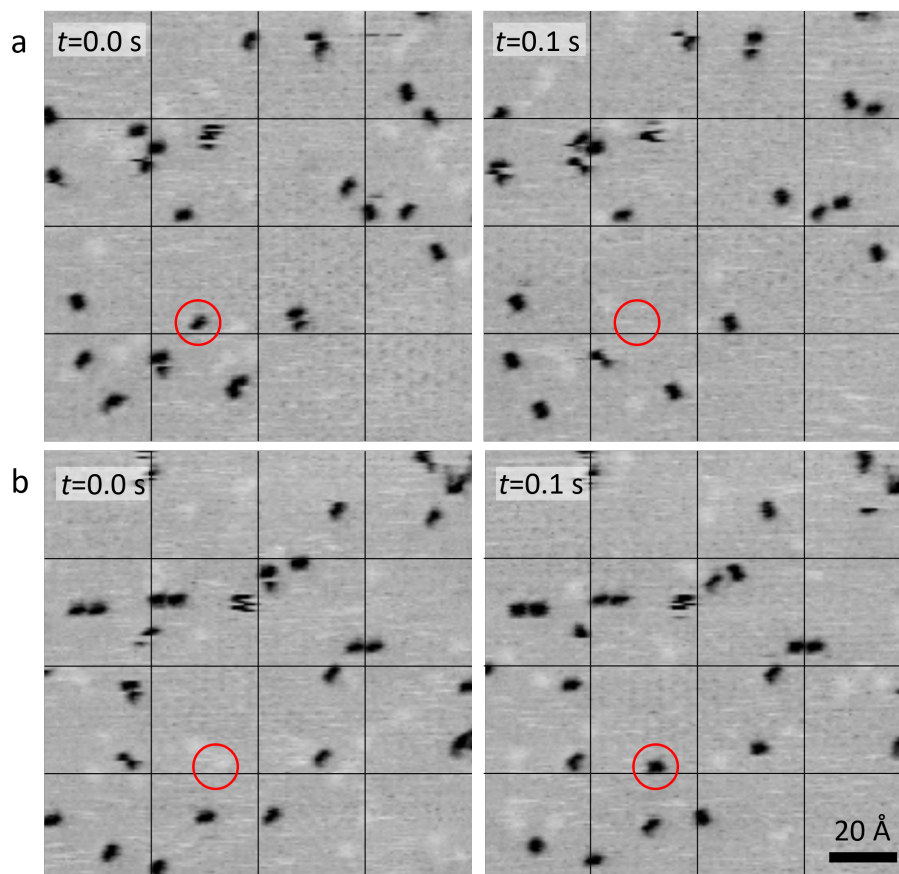
Figure 4.4 : Two pairs of consecutive frames from an STM movie with *dimer* particles on the Ru(0001) surface at a hydrogen background pressure of $p_{H_2} = 2 \times 10^{-8}$ Torr, recorded at $T = 112$ °C. The grid helps to follow the movement of the particles. a) The red circles marks a *dimer* particle that disappears in the following frame; b) the red circle marks the position where a *dimer* particle appears in the following frame, $V_t = -0.8$ V, $I_t = 3$ nA, 10 fps.

Table 4.3 : Experiments and numbers of *dimer* particles disappearing and appearing, with and without hydrogen.

p_{H_2} [Torr]	T [°C]	Frames [#]	Time [min]	disappear [#]	appear [#]
2.3×10^{-9}		3731	06:13	2	4
2.0×10^{-8}	112	3731	06:13	13	6
1.0×10^{-7}		3112	05:11	9	3
1.8×10^{-8}		2606	04:21	14	5
1.1×10^{-7}	143	2091	03:29	23	3
1.1×10^{-7}		1778	02:58	8	6
$\sum$		**17049**	**28:25**	**69**	**27**
		3731	06:13	1	1
		3731	06:13	2	1
		3731	06:13	1	0
no hydrogen	123	3731	06:13	2	1
		3731	06:13	1	2
		3731	06:13	0	1
		1122	01:52	0	0
		1870	03:07	0	0
$\sum$		**25378**	**42:17**	**7**	**6**
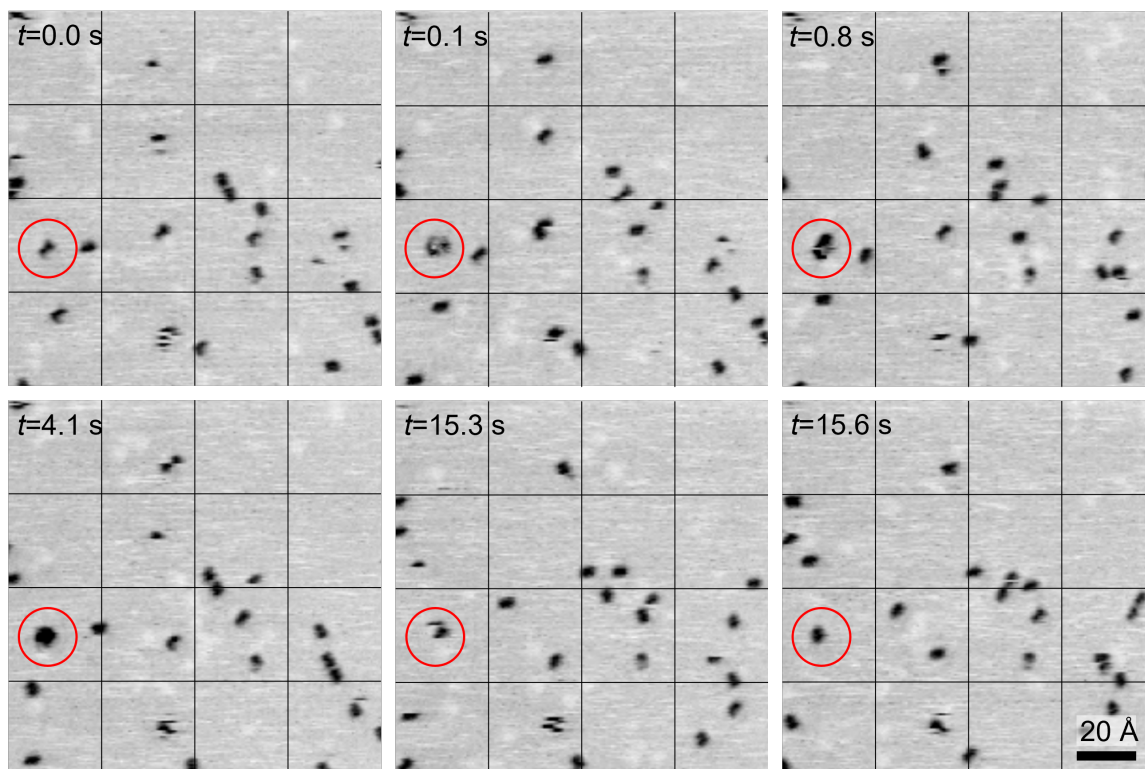
Figure 4.5 : Six frames from an STM movie of *dimer* particles on the Ru(0001) surface, at a hydrogen background pressure of $p_{H_2} = 2 \times 10^{-9}$ Torr. One *dimer* particle changes its appearance (marked with a red circle), $V_t = -0.8$ V, $I_t = 3$ nA, 10 fps, $T = 112$ °C.

Summarizing, the treatment of the *dimer* particles with hydrogen at elevated temperatures had two effects. *Dimer* particles were observed to disappear or appear much more often than in the absence of H_2, and they occasionally changed their shape in a reversible way. Disappearing particles may be explained when the attachment of H atoms leads to a weakly bound molecule that desorbs at the experimental temperature. Of course, the observed reverse process is hard to understand within this picture. More likely is the formation of a bound but highly mobile species that is no longer resolved by the STM. However, when the H atom or atoms are split off again, it gives the original *dimer* species. Shape changes can be explained by other H-induced changes in the configuration. It cannot be excluded that these effects, as is generally possible in STM experiments, are influenced by the tip. That only relatively few such events were observed may be explained by the fact that the desorption peak of hydrogen (depending on the hydrogen coverage) already begins at temperatures lower than 112 °C,[75], the temperature range in which the STM measurements and hydrogen treatments were performed. Taken together, it can be concluded that the *dimer* features are able to bind additional H atoms, confirming the interpretation as adsorbed, unsaturated hydrocarbon fragments.

4.2.2. Experiments with acetylene

In an attempt to identify the chemical nature of the *dimer* particles, acetylene was adsorbed on the Ru(0001) surface. Because the *dimers* are formed by partial decomposition of the ethylene molecules, or by reaction of the C species from the evaporator with adsorbed hydrogen, adsorbed acetylene was one of the possibilities. Alternatively, it could be that acetylene decomposes to the same fragments as ethylene, which may help narrow down the possibilities.

For the experiments in this work, acetylene was not dosed in pure form (pure acetylene gas decomposes) but diluted to 1 Vol% in a mixture with N_2 at room temperature. At a dosage of only 2 L of acetylene, no significant difference to the clean surface was observed (not shown), apart from a somewhat higher coverage of N atoms.

Figure 4.6 shows an STM image of the surface when the dosage was increased to 20 L. The surface is almost entirely covered with undefined features of different heights, and it is hard to distinguish between individual particles. Figure 4.6 (a) and (b) show bright, mostly round features, and the rest of the surface is covered with grey features, which agglomerate in groups. No preferred alignment of the observed features with the Ru(0001) substrate is noticeable.

In the STM movies (figure 4.6 (c) and (d)), some movement and fluctuations of the grey features were observed (left squares of the black grid), while the dark features are immobile. Both STM frames display the same surface area (27.2 s apart), but are recorded at different tunneling voltages, $V_t = -0.2$ V in figure 4.6 (c) and -1.2 V in figure 4.6 (d), respectively. Some of the grey features turn dark at the higher negative voltage. Thus, V_t influences the imaging of the adsorbed species.

The STM images of the Ru(0001) surface covered with adsorbates and decomposition products of acetylene are difficult to interpret. No structures and no features could be identified by the STM that resemble the *dimer* particles. Thus, these experiments were not pursued further.
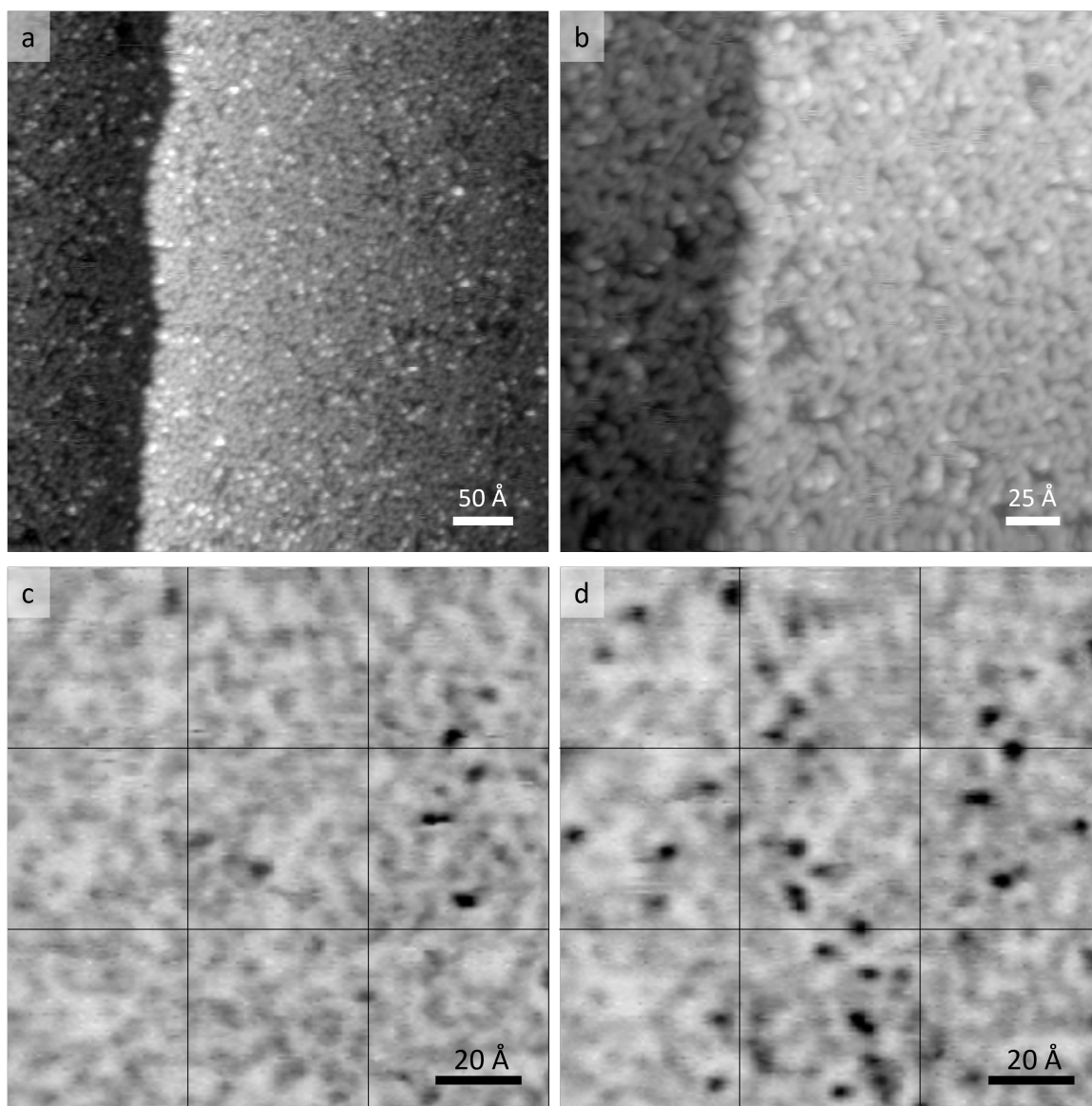
Figure 4.6 : STM images of the Ru(0001) surface with adsorbed acetylene (20 L) at room temperature. a) and b) slow constant current mode, $I_t = 1$ nA, $V_t = -1.0$ V in a) and $V_t = -0.2$ V in b); c) and d) frames from an STM movie of the same surface area (27.6 s apart), $I_t = 3$ nA, 10 fps, $V_t = -0.2$ V in c) and $V_t = -1.2$ V in d).

4.2.3. Low-temperature experiments with ethylene

In order to gain more information on the decomposition of the adsorbed ethylene on Ru(0001), low-temperature experiments were performed. Similar to the carbon evaporation experiments, decreasing the temperature slows down thermally activated processes and thus precursor species of the *dimer* particles were expected.

In these experiments, 1 L ethylene was dosed at a surface temperature of −118 °C, followed by dosing of 1 L CO. (The CO was used to protect the surface against the adsorption of foreign gases, primarily H_2 and H_2O, when the sample was cooled.) The sample was then further cooled down, and STM measurements were conducted at a sample temperature of −202 °C. After recording data at this temperature, the sample was flash annealed to increasingly higher temperatures in three steps (−43 °C, 25 °C, and 74°C). Each temperature was held for a few seconds, and then the sample was cooled to −202 °C. STM measurements were performed at this temperature.

After ethylene dosing at −118 °C: The initially observed features are shown in figure 4.7. Four STM frames from a movie are shown. The two images in (a) were recorded on the same surface area with a time interval of 3 s, and the two images in (b) were recorded on another area with a time interval of 6 s. Three different species can be distinguished. The first species is formed by small dark particles that are immobile (blue circles). Due to a thermal drift in figure 4.7 (b), the immobile particles are displaced with respect to the grid (black arrows). The second species is also imaged dark (green circles), but this species is mobile. The mobility is rather high, which does not allow tracking of the particles. The third species (yellow circles) is imaged bright grey and is well resolved in figure 4.7 (b). This species is very mobile. In figure 4.7 (b) at $t = 0.0$ s, this species is spread over the entire image. Six seconds later, it is only present in the upper quarter of the image, leaving empty areas in the rest of the image.

The observation of a directional diffusion behavior of a species, as is the case for the third species, has to be attributed to an effect of the tip. As CO has been dosed in this experiment, and single CO molecules are easily displaced by the tip, this species is assigned to CO. The first and second species, both of which are imaged dark but display different mobilities, are assigned to decomposition products of ethylene. The round shape of the particles indicates a high symmetry. However, an absolute assignment of the two observed species is not possible. The *dimer* particles have not been observed when ethylene was dosed at −118 °C. Obviously, their formation is thermally activated, and the particles do not form at this temperature.
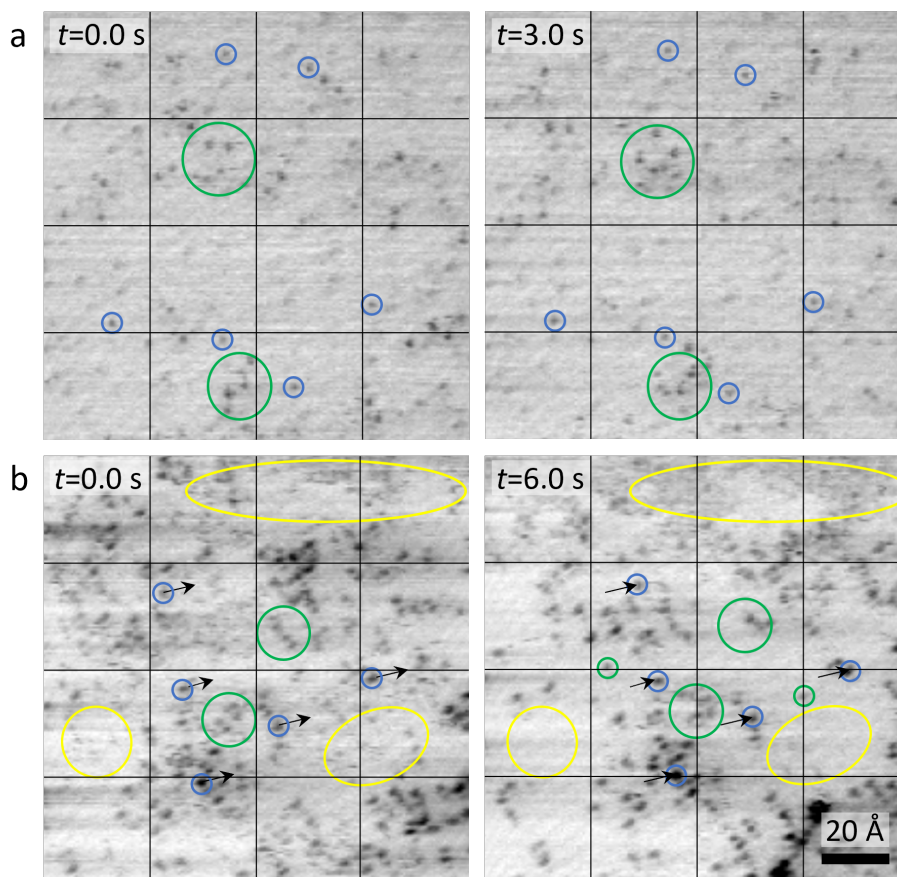
Figure 4.7 : Frames from an STM movie after dosing ethylene (1 L) and CO (1 L) on the cold Ru(0001) surface (−118 °C to −142 °C), recorded at −202 °C. a) Two frames at a time interval of 3 s, b) two frames at a time interval of 6 s; black arrows indicate the thermal drift, blue circles mark immobile species, green circles mark areas with mobile species, and yellow circles mark areas with very mobile species; $V_t = −0.2$ V, $I_t = 3$ nA, 10 fps.

After flash annealing to −43 °C (fig. 4.8 (a)): Four species are observed. The highly mobile bright grey particles interpreted as CO molecules cover the upper part of the image (yellow circle) and are unchanged after the temperature flash. The dark particles are almost all immobile and can be divided into two groups by their size (blue and orange circles). The mobile species in figure 4.7 (green circles) are no longer visible after this first annealing step. A new, larger round species has appeared instead (orange circles). Some of these particles change their appearance with time (visible in the movie, in fig. 4.8 these particles are marked by purple ellipses). This change is reversible and is assigned to a change in the molecular configuration. The change of the surface species in mobility, shape, and appearance leads to the conclusion that the temperature flash has changed the composition of the particles. However, *dimer* particles are still not observed.
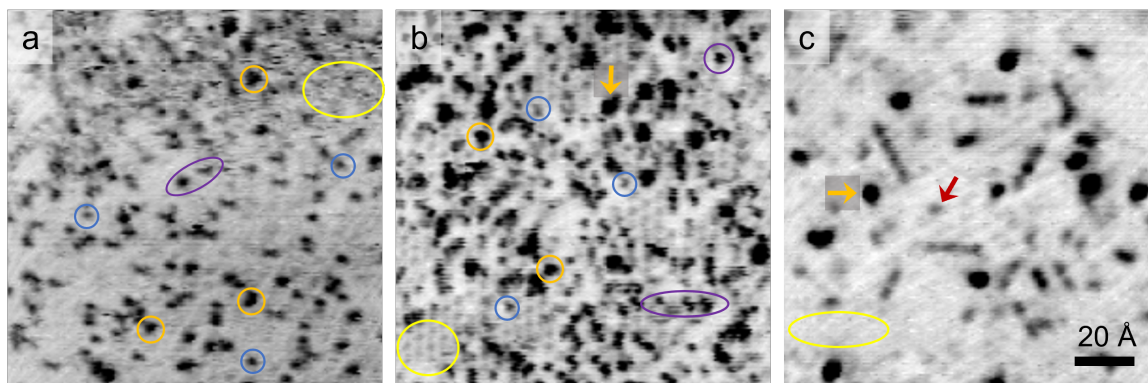
Figure 4.8 : Frames from STM movies of the Ru(0001) surface after dosing ethylene (1 L) and CO (1 L) on the cold sample (-118 °C to -142 °C) and then flash annealing and cooling to -202 °C. a) After flash annealing to -43 °C, b) to 25 °C, c) and to 74 °C; $V_t = -0.2$ V, $I_t = 3$ nA, 10 fps.

After flash annealing to 25 °C (fig. 4.8 (b)): After this flash, the ordered $(\sqrt{3} \times \sqrt{3})R30°$ superstructure of CO (yellow circle) is observed in the areas between the dark features. A new species consists of immobile, larger dark particles (orange arrow). This species has already been observed after preparation of the *dimer* particles at room temperature. Further, the surface shows smaller dark particles that are assigned to features already observed after annealing to -43 °C (blue and orange circles). In the areas marked in purple, the particles change their appearance. The new surface species indicate that another change in the molecular configuration of the hydrocarbon fragments has happened. However, the *dimer* particles have still not formed at 25 °C.

After flash annealing to 74°C (fig. 4.8 (c)): This temperature is a little bit higher than the usual sample temperature at which ethylene was dosed, and which led to the *dimer* particles (≈ 50 °C). As can be seen in figure 4.8 (c), *dimer* particles are now clearly present (red arrow). The surface is covered with the usual features that have been observed after the preparation described in subchapter 4.1.1, see figure 4.1. Apart from the *dimers*, there are also the larger dark features (already observed in chap. 4.1.1) (orange arrow), and the $(\sqrt{3} \times \sqrt{3})R30°$ superstructure of CO is slightly visible (yellow circle).

Table 4.4 gives an overview of the detected species and of the temperature at which they are present on the surface.

The experiments provide some insight into the surface species that result from the decomposition of ethylene and the complex reaction pattern of the fragments on the Ru(0001) surface at temperatures even below room temperature. The STM movies show immobile and mobile surface species that are assigned to fragmentation

products of the dosed ethylene, which vary in configuration, shape, and mobility. However, based on STM data alone, it is difficult to assign these particles to specific hydrocarbon fragments. The various possible molecular configurations are discussed in section 4.2.5, which presents vibrational spectroscopy data from the literature. What is clear, however, is that these species are precursors of the *dimer* particles, which are formed in thermally activated processes between 25 °C and 74 °C.

Table 4.4 : Species detected in STM measurements.

	temperature	−202 °C to −118 °C	up to −43 °C	up to 25 °C	74 °C
hydrocarbon from ethylene decomposition	small mobile particles	green circle			
	small immobile particles	blue circle	blue circle	blue circle	
	medium immobile particles		orange circle	orange circle	
	unstable, changing particles		purple circle	purple circle	
	large immobile particles			orange arrow	orange arrow
	dimer particles				red arrow
CO		yellow circle	mobile (tip influence)	$(\sqrt{3} \times \sqrt{3})R30°$	

4.2.4. Graphene growth experiments

The elliptical shape of the *dimer* particles indicates that the molecule to which the particles are assigned contains more than one carbon atom. An obvious possibility is that they consist of two C atoms, but a CH_2 species might also appear elliptical in STM. Moreover, coupling reactions might lead to larger units such as C_4H_x fragments that in STM might also appear elliptical. To determine the number of C atoms in the molecules, experiments were performed in which the molecules were completely decomposed to give graphene, a planar, sp^2-hybridized carbon network. On the Ru(0001) surface, graphene forms a well-studied structure with a known C coverage, so that the surface fraction of graphene determined in such an experiment can provide the amount of carbon originally present. The formation of graphene by the decomposition of ethylene on a Ru(0001) surface has been studied in detail in ref. [41]. It has been shown that graphene starts growing at 665 °C to 770 °C. A difficulty is that, when high temperatures are applied, the solubility of carbon in the bulk of the Ruthenium crystal has to be taken into account. At temperatures above 800 °C, the carbon adatom concentration on the surface decreases due to solution processes into the bulk; at temperatures below that value, carbon adatoms nucleate to form graphene.[43]

In the experiments presented here, the *dimer*-covered surface was annealed to temperatures below this critical value until graphene growth was detected. In the

experiments, *dimer* particles were prepared by ethylene dosing (0.5 L to 2 L) on the clean Ru(0001) surface at 50 °C. A subsequent annealing step to temperatures above 200 °C was performed with the sample mounted to the manipulator in order to prevent damage to the STM. STM images were recorded after the sample had cooled to room temperature. Figures 4.9 to 4.12 show the results after annealing to increasingly higher temperatures.
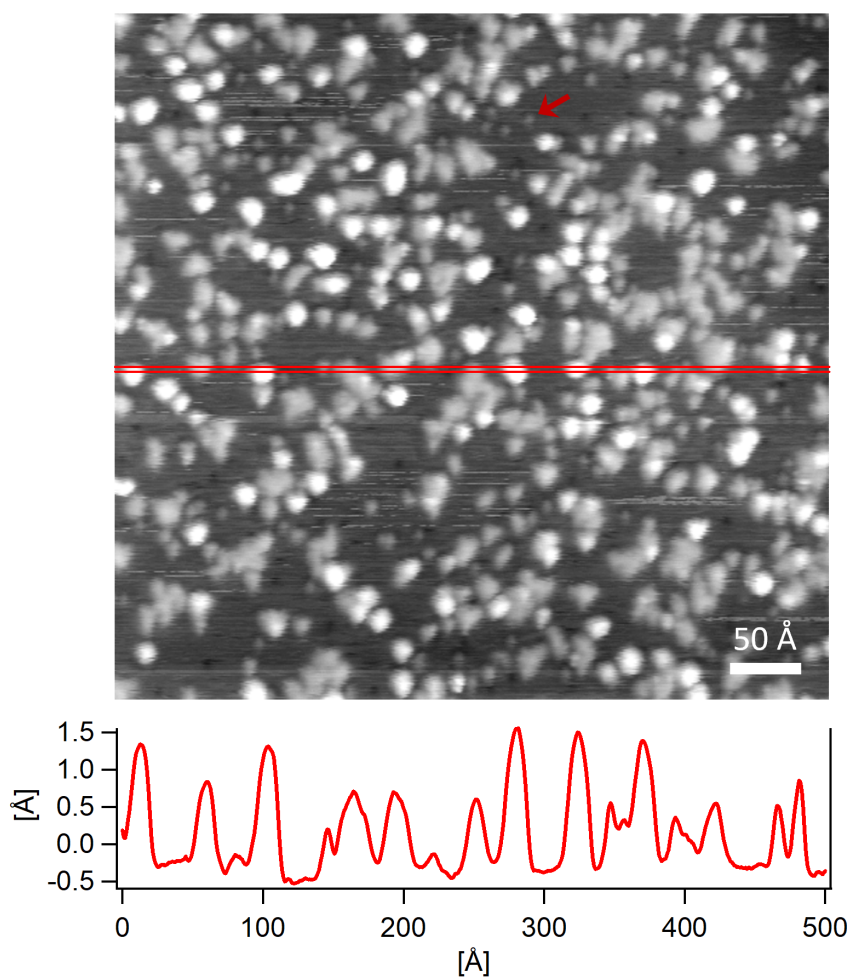
Figure 4.9 : Ru(0001) surface after annealing to 350 °C. *Dimer* particles were prepared by 2 L ethylene, the STM image was recorded at room temperature, $V_t = -1.0$ V, $I_t = 1$ nA.

Annealing to 350 °C: *Dimer* particles were prepared by dosing 2 L of ethylene; figure 4.9 displays the Ru(0001) surface after annealing to 350 °C. Three species are observed. The smallest grey particles are assigned to still existing *dimer* particles (marked with a red arrow). However, the majority of features are larger, and one can distinguish a grey species and a white species; the latter has about twice the height of the first (see height profile beneath the STM image). The white species are rather round, while the grey particles have different sizes, and the largest ones

have a triangular shape. These features are interpreted as the initial stage of a pure carbon-based network. Similar features have been observed in a study in which ethylene was dosed at 387 °C on Ru(0001).[41]

Annealing to 650 °C and 715 °C: The STM images shown in figure 4.10 have been recorded after annealing to 650 °C and 715 °C, respectively; the *dimer* particles were prepared by dosing 1 L of ethylene. Small graphene islands can be identified by the typical moiré structure (white arrows) that have grown on the terraces and at the atomic steps. Apart from graphene, there is an unidentified species on the surface that appears as bright dots. Thus, the applied temperatures were not sufficiently high that all carbon-containing surface species could react to give graphene.
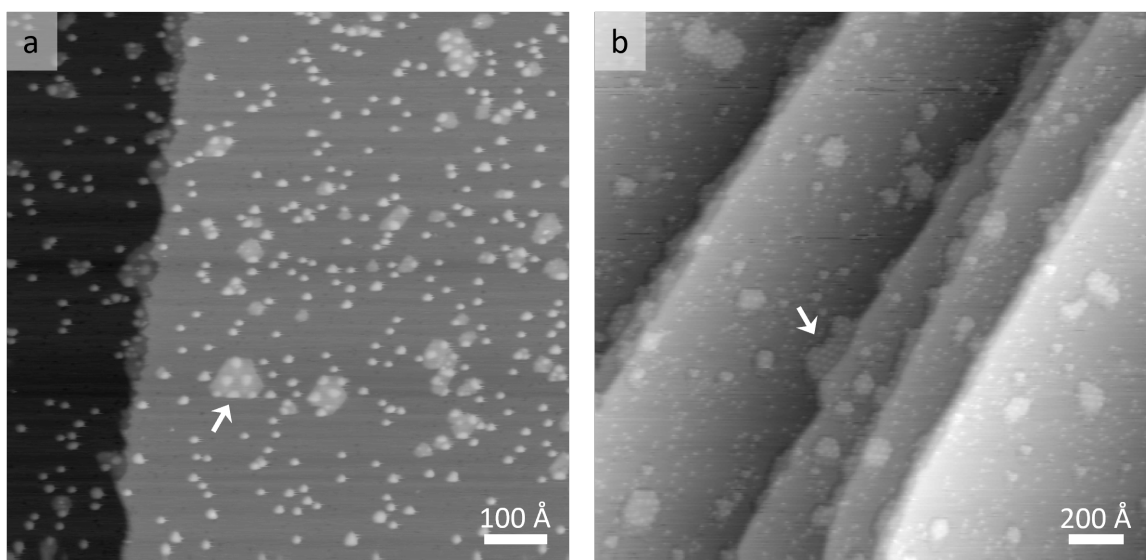
Figure 4.10 : Ru(0001) surface after dosing 1 L ethylene and, a) after annealing to 650 °C, $V_t = -0.2$ V, $I_t = 1$ nA, b) after annealing to 715 °C, $V_t = -1.0$ V, $I_t = 1$ nA; STM images recorded at room temperature.

Annealing to 770 °C (clean surface): A graphene layer on the Ru(0001) surface can also be prepared by segregation of bulk-dissolved carbon at high temperatures. Such an effect would obviously distort the information about the initial carbon coverage. For this reason, a reference experiment was performed in which the Ru(0001) sample without any *dimer* particles was annealed to 770 °C (figure 4.11). One can see that the annealed sample surface is unchanged to the clean Ru(0001) surface. The only surface species observed are small amounts of nitrogen and oxygen atoms (small dark particles), and a very low number of bright features. No graphene is detected. This experiment proves that no carbon segregates from the bulk by annealing the sample to 770 °C nor during subsequent cooling to room temperatures.
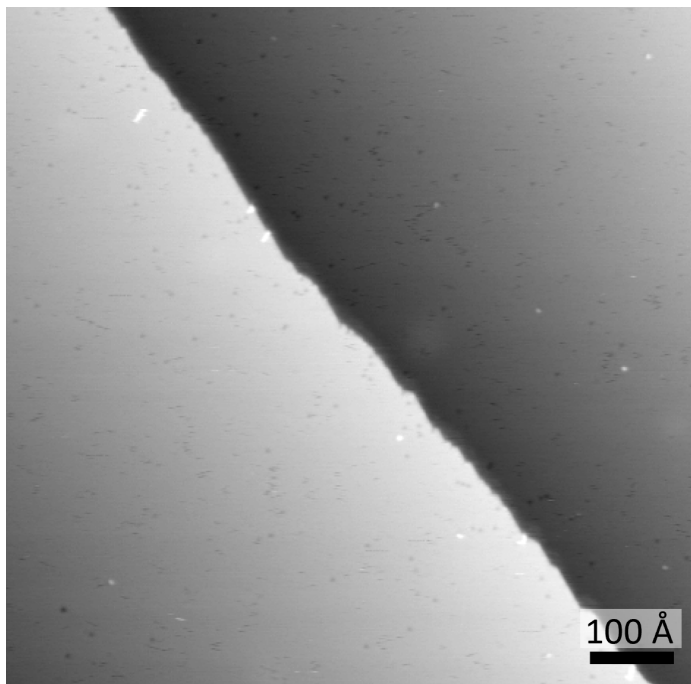
Figure 4.11 : Ru(0001) surface after annealing the clean Ru(0001) surface to 770 °C, recorded at room temperature, $V_\mathrm{t} = -1.0$ V, $I_\mathrm{t} = 1$ nA.

Annealing to 770 °C (*dimer*-covered surface): Figure 4.12 shows the *dimer*-covered Ru(0001) surface (0.5 L ethylene) at room temperature before and after annealing to 770 °C for 1 min. The *dimer*-covered surface shows a homogeneous distribution of particles (figure 4.12 (a)). The two main species are the *dimer* particles and the immobile larger particles. After annealing, the surface is only covered with graphene islands, and no other surface species are present (figure 4.12 (b)). A preferential growth of graphene at the step edges and from there to the lower terraces is observed. This growth mode is typically observed for graphene.[41]

In order to determine the number of carbon atoms per *dimer* particle (n_C^{dimer}), the coverage of the species before annealing, and the graphene-covered surface fraction after annealing were evaluated. A dosage of 0.5 L ethylene resulted in a coverage of 0.0217 ± 0.0033 *dimer* particles per Ru surface atom (θ_{dimer}). 18 images ((126 Å × 126 Å) movie frames) from different locations were analyzed, in which the individual *dimer* particles could clearly be identified. The number of immobile larger particles ("clusters") formed by ethylene dosing and present in addition to the *dimers* was also determined, and a coverage of 0.0072 ± 0.0019 particles per Ru atom was obtained (θ_cluster). Both species, the *dimers* and the clusters, contain carbon and therefore contribute to the graphene growth.

After annealing to 770 °C, graphene islands covered a fraction of 0.0449 ± 0.0254 of the surface area. 9 images with sizes of (1780 Å × 1750 Å) and (2670 Å × 2625 Å)
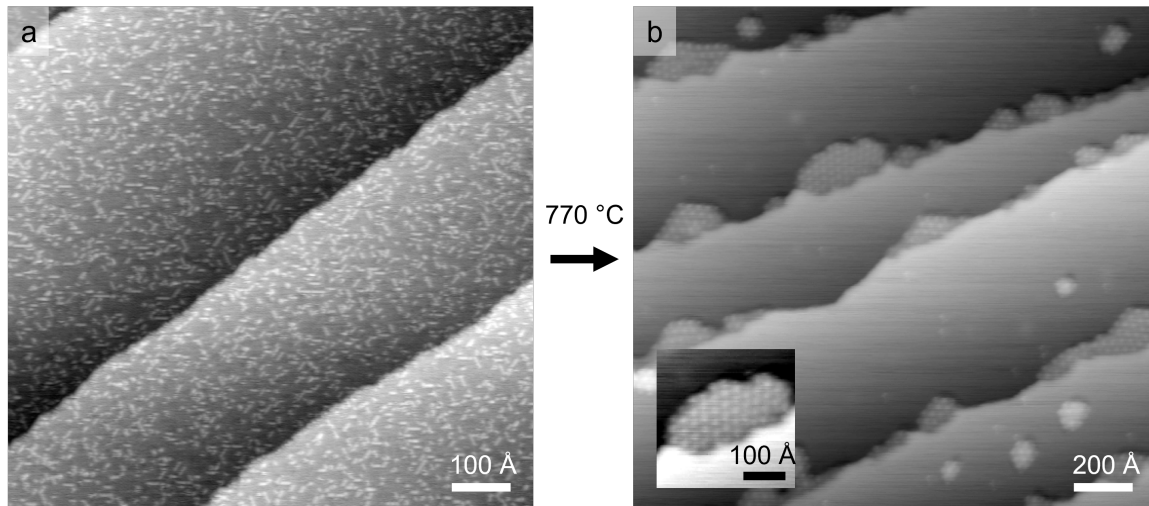
Figure 4.12 : *Dimer*-covered Ru(0001) surface before and after annealing to 770 °C. STM images recorded at room temperature. a) *Dimer* particles prepared by 0.5 L ethylene, $V_t = -1.0$ V, $I_t = 1$ nA, b) after annealing to 770 °C for 1 min, the largest graphene island is shown in the inset, $V_t = -0.2$ V, $I_t = 1$ nA.

from different locations were evaluated. The high error results from the fact that the distribution of graphene islands varied considerably from image to image. Graphene forms a (23×23) unit cell on the Ru(0001) surface which contains $2 \times (25 \times 25)$ C atoms.[76] With this relation, the coverage of carbon atoms in the graphene is 0.1060 ± 0.0508 carbon atoms per Ru surface atom (θ_C). The values are listed in table 4.5.

The carbon atoms in the graphene originate from the carbon contained in both the *dimer* particles and the clusters: $\theta_C = n_C^{dimer} \theta_{dimer} + n_C^{cluster} \theta_{cluster}$, where n_C^{dimer} and $n_C^{cluster}$ are the numbers of C atoms per *dimer* and cluster, respectively. Both numbers are unknown. Setting $n_C^{cluster} = 0$, n_C^{dimer} would be 4.88 ± 2.45, which is an upper limit, at least for this experiment. Setting sequentially $n_C^{dimer} = 4$, 3, 2, and 1, $n_C^{cluster}$ adopts the values given in the table. Because the clusters appear larger in the STM images than the *dimers*, one can argue that $n_C^{cluster}$ should be larger than n_C^{dimer}. Hence, by varying n_C^{dimer} and calculating the corresponding $n_C^{cluster}$ values, the most likely n_C^{dimer} value may be obtained. However, as table 4.5 shows for the 0.5 L data, this does not lead to a conclusive result. The errors of the $n_C^{cluster}$ values, calculated from the experimental coverages, are just too high. The major error source is the fraction of the graphene-covered surface area, which, as already mentioned, varied considerably in the series of images. n_C^{dimer} could therefore not be determined from the 0.5 L ethylene experiment.

A second graphene growth experiment was performed with a dosage of 1 L of ethylene; the values are also shown in table 4.5. 13 images before and 9 images after

Table 4.5 : Evaluation of the graphene growth experiments.

	0.5 L ethylene		1 L ethylene	
θ_{dimer}	0.0217 ± 0.0033		0.0437 ± 0.0036	
θ_{cluster}	0.0072 ± 0.0019		0.0133 ± 0.0017	
area fraction of graphene	0.0449 ± 0.0254		0.1300 ± 0.0184	
θ_{C}	0.1060 ± 0.0508		0.3071 ± 0.0368	
	n_{C}^{dimer}	$n_{\text{C}}^{\text{cluster}}$	n_{C}^{dimer}	$n_{\text{C}}^{\text{cluster}}$
	4.88 ± 2.45	0	7.03 ± 1.02	0
	4	2.66 ± 7.36	6	3.37 ± 3.22
	3	5.69 ± 7.38	5	6.64 ± 3.18
	2	8.73 ± 7.52	4	9.92 ± 3.23
	1	11.76 ± 7.77	3	13.2 ± 3.35
			2	16.48 ± 3.54
			1	19.76 ± 3.78

the graphene growth were evaluated. Here, the variations in the fractions of the graphene-covered surface were significantly lower, and the errors in the $n_{\text{C}}^{\text{cluster}}$ values are accordingly lower as well. One can see that for $n_{\text{C}}^{dimer} = 5$ to 1, $n_{\text{C}}^{\text{cluster}}$ is larger than n_{C}^{dimer}. Because the odd values, $n_{\text{C}}^{dimer} = 5$ and 3 appear unlikely from the symmetry of the *dimers*, and $n_{\text{C}}^{dimer} = 1$ and 2 give unphysically large $n_{\text{C}}^{\text{cluster}}$ values, the most likely result is $n_{\text{C}}^{dimer} = 4$.

If the *dimer* particles in fact consist of more than two carbon atoms, they cannot be simple products of the known decomposition process of ethylene on the Ru(0001) surface. A further process, like a coupling reaction (equation 4.1) that forms a carbon bond between to C_2-species, may take place to form the observed *dimer* molecules:

$$2\, C_2 H_x \; \rightarrow C_4 H_{x-y} \; + \; \frac{y}{2}\, H_2 \quad \text{with } x = 1, 2, 3 \text{ and } y = 0, ..., 6 \qquad (4.1)$$
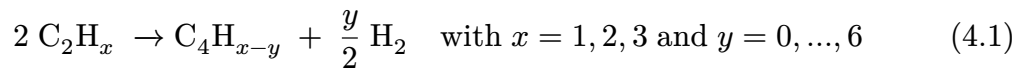
Because of the two-fold symmetry of the particles, four carbon atoms per molecule are preferentially considered in the following. That n_{C}^{dimer} is most likely larger than 2 may be related to a finding in a LEEM study by Loginova et al. In this study the growth kinetics of graphene on the Ru(0001) surface suggested that the graphene layer does not grow by the attachment of single C atoms but by the attachment of clusters of five C atoms.[45] Obviously, there is a possibility that adsorbed C atoms or CH_x fragments form stable clusters consisting of several C atoms.

4.2.5. Vibrational spectroscopy literature search

The decomposition of ethylene (and of acetylene) has been investigated in some detail in vibrational spectroscopy studies. The main method has been high-resolution electron energy loss spectroscopy (HREELS), which makes use of inelastically scattered electrons from a surface and gives information on the vibrational modes of the adsorbates on the surface. The energy losses range from 1 meV to 1 eV, which corresponds to the energy of light in the infrared (IR) area. A second method has been reflection-absorption infrared spectroscopy (RAIRS), which involves an IR beam reflected from the surface. Both methods only give high signals for adsorbates with vibrational modes perpendicular to the surface. A further surface-specific method to analyze adsorbates that has been used is vibrational sum frequency (VSF) spectroscopy, a laser-based technique. A pulsed infrared laser and a pulsed visible laser overlap spatially and temporally at the sample interface, while the observed sum frequency emission contains information on the vibrational transitions and the molecular orientation of the adsorbates.

In the investigations with these methods, ethylene and acetylene were dosed on the cold sample surface (in a range from -193 °C to -73 °C). The thermal stability of the surface species was then tested by annealing to higher temperatures, while the measurements themselves were performed at a low sample temperature. A key difference between these experiments and the STM experiments in this work is that the surface coverage of the adsorbates was much higher in the vibrational measurements, which were often performed at saturation coverage.

Ethylene adsorbs as an intact molecule on the Ru(0001) surface at temperatures lower than -73 °C or -123 °C, as consistently found by HREELS[77,78], RAIRS[79,80], and VSF spectroscopy[81]. All methods also agree on the most stable decomposition products, namely atomic carbon and methylidyne (CH). Complete dehydrogenation to atomic carbon takes place at temperatures between 227 °C[79] and 277 °C[80]. Methylidyne is formed between 52 °C[77,81] and 177 °C[80] and the stability ranges up to 327 °C.[81]

More diverse are the intermediate decomposition fragments before total dehydrogenation. The first fragment that has been detected is ethylidyne (CCH$_3$) (fig. 4.13) in a temperature range from -43 °C to 77 °C by VSF spectroscopy[81], which agrees with the temperatures reported in the HREELS and RAIRS studies. In some studies, the acetylide (CCH) fragment appears together with the ethylidyne (CCH$_3$) or at a slightly higher temperature of -23 °C. It is thermally stable up to 227 °C, depending on the publication. Ren et al. report the formation of CCH from CCH$_3$

at 47 °C.[80] Kirsch et al. report that at temperatures above 77 °C, CH is the only species left on the surface.[81]

With the more sensitive VSF spectroscopy, a further surface species was detected by Kirsch et al., the vinylidene (CCH_2) molecule, which is observed in the temperature range from -23 °C to 77 °C (prepared by methane adsorption, it is stable even up to 277 °C).[81] Vinylidene is also mentioned by Ren et al., but the spectroscopic evidence was not inconclusive.[80] Vinylidene has been reported earlier by Jakob et al. in a HREELS study, where it was prepared by acetylene dosing.[82] In general, the same decomposition products are observed both from ethylene and acetylene interaction with Ru(0001), namely CCH_3, CCH_2, CCH, CH, and C.[82,83]

In table 4.6, an overview of the decomposition products of ethylene on Ru(0001) is given, together with the temperature range in which the species are present on the surface. Figure 4.13 displays the most likely orientations of the species on the surface.

Table 4.6 : Thermal stability of decomposition fragments of ethylene on Ru(0001).

molecule/fragment		surface stability range	comment	literature
ethylene	C_2H_4	< -73 °C / < -123 °C		[77–81]
carbon	C	> 227 °C / > 277 °C		[77, 79, 80]
methylidyne	CH	52 °C / 177 °C to 327 °C		[77–81]
methylidene	CH_2	< 17 °C	only from methane decomposition	[84]
ethylidyne	CCH_3	-43 °C to -77 °C		[77–81]
vinylidene	CCH_2	-23 °C to 77 °C / 277 °C	higher thermal stability by preparation from methane	[80, 81]
acetylide	CCH	-23 °C to 227 °C		[77–81]
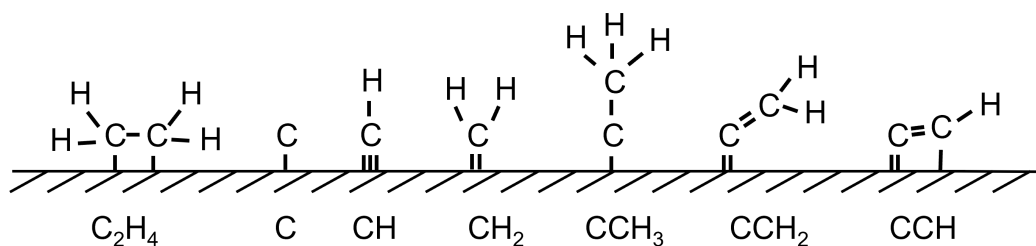
Figure 4.13 : Scheme of ethylene and its decomposition fragments on a surface.

The vibrational spectroscopy studies reveal several fragments that exist on the Ru(0001) surface in the temperature range in which the *dimer* particles have been studied (−13 °C to 350 °C). The most stable fragment, methylidyne (CH), does not match the elliptical shape of the *dimer* particles. From STM publications, CH is observed as a round protrusion with a dark ring around it.[42] In the present experiments in which ethylene was dosed on the cold surface (chapter 4.1), several small round particles with different mobilities were observed that might be assigned to CH. A methylidene (CH_2) fragment would fit the elongated shape of the *dimers*, but this fragment is only reported as a decomposition product of methane and is only stable below 17 °C and converts to CH at higher temperatures.[84] (The *dimer* particles are stable up to 350 °C.) Moreover, with only one C atom per particle ($n_C^{dimer} = 1$), an unrealistically high number of C atoms in the cluster species would result (tab. 4.5).

Ethylidyne (CCH_3), vinylidene (CCH_2), and acetylide (CCH) also bring some problems with them besides the fact that the graphene growth experiment revealed that the *dimer* particles probably contain more than two carbon atoms. The ethylidyne molecule adsorbs perpendicular to the surface and thus has a triangular rotation symmetry. This is in conflict with the elliptic shape of the *dimers*. DFT calculations show that the vinylidene and acetylide do not adsorb orthogonally to the Ru(0001) surface but are tilted towards it.[85,86] From the symmetry of the CH_2 group, CCH_2 would be consistent with the *dimers* in the STM. This is not the case for acetylide.

However, the thermal stability of the fragments is an issue. The *dimer* particles are very strongly bound to the Ru(0001) surface as no lateral diffusion is observed below 77 °C. In VSF spectroscopy measurements, only CH is detected on the surface at this temperature. However, the difference in the coverage of the adsorbates in the vibrational spectroscopy versus the STM measurements might influences the stability of the species. None of the vibrational studies reports particles with more than two C atoms per fragment. However, it is not clear whether such larger particles would be inconsistent with the spectra, or whether coupling reactions have just not been considered.

The *dimer* particles are formed by a thermally activated process at temperatures between 25 °C and 74 °C (see chapter 4.2.3). Therefore, I conclude that all the above described surface species, which result from the decomposition of ethylene, are precursors of the *dimer* particles.

4.2.6. Compiled information about the molecule

The information on the *dimer* particles is summarized in the following list to provide an overview of its characteristics. These characteristics strongly narrow down the nature of the molecules, but currently do not lead to a definite interpretation. The missing chemical information in the image data is a general problem of the STM technique.

The *dimer* particle:

- has an elliptic shape with twofold symmetry

- has an approximate length of 3 to 5 Å

- adsorbs on hollow sites (hcp or fcc) (chap. 4.1.2)

- is imaged as a protrusion in the slow scanning constant current mode (consistent with a depression in the fast scanning constant height mode with negative tunneling voltage), (chap. 4.1.1)

- contains carbon (prepared by carbon evaporation and by ethylene dosing) (chap. 3.2, chap. 4.1.1)

- contains hydrogen (ethylene dosing and TDS measurements) (chap. 4.1.1, chap. 3.2.1)

- probably contains more than two carbon atoms (most likely four) (chap. 4.2.4)

- is strongly bound to the Ru(0001) surface (up to $T \approx 80$ °C it only rotates around one Ru atom, at higher temperatures lateral diffusion by combination with a second rotation)

- its formation is thermally activated (25°C to 74 °C) (chap. 4.2.3)

- reacts with atomic/molecular hydrogen (chap. 4.2.1)

- is a precursor molecule for graphene growth (chap. 4.2.4)

- displays a diffusion process consisting of two rotation motions (around a Ru atom and around its own axis) with two very different energy barriers (chap. 4.3, 4.4)

- arranges in chains along close-packed directions of the Ru(0001) surface (chap. 4.1.1, 3.2.1)

4.3. Model of the diffusion mechanism

In this chapter, a model of the diffusion mechanism of the *dimer* particles is developed. It consists of two different rotations. The first rotation will be denoted triangular jumps, the second on-site rotation; both are displayed in figure 4.14.
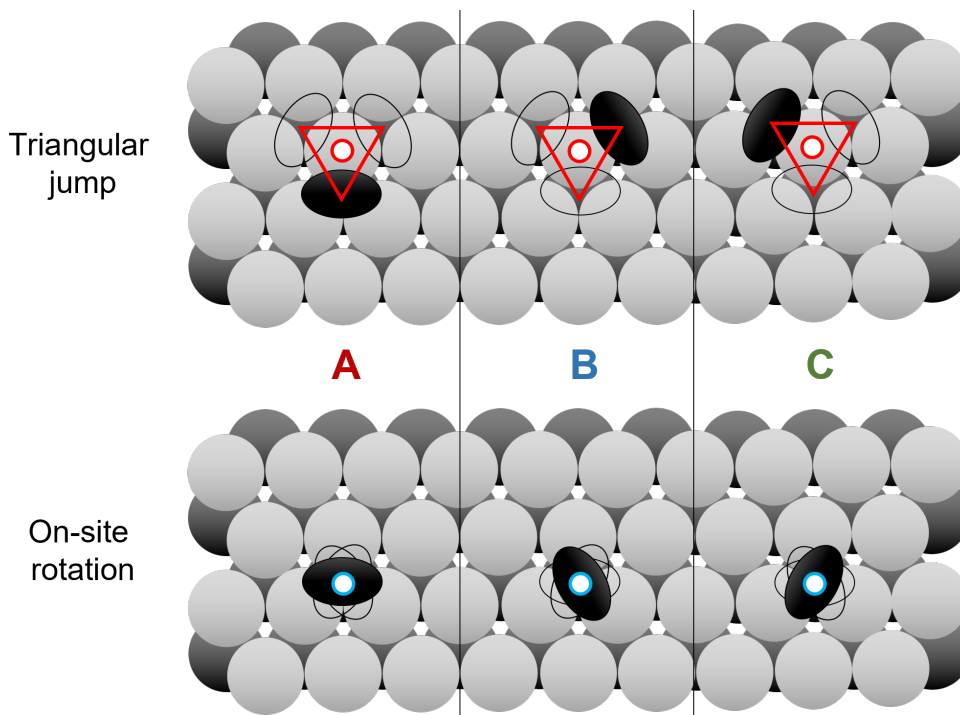
Figure 4.14 : Model of the triangular jump and the on-site rotation of the *dimer* particles on the Ru(0001) surface. The *dimer* particles, shown as black ellipses, are adsorbed on hcp sites in the model (fcc sites are equally possible) in three different orientations (A, B, and C). An open red circle marks the center of rotation of the triangular jumps and the red triangle connects the centers of gravity of the *dimer* particles. An open blue circle marks the center of rotation of the on-site rotation. Bright and dark grey filled circles indicate the Ru atoms of the first and second layer.

The triangular jumps are described as a rotation around a Ru atom. The *dimer* particle jumps between the three hcp adsorption sites around the central Ru atom. A, B, and C are the three orientations of the molecules. The long axis of the ellipse is always oriented perpendicular to the line connecting the center of gravity of the molecule and the center of rotation (open red circle). In that way, the center of gravity of the *dimer* particle draws an equilateral triangle (red triangle). At temperatures up to approximately 80 °C, this process is almost the only one observed. Consequently, the *dimer* particles do not diffuse laterally, but are pinned to the central Ru atom around which they rotate. This underlines the fact that the binding of the molecule towards the Ru surface is very strong.

The second process, the on-site rotation, is observed at temperatures above approximately 80 °C. In this process, the *dimer* particle changes its orientation (A, B, and C) while it does not change its center of mass on the surface. The center of rotation is the center of gravity of the *dimer* particle itself (open blue circle).

By combining these two rotations, a lateral motion of the adsorbed *dimer* particles on the Ru(0001) surface is realized: After the molecule has performed an on-site rotation, the following, faster triangular jumps are performed around a neighboring Ru atom, i.e., the molecule has moved laterally. For the analysis of the diffusion process, a hexagonal lattice is defined that consists of the hcp (or fcc) adsorption sites of the *dimers* (figure 4.15). The *dimer* particles are indicated by short colored lines that represent the orientation of the particle. A *dimer* particle in orientation A on the adsorption site $(0,0)$ can execute triangular jumps in the red triangle, where it switches between orientation B on site $(0,1)$ and orientation C on site $(-1,1)$. In order to enter the blue or green triangle, it first has to perform an on-site rotation to the orientations B or C on site $(0,0)$. The combination of the two rotational processes enables the particles to diffuse laterally across the surface and to reach every adsorption site.
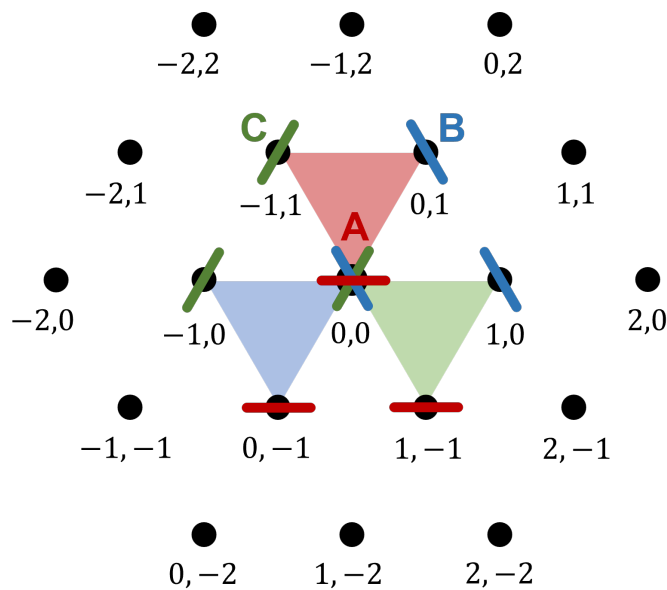
Figure 4.15 : Diffusion model of two jump processes of the *dimer* particles on a hexagonal lattice (black dots). The positions and orientations of the *dimer* particles are indicated by short colored lines: red (orientation A), blue (orientation B), and green (orientation C). Colored triangles mark the triangular jumps the molecule performs depending on the orientation of the *dimer* particle in position $(0,0)$.

Because of the A-B-A-B stacking of the hcp Ru, the triangles that point with their tips downward in figure 4.15, point with their tips upward on a neighboring terrace of

the Ru(0001) surface. The same results when fcc adsorption sites are chosen instead of hcp sites on the same terrace. Therefore, in the evaluation of the experimental data, extra care was taken to ensure that the triangles had the same orientation in all evaluated data. If this was not the case, the STM images were flipped accordingly.

4.4. Kinetic evaluation of the diffusion process

4.4.1. Tracking procedure and trajectories

STM movies of the *dimer* particles were recorded at 21 different temperatures ranging from −13 °C to 124 °C. In order to determine hopping frequencies, statistically significant jump distributions are needed, a requirement fulfilled by the large number of recorded frames (several thousand) at each temperature. The displacements of the observed *dimer* particles were followed between the consecutive images. For this procedure, a special tracking software was used that was originally developed for the diffusion study of oxygen atoms on a CO-covered Ru(0001) surface.[25] This project was part of the dissertation of Ann-Kathrin Kügler (Henß) and was based on *Matlab* scripts for the tracking of the particles and the evaluation of the jump frequencies.[24] Tracking of individual particles in a stack of up to 3000 frames is realized using a wavelet-based algorithm developed by Philipp Messer from the working group of Don C. Lamb at the LMU Munich.[23] Details about the analysis of the oxygen data can be found in the dissertation of Ann-Kathrin Kügler (Henß). In the following, I describe how this procedure was adapted to the data of the *dimer* particles.

First, a data set consisting of an STM movie is uploaded to the *Matlab* program. The original software was designed to track bright round particles in high-speed STM data. Since the *dimer* particles are imaged dark, the image contrast was inverted for the analysis. In the movie, sequences of frames are selected with stable images and in which the measurement parameters were not changed. In the next step, the wavelet algorithm is applied. Here, the center of gravity of the elliptic *dimer* particles is identified in each frame of the data set. (In the original version, spherical particles were tracked.) The tracked positions of the individual particles are then connected throughout the stack of images in consecutive frames. Parameters can be adjusted to specify the size of the particle, the number of frames that shall be skipped, and the radius the particle is allowed to be displaced between two consecutive frames. Afterwards, the obtained trajectories of the particles are corrected for thermal drift. Apart from the mobile *dimer* particles, there are usually also immobile features

present on the surface, which are also automatically detected by the software. These stable features help to identify the thermal drift vector. If a particle is not detected in more than (usually) five preceding frames, this particle is interpreted as new and has an individual new trajectory.

Of all tracked particles in one movie, those are manually selected for the further analysis that fulfill the following criteria: The particles are imaged as *dimers*, and they do not interact with any other *dimer* particle or feature on the surface during the time of the tracked sequence. If such an interaction occurs along the length of the trajectory, this part is discarded. Further, single frames in which the particle is not imaged correctly (for example, because of noise in the STM image or because of double imaging due to a jump during measurement, or the center of gravity is wrongly detected for other reasons) are removed manually.

In the next step, the experimental jump histogram from all selected particles in one data set is calculated. For this purpose, a hexagonal lattice is constructed over each trajectory, which is then used to calculate the jump vectors between two consecutive frames. The sum of all detected events results in the experimental displacement histogram. The jump frequency is then determined by a fit to the experimental distribution, which is described in chapter 4.4.4.

Figure 4.16 displays trajectories of tracked particles from an exemplary STM movie, recorded at room temperature. Figure 4.16 (a) shows a single STM frame; the sequence is 94 seconds long (940 individual frames) and five single *dimer* particles are visible that have no neighbors (each marked with a number). There are also two *dimer* particles in the top left corner next to each other that form a short chain. These particles and the undefined features were tracked but not selected in the further procedure. The trajectories of all detected particles are displayed in figure 4.16 (b). The trajectories of the *dimer* particles are triangular with tips pointing upward. In the STM movie, the *dimer* particles show the characteristic triangular jumps described in the diffusion mechanism above. Figure 4.16 (c) displays the trajectory of particle 2 with a color code representing time, so that the temporal diffusion of the particle can be followed. For consistency with the other experiments, the trajectory was mirrored, so that the triangle points downward. The particle stays in the corners of the triangle for several frames, but because of the finite precision of the experiment and the tracking method, short lines are observed in the three corners. The lines connecting the corners indicate jumps between the three adsorption sites (triangular jumps). The lengths of the jump lines are ≈ 3 Å, which corresponds to the lattice constant of Ru(0001) of 2.7 Å.
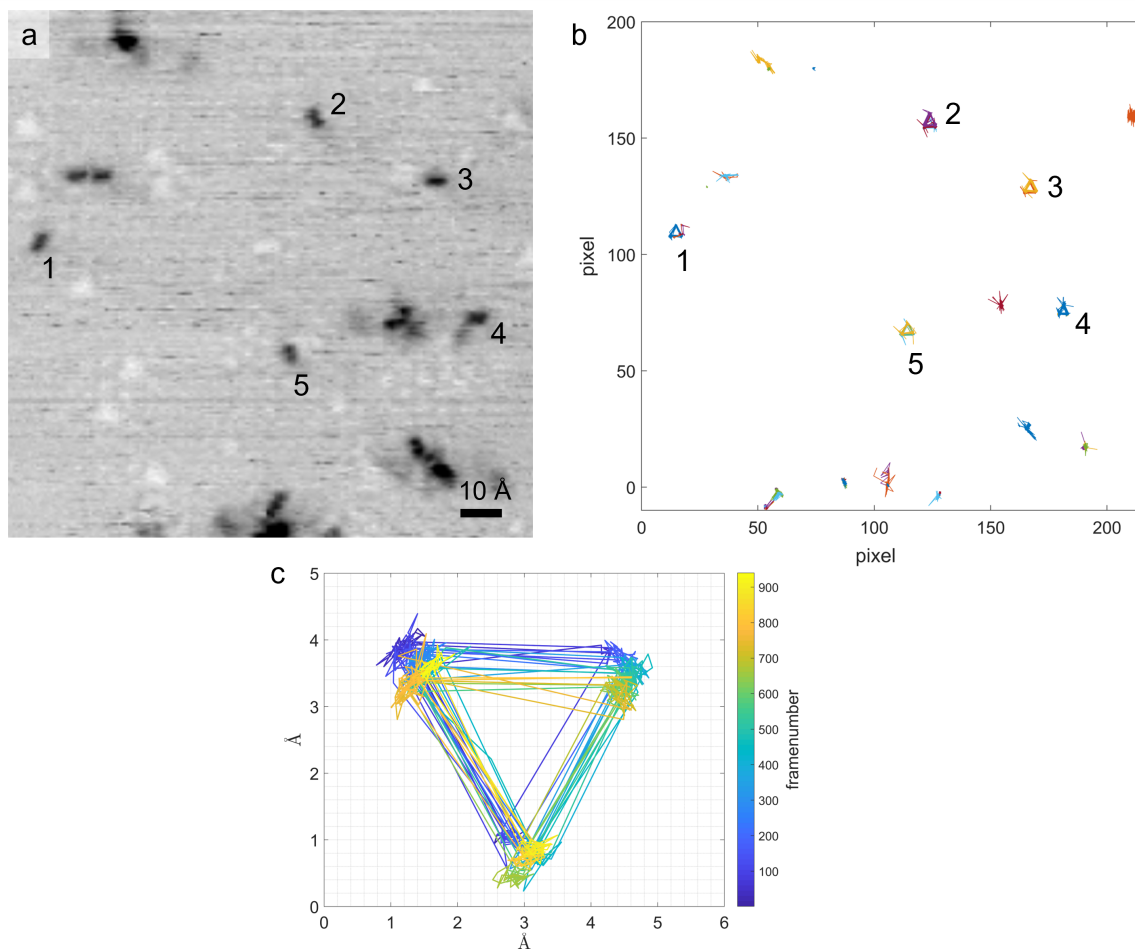
Figure 4.16 : Tracking of *dimer* particles in an STM movie at room temperature. a) Single STM frame from a movie of *dimer* particles prepared by carbon evaporation on the Ru(0001) surface, $C_{evap} = 20$ nAs, $V_t = -0.8$ V, $I_t = 3$ nA, 10 fps, $T = 24$ °C. b) All trajectories of all particles detected in the STM movie; numbers 1 to 5 mark the five *dimer* particles that have been selected for the evaluation. c) Trajectory of particle 2; the frames are time color-coded and the trace is flipped, so that the triangle points downwards.

Figure 4.17 shows two frames of an STM movie recorded at 108 °C and the trajectories of six *dimer* particles. In the STM images (a) and (c), apart from the six numbered *dimer* particles, there are areas of an ordered $(\sqrt{3} \times \sqrt{3})R30°$ structure of CO. The white round features are nitrogen atoms that are mobile at this temperature. Oxygen atoms, which are also imaged bright, jump at a much higher rate and are therefore imaged as stripes in single scan lines. The *dimer* particles also show a high mobility, so that in some of the frames the particles are not shown completely or cut into two pieces when they just moved when the STM tip scanned over the according region. Figure 4.17 (c) shows an exemplary frame in which four of the six particles are not imaged as complete *dimer* particles, and particle 6 appears fragmented. In such cases, where a particle is not imaged or tracked correctly in a

frame, that frame number is deleted from the trajectory of this particle. (This was carried out manually.)
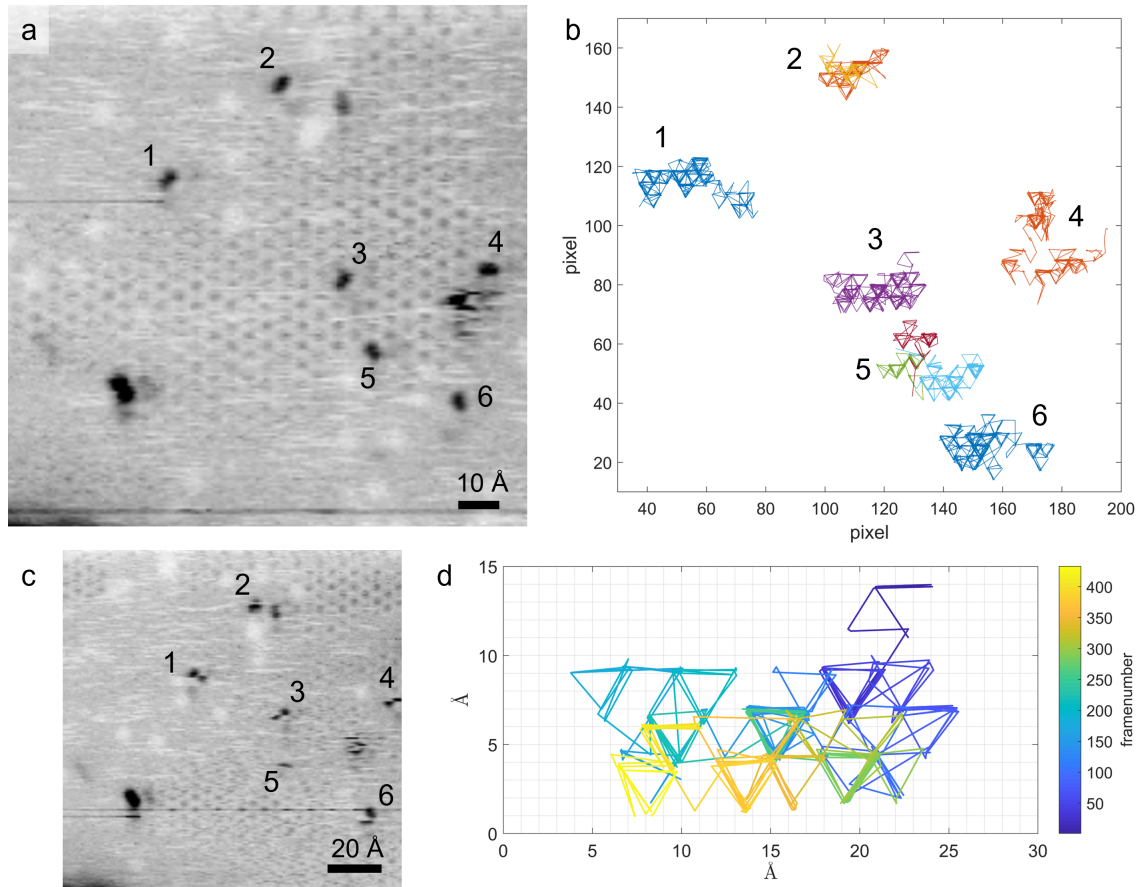

Figure 4.17 : Tracking of the *dimer* particles in an STM movie at elevated temperature. a) Single STM frame from a movie of *dimer* particles prepared by carbon evaporation on the Ru(0001) surface, $C_{evap} = 20$ nAs (as in fig. 4.16), $V_t = -0.5$ V, $I_t = 3$ nA, 10 fps, $T = 108$ °C. b) Trajectories of the six selected particles (numbers 1 to 6). c) Another STM frame from the same movie as in a); here some of the *dimer* particles are not imaged correctly. d) Trajectory of particle 3 with color-coded frame numbers.

The trajectories of the particles at temperatures above ≈ 80 °C (figure 4.17 at 108 °C) consist of triangles connected at their corners with neighboring triangles. The trajectories of all selected particles of this particular STM movie are displayed in figure 4.17 (b). The trajectory of particle 5 is divided into three shorter sections, each shown in a different color (red, light blue, and green). As mentioned earlier, if a particle is not tracked in several consecutive frames or the particle is fragmented, a new trace starts. During the evaluation procedure, the segments are joined together to form coherent trajectories, which is another manual task.

Figure 4.17 (d) displays the time color-coded trajectories of particle 3. The triangles point downward as the bottom row indicates best. One can see that at the higher

temperature the particle stays at one of the corners of one triangle often only for the time of one frame (0.1 s). The particles not only perform triangle jumps, but also rotate around their own axis (on-site rotation). As a consequence, the particles can change between neighboring triangles, and the trajectory extends over a larger area. In the next step, the trajectories are superimposed by a (1×1) lattice corresponding to the three-fold adsorption sites of the underlying Ru(0001) surface.

Jump histograms were calculated from all collected trajectories at the respective temperatures. For this purpose, jump vectors between the lattice points of two consecutive frames are determined. At temperatures below 80 °C, only triangular jumps are observed, and one expects a triangular displacement histogram. However, the tracking routine only identifies the positions of the particles, not their orientation A, B, or C. The routine, therefore, averages over the three triangles shown in figure 4.15, so that a hexagonal displacement histogram is expected (given the number of events is high enough).

Figure 4.18 shows two experimental histograms that belong to the two data sets described above, at room temperature (figure 4.16) and at 108 °C (figure 4.17). The middle bar at position $(0, 0)$ corresponds to all cases in which the particle is found on the same site in two consecutive frames. (This includes cases in which the particle has jumped more than once in the time period between two frames and happened to end on the same site again.) The fraction of particles on the $(0, 0)$ site decreases from ≈ 0.94 to ≈ 0.34, i.e., by almost a factor of three when the temperature was increased from 24 °C to 108 °C. At room temperature, there are six small bars of similar height around the middle bar located on the six nearest sites representing the hexagonal distribution. At 108 °C (figure 4.18 (b)), these bars increase and additional smaller bars appear at positions further away from the center. (The displayed displacement histograms only include the STM movie sequences described above. In the overall study, several STM movies are analyzed for each temperature so that a better statistic is obtained.)
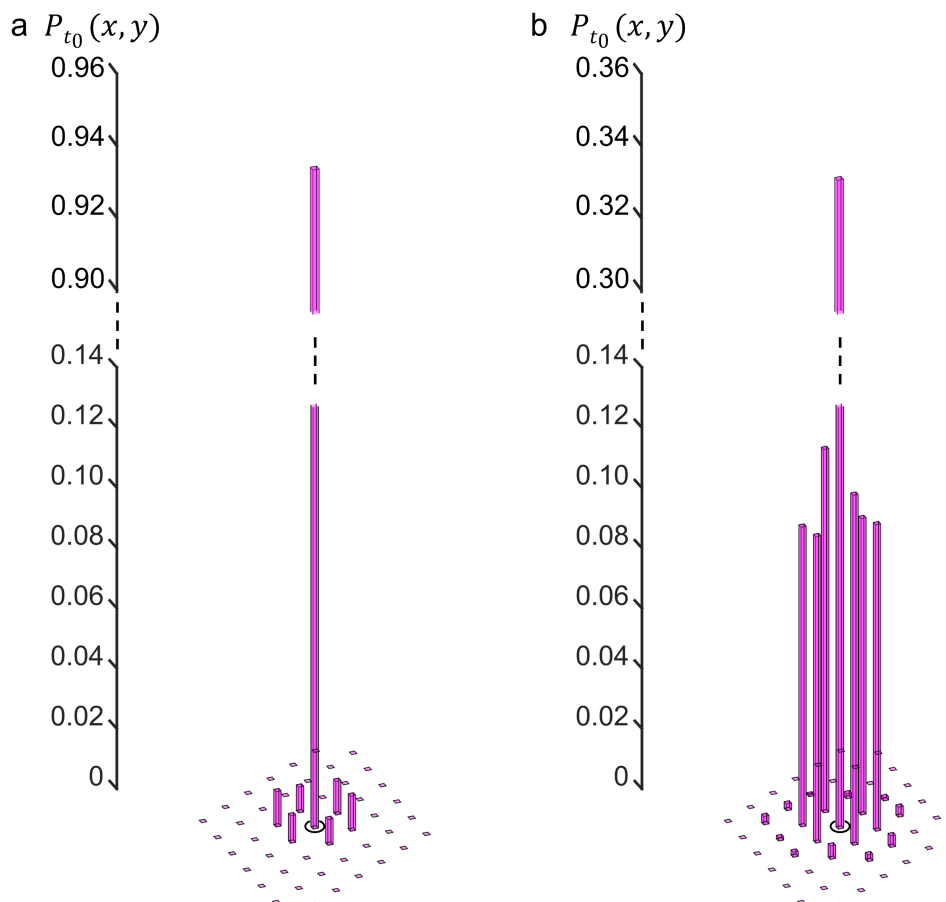
Figure 4.18 : Experimental displacement histograms from the *dimer* particles at two different temperatures. The y-axis is interrupted. The black circle marks the position $(0,0)$. a) Histogram form an STM movie recorded at $T = 24$ °C (see fig. 4.16) and b) from an STM movie recorded at $T = 108$ °C (see fig. 4.17).

4.4.2. Assessment of the influence of the scanning tip

The tunneling tip can interact with adsorbates on the sample surface and influence their mobility. This process is dependent on the tunneling parameters, like the tunneling current I_t and the tunneling voltage V_t. Tests were performed in order to check if the tip influences the mobility of the *dimer* particles under the chosen measurement conditions. The two processes of the diffusive motion of the *dimer* particles, the triangular jumps and the on-site rotations, are expected to have different diffusion barriers because the on-site rotation occurs at higher temperatures. As a triangular jump has a lower energy barrier, it is more likely to be influenced by the scanning tip.

Influence test 1: If there is an effect of the tunneling tip on the dynamics, it would add to the thermal effects. It should therefore still be present at low temperatures where thermal effects are suppressed. It was, therefore, investigated whether the

motion of the particles diminishes and effectively halts at very low temperatures. The *dimer*-covered Ru(0001) surface was cooled by liquid helium to a temperature of -208 °C to -203 °C. By varying the scanning parameters, I_t and V_t, it was tested whether these parameters influence the motion of the *dimer* particles. It was observed that at $I_t = 3$ nA (the commonly chosen current), combined with a tunneling voltage in the range of $V_t = -0.1$ V to -1.0 V, the motion of the particles was completely frozen. No triangular jumps and no on-site rotations were observed. Also, by decreasing the tunneling current to $I_t = 1$ nA or increasing it to $I_t = 10$ nA, no motion of the *dimer* particles could be detected at -203 °C.

Influence test 2: This test was performed at room temperature, where the triangular jumps are thermally activated. As in test 1, STM movies were recorded with different tunneling parameters, and the resulting jump frequencies were compared. (How the jump frequencies were obtained from the trajectories is the subject of chapter 4.4.4.) In figure 4.19, the jump frequency values are plotted versus the applied tunneling voltage V_t from -1.0 V to $+0.3$ V for the different currents. In the left graph 4.19 (a), the jump frequency of the triangular jumps is displayed; the values range from 0.30 Hz to 0.45 Hz for three different tunneling currents (1 nA, 3 nA, and 10 nA). The value at $V_t = -0.2$ V combined with $I_t = 1$ nA is somewhat higher, ~ 0.5 Hz. At $V_t = -0.3$ V and $I_t = 10$ nA, a similar increase is noticed. A pronounced deviation is the value of 2 Hz for the tunneling parameters $V_t = -0.05$ V and $I_t = 10$ nA. These are extreme parameters where the tip is quite close to the surface.
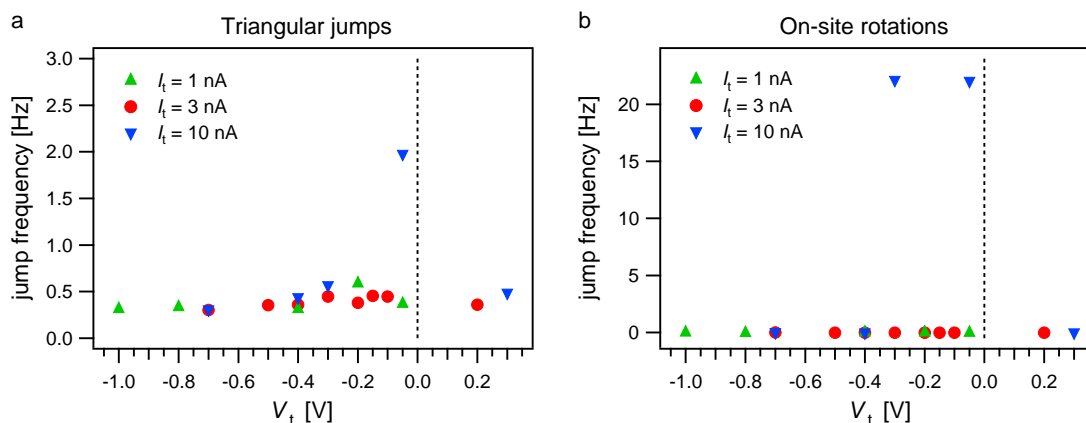
Figure 4.19 : Influence of the tunneling voltage V_t and tunneling current I_t on the jump frequency of the *dimer* particles. a) Jump frequency of triangular jumps, b) jump frequency of on-site rotations, different colors represent different I_t values, the STM movies were recorded at $T = 27 - 30$ °C.

Graph 4.19 (b) is a plot of the jump frequency of the on-site rotation. In the chosen temperature range of 27 °C to 30 °C and with the usually chosen tunneling parameters, the *dimer* particles only showed the triangular jumps; on-site rotations did not occur. For $I_t = 1$ nA and $I_t = 3$ nA, the on-site rotation jump frequency is zero in the whole range of applied tunneling voltages V_t. However, at $I_t = 10$ nA combined with $V_t = -0.3$ V and $V_t = -0.05$ V, the on-site rotation was obviously induced by the scanning tip, and a high jump frequency of 23 Hz was obtained. Under these conditions, also the directions of the trajectories of the *dimer* particles are affected. Figure 4.20 shows an example. One can see that the particle path, although still showing the characteristic triangles on a small scale, displays a clearly preferred direction along the y-axis on the scale of the entire image. The particle obviously follows the y-direction of the raster scan.
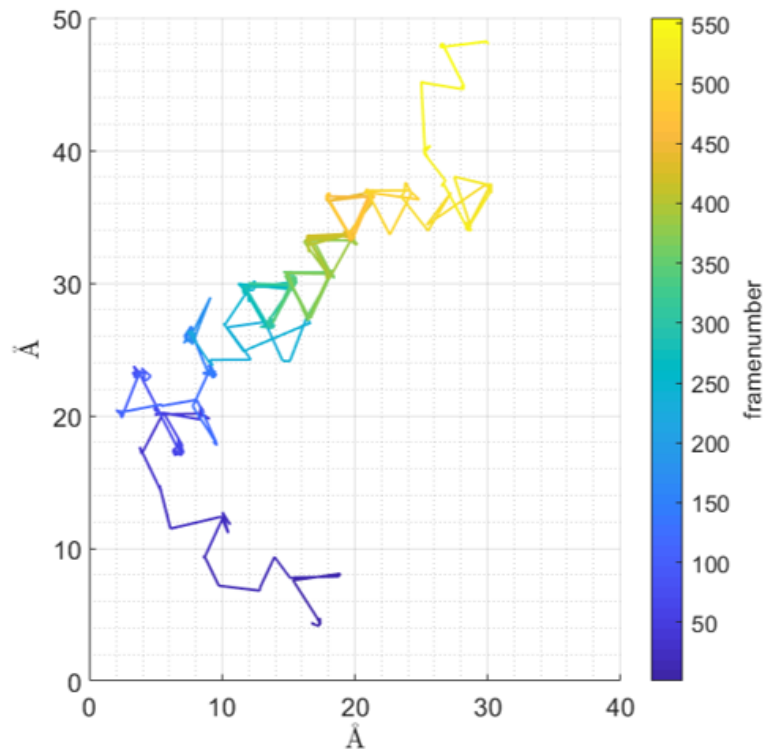
Figure 4.20 : Trajectory of a *dimer* particle under the influence of the tunneling tip. STM movie recorded at $V_t = -0.05$ V, $I_t = 10$ nA, 10 fps, $T = 30$ °C.

It is concluded that if the tip rasters at a too close distance over the sample, the diffusion of the *dimer* particles is influenced. The parameters where an interaction was clearly detected are $I_t = 10$ nA combined with $V_t = -0.05$ V to -0.3 V.
In all described experiments, I therefore used the following tunneling parameters for recording STM movies: $I_t = 3$ nA and V_t in the range from -0.1 V to -1.0 V. A tunneling current of 3 nA rather than 1 nA was used in order to enhance the

quality of the images. The tunnel voltage was chosen such that the *dimer* particles were imaged well.

4.4.3. Tracking of the particle orientation

The work described in this subchapter was performed in cooperation with Simon Wanninger of the working group of Prof. Don C. Lamb, LMU Munich. I provided the STM data and the kinetic evaluation and the diffusion model of the motion of the *dimer* particles. Simon Wanninger developed new *Matlab* scripts that were included in the existing evaluation routine.

The collaboration aimed at determining the orientations of the *dimer* molecules in addition to the positions of the centers of gravity, the only information determined in the standard analysis. According to the model shown in figure 4.15, the position of the center of gravity automatically corresponds to one of the orientations A, B, or C as long as the molecule only performs triangular jumps, e.g., in the red triangle shown in figure 4.15. However, when the molecule performs an on-site rotation, such an event is not directly visible because the center of gravity does not change. That such an event has happened becomes apparent in the standard analysis when in the following the molecule performs triangular jumps around another Ru atom (in the green or blue triangle in figure 4.15). In this way, on-site rotations can be implemented in a precise manner in a statistical analysis (as is done in chapter 4.4.4). However, obtaining this information directly rather than in this implicit way would of course be preferential.

In cooperation with Simon Wanninger, an orientation tracking tool was implemented in the existing *Matlab* evaluation routine. In the added procedure, the angles of the particles with respect to the x and y axes of the STM frame are determined. This is realized by an eigenvalue decomposition that defines a vector along the maximum variance of the object that represents the particle. The existing wavelet algorithm that identifies the particles in the data provides a 2D binary mask for each frame, i.e., an image only consisting of white and black pixels. In the new routine, the shapes of the particles in this mask are used to specify the angle for each particle and frame. In figure 4.21, two STM frames and the corresponding particle mask with the calculated angles next to each tracked particle are displayed. The selected *dimer* particles are labeled with numbers. In the ideal case, the routine would identify three populations of particles with similar angles, which can then be assigned to the three possible orientations A, B, and C of the particles as defined in the diffusion mechanism in chapter 4.3.
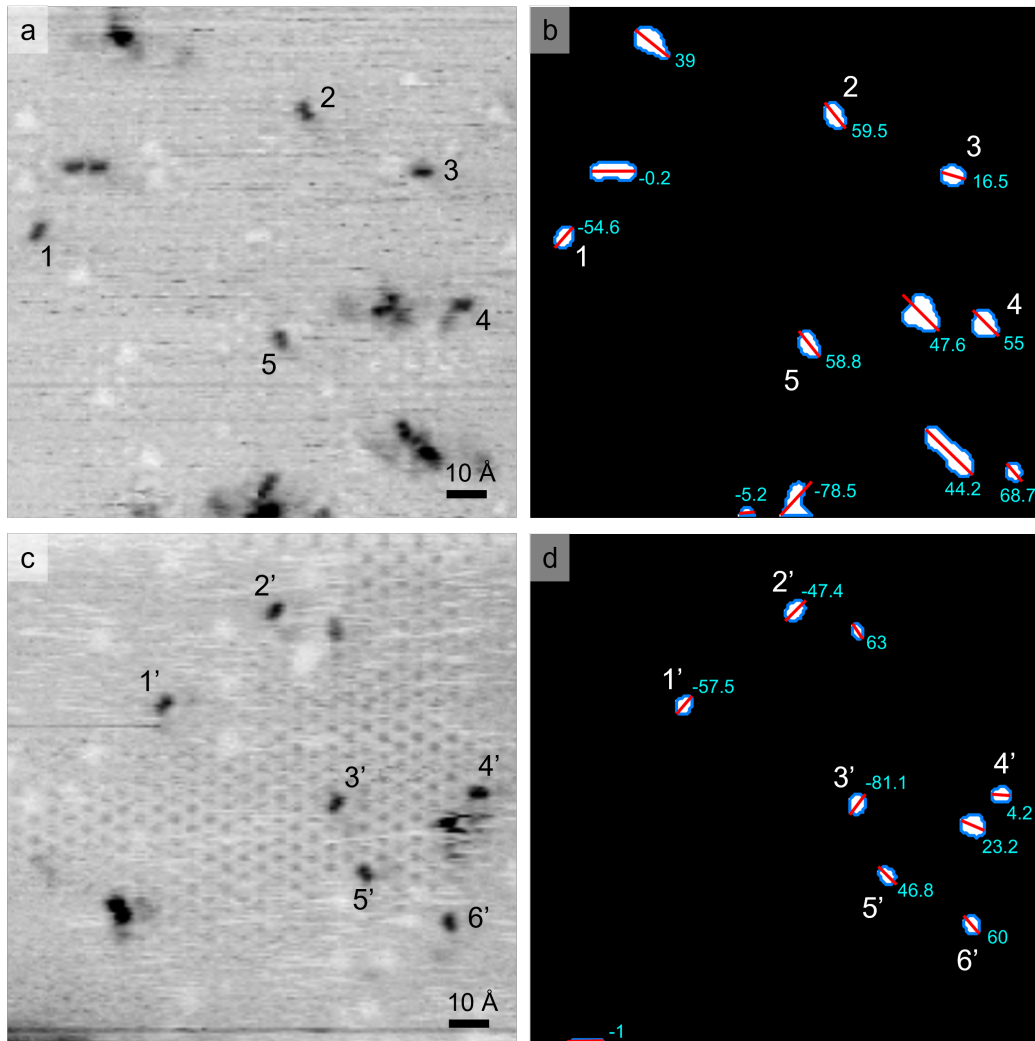
Figure 4.21 : STM images of *dimer* particles on the Ru(0001) surface and the corresponding 2D particle masks with angle information; the selected particles are numbered. a) Single STM frame from a movie with *dimer* particles prepared by carbon evaporation on Ru(0001), $C_{evap} = 20$ nAs, $V_t = -0.8$ V, $I_t = 3$ nA, 10 fps, $T = 24$ °C (same as in figure 4.16), b) single STM frame from a movie with *dimer* particles prepared as in a), $V_t = -0.5$ V, $I_t = 3$ nA, 10 fps, $T = 108$ °C (same as in figure 4.17).

Two angle histograms (figure 4.22) are derived from the data sets that contain the above 2D masks (figure 4.21) from the experiments at 24 °C and 108 °C, respectively. In both cases, three preferred angular orientations are found with maxima close to 0°, 60°, and −60°, matching the predictions of the model. In the next step, three ranges of angles are defined in the histograms and assigned to the three orientations A, B, and C for further analysis (black lines mark the ranges).
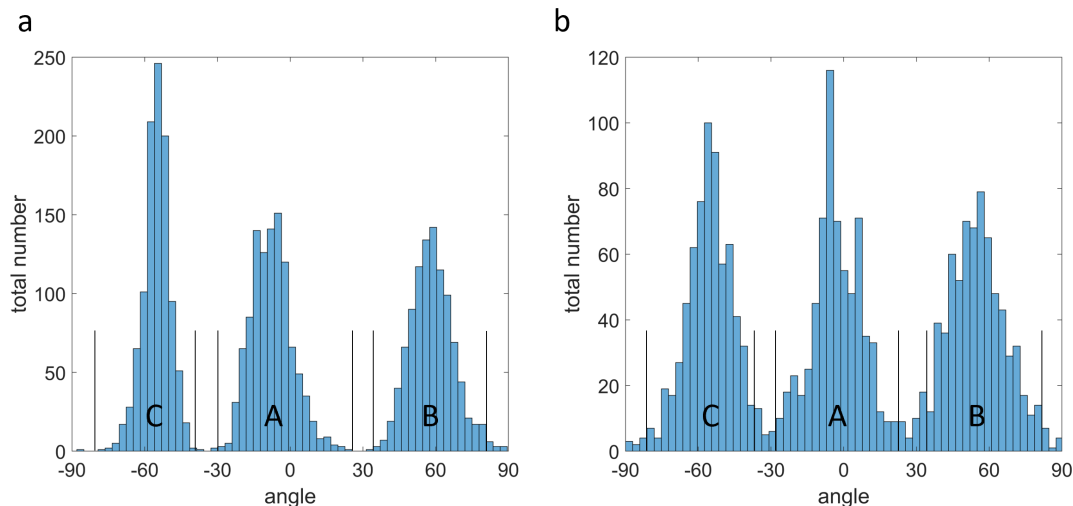
Figure 4.22 : Histograms of the angular distribution resulting from the orientation tracking of the *dimer* particles at two different temperatures of the same data sets as in figures 4.16, 4.17 and 4.18. a) From an STM movie recorded at $T = 24$ °C and b) from an STM movie recorded at $T = 108$ °C.

The frames manually eliminated at earlier analysis steps do not appear in the angular distribution. However, although the histograms show three well-separated distributions, problems with wrongly assigned orientations occur. For example, particle 4 in figure 4.21 (a) is visually clearly oriented in configuration A, but the assigned angle is 55° with respect to the x axis (figure 4.21 (b)), which belongs to the range assigned to orientation B. Due to the strange shape of the particle mask in that particular frame a wrong assignment is made.

These minor misassignments have significant effects on the statistics. The exemplary STM movie (figure 4.21 (a) and histogram 4.22 (a)), has been recorded at 24 °C. At this temperature, according to visual inspection, all particles only perform triangular jumps around given Ru atoms; no on-site rotations take place. The angle tracking algorithm leads to a correct orientation assignment for 2969 out of 2982 frames, a success rate of 99.56 % (13 wrong assignments, error rate 0.44 %).

A similar check for the data at higher temperatures, such as the data from figure 4.22 (b) at 108 °C, was not done. At this temperature, the *dimer* particles

perform both triangular jumps and on-site rotations, and the error of wrongly assigned angles cannot be specified unless every particle orientation in every frame would be manually checked. (This effort is too time-consuming.)

The low error rate in the room temperature data has an impact on the evaluated jump frequencies: the frequency of the on-site rotation is artificially increased (it ought to be zero at this temperature). For the data at temperatures above 80 °C (for which no error rate was determined), an increase of the jump frequencies of the on-site rotations is obtained compared to the values gained from the usual tracking procedure (without angle information). A few wrong assignments cause a large error in the obtained jump frequencies.

In conclusion, the elliptical shape of the particles is not well enough pronounced to prevent incorrect angle assignments. Tracking of angles and extracting orientation information of the *dimer* particles is possible, but the precision is not high enough to use the data for kinetic evaluations.

4.4.4. Jump frequencies and Arrhenius plot

This chapter presents the evaluation of the jump frequencies for both motions from the experimental displacement histograms obtained by the standard analysis. From the variations of the frequencies with temperature the activation energies of both processes are obtained. In total, STM movies of the *dimer* particles on Ru(0001) were recorded at 21 different temperatures in a range from -13 °C to 124 °C. The evaluation of the displacement histograms from the tracked particle trajectories has been presented in chapter 4.4.1.

The histograms are displacement distributions $P_{t_0}(x, y)$ that represent the probability that a molecule detected in one frame at a certain site has been displaced to a new site at position (x, y) in the following frame (at the applied rate of 10 frames per second, the time step is 0.1 s). The unit for the displacement vectors is the lattice constant 2.71 Å of the hexagonal Ru(0001) surface. The hexagonal symmetry of the distribution confirms that the jumps and rotational events happen in a uniform manner in all directions with the same statistical probability.

The model that has been used to describe the experiments is illustrated in figure 4.15. It is based on the assumption that the *dimer* particles only perform two types of motions: triangular jumps, which are relatively fast and in which the molecules rotate between three equivalent sites around a central Ru atom, and on-site rotations, which are slower, and in which the molecules rotate around their own axes on the same site. Each triangular jump is connected with a change of the

molecular axis in one of three orientations (A, B, and C), and each on-site rotation also changes the molecular axis in one of the same three orientations. It is further assumed that the molecules only occupy one type of threefold sites (hcp or fcc), so that a hexagonal lattice results, and that all events are statistically uncorrelated. Any memory effects and long jumps are ruled out.

For this model, the displacement distribution $P_{t_0}(x, y)$ is given by the following equation 4.2:

$$P_{t_0}(x, y) = \sum_{n_1=0}^{\infty} \sum_{n_2=0}^{\infty} \tilde{P}_{t_0}(n_1, n_2) \cdot \overline{w}_{n_1, n_2}(x, y) \tag{4.2}$$

x and y are the coordinates of the lattice sites, and t_0 is the time interval between two images. n_1 and n_2 are the numbers of triangular jumps and on-site rotations in the time period t_0, respectively. $\tilde{P}_{t_0}(n_1, n_2)$ is the probability that n_1 triangular jumps and n_2 on-site rotations happen in the time period t_0. $\overline{w}_{n_1, n_2}(x, y)$ is the average probability that a molecule travels to a site with coordinates (x, y) by the combination of n_1 and n_2 events. With the assumptions of the model, $\tilde{P}_{t_0}(n_1, n_2)$ is given by a product of two Poisson distributions:

$$\tilde{P}_{t_0}(n_1, n_2) = \frac{(\Gamma_1 \cdot t_0)^{n_1}}{n_1!} e^{-\Gamma_1 \cdot t_0} \cdot \frac{(\Gamma_2 \cdot t_0)^{n_2}}{n_2!} e^{-\Gamma_2 \cdot t_0} \tag{4.3}$$

Γ_1 and Γ_2 are the average frequencies of the triangular jumps and on-site rotations, respectively. These are the two quantities to be extracted from the analysis.

$\overline{w}_{n_1, n_2}(x, y)$ can be seen as a geometry factor that is determined by the paths the particles can travel on a hexagonal lattice by combinations of the two types of motion. It is determined by the recursion equations 4.4 to 4.9:

$$w_{n_1, n_2}(A, x, y) = \frac{1}{2} w_{n_1-1, n_2}(B, x, y+1) + \frac{1}{2} w_{n_1-1, n_2}(C, x-1, y+1) \tag{4.4}$$

$$w_{n_1, n_2}(B, x, y) = \frac{1}{2} w_{n_1-1, n_2}(A, x, y-1) + \frac{1}{2} w_{n_1-1, n_2}(C, x-1, y) \tag{4.5}$$

$$w_{n_1, n_2}(C, x, y) = \frac{1}{2} w_{n_1-1, n_2}(A, x+1, y-1) + \frac{1}{2} w_{n_1-1, n_2}(B, x+1, y) \tag{4.6}$$

$$w_{n_1, n_2}(A, x, y) = \frac{1}{2} w_{n_1, n_2-1}(B, x, y) + \frac{1}{2} w_{n_1, n_2-1}(C, x, y) \tag{4.7}$$

$$w_{n_1,n_2}(\mathrm{B},x,y) = \frac{1}{2}w_{n_1,n_2-1}(\mathrm{A},x,y) + \frac{1}{2}w_{n_1,n_2-1}(\mathrm{C},x,y) \qquad (4.8)$$

$$w_{n_1,n_2}(\mathrm{C},x,y) = \frac{1}{2}w_{n_1,n_2-1}(\mathrm{A},x,y) + \frac{1}{2}w_{n_1,n_2-1}(\mathrm{B},x,y) \qquad (4.9)$$

$w_{n_1,n_2}(\mathrm{A},x,y)$ in equation 4.4 is the probability that a particle that has moved to a site next to the given site (x,y) with orientation B by n_{1-1} triangular jumps and n_2 on-site rotations, or to a corresponding site with orientation C by the same combination of events, that this particle jumps to the site (x,y) with orientation A by one further triangular jump. Equation 4.5 and 4.6 are the equivalent equations for a particle at site (x,y) in orientation B and C, respectively. Equation 4.7 is the probability that a particle that has moved to a given site (x,y) with orientation B or C by a combination of n_1 triangular jumps and n_{2-1} on-site rotations, that this particle performs one further on-site rotation to obtain the orientation A on the same site. The set of equations is initialized by setting, e.g., $w_{0,0}(\mathrm{A},x,y) = 1$ and all other $w_{n_1,n_2}(\mathrm{Z},x,y) = 0$ ($\mathrm{Z} = \mathrm{A}, \mathrm{B},$ or C) (this is the configuration in figure 4.15 with the particle in A orientation at $(0,0)$), and then equations 4.4 to 4.9 are applied by increasing n_1 and n_2 in steps of one. In this way, for each combination of n_1 and n_2, a $w_{n_1,n_2}(\mathrm{Z},x,y)$ value is obtained for each lattice site (x,y) and the respective orientation $\mathrm{Z} = \mathrm{A}, \mathrm{B},$ or C.

However, as already mentioned, the standard version of the tracking algorithm does not discriminate between the orientations in the experimental data. In the model, this feature was included by additionally initializing the set of recursion equations by setting $w_{0,0}(\mathrm{B},x,y) = 1$ and $w_{0,0}(\mathrm{C},x,y) = 1$, applying the recursion equations with these two initializations, and finally averaging the three $w_{n_1,n_2}(\mathrm{Z},x,y)$ values to give $\overline{w}_{n_1,n_2}(x,y)$. (Alternatively, one can initialize the set of equations by setting $w_{0,0}(\mathrm{A},x,y) = w_{0,0}(\mathrm{B},x,y) = w_{0,0}(\mathrm{C},x,y) = \frac{1}{3}$ which gives the same results.) $\overline{w}_{n_1,n_2}(x,y)$ is the quantity that enters equation 4.2.

The size of the lattice was restricted to (23×23) lattice sites, which, considering the much smaller widths of the experimental displacement histograms, is more than sufficient. Mathematically, (23×23) matrices were constructed, one for every combination of n_1 and n_2 with the $\overline{w}_{n_1,n_2}(x,y)$ values as matrix elements. The recursion matrices were evaluated for n_1 up to 100 and n_2 up to 10, which are considered sufficiently large values. A difficulty for the evaluation of $\overline{w}_{n_1,n_2}(x,y)$ is the fact that the triangular jumps and the on-site rotations are not commutative (figure 4.15). Hence, the application of the recursion equations depends on the sequence of n_1

and n_2, and one has to calculate one matrix for each permutation of n_1 and n_2. For $n_1 = 100$ and $n_2 = 10$ the number of permutations, 4.7×10^{13}, is prohibitively high for any further analysis. However, in the dissertation of Ann-Kathrin Kügler (Henß), it was shown for a similar system of two types of hopping events that, when one works with average values, one can combine the two types of events in pairs, perform a sorting procedure and take averages for the resulting groups of pairs.[24] This procedure dramatically reduces the number of recursion matrices, in the present case to $100 \times 10 = 1000$. Within the present work, as a test, calculations were performed for $n_1 = 30$ and $n_2 = 5$ by using this procedure and, for comparison, by applying the full set of permutations. Identical results were obtained. Finally, according to equation 4.2, the matrices are multiplied by $\tilde{P}_{t_0}(n_1, n_2)$ and the product is summed from $n_1 = 0$ to 100 and from $n_2 = 0$ to 10.

The jump frequencies Γ_1 and Γ_2 are the only unknown parameters in equation 4.2. They are obtained by fitting $P_{t_0}(x, y)$ (eq. 4.2) to the experimental displacement histograms. Figures 4.23 (a) and (b) show the experimental and the fitted jump distributions for two temperatures, 25 °C and 108 °C. The experimental distributions are averages over several STM movies at the respective temperature. The blue bars in the histograms are the fitted distributions from equation 4.2. The experimental and fitted distributions match very well, as shown by the residual plots in figure 4.23 (c) and (d).

The results for the Γ_1 and Γ_2 values are listed in table 4.7. The data are sorted by the preparation method for the *dimer* particles, i.e., carbon evaporation or ethylene dosing. The sums of the detected events are also listed. An event means that in two consecutive STM frames, a *dimer* particle has been observed, tracked, and a jump vector has been calculated that enters the displacement histogram. At temperatures < 80 °C, no or only few events of on-site rotations were observed. In these cases, the fitting routine often gave small negative Γ_2 values, indicating that the corresponding events are statistically insignificant. For that reason, the few positive Γ_2 values, which are in the same $10^{-3} - 10^{-6}$ s^{-1} order of magnitude, were also not included in the further analysis.
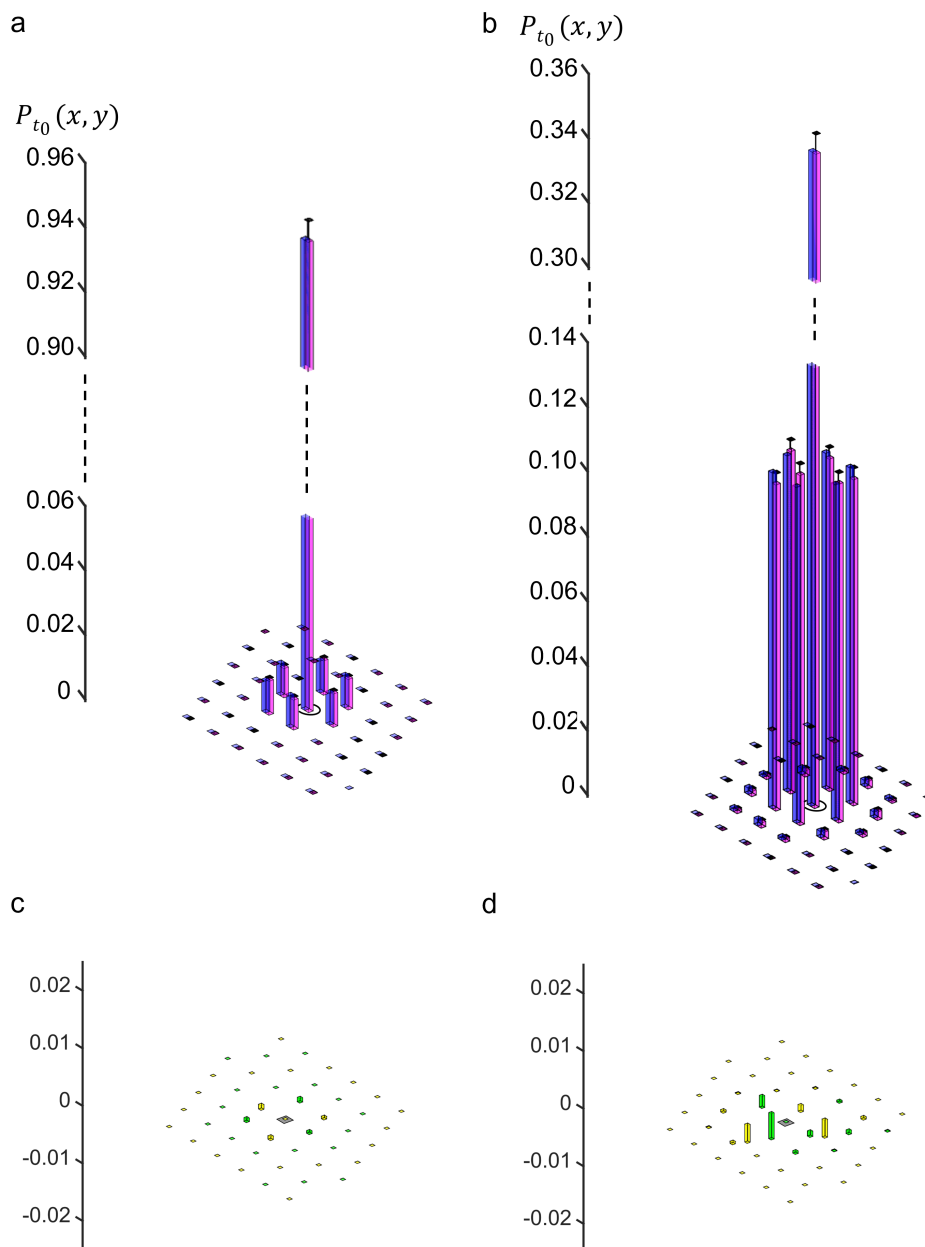
Figure 4.23 : Experimental (in pink) and fitted displacement histograms (in blue) of the *dimer* particles at two different temperatures. The black circle marks the $(0,0)$ position. a) Histogram from STM movie recorded at $T = 24$ °C (see fig. 4.16) and b) at $T = 108$ °C (see fig. 4.17), c) residual plot of the fit in a) and d) residual plot of the fit in b) with green bars indicating positive values and yellow bars indicating negative values.

Table 4.7 : List of experiments used for the determination of Γ_1 and Γ_2, together with the temperatures, the number of events #, and the tunneling voltages; $I_t = 3$ nA in all measurements.

prepara-tion method	T [°C]	T [K]	#	V_t [V]	Γ_1 $[s^{-1}]$	Γ_2 $[s^{-1}]$
carbon evaporation	24	297.15	23379	$-0.7; -0.8$	0.621	-0.00286
	41.8	314.95	28215	$-0.2; -0.54$	3.47	-0.000800
	43.3	316.45	10971	-0.54	3.26	-0.000529
	57	330.15	12699	-0.2	6.12	-2.72×10^{-6}
	78	351.15	4938	-0.2	13.4	0.0238
	79.7	352.85	10306	-0.2	5.85	0.168
	108	381.15	9697	$-0.1; -0.5$	23.5	1.20
	124	397.15	5208	-0.2	20.5	13.1
ethylene dosing	-13	260.15	12862	-0.2	0.176	-0.000858
	2	275.15	8438	-1.0	0.300	-5.95×10^{-5}
	6	279.15	6969	$-0.1; -0.2$	0.487	-0.00925
	12	285.15	10298	-0.6	0.787	-0.000427
	25	298.15	24808	-0.2	0.728	-0.000912
	26	299.15	8873	-0.4	0.361	-0.0255
	26	299.15	8307	-0.5	0.355	-0.0266
	26	299.15	19511	-0.7	0.303	1.47×10^{-6}
	27	300.15	11635	-0.1	0.447	-0.0128
	27	300.15	4609	-0.15	0.456	-0.0119
	27	300.15	4295	-0.2	0.381	-0.0216
	27	300.15	12971	-0.3	0.447	-0.0128
	31	304.15	22143	-1.5	1.11	1.66×10^{-5}
	42.4	315.55	32567	-0.2	2.86	-0.000201
	64	337.15	12601	-0.2	7.58	2.20×10^{-5}
	86	359.15	10553	$-1.0; -0.5$	3.20	0.293
	90	363.15	11176	-0.8	4.22	0.431
	106	379.15	5397	-0.2	21.3	0.869

The remaining data are plotted in an Arrhenius diagram (figure 4.24). As one can see, both sets of frequencies, Γ_1 and Γ_2, are well described by linear fits. (The three extremely low Γ_2 values were not included, as already mentioned.) It can be concluded that the Arrhenius law:

$$\Gamma = \Gamma^0 \cdot e^{\left(\frac{-E^*}{k_\mathrm{B} T}\right)} \tag{4.10}$$

for activated processes describes the data well.

Γ is the jump frequency, Γ^0 the preexponential factor, E^* the activation energy, k_B the Boltzmann constant and T the temperature in Kelvin.

The slopes of the linear fits provide the activation energies of the two processes, $E_1^* = 0.36 \pm 0.03$ eV for the triangular jumps and $E_2^* = 1.27 \pm 0.21$ eV for the on-site rotations (table 4.8). The preexponential factors extracted from the intersection with the y-axis are $\Gamma_1^0 = 10^{5.94 \pm 0.5}$ Hz and $\Gamma_2^0 = 10^{17.0 \pm 2.9}$ Hz, respectively. Both preexponential factors strongly deviate from the expected value of 10^{12} to 10^{13} Hz.[1,87,88]

The Arrhenius plot of the two types of motion of the small hydrocarbon molecule (*dimers*) shows an unusual crossing of the two linear fits within the plotted temperature range. Usually the crossing is expected at the y-axis. This phenomenon is called the compensation effect. It will be discussed in greater detail in chapter 4.6.
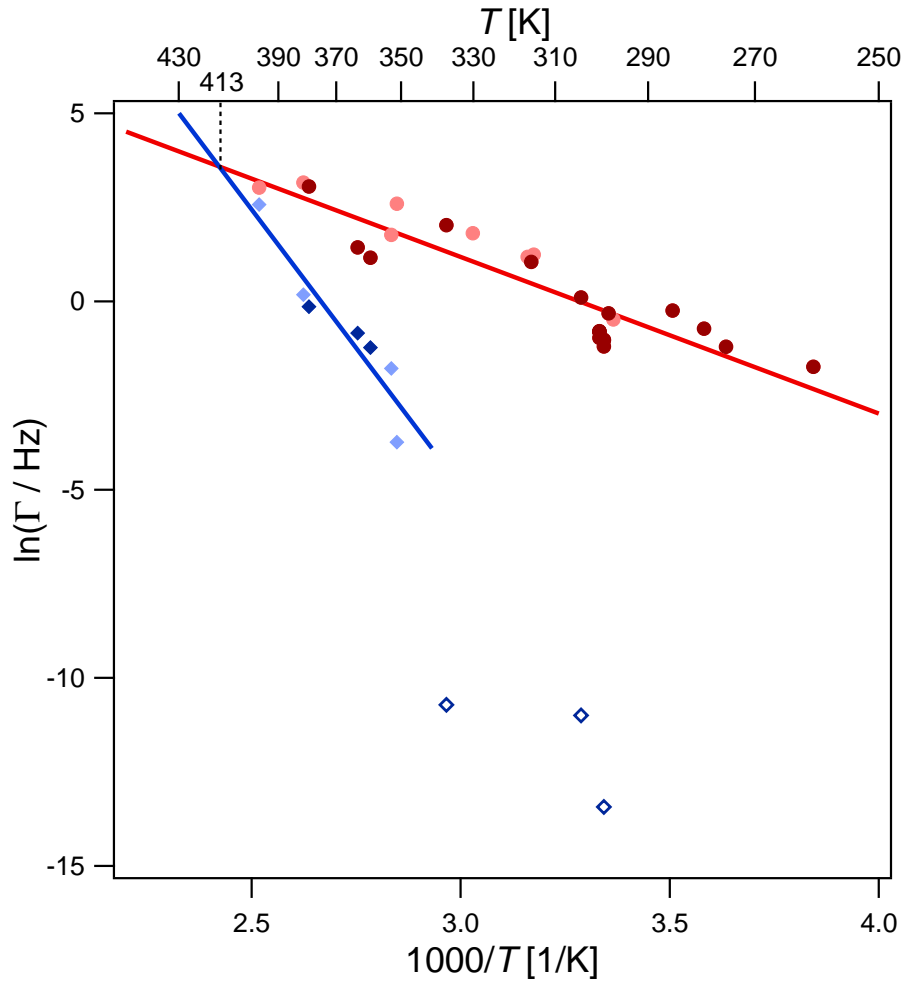
Figure 4.24 : Arrhenius plot of the temperature dependency of the two processes of the *dimer* particles. The triangular jumps are represented by the red dots, and the on-site rotations are represented by the blue squares. Darker color indicates data obtained from *dimers* prepared by ethylene dosing, lighter color from by carbon evaporation. The three open blue squares are not included in the fit.

Table 4.8 : Activation energies E^* and preexponential factors Γ^0 of the two processes from the Arrhenius plot.

	triangular jump	on-site rotation
E^*	0.36 ± 0.03 eV	1.27 ± 0.21 eV
Γ^0	$10^{5.94 \pm 0.5}$ Hz	$10^{17.0 \pm 2.9}$ Hz

4.5. DFT investigations on possible molecular configurations

In order to gain more information on the possible molecular candidates for the *dimer* particles, a cooperation with Sung Sakong of the theoretical chemistry group of Axel Groß in Ulm was established. A final match between experiment and theory has not been reached so far. The experimental results are the characteristics listed in chapter 4.2.6 and the activation energies from the temperature dependence of the processes. The DFT calculations were performed with similar parameters as those applied in the joint papers with S. Sakong and A. Groß[89,90], see chapters 5.2 and 5.3.

Although the system, the fragment of a small hydrocarbon molecule consisting of a few atoms, seems simple at first glance, the number of possibilities to be considered is large. Thus, the ethylene molecule and its most likely decomposition products on Ru(0001) were used as starting guesses. The elongated shape of the particle rules out a few options, such as a bare carbon atom and methylidyne (CH), although these are the most stable species formed by carbon and hydrogen on a Ru(0001) surface. CH_3 is also ruled out by symmetry. CH_2 has the correct symmetry but is ruled out by the current DFT calculations. The ethylidyne (CCH_3) fragment, which adsorbs on hcp sites with an upright orientation, is also ruled out due to symmetry reasons.

In a previous combined STM and DFT study, Gao et al. investigated the growth of graphene on a Ru(0001) by thermally decomposing a predosed amount of ethylene. For conditions in which the surface was only partially covered with graphene, the graphene-free areas were covered with elliptic particles that looked like the *dimer* particles described here. The authors claimed that these particles are chains of CH_2 fragments and C_2H_4 segments and that these species are direct precursors of graphene.[91] However, intact C_2H_4 molecules have clearly been ruled out by vibrational spectroscopy for the conditions in this experiment[77–81], and in the DFT calculations by S. Sakong, the CH_2 fragments are found to be a unstable and to decompose to give CH.

Decomposition products of ethylene: The analysis of the vibrational spectroscopy data from literature (see chapter 4.2.5) gives some insight into the decomposition products of ethylene. Two candidate molecules containing two carbon atoms are shortly discussed here, the acetylide (CCH) and the vinylidene (CCH_2). The acetylide (CCH) molecule adsorbs with the hydrogen-free carbon on an hcp

site and the C-H bond above a fcc site (fig. 4.13). This leads to six possible orientations, which does not comply with the observed diffusion process. Nevertheless, the diffusion behavior of the CCH was evaluated by DFT, and a sliding motion was obtained with a barrier of 0.8 eV in which the C-C bond is first stretched. In the transition state the CH-part of the molecule is on the hcp and the C-part on the neighboring fcc site. The sliding motion does not lead to a change of the orientation of the molecule and does, therefore, not match the experimentally found rotation, another argument against this molecule.

A more promising candidate is vinylidene (CCH_2), which adsorbs with the hydrogen-free carbon atom on an hcp site and with the CH_2 over an on-top site. This configuration results in three possible orientations on the surface. The elongated shapes of the particles in the STM measurements could be caused by the two hydrogen atoms that protrude outward. Moreover, there are two different rotations possible for vinylidene. In the first, the lower carbon atom stays on the hcp site, and the CH_2 rotates between the three neighboring on-top sites. In the second, the lower carbon atom jumps between the three hcp sites around the on-top site to which the CH_2 is bound. However, the DFT calculations result in very similar energy barriers for both motions, 0.52 eV and 0.61 eV, respectively. Since the large difference in the energy barriers of the two motions is one of the important characteristics of the *dimer* particles, the CCH_2 molecule is ruled out.

Dicarbon: Molecules with the composition C_2H_x with more than three hydrogen atoms have not been found by vibrational spectroscopy, and DFT calculations find that these species are unstable with respect to molecules with fewer hydrogen atoms like CCH_3 and CCH_2. Rather than adding more hydrogen to find the target molecule, it appears more promising to remove hydrogen entirely, which results in a carbon dimer. However, according to DFT, a C_2 molecule is not stable as the C-C interaction is repulsive, and two single carbon atoms adsorbed on Ru are more stable. Furthermore, there is an experimental study by low-temperature STM in which no C_2 formation from single carbon atoms has been observed.[42] A theoretical study reported an energy barrier for the C_2 formation of two single C atoms of 1.49 eV and predicted the dimerization to take place at step edges of the Ru(0001) surface.[92] However, carbon dimerization is not energetically favored on metals such as Ru that strongly bind carbon. Thus, a simple carbon dimer (C_2) is ruled out.

Surface reconstructions: A possibility that has to be considered is that the *dimer* particles are not just adsorbed on the unchanged Ru surface but that a local reconstruction is involved. Examples are a Ru vacancy or a Ru adatom, whereas larger reconstructions involving more than one Ru atom would most likely have

been resolved in the STM data.

Ru vacancies in the first surface layer: The formation enthalpy of a vacancy in the Ru(0001) surface is 1.46 eV with respect to Ru bulk.[93] With this value, one can estimate the concentration of surface vacancies at room temperature. An extremely low value is obtained. The observed concentration of *dimer* particles could not be understood in this way. A possibility is that the presence of the *dimer* particle somehow stabilizes a vacancy. Several calculations were performed in which possible hydrocarbon fragments were put into the vacancy or at its edge (keeping the boundary condition that the STM should image a *dimer* feature). It was found that two C atoms are still repulsive, and two methylidyne fragments (CH) leave the vacancy due to repulsive interactions. Attempts to find another hydrocarbon molecule C_2H_x that fits into the vacancy were also unsuccessful. For example, for the vinylidene CCH_2 molecule no stable configuration in or close to a surface vacancy was found.

Ru adatom formation: The two possible ways to form a Ru adatom on the surface have been investigated in previous DFT work. Formation from a step costs an energy of 1.57 eV, and formation on a terrace costs 2.88 eV.[94] In the same study, the influence of different surface species on the adatom formation was investigated. Hydrogen, carbon, CO, CH, and CH_2 are found to hinder adatom formation, while CH_3 has a very slight facilitating effect in comparison to the free surface. Hence, the question arises how these activation energies can be brought up in the case of the formation of the *dimer* particles. The formation of the *dimer* particles is thermally activated, but room temperature is already sufficient. According to Xu and Mavrikakis, an adatom formation energy of 0.75 eV leads to a rate of one event per second.[94] In the case of the Ru(0001) surface, where the calculated energies are higher than 1.5 eV for an adatom formation, any measurable rate at room temperature is ruled out.

Both Ru reconstructions are connected with structural changes at the surface steps. However, in the experimental STM images of steps on the Ru(0001) surface, there are no indications of vacancies or adatom reconstructions. To conclude, the formation energy of a vacancy or adatom is too high, and no reasonable carbon species was identified that interacts in a suitable way with the Ru reconstructions.

Subsurfaces species: An often discussed idea when an adsorption structure is hard to understand is the possibility of a site underneath the top layer. Because of size restrictions, only bare C atoms come into question. However, the preferred

adsorption sites of C atoms on Ru(0001) are hcp surface sites and not octahedral or tetraedral subsurface sites.[92] Furthermore, the experimental conditions under which the *dimer* particles are observed do not fall in a temperature range where carbon either segregates to the surface from the bulk or dissolves in the bulk. The temperature for such events is higher than 730 °C.[43,95] In addition, a subsurface configuration that matches the two characteristic jump types of the *dimer* particles appears quite challenging. Subsurface species are also ruled out.

C_4H_x **derivates**: So far, only molecules that derive from the decomposition of ethylene have been discussed. However, the graphene growth experiments revealed that the *dimer* particles probably contain more than two, most likely four, carbon atoms (chapter 4.2.4). The formation of larger hydrocarbon fragments requires a coupling reaction of the decomposition products of ethylene. The most stable decomposition product is methylidyne (CH). In order to form a C_4H_x molecule from CH fragments, three C-C bonds have to be formed. Alternatively, two C_2-species could couple, which only requires the formation of one C-C bond. The partially hydrogenated C_2 molecules, such as CCH_2 and CCH, adsorb rather strongly with the hydrogen-free carbon atom to the Ru surface, whereas the second carbon atom in the CH_x group is bound more weakly. This means that only two weak C-Ru bonds have to be broken to form one strong C-C bond, which would lead to a stable C_4H_x species.

In the DFT calculations, the presence of CO molecules on the surface was also considered, as in the experiments CO was always present. It was found that a CO vacancy in the $(\sqrt{3} \times \sqrt{3})R30°$ superstructure could serve as a suitable environment for a coupling reaction. In the CO vacancy, the energy gain for a coupling reaction of two dicarbon molecules (C_2H_x, x = 0, 1, 2, 3) to a bidentate (C_4H_x, x = 0, 1, 2, ..., 6) is increased compared to the clean Ru(0001) surface. The following bidentate molecules show an energy gain by forming the C-C bond: CCH-HCC, CCH_2-H_2CC, CCH_2-HCC, HCCH-HCC, $HCCH_2$-HCC, and $HCCH_2$-H_2CC. Due to symmetry reasons, the asymmetric molecules can be ruled out. The most stable C_4H_x configuration is the CCH-HCC molecule. This molecule has therefore been chosen for in-depth DFT analysis of its diffusion processes on the Ru(0001) surface.

The **CCH-HCC** molecule adsorbs with the two outer hydrogen-free carbon atoms on hcp sites, and the two CH groups in the middle protrude from the surface. In that way, the molecule forms a bridge from one hcp site to a neighboring hcp site. Moreover, it is slightly tilted away from the on-top site so that the middle part is above the fcc site between the hcp sites. Figure 4.25 shows a model of the configuration and a simulated STM image based on the Tersoff-Hamman approximation.[30]

The simulation corresponds to an experimental STM image recorded in constant height mode with a negative tunneling voltage. The molecule has a two-lobe shape and appears dark, which fulfills the requirement of the experimental symmetry and the image contrast in the STM. Furthermore, it displays two distinguishable rotational movements on the surface. The triangular jumps of a *dimer* particle could be assigned to a rotation of the CCH-HCC molecule around the Ru atom that is bridged by the molecule. The on-site rotation could correspond to the rotation of the molecule around the central fcc site. These two motions were analyzed by DFT in detail and the results are described above. However, the calculated energy barriers of the diffusion motions of the CCH-HCC molecule do not match the experimental results of the *dimer* particles.
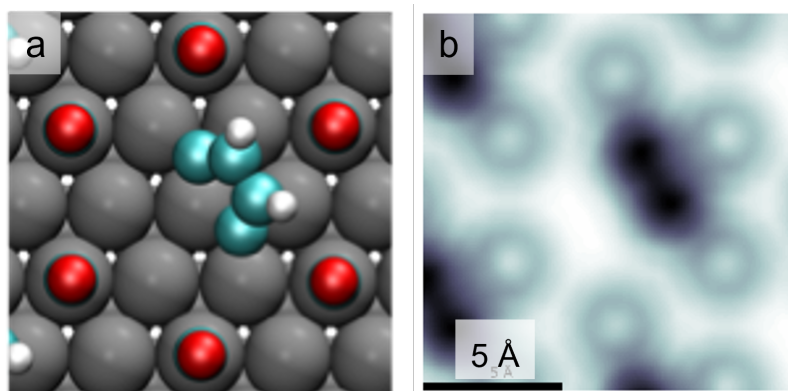
Figure 4.25 : Atomic model and simulated STM image of the CCH-HCC molecule on a Ru(0001) surface in a CO vacancy of the $(\sqrt{3} \times \sqrt{3})R30°$ CO structure. a) Atomic model with carbon indicated as turquoise, hydrogen as white, oxygen as red, and Ruthenium as grey spheres. b) Tersoff-Hamman STM simulation of the molecule, corresponding to an STM image recorded with negative tunneling voltage in the constant height mode. (figure credits: S. Sakong)

The on-site rotation of the CCH-HCC is realized by an "one-leg" motion. Leg refers to one of the two CCH halves that bind to the surface with the terminating C atom. The motion consists of three steps. Figure 4.26 shows snapshots of the diffusion process. First, the upper leg moves from its hcp site to the fcc site next to the other leg. The lower leg only slightly gives way. Second, the upper leg continues to move to the next hcp site. And third, the entire molecule flips, positioning the middle part over the same fcc site as before. The activation barrier for this process is 1.127 eV.

The triangular jump can be realized in two ways. Either by a two-leg motion or by a flip. For the two-leg motion, the process starts like the on-site rotation. However, when the molecule is in the transition state (figure 4.26 (b)) with the upper leg over the fcc site, the lower leg moves to the fcc site to the left. In that way, the molecule
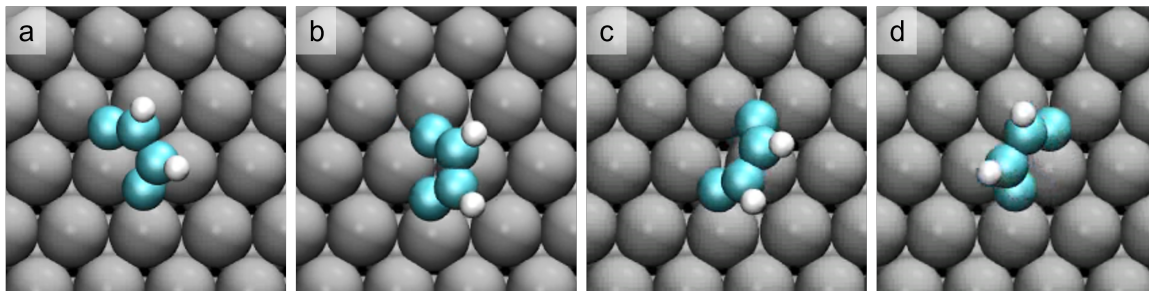
Figure 4.26 : Model of the one-leg rotation motion of the CCH-HCC molecule on Ru(0001) that results in an on-site rotation. a) Stable adsorption geometry, b) upper leg moves to fcc site, c) upper leg moves to hcp site, d) molecule flips. (figure credits: S. Sakong)

continues to move around the central Ru atom. The lower leg then moves to the hcp site on the left while the upper leg follows and ends up on the hcp site to which the lower leg was originally bound. The two-leg motion has an overall activation barrier of 1.242 eV, ≈ 0.1 eV higher than the one-leg on-site rotation movement.

For the flip motion, the middle part of the molecule is lifted above the central Ru atom in the transition state, and then one of the legs moves via an fcc site to the free hcp site at the same Ru atom. In figure 4.27, snapshots of the processes are shown. The activation barrier for a flip is 0.958 eV and thus lower than both other motions (table 4.9).
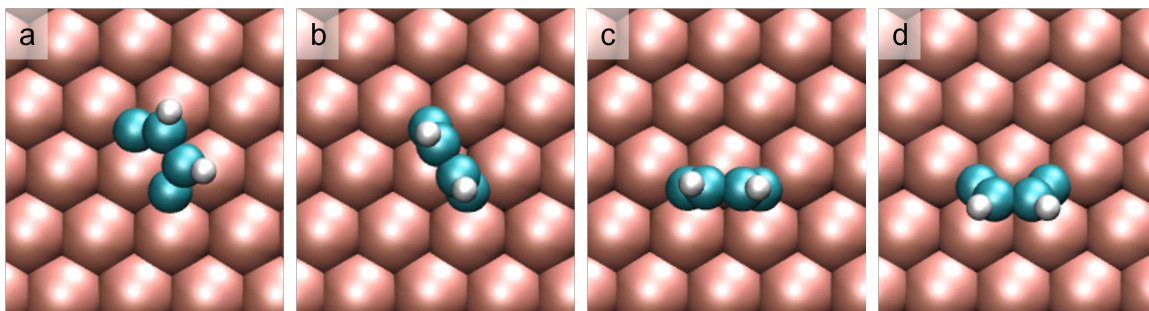
Figure 4.27 : Model of the flip of the CCH-HCC molecule on Ru(0001) that results in a triangular jump around one Ru atom. a) Original adsorption site, b) middle part of the molecule rises above the Ru atom, c) one leg is lifted and moves to the other hcp site, d) middle part of the molecule flips back to a relaxed position, color code as in figure 4.25 but Ru imaged light brown. (figure credits: S. Sakong)

This model nicely reproduces the two motions observed in the experiment, but the difference between the two activation energies is much smaller (for the two-leg triangular jump it even has the opposite sign). It was tried to expand this model by including the experimental fact that there are coadsorbed H atoms on the surface. It could be that the triangular jump is H-assisted, whereas, for some reason, the on-site rotation is unaffected. For a H-assisted mechanism, a hydrogen atom could

bind to one of the legs of the molecule. This leads to a significant decrease in the bond strength of that carbon to the Ru surface, and the respective leg becomes more mobile. The hydrogen atom could be detached at the end of the process, working like a catalyst for the motion. In that way, the activation barrier for the flip is lowered to 0.770 eV. If hydrogen atoms are attached to both legs, the barrier for a rotation is 0.790 eV, and the molecule does not flip over the Ru atom as the molecule geometry with two additional H atoms is different; it adsorbs rather parallel to the surface. By attaching two hydrogen atoms to one of the carbon legs, the barrier for the flip decreases to 0.031 eV (table 4.9). Hydrogen-assisted pathways are the processes with the lowest energy barrier that were found computationally.

Table 4.9 : Comparison of the experimental diffusion energy barriers E^* of the *dimer* particles with the calculated values for the CCH-HCC molecule.

	on-site rotation	triangular jump
dimer particle	1.27 ± 0.21 eV	0.36 ± 0.03 eV
CCH-HCC	1.127 eV (one-leg)	1.242 eV (two-legs)
		0.958 eV (flip)
		0.770 eV (flip, hydrogen assisted, 1 H)
		0.031 eV (flip, hydrogen assisted, 2 H)

The experimental activation energy of 0.36 eV for the triangular jumps is not obtained in the DFT calculations of the CCH-HCC molecule. Assistance by a H atom lowers the calculated barrier but it does not come close to the experiment. Assistance by two H atoms strongly overshoots, and the barrier becomes too low. By contrast, for the on-site rotation, the one-leg mechanism provides a value that is in reasonable agreement with the experiment.

In summary, a lot of effort has been invested to identify the atomic configuration of the *dimer* particles. The decomposition products of ethylene to give smaller fragments could be ruled out for several experimental and theoretical reasons. Attempts to insert a surface reconstruction (Ru vacancy or adatom) into the system did not lead to any plausible result. It is more reasonable that a coupling reaction involving two fragments of the ethylene decomposition takes place. The reaction to give a bidentate C_4H_x (with x = 0, 1, 2, ..., 5) is favorable in comparison to smaller dicarbon molecules. The CCH-HCC molecule is the energetically most stable one of the optional molecules, but the calculated activation barriers for the diffusion processes do not match the experimental results. Expanding the investigations to larger

molecules containing five or more carbon atoms results in a drastic increase in the number of possible configurations, resulting in more costly calculations. In sum, the available experimental and computational methods could not unambiguously determine the identity of the observed surface species.

4.6. The compensation effect

In general, the rate constant k of a process, i.e., a reaction or a diffusion process, is related to the activation energy E_A by the Arrhenius equation:

$$k = A \cdot e^{\left(\frac{-E_A}{RT}\right)}$$

(4.11)

A is the preexponential factor, also referred to as frequency factor or attempt frequency.

Usually, the preexponential factor A is considered to be constant for a set of similar processes of the same type, like for the diffusion of atoms and molecules on surfaces. A and E_A are considered to be independent of each other. However, if this is not the case and the two parameters are correlated, this is called the compensation effect. The compensation effect implies that an increase of the activation energy, which lowers the rate of a process, can be compensated by an increase of the preexponential factor, which increases the rate. Often, a linear dependence of the two parameters is found:

$$\ln A = aE_A + b$$

(4.12)

where a and b are two constants.[96,97]

When several similar and comparable processes are evaluated together in one Arrhenius plot, the existence of a compensation effect becomes obvious when the linear fits intersect at one point instead of intersecting on the y-axis at $1/T = 0$ (figure 4.28). The temperature at which the graphs intersect is called the isokinetic temperature. At this temperature, processes display the same rate, even though they have different activation energies. The compensation effect is therefore also called the isokinetic relationship.
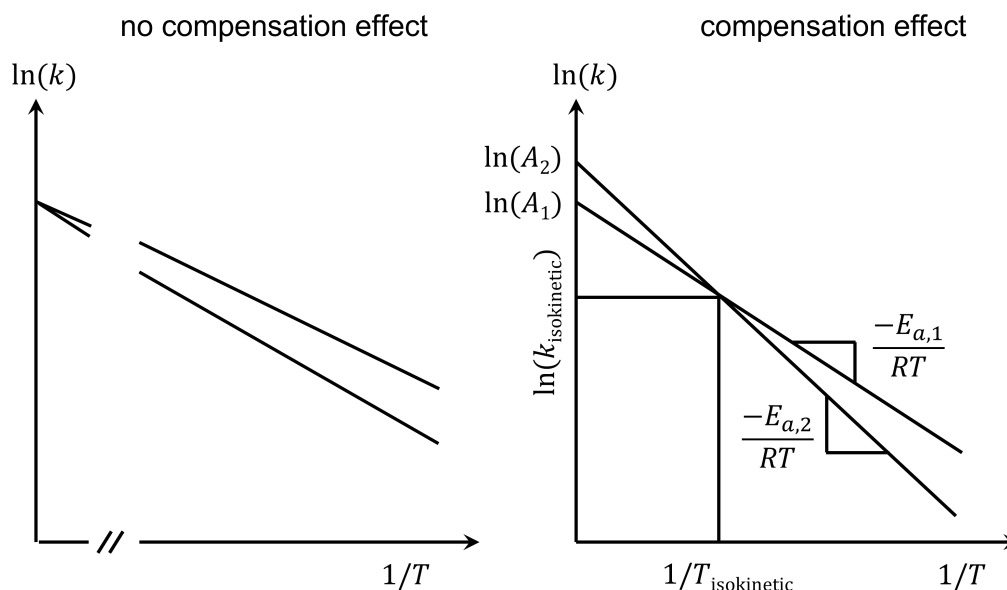
Figure 4.28 : Arrhenius plots without and with compensation effect.

There are many reports of compensation effects in all kinds of solid state systems. In heterogeneous catalytic reactions it has been detected when the same reactions on similar catalysts or similar reactions on the same catalyst were compared.[98–101] However, the reason for and the validation of the compensation effect are still vividly discussed. Some of the suggested causes for the compensation effect are:

Experimental errors: The effect could just be the result of errors in the experimental data, like in the temperature measurement or in a temperature gradient over the sample. In these cases, one speaks of an apparent compensation effect.[101,102] An important precondition for a real effect is that the kinetic properties of the investigated surface process are based on meaningful statistics.[103]

Mathematical consequence: Koga et al. argue that the kinetic compensation effect is merely a mathematical consequence due to the exponential form of the Arrhenius equation.[104] The analysis in this paper is incomprehensible.

Complexity of heterogeneous reactions: Especially when chemical reactions in heterogeneous catalysis are investigated, it has been argued that the complexity of these reactions may lead to a compensation effect. This is the case when, in contrast to the assumption, the reactions that are compared are not really based on the same or similar processes. For example, active sites may be different.[101,103]

Switching between kinetic regimes: Bligaard et al. argue that the compensation effect in heterogeneous catalysis is caused by switching between different kinetic regimes.[97] In their study, a simple process, the dissociation of N_2 on two different

metal surfaces, Ru and Pd, has been compared. The transition states of the nitrogen molecule are calculated by DFT and found to be similar on both metals. Hence, there is no large difference in the entropy of the activated state of the molecule. However, a change in the coverage on the surface impacts the apparent activation energy, as empty surface sites are required for the adsorption and the reaction. The activation energy is larger for a higher coverage because the energy to create an empty surface site by desorption is additionally required. For the overall reaction, a linear relationship between $\ln A$ and E_A has been observed, which is consistent with the compensation effect.[97]

Transition state theory: One approach to explain the compensation effect in a more general way is to explore the transition state theory by Eyring.[96,105] In this theory, the rate constant k is related to the activation enthalpy $\Delta H^\ddagger$ and to the activation entropy $\Delta S^\ddagger$ in an Arrhenius-like fashion:

$$k = \frac{k_\mathrm{B}T}{h}\, e^{\Delta S^\ddagger/R}\, e^{-\Delta H^\ddagger/RT} \qquad (4.13)$$

For an elementary reaction, $\Delta H^\ddagger$ (in eq. 4.13) and E_A (in eq. 4.11) can be considered as equal. As a consequence, the preexponential factor A (in eq. 4.11) equals $\frac{k_B T}{h}\, e^{\Delta S^\ddagger/R}$ and contains an entropy term. A change in the preexponential factor A is therefore linked to a change in the entropy difference between the transition state and the ground state.

A compensation effect is observed when both $\Delta H^\ddagger$ and $e^{\Delta S^\ddagger/R}$ decrease or increase. It has been proposed by Conner that a lowering of the transition state energy generally leads to a higher curvature of the potential energy.[96] The separation of the vibrational levels widens, the vibrational partition function decreases, and accordingly the activation entropy and the preexponential factor decrease. This is what the compensation effect predicts.

Phonon excitation: Another name for the compensation effect is the Meyer-Neldel rule. Initially, it only described the empirically found phenomenon of the compensation behavior in electrical conduction studies.[106] The term is used by Yelon et al., who approach a more general explanation of the phenomenon through microscopic models and statistical physics.[107,108] In the case of surface diffusion, the excitation of a jump event is caused by phonons (with the energy ϵ_ph) from a defined interaction volume. For a single molecule, the Arrhenius equation can be written as follows (lower case h and s refer to the enthalpy and entropy of a single

particle in eV):

$$k = \frac{k_B T}{h} e^{\Delta s^\ddagger / k_B} e^{-\Delta h^\ddagger / k_B T} \tag{4.14}$$

If n is the number of required phonons and N the number of available phonons in the interaction volume, the number of possibilities w for the excitation in a multiphonon process is: $w = \frac{N!}{n!(N-n)!}$. The activation entropy becomes: $\frac{\Delta s^\ddagger}{k_B} = \frac{\Delta h^\ddagger}{\epsilon_{ph}} ln\left(\frac{N}{n}\right)$. Consequently, the logarithm of the preexponential factor $\left(\sim \frac{\Delta s^\ddagger}{k_B}\right)$ linearly increases with $\Delta h^\ddagger$, which is the compensation effect. This result does only apply in cases where $\Delta h^\ddagger > \epsilon_{ph}$. Thus, preexponential factors (for surface processes) lower than 10^{12} Hz cannot be explained by this model.

STM studies on rotational motions: Most studies that report compensation effects investigate reaction kinetics. In surface diffusion studies the effect has not been reported so far, to the best of my knowledge. However, in several STM studies that investigate rotational motions of molecules, rather low experimental values for the attempt frequencies, ranging from $10^6 - 10^9$ Hz paired with rather low energy barriers are reported.[62,70,71,73] For example, the energy barrier for the rotation of naphthalene ($C_{10}H_8$) on Pt(111) is 0.67 eV, and the preexponential factor is 4×10^9 Hz.[62] Several low-temperature studies examine the rotation of symmetric and asymmetric dialkyl sulfides ($C_nH_{2n+1}SC_mH_{2m+1}$, with $n, m = 1, 2, ..., 6$) on Au(111).[70,71,73] Very low energy barriers (in the range of 1 kJ/mol = 0.01 eV) paired with low preexponential factors $10^6 - 10^9$ Hz are reported. Mulitstep processes that constrain the transition states and entropic effects have been proposed as explanations.

The case of the *dimer* particles:

The present case of a compensation effect differs from catalytic reactions by the aspect that single particles are investigated. That for a hydrocarbon molecule (*dimer* particle) adsorbed on a Ru(0001) surface a clear compensation effect was found contradicts the statement of Nilekar et al. that "there is practically no compensation effect between the preexponential factor and the activation energy barrier for diffusion of adsorbed species on transition-metal surfaces."[109]

The so-called isokinetic temperature T_{inter} where the rate constants of the two processes are equal is found at:

$$\frac{-E_1^*}{k_B T_{inter}} + ln(A_1) = \frac{-E_2^*}{k_B T_{inter}} + ln(A_2) \tag{4.15}$$

$$T_{\text{inter}} = \frac{E_2^* - E_1^*}{k_{\text{B}} \cdot ln\left(\frac{A_2}{A_1}\right)} \tag{4.16}$$

With the experimental activation energies and preexponential factors, the value of T_{inter} is 140 °C. This temperature is somewhat above the highest temperature of 124 °C applied in the measurements. At higher temperatures than 140 °C, it is thus expected that the jump frequencies of the on-site rotations exceed the jump frequencies of the triangular jumps. As the rate of the on-site rotation will then dominate the diffusion process, the trajectories will no longer appear triangular but hexagonal. Because of the high velocity of the particles above T_{inter} this range is no longer experimentally accessible.

Schematic energy diagrams of the triangular jump and the on-site rotation are shown in figure 4.29. In both processes the initial states and the final states are the same, with exactly the same energies and entropies. Only the transition states are different.
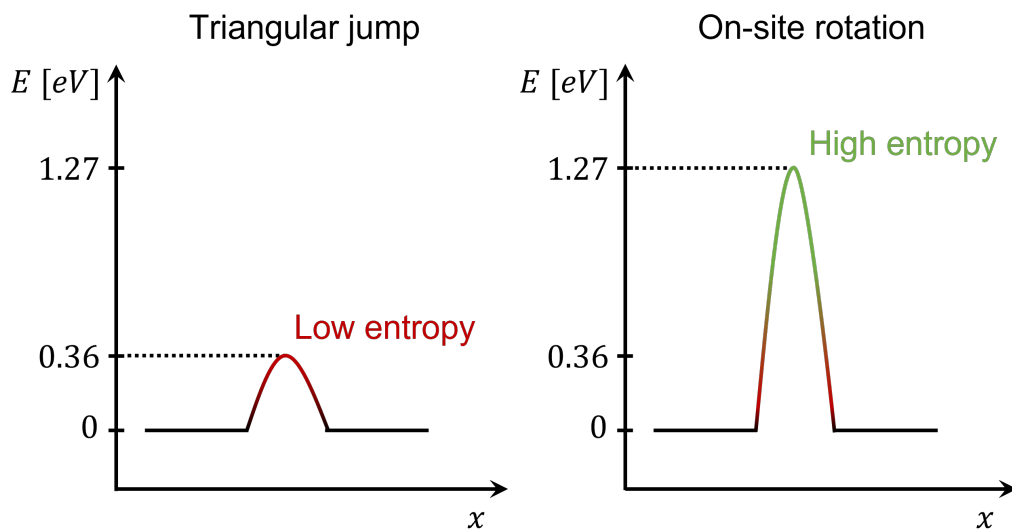
Figure 4.29 : Energy schemes of the two diffusion processes of the *dimer* particles on the Ru(0001) surface.

The question arises: What is the reason for the high/low energy barrier paired with a high/low preexponential factor?

What can be excluded are experimental errors. The two frequencies Γ_1 and Γ_2 were extracted from the same experiment, so that errors in the temperature measurements cannot play a role. Influences of the tunneling tip have been carefully excluded.

Transition state theory:

Triangular jumps (E_A low, A low): A low preexponential factor can be caused by a reduced number of available configurations in the transition state. For the triangular jumps, the *dimer* particle has to pass either a hollow site or an on-top site. Which of the pathways is energetically favored depends on the exact configuration of the molecule. A strong binding of the molecule to the surface in the transition state and a corresponding spreading of the energy levels might reduce its entropy.

On-site rotation (E_A high, A high): The opposite is the case for the on-site rotation of the molecule. From the transition state theory, a high entropy implies that the transition state of the molecule during the on-site rotation has fewer constraints corresponding to many configurations of the molecule in the transition state or to more closely spaced energy levels. The exact molecular configuration is not known. For the CCH-HCC fragment analyzed by DFT, the on-site rotation can be realized by a one-legged motion, and it is also possible that in the transition state both legs are lifted, which might be correlated with an increased flexibility.

Phonon excitation:

On-site rotation ($A = 10^{17}$ Hz): The activation energy of 1.27 eV is considerably higher than phonon energies, implying that several phonons are required to excite the molecule to overcome the activation energy for the on-site rotation. Such a multiphonon process is connected with an increase in the entropy, because the number of phonons involved in the process is increased. Consequently, the high energy barrier for the on-site rotation is compensated by a large entropy term.

Triangular jumps ($A = 10^6$ Hz): Phonon energies of Ru are still lower than the activation energy of 0.36 eV of the triangular jumps, so that the phonon model in principle still works. A decrease of the preexponential factor with respect to the on-site rotation is expected, but it cannot drop below 10^{12} Hz in this model. The experimental value of 10^6 Hz is hard to understand within this model.

Figure 4.30 is an overview of the results marked in the Arrhenius plot of the jump frequencies. On the right side, the possible precursor molecules are listed. The *dimer* particles have been formed either from evaporated carbon (by reaction with hydrogen present on the surface) or by ethylene decomposition in a thermally activated process. In a regime from 25 °C to 80 °C, triangular jumps of the *dimer* particles dominate the diffusion motion. The trajectories are simple triangles. At about 80 °C, on-site rotations take place at a rate of one event per minute, and the *dimer* particles start to diffuse by a combination of the two rotational motions. The crossover of the two linear fits of the two diffusion processes at 140 °C marks a change above which the frequency of the on-site rotations is higher than of the

triangular jumps. At this temperature it is expected that the elongated shape of the particles is not resolved anymore and the trajectories show no triangular pattern. Further heating to 350 °C causes a decomposition of the *dimer* particles and the formation of a network that leads to graphene.

One main result is that the presented (rather) small hydrocarbon molecule is extraordinary in its dynamic behavior. It reveals the compensation effect in a single-molecule system.
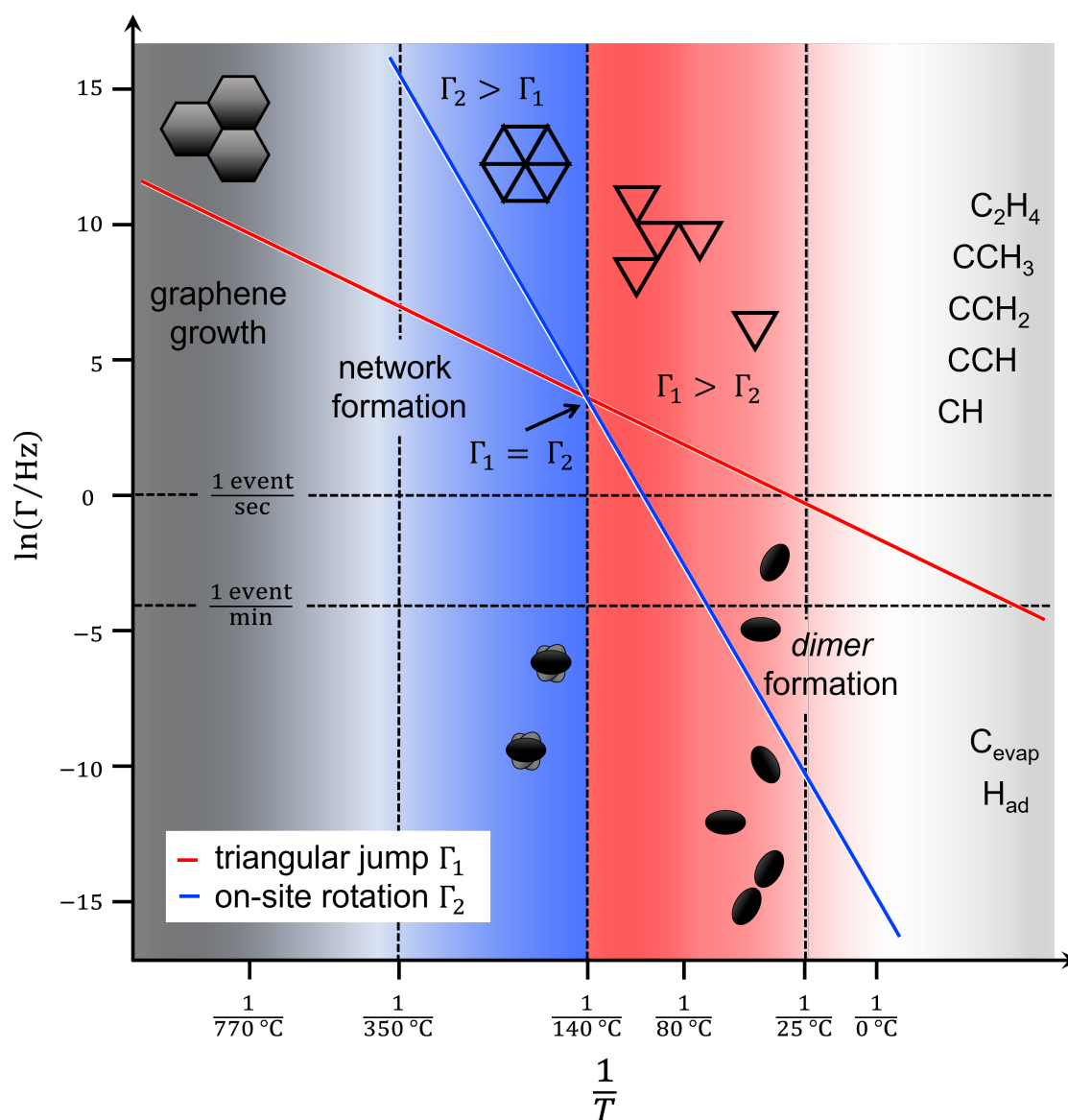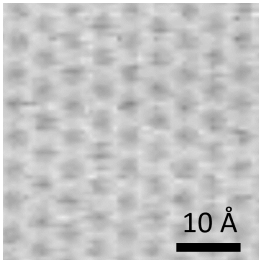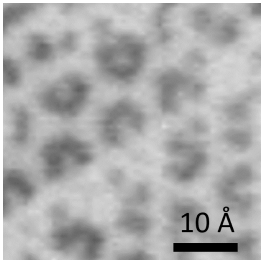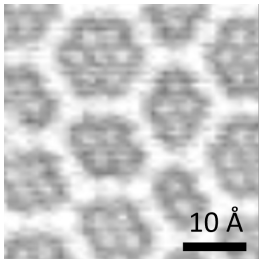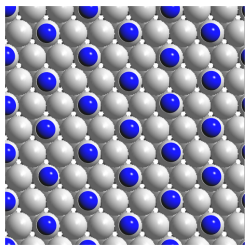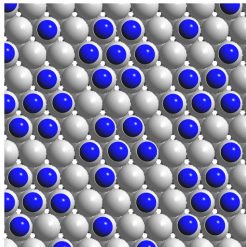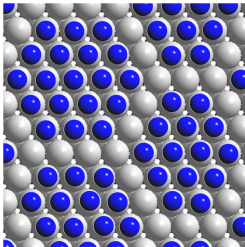

Figure 4.30 : Collected results from the different temperature regimes illustrated in the Arrhenius plot.

5. Oxygen Diffusion on a CO-covered Ru(0001) Surface

Surface diffusion plays a fundamental role in catalytic surface reactions as it determines the collision rates of adsorbed particles and their transport to active sites. In microkinetic analyses, surface diffusion is usually neglected, which can be justified by the fact that diffusion is fast and not rate-limiting. However, in industrial processes, pressures are usually high resulting in highly covered surfaces. Surfaces must be densely covered by reactants, reaction products, side products, and possible contaminants. In such crowded situations, surface diffusion might no longer be fast and certainly no longer a simple random walk between empty adsorption sites. In the following publications, these situations have been studied by high-speed STM.

As a model of such situations, the diffusion of single oxygen atoms on a carbon monoxide covered Ru(0001) surface was studied. The underlying structures are well investigated both experimentally with surface science methods and theoretically by DFT.[25,110–115] Oxygen atoms adsorb on Ru(0001) on hcp sites, and at higher coverages the oxygen atoms form a (2×2) superstructure.[116,117] Carbon monoxide adsorbs on on-top sites with the carbon atom bound to the surface.[118,119] The CO molecules form ordered superstructures on the Ru(0001), a $(\sqrt{3} \times \sqrt{3})R30°$ structure at a coverage of a third of a monolayer is the most common. At higher CO coverage, a $(2\sqrt{3} \times 2\sqrt{3})R30°$ is formed at 0.58 ML, but it is only ordered at temperatures below -73 °C. At somewhat lower coverage of 0.47 ML, structure elements of the $(2\sqrt{3} \times 2\sqrt{3})R30°$ are present. At a CO coverage of 0.66 ML, the CO layer forms a compact cluster structure that represents the saturation coverage under UHV conditions. The solution of this high coverage structure is presented in chapter 5.2, where it is shown that the CO clusters are formed by compact islands consisting of 7-19 CO molecules. Table 5.1 shows the three different CO structures.

Table 5.1 : CO structures on Ru(0001).

structure	$(\sqrt{3} \times \sqrt{3})R30°$	(incomplete) $(2\sqrt{3} \times 2\sqrt{3})R30°$	compact cluster structure
$\theta(CO)$	0.33 ML	0.47 ML	0.66 ML
preparation	1 L CO	50 L CO at RT	50 L CO at RT + 16 L CO while cooling
ordered	until CO desorption at $> 127\ °C$	$< -73\ °C$	until CO desorption at $> 127\ °C$
STM image			
model			

The following publications are built upon two previous studies. The first is the dissertation of Ann-Kathrin Kügler (Henß) on the diffusion of O atoms through the $(\sqrt{3} \times \sqrt{3})R30°$ CO structure.[25] The O atoms occupy CO vacancies in this structure in which they bind to one of three hcp sites. The diffusion mechanism of the O atoms consists of two processes with different diffusion barriers. In the first process, an oxygen atom can jump between the three hcp sites within the cage of CO molecules around the vacancy with a small energy barrier. The second process is an exchange of the O atom with a CO molecule from the rim of the cage. It is not a direct exchange but a step-wise process initiated by fluctuations within the ordered CO layer that open up low-energy pathways on which the oxygen atom can leave the cage. This process, which has been termed door-opening mechanism, is connected with a higher barrier. In a follow-up study, it was shown that at a CO

coverage of 0.47 ML, the door-opening mechanism is unchanged and the mobility of the oxygen atoms is even enhanced.[89]

In the present work three further studies were performed that shed light on new aspects on the O/CO/Ru(0001) system (chap. 5.1 to 5.3).

The first project 5.1 dealt with oxygen diffusion along domain boundaries of the $(\sqrt{3} \times \sqrt{3})R30°$ CO superstructure. The second and the third projects studied the saturation coverage of CO on Ru(0001). In chapter 5.2, the solution of the structure of the high-coverage CO layer on Ru(0001) is described, and chapter 5.3 presents the results on the diffusion of single oxygen atoms within the CO cluster structure.

5.1. An STM study on the diffusion of O atoms on a CO-covered Ru(0001) surface – The role of domain boundaries

In 3D solids, diffusion at the grain boundaries is significantly higher than through the bulk of the grains.[120,121] Grain boundary diffusion can be enhanced by 5 to 6 orders of magnitude compared to bulk diffusion. For surface diffusion of adsorbed particles, domain boundaries in an ordered adsorption layer may show similar effects. This phenomenon has been studied in a publication on the system of single oxygen atoms embedded in a CO adlayer on Ru(0001). The ordered $(\sqrt{3} \times \sqrt{3})R30°$ structure of CO forms three translational domains on the Ru(0001) surface, and domain boundaries are observed in the STM data as disordered and fluctuating stripes. Using the high-speed mode of the STM setup, the diffusion of single oxygen atoms along the domain boundaries of the ordered CO adlayer has been observed and evaluated. The key results of the publication are:

- The diffusion trajectories of the oxygen atoms at the domain boundaries differ considerably from the trajectories within the domains of the $(\sqrt{3} \times \sqrt{3})R30°$ CO structure, which consist of connected triangles. The trajectories follow the directions of the domain boundaries in a zig-zag way along free hcp sites, indicating that the O atoms preferentially move along the domain boundaries.

- The diffusion constant of the oxygen atoms in the domain boundaries is 1 to 2 orders of magnitude higher compared to the diffusion within the ordered $(\sqrt{3} \times \sqrt{3})R30°$ domains of CO.

- The domain boundaries of the $(\sqrt{3} \times \sqrt{3})R30°$ CO structure are imaged as fuzzy and blurred stripes. The CO molecules in these regions rapidly fluctuate. Heavy or light domain walls, with locally higher respectively lower CO coverage than in the ordered $(\sqrt{3} \times \sqrt{3})R30°$ domains, are possible.

- Several effects can lower the activation barrier for oxygen diffusion in the domain boundaries. In the case of heavy domain walls, the repulsion between O atoms and CO molecules is increased, resulting in a lower adsorption energy of the O atoms and therefore lower jump barrier. In addition, the fluctuations in the CO layer, the basis of the door-opening mechanism, can happen more easily in the disordered heavy domain walls. In the case of light domain walls, the absence of closer CO-CO and CO-O configurations results in more available hcp sites for the O atoms, which increases the diffusion constant.

- The diffusion constant is almost identical to the diffusion constant measured on the disordered CO layer at 0.47 ML coverage. It is concluded that the door-opening mechanism is also active in the disordered areas of the domain boundaries.

Author contributions:
Ann-Kathrin Kügler: Visualization, Validation, Software, Methodology, Investigation, Formal analysis, Data curation, Conceptualization, Writing – review and editing.
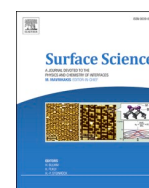Hannah Illner: Visualization, Software, Formal analysis, Data curation, Writing – review and editing.
Joost Wintterlin: Validation, Supervision, Project administration, Conceptualization, Writing – original draft, Writing – review and editing.

Contents lists available at ScienceDirect

Surface Science

journal homepage: www.elsevier.com/locate/susc

An STM study on the diffusion of O atoms on a CO-covered Ru(0001) surface—The role of domain boundaries

Ann-Kathrin Kügler [a], Hannah Illner [a], Joost Wintterlin [a,b,*]

[a] *Department of Chemistry, Ludwig-Maximilians-Universität München, 81377, Munich, Germany*
[b] *Center for NanoScience, Schellingstr. 4, 80799, Munich, Germany*

ARTICLE INFO

ABSTRACT

We investigate tracer diffusion at the domain boundaries in an adsorption layer, an effect that corresponds to grain boundary diffusion in 3D polycrystalline solids. Experiments were performed on adsorbed O atoms on a Ru (0001) surface in a layer of CO molecules. The CO molecules form a $(\sqrt{3} \ x \ \sqrt{3})R30°$ structure which displays translational domains. High-speed scanning tunneling microscopy (STM) was used to image the motion of the O atoms. The data show that single O atoms preferentially move along the domain walls which in the STM movies appear as disordered, fluctuating stripes between the ordered domains. The diffusion coefficient of the O atoms is one order of magnitude higher than the diffusion coefficient in the ordered domains. By comparison with previous experiments on completely disordered CO layers, it is concluded that the diffusion is similarly promoted by the enhanced fluctuations in the disordered domain walls.

1. Introduction

Grain boundary diffusion, the transport of atoms along the interfaces between the single crystalline domains of a three-dimensional polycrystalline solid, is much faster than diffusion through the bulk of the crystals [1]. For example, for self-diffusion in polycrystalline Cu, the grain boundary diffusion coefficient at temperatures between 800 and 1000 K is 5 - 6 orders of magnitude higher than the diffusion coefficient in the Cu lattice [2]. Properties of materials that are based on mass transport like, e.g., sintering or some forms of plastic deformation, are therefore strongly determined by grain boundary diffusion. The underlying atomic mechanisms are complex, but there is evidence that they are not just variations of the standard 3D lattice diffusion mechanisms such as the vacancy or the interstitial mechanisms [3,4].

Adsorption layers on single crystal surfaces can be expected to display corresponding effects in 2D for the diffusion of adsorbed atoms or molecules in the layers. In most cases, the unit cell of an adsorption superstructure is larger than the unit cell of the underlying surface and/or has a lower symmetry, giving rise to translational, rotational, and mirror domains. An ordered adsorption layer that forms a 2D solid is therefore usually polycrystalline, and one can ask whether the domain walls in such a layer might play a similar role for mass transport on a surface as the grain boundaries in a 3D solid. Scanning tunneling

microscopy (STM) is, in principle, suitable for investigating such effects, but one finds that domain boundary diffusion has only rarely been observed. It has been seen in electrochemical work on a Cu(100) electrode which was covered with a c(2x2) structure of Cl atoms. It was shown that co-adsorbed S atoms moved faster along the domain boundaries of the Cl structure than in the c(2x2) lattice [5]. By contrast, on an Au(100) electrode, the mobility of Cl atoms in the domain boundaries of the c(2x2)Cl structure was low [6]. For catalytic reactions, the role of domain boundary diffusion has been investigated by theory for the CO oxidation on (100) surfaces of fcc platinum metals [7]. The spatio-temporal patterns displayed by this reaction under certain conditions require surface diffusion of adsorbed CO molecules on a partially O-covered surface. It was shown that the diffusion takes place at the domain boundaries of the c(2x2) structure formed by the O atoms.

In our own previous studies on surface diffusion by high-speed STM we have investigated tracer diffusion of O atoms through layers of adsorbed CO molecules on a Ru(0001) surface. Experiments were performed with 0.33 monolayers of CO (ML, in units of CO molecules per Ru atom) [8,9], a coverage at which the molecules form an ordered $(\sqrt{3} \ x \ \sqrt{3})R30°$ structure, and also at a higher CO coverage of $\Theta = 0.47$ ML, where the CO layer is disordered [10]. At a coverage of $\Theta = 0.33$ ML, it was shown that the O atoms move by what we called a "door-opening mechanism". It consists of local density fluctuations of the CO

---

layer which open low-energy paths along which the O atoms can move through the CO layer. The mechanism is different from the vacancy and interstitial mechanisms known from 3D lattice diffusion. In the disordered layer at a CO coverage of $\Theta = 0.47$ ML, local density fluctuations are stronger, so that low-energy paths for the jumps of the O atoms open more frequently and, correspondingly, the mobility of the O atoms is higher [10].

From its symmetry, the $(\sqrt{3} \ x \ \sqrt{3})R30°$-CO structure can form three translational domains, so that the adsorption layer at $\Theta = 0.33$ ML can display domain boundaries. The STM data show such boundaries and, moreover, they show that the boundaries affect the tracer diffusion of the O atoms. Here we analyze the effect quantitatively and extract a mechanism. Like for grain boundary diffusion in 3D solids, we find an increased diffusion coefficient with respect to lattice diffusion. However, the enhancement is considerably lower than typically observed for 3D solids.

2. Experimental

The experiments were performed in an ultra-high vacuum (UHV) chamber at a base pressure of 1×10^{-10} mbar. The UHV system is equipped with an Auger electron spectrometer (AES), an ion gun for sputtering, a quadrupole mass spectrometer (QMS) for residual gas analysis, a sample manipulator, and a variable-temperature, high-speed STM. In the STM experiments, sample temperatures can be varied between approximately 50 and 500 K. At temperatures below 300 K this is achieved by liquid He cooling and simultaneous heating by a hot filament at the back of the sample. A type S thermocouple spot-welded to the sample is used for temperature measurements, and a clamp provides contact between the thermocouple at the sample and corresponding wires at the mounting stage when the sample is transferred from the manipulator to the STM. Details of the STM setup have been described previously [11].

The Ru(0001) sample was prepared by Ar$^+$ ion sputtering (1 keV, 10 min), dosing of $2 - 10$ Langmuirs (L, with 1 L $= 1.33 \times 10^{-6}$ mbar s) of oxygen at 500 - 600 °C to oxidize residual surface carbon, and flash annealing to 1450 °C to anneal sputter defects and desorb excess oxygen. To prepare the adsorption layers, first 0.05 L of O_2 were dosed with the sample at room temperature, which leads to a low coverage of adsorbed O atoms. Then 1.0 L of CO were dosed to prepare the $(\sqrt{3} \ x \ \sqrt{3})R30°$-CO structure. Finally, the temperature was set, and the STM experiments were started.

The STM images presented here are single frames from movies acquired at a rate of 12 frames s^{-1}. The movies were recorded in the constant height mode at negative bias voltages. Under these conditions, the oxygen atoms appear bright and the CO molecules appear dark, corresponding to an inverted image contrast with respect to the contrast in the standard constant height mode. Because of the sinusoidal scanning voltage applied in the high-speed mode the raw data display a distortion that is removed by the image processing software. Filtering or other image processing routines are not applied. The distributions of directions of the (exchange) jumps in the ordered $(\sqrt{3} \ x \ \sqrt{3})R30°$ structure and in the fully disordered structure were uniform, verifying that the scanning of the tip had no measurable effect on the diffusion. The trajectories of the O atoms are determined by a software based on a wavelet transformation that identifies and tracks the atoms at the enhanced noise of the movie data (compared to standard, slow constant height data) [12]. During a movie, it occasionally happens that two O atoms come close together up to a distance where they start to interact with each other, an effect that slows down the motion; to prevent an impact on the diffusion parameters, these sections of the trajectories are automatically removed by the tracking software.

3. Results

Fig. 1(a) shows one frame from an STM movie (3731 frames, 1450 of which on the same position), recorded at 272 K. The hexagonally ordered pattern of dark dots is the $(\sqrt{3} \ x \ \sqrt{3})R30°$ structure of CO molecules, and the blurred stripe running from the top edge of the image to the right edge is a boundary between two translational domains of the structure. The fuzziness of the domain wall is a dynamic effect caused by rapid fluctuations of the positions of the CO molecules in the boundary. On the time scale of one frame (1/12 s) the width of these fluctuations is of the order of 10 Å, and on the time scale of the 1450 frames (121 s) the average position of the boundary changes by approximately the same distance (SI, movie S1). Upon closer inspection, one can identify four bright atomic features located at or in the domain wall (red arrows). These features, from their positions with respect to the CO molecules in the $(\sqrt{3} \ x \ \sqrt{3})R30°$ structure and from their appearance in the STM, can safely be interpreted as O atoms. The experiments occasionally showed that domain boundaries originated at small (2×2) islands of O atoms, indicating that these islands pin the boundaries or induce their formation when the CO layer forms during CO dosing. We rule out that the boundaries are thermally excited because, at $\Theta = 0.33$ ML, the order-disorder transition of the $(\sqrt{3} \ x \ \sqrt{3})R30°$-CO structure is theoretically predicted to happen at a temperature significantly higher than 400 K (CO desorbs before) [13,14].

A model of the marked area in Fig. 1(a) is shown in Fig. 1(b) with the two translational domains color-coded. The information about the adsorption sites, i.e., that the CO molecules (blue balls) occupy on-top sites and the O atoms (red balls) occupy threefold hcp sites, is based on the extensive vibrational spectroscopy and structure analysis literature, and also on theory [15–19]. The model shown in Fig. 1(b) suggests a heavy domain wall, i.e., a boundary with a locally higher CO coverage than $\Theta = 0.33$ ML in the neighboring ordered domains. However, because of the high jump rates of the CO molecules - with the calculated barrier of 0.3 eV [8] one estimates a jump rate of 3×10^7 s^{-1} at 272 K - the exact locations of some of the CO molecules in the domain boundary are uncertain; e.g., the apparent pairs of CO molecules on neighboring sites in the model could also be interpreted as single molecules that rapidly change positions. A light domain wall with a local coverage lower than 0.33 ML is therefore also possible [Fig. 1(c). In both cases, the atomic configurations vary depending on the local direction along which the boundary runs. However, no systematic effect of the directions was observed on the diffusion rate of the O atoms. Note that the models are only snapshots of rapidly changing configurations.

Fig. 2 shows two frames from a second movie (2327 frames, 2169 on the same area, SI movie S2) taken at 272 K on the same area as Fig. 1. In Fig. 2(a), the arrows mark the four O atoms which are still found in the imaged area but have moved to other positions. In Fig. 2(b) we have overlaid (on another frame of the movie) the trajectories of these atoms (from 2169 frames). Obviously, the trajectories preferentially run along the domain boundary and extend only little beyond the width of the short-time boundary fluctuations of ~10 Å. That the trajectories in the upper part of Fig. 2(b) seem to extend more deeply into the ordered $(\sqrt{3} \ x \ \sqrt{3})R30°$ domain is mainly caused by the fact that on the time scale of the 2169 frames (181 s) the average position of the boundary varies more strongly than the positions of the O atoms perpendicularly to the boundary. Overall, the O atoms are only rarely found outside the domain wall. The data thus show 2D domain boundary diffusion.

The shapes of the trajectories contain information about what happens atomically in the domain wall during this diffusion process. Fig. 3 (a) shows another frame of the same STM movie as Fig. 2 overlaid with only two of the trajectories, and Fig. 3(b) and (c) show expanded versions of the two trajectories with color-coded frame numbers. In the upper trajectory [Fig. 3(b)] one can identify at least two different types of motions of the O atom. For certain time periods (e.g., during the yellow vertical zig-zag line, frames 843–962) it travels along the
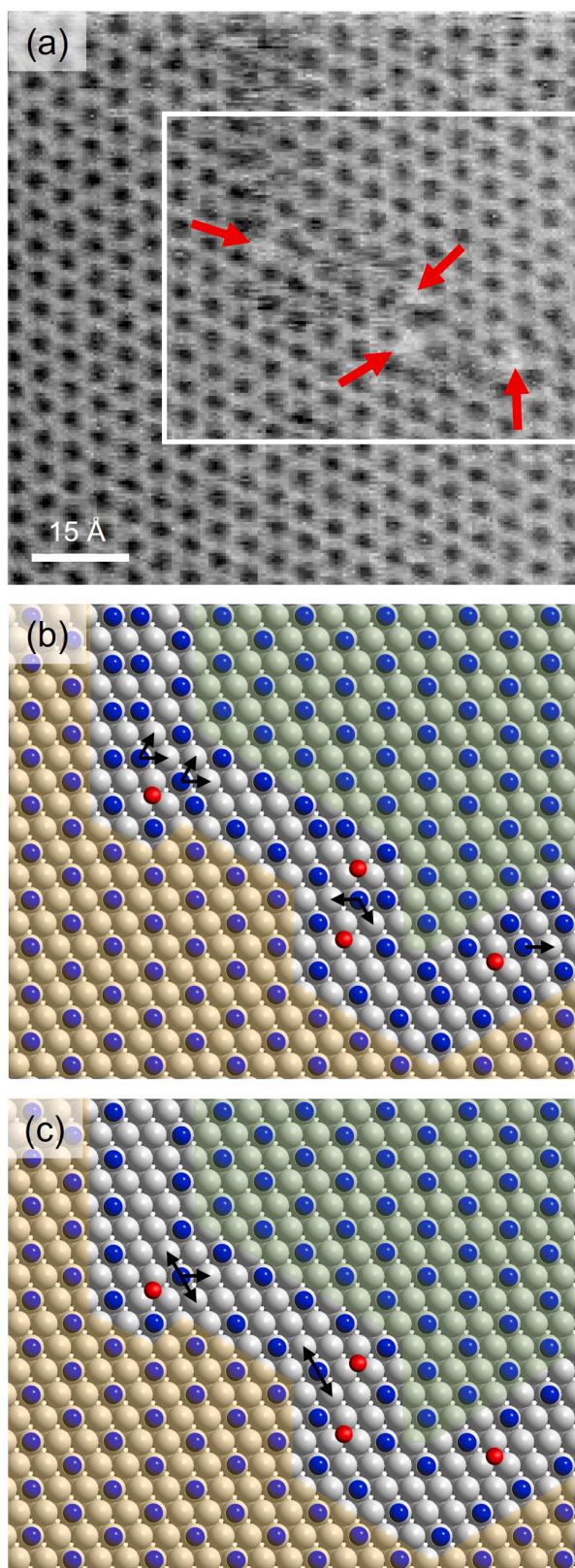
Fig. 1. (a) Single frame from an STM movie of the $(\sqrt{3} \ x \ \sqrt{3})R30°$-CO structure with coadsorbed O atoms (indicated by red arrows) in a domain boundary. STM parameters: Tunneling voltage: $V_t = -0.7$ V, tunneling current: $I_t = 3$ nA, image size: 89 Å x 89 Å, imaging rate: 12 frames s^{-1}. (b) Model of the area marked in (a) assuming a heavy domain wall. Translational domains are indicated by yellow and green shading, CO molecules by blue balls, O atoms by red balls, and Ru atoms by grey balls. Black arrows are possible CO displacements that create diffusional paths for the O atoms by forming single additional nearest-neighbor CO pairs. (c) Model of the same area assuming a light domain wall. Arrows are CO displacements that create diffusional paths for the O atoms along some still blocked directions by forming single (or no) nearest-neighbor CO pairs.

direction of the domain wall, jumping along a row of neighboring hcp sites (in the $\sqrt{3}$ direction of the Ru(0001) surface the hcp sites form zig-zag lines). For other time periods (at the outer parts to the left and right of the yellow line) the atom travels between and partially also through the rims of the ordered domains. The small triangles visible in these periods (arrow marks) are characteristic features caused by jumps of the O atoms between the three hcp sites in the vacancies of the ordered $(\sqrt{3} \ x \ \sqrt{3})R30°$ structure [8]. These periods are not so much caused by the O atoms moving into the ordered domain but more by the rapidly fluctuating position of the domain boundary (see movies S1 and S2). Not all trajectories are affected by these fluctuations which are a random effect possibly related to the curvature in the geometric directions of the domain wall. For example, the lower trajectory doesn't show the triangles, and the O atom mainly jumps along the direction of the domain wall.

We find that diffusion of the O atoms along the boundaries is significantly faster than diffusion in the ordered $(\sqrt{3} \ x \ \sqrt{3})R30°$ phase at the same temperature. For a quantitative comparison we cannot use the O hopping rates, the quantities evaluated in our previous work on the $(\sqrt{3} \ x \ \sqrt{3})R30°$ structure [8], because the coordination of the O atoms by CO molecules in the domain walls permanently changes between two (or even more) qualitatively different situations (in particular between ordered and disordered areas). This complexity precludes constructing an atomic hopping model which would be needed to extract jump rates from the displacement distributions of the O atoms [8, 10]. What we did instead was to evaluate a diffusion coefficient in the domain boundaries, D_{db}, which contains the various processes in an averaged way, by using the mean square displacements $\langle r^2 \rangle$ per frame extracted from the trajectories. From the dataset of Fig. 2, from altogether 4870 measurement points, a value of $\langle r^2 \rangle = (4.63 \pm 0.64)$ Å^2 is obtained. With the time period of $t = 1/12$ s given by the frame rate, one obtains, for the 2D case of an isotropic surface, a diffusion coefficient of $D_{db} = \langle r^2 \rangle /4t = (13.9 \pm 1.9)$ x 10^{-16} cm^2 s^{-1}. For purely 1D diffusion, the diffusion coefficient is $D_{db} = \langle r^2 \rangle /2t = (27.8 \pm 3.8)$ x 10^{-16} cm^2 s^{-1}. Because of the finite width of the domain walls, the actual situation is somewhere in between 1D and 2D, so that the diffusion coefficient is between these limits. These values represent averages over the relatively fast processes within the domain walls and the slower processes when the O atom is intermediately in the ordered domains.

For the diffusion in the reference system, the ordered $(\sqrt{3} \ x \ \sqrt{3})R30°$ lattice, precise hopping rates are available [8]. A minor complication with these data is the fact that the motion of an O atom in this lattice consists of two processes, a fast wiggling of the O atom between the three hcp sites inside a vacancy in the CO layer, and a slower exchange with neighboring CO molecules. However, only the latter leads to diffusional transport, so that we can just use the corresponding hopping rate, Γ_2, of this latter process [8]. At 272 K, we obtain, by applying the experimental Arrhenius parameters, a Γ_2 value of 0.27 s^{-1} [8]. The jump length of the O atom is one lattice constant of the Ru (0001) surface, $a = 2.706$ Å. However, after the O atom has jumped and exchanged sites with a CO molecule, the wiggling in the vacancy quickly randomizes the position within the vacancy. The site inside the original

A.-K. Kügler et al.
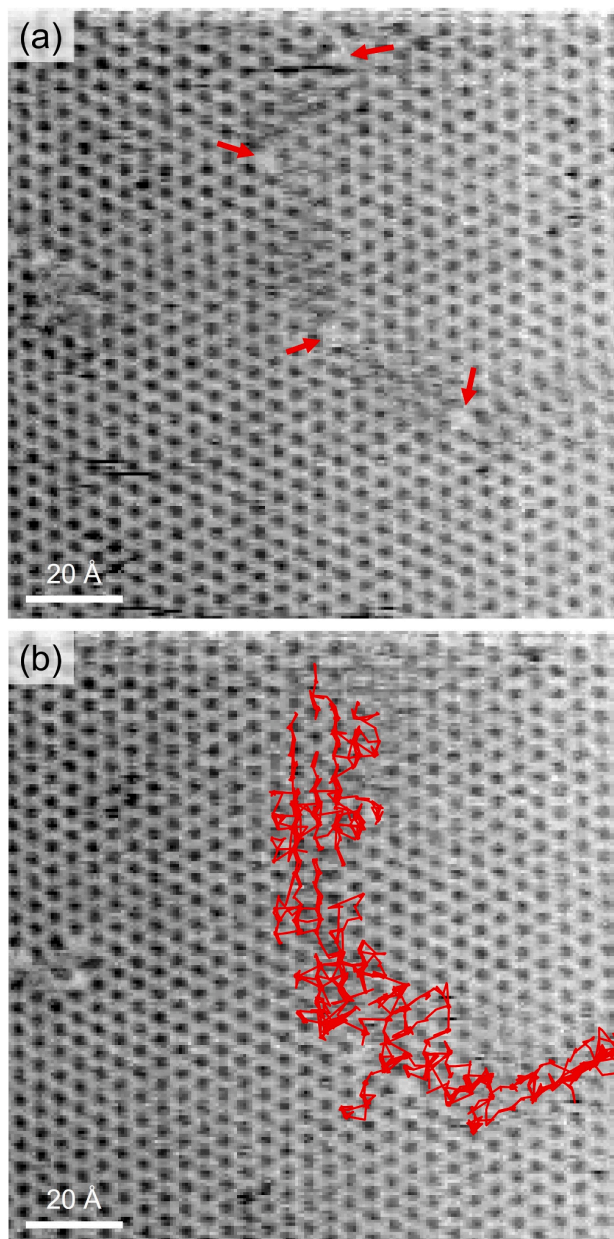
Fig. 2. Two frames from another STM movie of the same area as in Fig. 1, recorded at two different time instants. $V_t = -0.7$ V, $I_t = 3$ nA, 129 Å x 129 Å, 12 frames s^{-1}. (a) The arrows mark four O atoms. (b) Red lines are the trajectories of the four O atoms.

vacancy, before the exchange with CO, is also randomized by the wiggling. The diffusion length that appears in the lattice diffusion equation is, therefore, the distance between two vacancies in the $\left(\sqrt{3} \times \sqrt{3}\right)R30°$ structure, i.e., $d = \sqrt{3}a$. With $D_{\sqrt{3}} = \left(d^2/4\right)\Gamma_2$, we thus obtain a diffusion coefficient of $D_{\sqrt{3}} = 1.48 \times 10^{-16}$ cm^2 s^{-1} for the motion in the ordered $\left(\sqrt{3} \times \sqrt{3}\right)R30°$ structure.

As a result, we find that the domain boundary diffusion coefficient is one order of magnitude higher than the lattice diffusion coefficient at the same temperature.
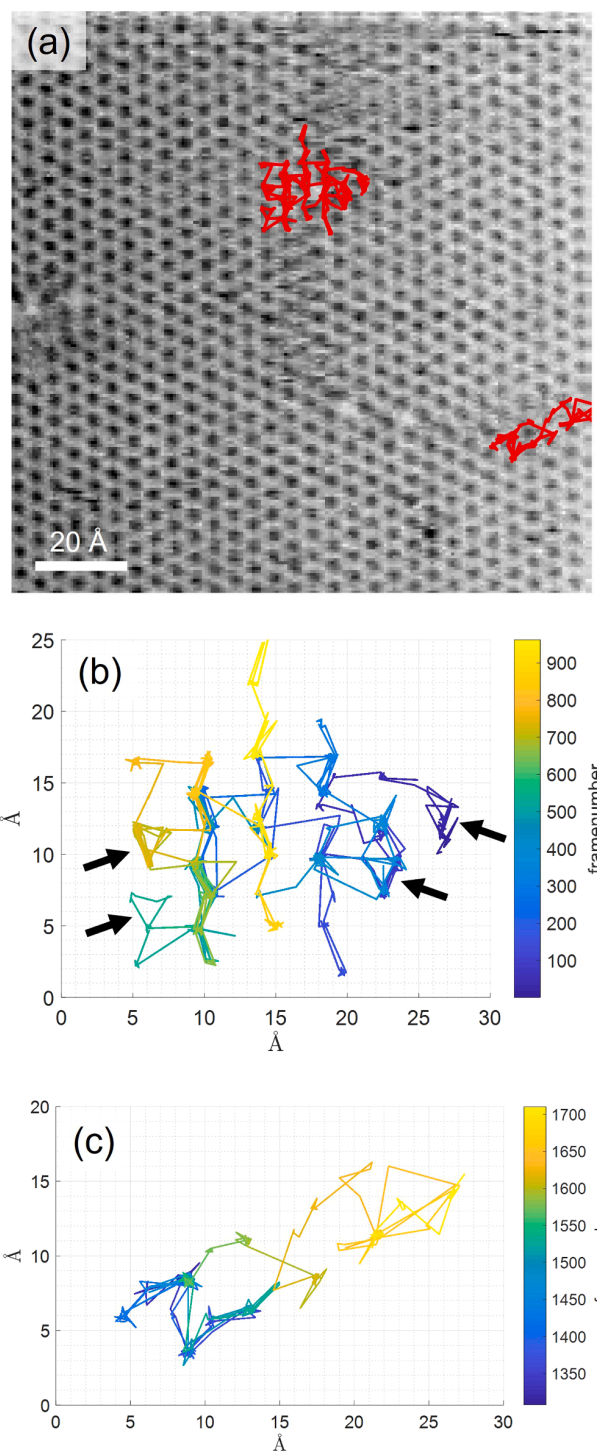
Fig. 3. (a) Another frame from the movie of Fig. 2 (movie S2) with only two overlaid trajectories. (b) shows the upper one of the two trajectories in (a) with color-coded frame numbers, and (c) shows the lower one of the two trajectories in (a), also with color-coded frame numbers. $V_t = -0.7$ V, $I_t = 3$ nA, 129 Å x 129 Å, 12 frames s^{-1}.

4. Discussion

Diffusion of O atoms along the domain boundaries of the $\left(\sqrt{3} \times \sqrt{3}\right)R30°$-CO structure on Ru(0001) is thus distinctly faster than

diffusion through the ordered lattice. On the other hand, the enhancement by one order of magnitude is much lower than the enhancement factors of 5 - 6 orders of magnitude typically found for grain boundary diffusion with respect to lattice diffusion in 3D solids (at temperatures below roughly 0.6 T_m, where T_m is the melting temperature of the solid) [1].

This discrepancy points to distinct mechanistic differences. For 3D solids, the newer literature assumes that grain boundary diffusion follows mechanisms that are qualitatively different from the usual lattice diffusion mechanisms [3,4]. For example, lattice self-diffusion in metals usually follows a vacancy mechanism, whereas in the grain boundaries, according to kinetic Monte-Carlo and molecular dynamics simulations, interstitial atoms and collective motions of several atoms play an equally important role [4].

We propose that the discrepancy between the $(\sqrt{3} \ x \ \sqrt{3})R30°$-CO/ O case on the one hand and the 3D solids on the other can be explained by the fact that in the adsorption layer no such qualitative differences between domain boundary and lattice diffusion exist and that the mechanisms are, in principle, equivalent. Within this hypothesis, the enhanced diffusion along the domain boundaries is explained by easier excitations of the same atomic processes as in the lattice.

We thus claim that the mechanism in the domain boundaries is equivalent to the previously derived "door-opening mechanism" of surface diffusion of O atoms in the ordered $(\sqrt{3} \ x \ \sqrt{3})R30°$-CO lattice [8]. In this mechanism, a hopping event of an O atom that leads to an exchange with a CO molecule, has two steps that affect the rate. In the first step, one of the CO molecules at the rim of the vacancy, in which the O atom is located, is displaced to an interstitial site of the $(\sqrt{3} \ x \ \sqrt{3})R30°$-CO lattice. This step costs an activation energy of 0.3 eV. It also lifts the ground state energy by 0.16 eV compared to the original configuration because the displaced CO molecule has two CO molecules on nearest-neighbor sites. Nearest-neighbor configurations are repulsive by 75 – 85 meV per CO-CO pair [9]. (The energies are from DFT calculations.) Because of the low barrier, the CO displacement is a fast pre-equilibrium that affects the rate by the lifted ground state energy (not by its own barrier). In the second step, the O atom can jump through the door opened by the displaced CO molecule to a site outside the original vacancy. The atom takes a path from its original hcp site over a bridge site to an intermediate fcc site and from there over a second bridge site to a neighboring hcp site, connected with an activation energy of 0.62 eV. In a third step, several CO molecules rearrange to give a configuration equivalent to the original configuration; this process is fast and does not appear in the overall rate. The overall activation energy of 0.16 eV + 0.62 eV = 0.78 eV was in reasonable agreement with the experimental value of 0.63 eV [8].

In a heavy domain wall of the $(\sqrt{3} \ x \ \sqrt{3})R30°$-CO structure, one can devise a similar sequence of steps consisting of displacements of CO molecules and subsequent jumps of O atoms. Also in this case, an O atom can only jump to a site outside its CO vacancy, when a neighboring hcp site is empty, i.e., when all three Ru atoms forming the hcp site do not have an adsorbed CO molecule. This is achieved by displacements of CO molecules.

What is different in the heavy domain boundary is the coordination of the CO molecules around the O atom. As shown in the model of Fig. 1 (b), all four O atoms in this particular situation are coordinated by CO molecules of which at least one molecule already has a second CO molecule on a nearest-neighbor site. When these molecules are displaced to neighboring on-top sites, e.g., along the directions indicated by black arrows, creating an empty hcp site for the jump of an O atom, the number of nearest-neighbor CO pairs increases by one rather than by two as in the $(\sqrt{3} \ x \ \sqrt{3})R30°$-CO lattice. The ground state energy therefore increases by ~80 meV rather than by 0.16 eV. Accordingly, the overall activation energy is ~80 meV lower than in the ordered lattice. A second effect working in the same direction is the shorter average distances between the O atoms and the surrounding CO molecules at the

higher coverage in the heavy domain wall. The repulsion between O and CO corresponds to a lower adsorption energy of the O atoms, resulting in a lower jump barrier. This effect is weaker, ~40 meV or less [10]. Overall, the barrier is lowered by a value of the order of 100 meV. Similar arguments have previously been used to explain the faster diffusion of O atoms through the disordered CO layer at a coverage of 0.47 ML [10].

For the alternative light domain walls, one can construct a model by removing all CO molecules from nearest-neighbor pair configurations. As shown in Fig. 1(c), most O trajectories through such a configuration do not require CO displacements at all, and only for jumps in certain directions displacements are required that create single CO-CO pairs on nearest-neighbor sites. Accordingly, the barrier with respect to the ordered lattice would be reduced by 0.16 eV or less. There are no configurations with closer O/CO distances than in the $(\sqrt{3} \ x \ \sqrt{3})R30°$-CO lattice, so that the barrier would not further be lowered by this effect. Hence, in light domain walls, the barrier would also be lowered by a value of the order of 100 meV.

There are two observations that support these considerations. Firstly, when we interpret the ratio of domain boundary and lattice diffusion coefficients entirely in terms of activation energies, neglecting possible differences between the preexponential factors, then application of Arrhenius equations for both types of diffusions gives

$$\Delta E^* = -k_B T \ln \frac{D_{\text{db}}}{D_{\sqrt{3}}}.$$

$\Delta E^* = E_{\text{db}}^* - E_{\sqrt{3}}^*$ is the difference between the activation energies of the domain boundary and $(\sqrt{3} \ x \ \sqrt{3})R30°$-CO lattice diffusion. With $T = 272$ K and using the D_{db} values from the present study and the above evaluated $D_{\sqrt{3}}$ value from the previous work, we obtain $\Delta E^* = -(52 - 69)$ meV (the range is given by the two D_{db} values for the purely 2D and 1D cases). The domain boundary diffusion barrier is thus lower than the lattice diffusion barrier by a value of the order of 100 meV. This reduction is in quite good agreement with the values estimated above by using DFT data for the processes in the disordered CO layer. Note that the activation energies for a 3D case like Cu self-diffusion by grain boundary and lattice diffusion, 1.24 eV and 2.04–2.19 eV [20–22], respectively, differ by a value that is one order of magnitude higher than the difference obtained in the present case, consistent with the much higher ratio of the grain boundary and lattice diffusion coefficients.

Secondly, D_{db} can also be compared with an experimental value. It has been observed that in a disordered CO layer at a CO coverage of $\Theta = 0.47$ ML the oxygen hopping rate is higher than in the ordered structure [10]. Using the Arrhenius parameters determined in these experiments, the hopping rate of the O atoms in the disordered layer at 272 K is $\Gamma = 6.66$ s^{-1}. With $D_{\text{dis}} = (a^2/4)\Gamma$, this value translates into a diffusion coefficient of $D_{\text{dis}} = 12.19 \times 10^{-16}$ cm^2 s^{-1}. (For D_{dis} we here use the fact that at the higher CO coverage the O atoms do not wiggle in the smaller vacancies, so that the effective jump length is just $a = 2.706$ Å.) The value thus obtained almost quantitatively agrees with the present D_{db} values for the domain walls, indicating that the same effects operate in the disordered layer and in the domain walls. In both cases, diffusion follows an enhanced door-opening mechanism.

5. Conclusions

High-speed STM has been used to study the diffusion of O atoms on a Ru(0001) surface covered by 0.33 ML of CO. In contrast to our previous studies on the diffusion of adsorbed O atoms on the ordered lattice of the $(\sqrt{3} \ x \ \sqrt{3})R30°$-CO structure [8,9], we here investigated diffusion at domain boundaries. In the STM, the boundaries appear as disordered, fluctuating stripes. We find that the O atoms preferentially move along the domain boundaries and that the diffusion coefficient in the domain

walls is one order of magnitude higher than the diffusion coefficient in the ordered $(\sqrt{3} \, x \, \sqrt{3})R30°$ domains. It is almost identical to the diffusion coefficient in the disordered CO layer at $\Theta = 0.47$ ML at the same temperature [10], indicating that it follows the same mechanism. We propose that the domain boundary diffusion is based on the same CO displacement and O hopping processes as in the door-opening mechanism in the ordered $(\sqrt{3} \, x \, \sqrt{3})R30°$-CO structure. However, these processes happen at an increased rate in the disordered configurations in the domain walls.

CRediT authorship contribution statement

Ann-Kathrin Kügler: Writing – review & editing, Visualization, Validation, Software, Methodology, Investigation, Formal analysis, Data curation, Conceptualization. **Hannah Illner:** Writing – review & editing, Visualization, Software, Formal analysis, Data curation. **Joost Wintterlin:** Writing – review & editing, Writing – original draft, Validation, Supervision, Project administration, Conceptualization.

Declaration of competing interest

The authors declare that they have no known competing financial interests or personal relationships that could have appeared to influence the work reported in this paper.

Data availability

The data that support the findings of this study are available in the Open Data LMU repository at https://doi.org/10.5282/ubm/data.502 or can be obtained from the authors upon reasonable request.

Supplementary materials

Supplementary material associated with this article can be found, in the online version, at doi:10.1016/j.susc.2024.122597.

References

[1] Y.M.I. Kaur, W. Gust, Fundamentals of Grain and Interface Boundary Diffusion, Wiley, Chichester, 1995.

[2] I. Kaur, W. Gust, L. Kozma, Handbook of Grain and Interphase Boundary Diffusion Data, Ziegler, Stuttgart, 1989.

[3] H. Mehrer, Diffusion in Solids, 1st. ed., Springer, Berlin, Heidelberg, 2007.

[4] A. Suzuki, Y. Mishin, Atomic mechanisms of grain boundary diffusion: low versus high temperatures, J. Mat. Sci. 40 (2005) 3155–3161.

[5] T. Tansel, A. Taranovskyy, O.M. Magnussen, In situ video-STM studies of adsorbate dynamics at electrochemical interfaces, ChemPhysChem 11 (2010) 1438–1445.

[6] Y.-C. Yang, K. Hecker, O.M. Magnussen, In situ video-scanning tunneling microscopy studies of the structure and dynamics of Cl adlayers on Au(100) electrodes, Electrochim. Acta 112 (2013) 881–886.

[7] D.-J. Liu, J.W. Evans, Surface diffusion in mixed overlayers with superlattice ordering: percolative transport around obstacles and along domain boundaries, J. Chem. Phys. 113 (2000) 10252–10264.

[8] A.-K Henß, S. Sakong, P.K. Messer, J. Wiechers, R. Schuster, D.C. Lamb, A. Groß, J. Wintterlin, Density fluctuations as door-opener for diffusion on crowded surfaces, Science 363 (2019) 715–718.

[9] S. Sakong, A.-K. Henß, J. Wintterlin, A. Groß, Diffusion on a crowded surface: KMC simulations, J. Phys. Chem. C 124 (2020) 15216–15224.

[10] H. Illner, S. Sakong, A.-K. Henß, A. Groß, J. Wintterlin, Diffusion of O atoms on a CO-covered Ru(0001) surface-a combined high-speed scanning tunneling microscopy and density functional theory study at an enhanced CO coverage, J. Phys. Chem. C 127 (2023) 7197–7210.

[11] A.K. Henß, J. Wiechers, R. Schuster, V. Platschkowski, J. Wintterlin, A beetle-type, variable-temperature scanning tunneling microscope for video-rate imaging, Jpn. J. Appl. Phys. 59 (2020) SN1007.

[12] P.K. Messer, A.K. Henß, D.C. Lamb, J. Wintterlin, A multiscale wavelet algorithm for atom tracking in STM movies, New J. Phys. 24 (2022) 033016.

[13] H. Pfnür, D. Menzel, Lateral interactions for CO/Ru(001): order-disorder transitions of the $\sqrt{3}$ structure, Surf. Sci. 148 (1984) 411–438.

[14] H. Pfnür, H.J. Heier, Order-disorder phenomena in the system CO/Ru(001), Ber. Bunsenges. Phys. Chem. 90 (1986) 272–277.

[15] G.E. Thomas, W.H. Weinberg, The vibrational spectrum and adsorption site of CO on the Ru(001) surface, J. Chem. Phys. 70 (1979) 1437–1439.

[16] H. Pfnür, D. Menzel, F.M. Hoffmann, A. Ortega, A.M. Bradshaw, High resolution vibrational spectroscopy of CO on Ru(001): the importance of lateral interactions, Surf. Sci. 93 (1980) 431–452.

[17] G. Michalk, W. Moritz, H. Pfnür, D. Menzel, A LEED determination of the structures of Ru(001) and of CO/Ru(001)$-\sqrt{3} \times \sqrt{3}$ R30°, Surf. Sci. 129 (1983) 92–106.

[18] M. Lindroos, H. Pfnür, G. Held, D. Menzel, Adsorbate induced reconstruction by strong chemisorption: Ru(001)p(2×2)-O, Surf. Sci. 222 (1989) 451–463.

[19] C. Stampfl, M. Scheffler, Theoretical study of O adlayers on Ru(0001), Phys. Rev. B 54 (1996) 2868–2872.

[20] B. Burton, G.W. Greenwood, The contribution of grain-boundary diffusion to creep at low stresses, Met. Sci. J. 4 (1970) 215–218.

[21] A. Kuper, H. Letaw, L. Slifkin, E. Sonder, C.T. Tomizuka, Self-diffusion in copper, Phys. Rev. 98 (1955) 1870.

[22] D.B. Butrymowicz, J.R. Manning, M.E. Read, Diffusion in copper and copper alloys. Part I. volume and surface self-diffusion in copper, J. Phys. Chem. Ref. Data 2 (1973) 643–656.

Supplementary Information

An STM study on the diffusion of O atoms on a CO-covered Ru(0001) surface - The role of domain boundaries

Ann-Kathrin Kügler[1], Hannah Illner[1], Joost Wintterlin[1,2]*

[1]Department of Chemistry, Ludwig-Maximilians-Universität München, 81377 Munich, Germany

[2]Center for NanoScience, Schellingstr. 4, 80799 Munich, Germany

*Corresponding author, wintterlin@cup.uni-muenchen.de

Movie S1: STM movie at 272 K

STM movie showing the diffusion of oxygen atoms along a domain boundary of the $(\sqrt{3} \; x \; \sqrt{3})R30°$-CO structure on a Ru(0001) surface. T = 272 K; 1450 frames; frame rate 12 s^{-1}; Θ_{CO} = 0.33 ML; tunneling voltage V_t = -0.70 V; tunneling current I_t = 3 nA; frame size 89 Å x 89 Å. Figure 1 in the main text shows the second frame of the movie.

The oxygen atoms appear as bright, mobile features, and the CO molecules of the $(\sqrt{3} \; x \; \sqrt{3})R30°$-CO structure appear as dark features. The domain boundary is the fluctuating, blurred stripe running from the top edge through the center to the right edge of the frames.

Movie S2: STM movie at 272 K

STM movie showing the diffusion of oxygen atoms along the domain boundary of the $(\sqrt{3} \; x \; \sqrt{3})R30°$-CO structure on a Ru(0001) surface. T = 272 K; 2169 frames; frame rate 12 s^{-1}; Θ_{CO} = 0.33 ML; tunneling voltage V_t = -0.70 V; tunneling current I_t = 3 nA; frame size 129 Å x 129 Å. Figure 2a in the main text shows frame 733, fig. 2b shows frame 23.

The assignment of the oxygen atoms and CO molecules is the same as in Movie S1. The position of the domain boundary is about the same as in Movie S1.

5.2. Solution of the structure of the high-coverage CO layer on the Ru(0001) surface − A combined study by density functional theory and scanning tunneling microscopy

High coverage structures of adsorbates on metal surfaces are difficult to predict, as their formation depends on the complex interplay of the adsorbate-metal interaction and the adsorbate-adsorbate interaction. At higher coverages, the latter becomes increasingly important and often competes with the preferred adsorption geometries dictated by the adsorbate-metal interaction. Various high-coverage CO structures on (0001) and (111) surfaces of several transition metals like Co, Ni, Cu, Ru, Rh, Pd, Ir, and Pt are known.[123] Carbon monoxide has a somewhat larger van-der-Waals diameter (3.11 to 3.35 Å) than the surface lattice constant of these metals.[124,125] CO can, therefore, not occupy all lattice sites in a (1×1) structure which gives rise to a rich variety of complex saturation structures.

There is a long-standing conflict over the high coverage structure of CO on Ru(0001). Early LEED experiments suggested the formation of a moiré-type structure, where the CO molecules form a hexagonal superstructure that is not commensurate with the Ru substrate.[118,126] In such a structure, the precise adsorption site is less important and CO-CO interactions dominate over the CO-metal bonding. However, a moiré structure contradicts vibrational spectroscopy results, which showed that all CO molecules are bound to on-top sites.[119,127,128]

This long-standing conflict has been solved by combining STM measurements and DFT calculations. The key results of the publication are:

- STM images showed that the Ru(0001) surface is entirely covered with different-sized clusters of CO molecules. The clusters are not randomly arranged but follow strict tiling rules. The surface coverage is 0.66 ML, which is in agreement with the CO saturation coverage found in vibrational spectroscopy and LEED data.

- Fourier transformations of the STM images reproduce the LEED pattern of the CO-saturated Ru(0001) surface and provide a new interpretation. The spots in the reflection pattern are formed by multiple scattering at the substrate and the quasi-hexagonal cluster lattice, in agreement with the compact cluster structure model.

- DFT calculations showed that compact islands consisting of 7 to 37 CO molecules are found to be the most stable configurations. The inner structure of the islands is a pseudo (1×1) structure, and the cluster islands are separated by single rows of empty Ru atoms.

- Tersoff-Haman simulations of the STM images match the experimental findings in the low-temperature STM experiments. The CO molecules in the centers of the clusters on the on-top sites appear as dark or light spots (depending on the recording mode and sign of V_t). The CO molecules on the cluster rims are tilted outward and appear as almost structureless rims around the clusters.

Author contributions:
Hannah Illner: Conceptualization, Investigation, Visualization, Writing – original draft, Writing – review and editing.
Sung Sakong: Conceptualization, Investigation, Visualization, Writing – original draft, Writing – review and editing.
Axel Groß: Funding acquisition, Supervision (supporting), Writing – review and editing.
Joost Wintterlin: Conceptualization, Supervision (lead), Writing – original draft, Writing – review and editing.

Solution of the structure of the high-coverage CO layer on the Ru(0001) surface—A combined study by density functional theory and scanning tunneling microscopy

Hannah Illner,[1] [iD] Sung Sakong,[2] [iD] Axel Groß,[2] [iD] and Joost Wintterlin[1,3,a)] [iD]

AFFILIATIONS

[1] Department of Chemistry, Ludwig-Maximilians-Universität München, 81377 Munich, Germany
[2] Institute of Theoretical Chemistry, University of Ulm, 89081 Ulm, Germany
[3] Center for NanoScience, Schellingstr. 4, 80799 Munich, Germany

[a)]Author to whom correspondence should be addressed: wintterlin@cup.uni-muenchen.de

ABSTRACT

Structures formed by dense CO adsorption layers can provide information about the balance between molecule–surface and molecule–molecule interactions. However, in many cases, the structure models are not clear. Using density functional theory (DFT) and scanning tunneling microscopy (STM), we have investigated the high-coverage CO layer on the Ru(0001) surface. Previous investigations by low-energy electron diffraction (LEED) and vibrational spectroscopy led to conflicting results about the structure. In the present study, 88 models with coverages between 0.58 and 0.77 monolayers have been analyzed by DFT. The most stable structures consist of small, compact CO clusters with an internal pseudo (1×1) structure. The CO molecules in the cluster centers occupy on-top sites in an upright position, whereas the molecules farther outside are slightly shifted from these sites and tilted outward. STM data of the CO-saturated surface at low temperatures, corresponding to a coverage of 0.66 monolayers, show a quasi-hexagonal pattern of features with an internal hexagonal fine structure. Simulated images based on the cluster model agree with the experimental data. It is concluded that the high-coverage CO layer consists of the close-packed clusters predicted by DFT as the most stable structure elements. In the experiment, the sizes and shapes of the clusters vary. However, the arrangement is not random but follows defined tiling rules. The structure remains ordered, almost up to room temperature. The LEED data are re-interpreted on the basis of the Fourier transforms of the STM data, solving the long-standing conflict about the structure.

Published under an exclusive license by AIP Publishing. https://doi.org/10.1063/5.0215872

INTRODUCTION

Dense layers of adsorbed CO molecules on transition metal surfaces show, in an exemplary way, how the structure of an adsorption layer can be determined by counteracting molecule–surface and molecule–molecule interactions. The CO–metal bond is relatively strong, and the molecules preferentially bind to defined adsorption sites, but it is not strong enough to prevent displacements from these sites when repulsive interactions between neighboring molecules become important. At high coverage, these two interactions have to be balanced in some way.

On the hexagonally close-packed surfaces of the fcc and hcp transition metals, the preferred CO binding positions are the high-symmetry sites on-top, bridge, hcp threefold hollow, and fcc three-fold hollow. Which site is most favored depends on the metal. However, the size of the CO molecule prevents all sites of the same type from being occupied at the same time, and coverages (Θ) of one monolayer (ML, in units of CO molecules per metal surface atom) cannot be reached. The size of a CO molecule, approximately its van-der-Waals diameter, can be estimated from the saturation coverages of CO on the Co(0001) and Pt(111) surfaces, giving values between 3.11 and 3.36 Å.[1,2] These values are, in all cases, higher than

the spacings between equivalent adsorption sites, which are given by the lattice constants of the surfaces. The resulting restrictions for the arrangements of the molecules give rise to a rich variety of different high-coverage structures on the (0001) or (111) surfaces of Co, Ni, Cu, Rh, Pd, Ir, and Pt.[3] The structure that is formed in a given case is determined by the electronic structure and lattice constant of the metal and by the exact CO coverage. However, recent theory work found very low energy differences between different high-coverage structures, indicating that predictions about a structure are difficult.[4]

What can be done is to classify the high-coverage CO structures on these surfaces according to common construction principles. Four types of models can be identified: (1) Models with mixed adsorption sites: In these models, one fraction of molecules occupies their most preferred sites, whereas a second fraction occupies "second-best" sites in between. CO–metal interactions still dominate. Examples are the $c(4 \times 2)$ CO structure on Pt(111) ($\Theta = 0.50$ ML) and the $(\sqrt{7} \times \sqrt{7})R19°$ structure on Ni(111) ($\Theta = 0.57$ ML).[5,6] (2) Moiré models: In these models, the CO molecules form hexagonally close-packed layers with larger internal lattice constants than the underlying metal. The mismatch of the two lattices gives rise to a moiré effect. Repulsive interactions between the CO molecules dominate. Most of the early low-energy electron diffraction (LEED) studies on hexagonally close-packed metal surfaces have assumed such models. Cases confirmed by scanning tunneling microscopy (STM) are the CO layers on Pt(111) at $\Theta = 0.51$–0.68 ML at 300 K and on Co(0001) at $\Theta = 0.63$–0.65 ML at 300 K.[1,2] (3) Antiphase domain boundary models:[3,7] In these models, the CO molecules form narrow, one-dimensionally extended domains with a simple or mixed site internal structure in which all CO molecules occupy high-symmetry sites. The domains are separated by "heavy domain walls" with a denser CO packing. There is also the inverse case: dense domains separated by light domain walls. CO–metal interactions dominate. Such structures have been observed for Pt(111) and Co(0001) at low temperatures.[8,9] (4) Cluster models: These models consist of small islands in which the molecules occupy all high-symmetry sites of the same type; CO–metal interactions dominate. The repulsions between the CO molecules lead to deviations from perfect internal (1×1) structures [one may speak of pseudo (1×1) structures], and the cluster sizes are limited to a few molecules. Examples are the $(3\sqrt{3} \times 3\sqrt{3})R30°$ structure on Ir(111) at $\Theta = 0.70$ ML and the $(2\sqrt{3} \times 2\sqrt{3})R30°$ structure on Ru(0001) at $\Theta = 0.58$ ML.[10–12]

CO layers on Ru(0001) at higher coverages than 0.58 ML do not seem to fit into this classification. Early LEED experiments showed diffraction patterns at coverages between $\Theta = 0.58$ and 0.65 ML (0.66 ML in the second publication) [Fig. 1(a)] that clearly pointed to moiré structures (at that time termed compressed or hexagonal phases).[13,14] Arguments for moiré structures are, first, that the most intense diffraction spots of the adsorption layer (reciprocal lattice vectors $\vec{h}_1^{CO}$, $\vec{h}_2^{CO}$, and symmetry equivalents) close to the first order diffraction spots of the Ru substrate (reciprocal lattice vectors $\vec{g}_1^{Ru}$, $\vec{g}_2^{Ru}$, and symmetry equivalents) can, in a straightforward manner, be explained by diffraction at a hexagonal, rotated layer of CO molecules with a larger lattice constant than the substrate [Fig. 1(b)]. The fact that the superstructure spots appear as pairs can be accounted for by the two possible rotational domains. The

six superstructure spots close to the origin can be explained by multiple scattering. Second, when the CO coverage was increased from $\Theta = 0.58$ to 0.65 ML (0.66 ML), the superstructure spots continuously shifted toward the nearest substrate spots.[13,14] This is exactly what is expected for a moiré structure that is compressed when it adopts additional molecules. Third, for a hexagonally close-packed CO layer, one expects that saturation is reached when the internal lattice constant of the layer gets close to the van-der-Waals diameter of CO. Using the saturation coverage of 0.66 ML, a value determined independently of a structure model,[14] the moiré model gives a CO–CO distance of 3.33 Å. This value is, in fact, in the range of the van-der-Waals diameters of CO.

On the other hand, high-resolution electron energy loss spectroscopy (HREELS) and reflection absorption infrared spectroscopy (RAIRS) showed only one vibrational C–O mode over the entire range of coverages up to saturation.[15,16] The peak displayed some shift with increasing coverage, which can be explained by dipole–dipole coupling and an additional weakening of the CO–metal bond,[17,18] but it remained in the range of on-top-bonded CO. This observation is in obvious contradiction to moiré structures, which contain CO molecules on all kinds of sites [Fig. 1(b)].

There have been ideas on how this discrepancy can be resolved. One has been that the vibrational spectra may have to be interpreted differently. The observed C–O mode may, in general, not exclusively mark on-top CO,[15] or, at least in a situation where molecule–molecule interactions dominate, it may no longer be valid to attribute a certain vibrational C–O frequency to a certain binding site.[16] Another idea has been that the LEED pattern can alternatively be interpreted by an antiphase domain boundary model.[3] In this model, CO molecules would form long, narrow domains with an internal (1×1) structure, in which all molecules occupy on-top positions. Domain boundaries formed by empty Ru sites would allow for relaxations perpendicularly to the domains. There would be three rotational domains, and the superimposed diffraction patterns from these domains would give the same LEED pattern as the one shown in Fig. 1(a). Monte-Carlo simulations supported this model.[19] Observations by electron stimulated desorption ion angular distribution (ESDIAD) that the molecular axes at saturation are tilted from the surface normal by a few degrees can be explained by the relaxations expected for such a model.[20] However, a recent STM investigation of CO/H co-adsorbed layers on Ru(0001) was in disagreement with the antiphase domain model.[21] Images recorded at high CO coverage, where H was most likely absent, showed some hexagonal pattern rather than the one-dimensional features one would expect. No structure model was proposed.

Here, we present an investigation of the high-coverage CO layer on Ru(0001) by density functional theory (DFT) and STM. Fourier transformations of the STM data are used for comparison with the LEED pattern. We find a structure model that is in agreement with all previous experimental observations. In particular, it solves the seeming conflict between the vibrational spectroscopy and the LEED data.

EXPERIMENTAL SECTION

The experiments were performed in an ultra-high vacuum (UHV) chamber (base pressure $<1 \times 10^{-10}$ mbar) by means of a
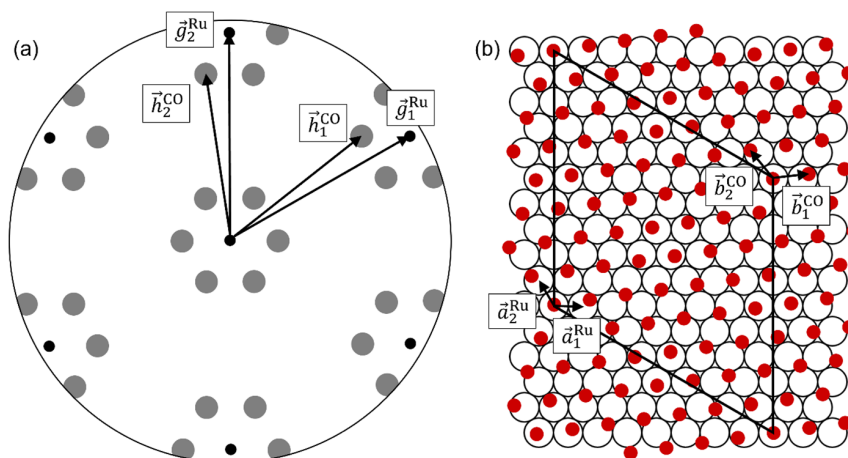
FIG. 1. LEED and structure model of the saturated CO layer on Ru(0001) from the literature. (a) Schematic LEED pattern, showing the substrate spots (black) and the superstructure spots (gray).[13,14] $\vec{g}_1^{Ru}$, $\vec{g}_2^{Ru}$, $\vec{h}_1^{CO}$, and $\vec{h}_2^{CO}$ are the reciprocal basis vectors of the Ru surface and of the hexagonal CO layer, respectively. (b) Previously proposed moiré structure model.[13] $\vec{a}_1^{Ru}$, $\vec{a}_2^{Ru}$, $\vec{b}_1^{CO}$, and $\vec{b}_2^{CO}$ are the real-space basis vectors of the Ru surface and of the CO layer, respectively, and the rhombus is the unit cell of the $\left(5\sqrt{3} \times 5\sqrt{3}\right)R30°$ structure that had been derived from the LEED pattern.

home-built, beetle-type scanning tunneling microscope. With this setup, sample temperatures can be varied between 50 and 500 K by a liquid He flow cryostat that cools the sample holder of the STM and by simultaneous radiative heating from a filament at the back of the sample. Details of the setup have been described previously.[22] Images were recorded in the standard, slow constant current mode and also in the fast constant height mode. For the present analysis, we do not make use of the high time resolution of this mode. The chamber was additionally equipped with an Auger electron spectrometer (AES), a low-energy electron diffraction system, an ion gun, a quadrupole mass spectrometer, and a sample manipulator.

For preparation, the Ru(0001) sample was repeatedly sputtered, annealed, oxidized, and annealed again. The sample was first sputtered with 1 keV Ar ions for 10–15 min and then flash-annealed to 1470 K. Residual carbon was then oxidized by dosing O_2 in various amounts. For higher amounts of carbon, the chamber was backfilled with 2×10^{-7} mbar of O_2 for 10–15 min at 910 K. For lower carbon coverages, dosing 2–20 L of O_2 at 298–423 K was sufficient [1 Langmuir (L) = 1.33×10^{-6} mbar s]. To induce reaction of the adsorbed oxygen with the carbon and desorb excess oxygen, the sample was flash-annealed to 1700 K. This sequence was repeated until the AES showed a clean sample. The problem with AES of the overlapping carbon KLL peak at 272 eV with the Ru MNN peak at 273 eV was solved by the known procedure to use the asymmetry of the overlapped peaks as a measure of the carbon coverage.[23–25] Directly before an experiment, the sample was briefly annealed to 623 K to desorb any molecules that had adsorbed in the time period after the last high-temperature flash. Then the sample was transferred to the STM.

High coverages of CO were prepared in two steps. First, 50 L of CO were dosed on the freshly prepared surface at a temperature slightly above 300 K. This treatment led to an incomplete $\left(2\sqrt{3} \times 2\sqrt{3}\right)R30°$ structure, the CO structure described in a recent

publication.[12] The coverage of $\Theta = 0.47$ ML of this structure is close to the saturation coverage attainable by dosing CO at room temperature. This procedure was used to protect the surface, by means of the CO layer, against the adsorption of foreign gases, mainly H_2 and H_2O, when the sample cooled to the measurement temperature. In a second step, an additional 15 L of CO were dosed while the sample cooled from room temperature to 60–70 K. In this way, a coverage of 0.66 ML of CO was obtained. In an additional STM experiment, the temperature was gradually raised to room temperature to detect possible phase transitions.

Setup of the density functional theory calculations

The VASP software package was used to compute the adsorption energy of the CO adlayer on the Ru(0001) surface based on periodic DFT.[26] The revised version of the Perdew–Burke–Ernzerhof (RPBE) functional was employed to account for exchange–correlation effects.[27] The electronic wave functions were expanded in a plane-wave basis set up to an energy cutoff of 350 eV. The ionic cores were taken into account by the projector augmented wave (PAW) potential.[28] Dispersion interactions between the CO molecules and the first layer of the Ru slab were computed by the D3 correction scheme of Grimme *et al.*[29] Note that the RPBE + D3 approach employed here has been shown to yield rather reliable molecular adsorption energies.[30]

We modeled the Ru(0001) surface using a slab consisting of three atomic layers. For the Ru hcp bulk structure, lattice parameters of $a = 2.74$ Å and $c/a = 1.58$ were obtained, in good agreement with the experimental values of $a = 2.706$ Å and $c/a = 1.58$. The CO molecules were placed at on-top sites in all investigated structures, which are more stable than the hcp hollow, fcc hollow, and bridge sites by 0.30, 0.34, and 0.32 eV, respectively. These values are only slightly affected by the presence of CO molecules on neighboring

17 December 2024 10:31:24

on-top sites. Relaxations from the exact on-top positions were allowed, but structures with other CO positions were not considered.

A first set of structures was formed by clusters consisting of 7, 10, 12, 14, 16, and 19 CO molecules, all bonded at on-top positions (Fig. 2; a further configuration with 37 CO molecules is not shown) and separated by rows of uncovered Ru atoms (unit cells are marked). The first Brillouin zones of these configurations were integrated using 6×6, 6×6, 3×3, 5×5, 3×3, 4×4, and 2×2 k-point meshes for the corresponding surface unit cells. In all cases, we optimized the energy minimum configurations by relaxing the topmost Ru layers of the slabs and the CO molecules until the forces converged to 0.01 eV/Å. Periodic images of the slab were separated by vacuum layers of 15 Å, and dipole corrections were applied to compensate for any dipole field between the periodic images.

In addition to the cluster configurations, we considered further CO adlayer configurations on a $\left(4\sqrt{3} \times 4\sqrt{3}\right)R30°$ unit cell, corresponding to a coverage variation from 0.58 to 0.77 ML. We added CO molecules to the configuration consisting of 7 CO clusters and displaced CO molecules from their positions in the clusters. In addition, we considered configurations with CO vacancies in a honeycomb structure (0.75 ML) to probe a possible adlayer phase change from a $\left(2\sqrt{3} \times 2\sqrt{3}\right)R30°$ cluster structure to a (2×2) honeycomb structure. Altogether, 88 structures were analyzed.

The relative adsorption energies of the CO adlayers (E_{ads}) were computed with respect to the adsorption energy of an isolated CO molecule on the clean Ru(0001) surface,

$$E_{ads} = \frac{E_{tot} - E_{\text{Ru}(0001)} - n_{CO}E_{CO}}{n_{CO}}. \qquad (1)$$

E_{tot} is the total energy of the CO adlayer on the Ru surface, $E_{\text{Ru}(0001)}$ is the energy of the clean Ru(0001) slab, E_{CO} is the energy of a single CO molecule on the Ru surface given by the sum of the energy of a CO molecule in the gas phase and its adsorption energy of −1.92 eV, and n_{CO} is the number of CO molecules in the unit cell. Because of the repulsion between the adsorbed CO molecules, all E_{ads} values at finite coverages are positive.

We have also performed simulations of constant height STM images using the Tersoff–Hamman approximation.[31] For this purpose, densities of states were integrated over the energy ranges of 0.0 eV (the Fermi energy) to −0.2, −0.4, −0.5, −0.8, and −1.0 eV. The negative signs, which reflect the negative tunneling voltages (V_t) chosen in the experiments, correspond to occupied states. The charges were calculated in steps of 0.1 Å above the uppermost O atoms in a range from 1.6 to 3.6 Å, and the resulting charge grids were then linearly interpolated to compute the images. Good agreement with the experimental constant height images was obtained for the integration range of 0.0 to −1.0 eV and a distance of 2.5 Å. The experiments only showed minor variations of the contrast between $V_t = -0.2$ and −1.6 V, and we note that the absolute tunneling distance is not an experimentally available parameter.

RESULTS AND DISCUSSION

DFT calculations

We first present the high-coverage structure models analyzed by DFT and then compare these models with the STM data. The

calculations were numerically demanding because of the relatively large unit cells and the correspondingly high number of molecules in the cells. An analysis of all possible CO configurations was, therefore, not feasible. To reduce the number of possibilities, we used the $\left(2\sqrt{3} \times 2\sqrt{3}\right)R30°$-CO structure ($\Theta = 0.58$ ML) for which a validated structure model exists to define elements that a stable high-coverage structure most likely contains. The $\left(2\sqrt{3} \times 2\sqrt{3}\right)R30°$ structure belongs to the class of cluster models mentioned above.[11,12] It is formed by clusters consisting of seven CO molecules, one central molecule in an upright position, and a ring of six surrounding molecules that are slightly tilted away from the center [Fig. 2(a)]. Rows of CO-free Ru atoms separate these clusters. At the junctions of three empty Ru rows, three CO molecules form triangles with $\sqrt{3}a$ long edges [blue mark in Fig. 2(a)]. We find that these triangle configurations significantly contribute to the local stability of the structure. This can be seen, e.g., by the 0.22 eV energy increase when a CO molecule is moved from the triangular edge of the 7 CO cluster to the center of the triangle. The $\left(2\sqrt{3} \times 2\sqrt{3}\right)R30°$ structure is quite stable, and one can remove several CO molecules without destabilizing it. For example, the CO structure at $\Theta = 0.47$ ML is formed from CO-deficient clusters but still follows the same construction principle.[12]

To model the CO layer at higher coverages than 0.58 ML, the following assumptions were made: CO molecules exclusively occupy the on-top sites at all coverages, a condition based on the corresponding findings by vibrational spectroscopy.[15,16] When the coverage is increased, the layer maintains a cluster structure, but the internal structures and/or sizes of the clusters change. The clusters are separated by one-atom-wide rows of unoccupied, or only partially occupied, Ru atoms. These non-covered Ru sites allow the molecules to relax the stress in the densely packed clusters. Larger, empty areas are not permitted. The CO triangles at the junctions of the empty rows are preserved in all models, which puts limits on possible arrangements, sizes, and shapes of the clusters. When, upon a coverage change, a new distribution of junctions becomes energetically favored, the CO molecules are assumed to regroup immediately; kinetic restrictions are not considered because of the low hopping barrier of CO. 88 CO configurations were investigated in the coverage range from 0.58 to 0.77 ML and tested for their stabilities; energies are plotted in Fig. 4 as a function of the CO coverage. At a given CO coverage, a configuration with lower relative adsorption energy [Eq. (1)] corresponds to a more stable structure.

We probed the energetics of three types of models that satisfy the mentioned assumptions. The first type of model consists of compact clusters of increasing size. Figures 2(a)–2(f) show the first six of these configurations, with clusters consisting of 7, 10, $2 \times 12 + 7$, 14, $2 \times 16 + 10$, and 19 CO molecules, with internal pseudo (1×1) configurations in all cases. The models correspond to coverages between $\Theta = 0.58$ and 0.70 ML. Models only consisting of 12-CO or 16-CO clusters cannot be constructed within the given constrictions, and one 7-CO or 10-CO cluster, respectively, has to be added to the unit cells. A model with 37-CO clusters ($\Theta = 0.77$ ML) has also been considered; it was formed from the 19-CO cluster model by adding a complete ring of CO molecules around the 19-CO clusters (not shown).

After optimization, the DFT calculations show that, except for the CO molecules at the cluster centers, the molecules are no longer
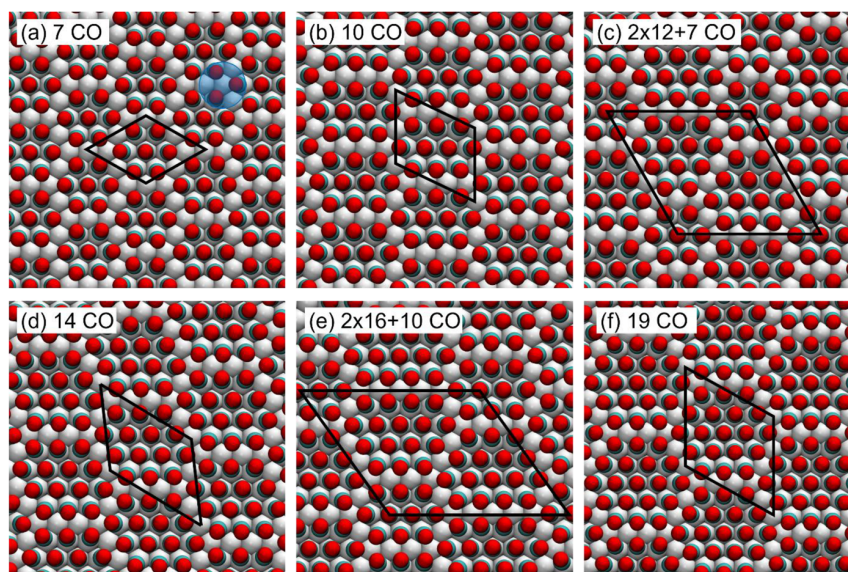
FIG. 2. Structures of the first six cluster models (model type 1) analyzed by DFT. Red balls are the O atoms, petrol balls are the C atoms, gray balls are the Ru atoms, and black rhombuses are the unit cells. The blue circle in (a) marks a CO triangle. Coverages: (a) 0.583 ML, (b) 0.625 ML, (c) 0.633 ML, (d) 0.667 ML, (e) 0.667 ML, and (f) 0.704 ML.

exactly on-top of the Ru atoms. The C atoms are displaced from the centers of the Ru atoms by distances that increase with the size of the clusters to a value of 0.7 Å. There are also deviations of the molecular axes from the surface normal. The molecule at the center of a cluster is in an upright position, but the surrounding molecules are tilted outward by an angle that increases with increasing distance from the cluster center. The maximum tilt at the rims is $16°$. Shifts and tilts are caused by the dense pseudo (1×1) packing of the CO molecules in the clusters. Figure 4 shows the relative energies of these models (pink hexagons). The energy increases almost linearly with coverage, which reflects the increasing average repulsion with increasing cluster size.

The data contain information about the question of whether the relative positions of the triangles, which are formed by the CO molecules at the edges of the clusters, play a role. As shown in Fig. 2, each model of this type has a different periodicity of CO triangles. On the other hand, two pairs of different models almost have the same CO coverage. The $2 \times 12 + 7$- and the 10-CO models have CO coverages of 0.633 and 0.625 ML, and the $2 \times 16 + 10$ and the 14-CO models even have identical CO coverages of 0.667 ML. The coverages of triangles (also in ML units, i.e., average numbers of triangles per Ru atom) are also almost pairwise identical: 0.122 and 0.125 ML for the $2 \times 12 + 7$- and the 10-CO models, and 0.095 ML for the $2 \times 16 + 10$- and the 14-CO models. Figure 4 shows that these pairs of models almost have the same energy. This fact shows that the stability of the models of this type is mainly determined by the overall CO coverage. It does not play a significant role whether the model contains clusters of one size or two different sizes and how the triangles are arranged with respect to each other. The effect of the CO

triangles is a local one; it does not extend to the nearest neighbor triangle.

The second type of model is based on interstitial CO molecules in the $\left(2\sqrt{3} \times 2\sqrt{3}\right)R30°$-CO structure. In these models, the 7-CO clusters were kept in their original positions, and additional CO molecules were filled in. The simulations were performed on $\left(4\sqrt{3} \times 4\sqrt{3}\right)R30°$ unit cells that contain four of the 7-CO clusters. Figures 3(a)–3(c) show configurations created by adding one, two, and three CO molecules to this cell. The additional molecules occupy sites on the empty Ru rows where they have four CO neighbors. In this way, bridges between neighboring clusters are formed. Various configurations of this type were explored by moving the added CO molecules between the empty Ru sites. The positions of the 7-CO clusters were left unchanged. To create higher coverages, the sites inside the CO triangles were also occupied. In this way, the number of connected clusters is minimized, and new, larger clusters are created. The resulting larger clusters mostly appear in triangular shapes with concave edges.

Figure 4 (blue squares) shows that, for each coverage, the energies of the models of this second type vary depending on the exact local configurations. At coverages below 0.63 ML, the most stable configurations are energetically comparable to the first type of model (pink hexagons) at the same coverages. Hence, adding a small number of CO molecules to the $\left(2\sqrt{3} \times 2\sqrt{3}\right)R30°$-CO structure does not necessarily lift the 7-CO cluster structure. However, as the coverage is increased to ≥0.67 ML, all considered structures based on the 7-CO cluster model become less stable than the structures based on the compact, larger clusters.
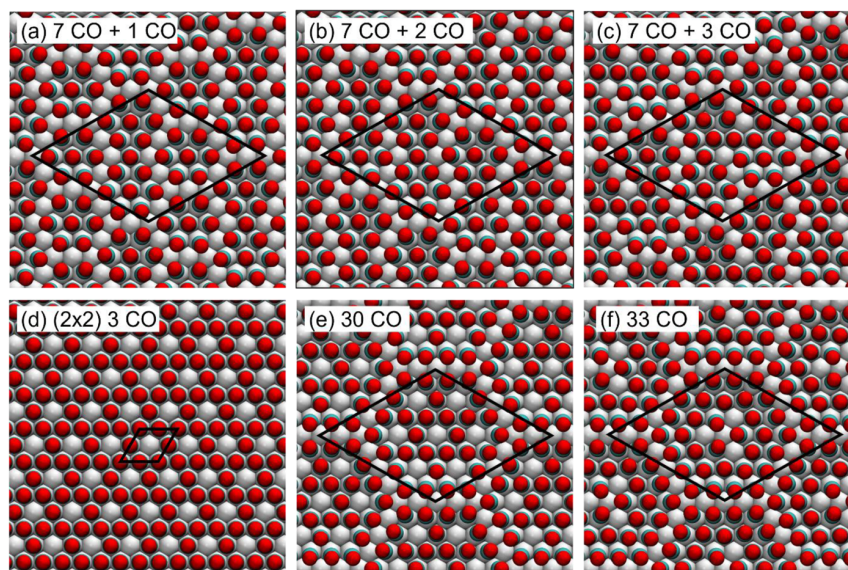
FIG. 3. Structures of model types 2 and 3 analyzed by DFT. Color code as shown in Fig. 2. Figures 3(a)–3(c) are structures of model type 2, with one, two, and three added CO molecules to the $(2\sqrt{3} \times 2\sqrt{3})R30°$ structure. Coverages: (a) 0.604, (b) 0.625 ML, and (c) 0.646 ML. (d)–(f) Are structures and modified structures of model type 3. Coverages: (d) 0.750 ML, (e) 0.625 ML, and (f) 0.688 ML.
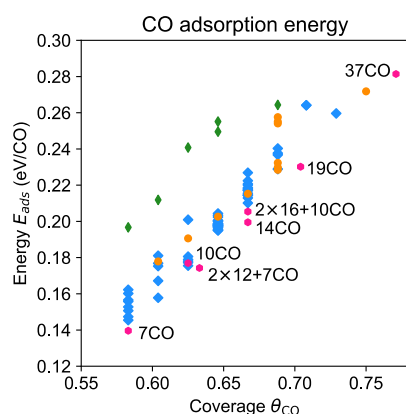
FIG. 4. CO adsorption energies calculated for the three models investigated by DFT as a function of the CO coverage. The values are relative to the adsorption energy of an isolated adsorbed CO molecule. Pink hexagons: model type 1, blue squares: model type 2, green diamonds: model type 3, and orange dots: modified type 3 model.

The third type of model is based on a (2×2)-CO structure in which the CO molecules form a honeycomb network of open rings, corresponding to a coverage of 0.75 ML [Fig. 3(d)]. To derive models from this structure, CO molecules were removed, and the remaining molecules were rearranged to form clusters with an internal (2×2) structure. As for the other two model types, the clusters were arranged such that their edges form CO triangles. Again, a

$(4\sqrt{3} \times 4\sqrt{3})R30°$ simulation cell was used. An example with seven open rings inside the clusters is shown in Fig. 3(e) ($\Theta = 0.625$ ML). It is found that all configurations derived from this model type are less stable than the other two models (Fig. 4, green diamonds). Vacancies in the (2×2) matrix just cause CO disorder in the whole simulation cell, whereas a symmetric distribution of CO vacancies can lead to a cluster configuration. We have also modified the internal structure of the clusters by replacing the (2×2) rings with CO triangles [Fig. 3(f)], which leads to intermediate models between the third and the first type. These structures are more stable than those with (2×2) rings, and they can be further stabilized by shifting CO molecules to new sites, locally restoring 7-CO clusters. The energies (Fig. 4, orange dots) become similar to those of the 7-CO cluster models.

However, when one considers the full range of coverages from 0.58 to 0.77 ML, the models formed by compact clusters have the lowest energies.

STM results

Figure 5(a) shows an STM image of the high-coverage CO layer recorded at 62 K in the standard constant current mode. One can see structure elements of various sizes arranged in a partially ordered hexagonal pattern with a periodicity of ~12 Å. The rows of structure elements are roughly aligned to the $\sqrt{3}$ directions of the Ru surface, but because of the uneven sizes and shapes of the features, the rows are not exactly straight, and the directions of the rows deviate by small angles from the crystallographic $\sqrt{3}$ directions. The features themselves display an internal fine structure of dark dots, the numbers of which vary from one for the smallest feature to seven for the
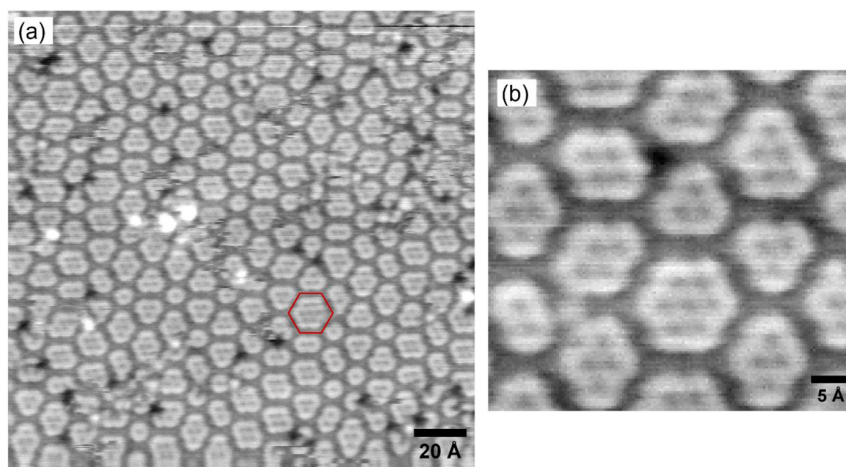
FIG. 5. STM images of the high-coverage CO structure on Ru(0001). (a) Constant current STM image of the CO saturated surface at 62 K. Tunneling voltage (V_t) = −1.0 V, tunneling current (I_t) = 1 nA, and image size 178 × 175 Å². The few small black spots are some N or O atoms. (b) Detail of a constant current STM image of the CO saturated surface at 62 K. V_t = −1.0 V, I_t = 1 nA, and image size 49 × 46 Å².

largest (one is marked red). Figure 5(b) shows that the dark dots inside the features form a hexagonal structure; spacings are 3.3 Å, and directions are the close-packed directions of the Ru surface, corresponding to a pseudo (1 × 1) structure.

A moiré structure can be ruled out by these observations. Moiré structures would display extended hexagonal, periodic patterns superimposed by a continuous hexagonal fine structure. The actually observed structure is only poorly ordered, and the hexagonal fine structure is restricted to the interiors of the features, which is in conflict with this expectation. Similarly, antiphase domain boundary models can be ruled out. Regardless of the exact arrangements of the CO molecules in such a model, STM images would display extended one-dimensional features rather than the quasi-hexagonal pattern actually seen.

The general appearance of the STM data suggests a cluster model. Of the three types we have investigated by DFT, we can rule out models with interstitial CO molecules in the preserved $(2\sqrt{3} \times 2\sqrt{3})R30°$-CO structure. The $(2\sqrt{3} \times 2\sqrt{3})R30°$ lattice is clearly lifted. Cluster models with internal (2 × 2) or $\sqrt{3}$ structures are in conflict with the observed pseudo (1 × 1) fine structure. The only remaining model is the first type, which consists of compact clusters with an internal pseudo (1 × 1) structure. If this model is correct, the dark dots within the structure elements would represent the innermost CO molecules of the clusters, and the dark spaces between the features would represent the more strongly tilted molecules at the rims.

To test this interpretation, we have simulated constant-height STM images. An experimental constant-height image is shown in Fig. 6 (center). It was recorded with a negative tunneling voltage, which, in the constant-height mode, leads to an inverted contrast from the images recorded in the constant-current mode (Fig. 5). Accordingly, the fine structure of the features is formed by bright

dots, and the spaces between the features are formed by almost continuous bright stripes.

The panels around the STM image are the simulated constant-height images from the six cluster models in Fig. 2, also with inverted contrast. Considering, e.g., the simulated image of the 19-CO model, one can see structure elements with seven internal bright dots and bright, almost smooth spacings between the elements. The internal bright dots are at the positions of the seven innermost CO molecules, and the bright space is close to the positions of the 12 tilted outer molecules. The rows of unoccupied Ru atoms between the clusters do not provide any additional contrast. In the experimental image, the same structure elements, with seven bright dots and bright spacings, can be found, which can, therefore, be interpreted as 19-CO clusters (see the mark). These are the largest elements observed. Similarly good agreement between the simulations and the experiment is found for the smaller clusters of the five other configurations in Fig. 2 and the structure elements in the STM. Almost all features in the experiment have corresponding counterparts in the simulations. This agreement is strong evidence that the model of compact pseudo (1 × 1) clusters, with relaxed positions and tilting angles of the molecules, describes the structure correctly.

Figure 7 shows the resulting structure model for a section of the STM image in Fig. 6 (black rectangle). Quite clearly, the high-coverage CO structure on Ru(0001) belongs to the class of cluster models, such as the $(3\sqrt{3} \times 3\sqrt{3})R30°$ structure on Ir(111) and the $(2\sqrt{3} \times 2\sqrt{3})R30°$ structure on Ru(0001).[10,11] However, in contrast to an ideal cluster model, the clusters on Ru(0001) display distributions of sizes and orientations, and their arrangements are not exactly periodic. Nevertheless, the configurations of the clusters are not random but follow strict "tiling rules." There is only a limited set of different clusters, and the relative orientations are such that between two neighboring clusters, a one-atom-wide row
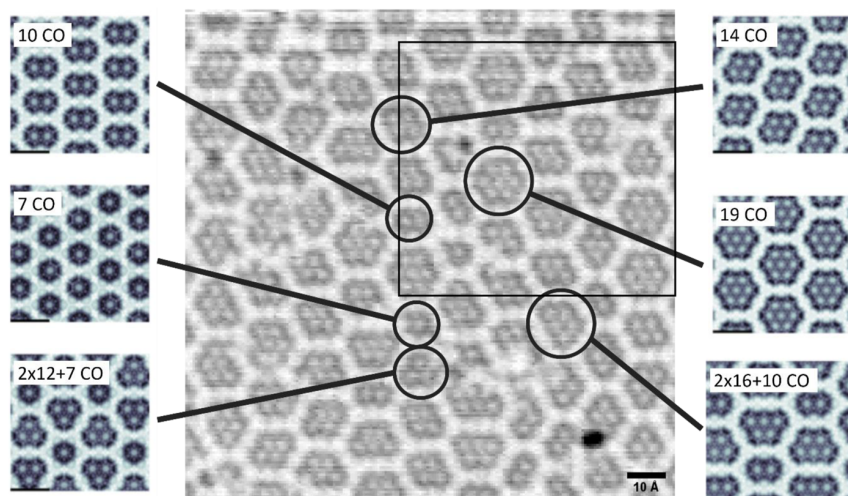
FIG. 6. STM image and comparison with simulated images. Center: Constant height STM image of the CO-saturated surface at 62 K. $V_t = -1.4$ V, $I_t = 3$ nA, and image size 126×126 Å^2. Outer panels: Simulated constant height images for the six structure models in Fig. 2 (integration range 0.0 to -1.0 eV, distance from the O atoms 2.5 Å). The black rectangle is the region shown in Fig. 7.
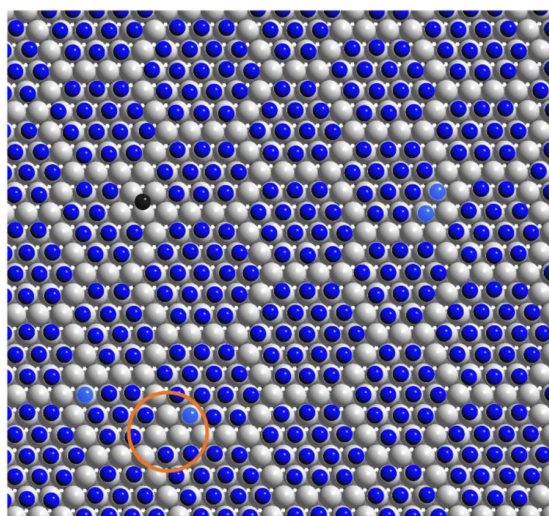
FIG. 7. Model of the CO layer on the Ru(0001) surface at saturation (black rectangular region in Fig. 6). Blue balls are CO molecules, and gray balls are Ru atoms. Shown in light blue are some CO molecules, the positions of which are unclear. The orange circle marks an area where the CO molecules do not form a triangle configuration. The STM image (Fig. 6) shows instabilities in this area.

of empty Ru atoms is left. At the edges between three neighboring clusters, the CO molecules form triangle configurations. In the entire area of Fig. 7, there are only a few locations where the edges do not form such triangles (one is marked orange), and just there the STM shows instabilities, probably caused by site exchanges of CO molecules. This model is in agreement with all previous findings:

The molecules only occupy on-top sites in agreement with the vibrational spectra;[15,16] most of the molecules are tilted, which agrees with the ESDIAD data;[20] and the CO saturation coverage, determined by counting the clusters in the STM images, is 0.66 ML, in good agreement with the previously measured values of 0.65 and 0.66 ML.[13,14]

To test the stability of the structure, the temperature was raised in steps of ~30 K, starting at 62 K, up to room temperature. Until 281 K, the structure was continuously well resolved by the STM without any enhanced fluctuations of the cluster features. At 298 K, the structure had disappeared, most likely because a fraction of the CO layer had desorbed. These observations contrast with our previous experiments on the partial $\left(2\sqrt{3} \times 2\sqrt{3}\right)R30°$-CO structure,[12] which showed a defined structure at 70 K but structureless images at $T \geq 239$ K, although no CO has been lost by desorption. This fact was explained by the order–disorder transition observed in previous LEED experiments,[14] connected with an enhanced mobility of the molecules. The high-coverage structure of the present study does not undergo such an order–disorder transition, which also agrees with previous LEED results.[14]

A previous study by near-ambient pressure x-ray photoelectron spectroscopy (NAP-XPS) indicated that at 300 K under a constant CO pressure of 1 Torr, a bridge-bonded CO might exist on Ru(0001) in addition to the on-top CO.[32] In our experiments, a temperature of 300 K could not be adjusted without desorbing part of the CO, so we cannot comment on such a possibility.

Simulations of the diffraction pattern

What remains to be clarified is the interpretation of the LEED data. As mentioned in the introduction, the LEED pattern suggested a moiré structure.[13,14] To make sure that the CO layer in our experiments is comparable with these studies, we have performed
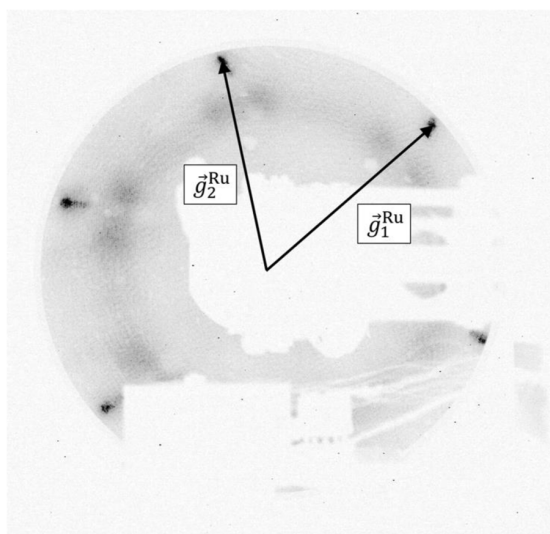
**FIG. 8.** LEED pattern of the CO-saturated Ru(0001) surface. Electron energy = 50 eV and T = 150 K. The splitting of the substrate spots results from a defect in the electron gun. $\vec{g}_1^{Ru}$ and $\vec{g}_2^{Ru}$ are the reciprocal basis vectors of the Ru surface. The six spots close to the origin are behind the manipulator.

some own LEED measurements. CO was dosed like in the STM experiments in two portions, the first at room temperature, the second during cooling, and only the final temperature was not as low because the sample, which was mounted to the manipulator in these experiments, was cooled by liquid N_2 instead of He. Figure 8 shows the LEED pattern at 150 K. One can see two broad diffraction spots close to the Ru substrate spots, at the same positions as in the schematic LEED pattern of Fig. 1(a).[13,14] It can be concluded that we have prepared the same structure.

To simulate the LEED pattern, we Fourier-transformed our STM data; Fig. 9(a) shows the result for the STM image in Fig. 6. Around the origin one can see a hexagonal, periodic pattern of spots that represent the first Fourier components of the quasi-hexagonal configuration of the cluster features. However, the outermost six groups of pairs of spots (one group is marked) are different; they are somewhat displaced with respect to the (reciprocal) lattice one can construct from the inner spots.

To better understand these displacements, we constructed a strongly simplified model of the STM image and then Fourier-transformed this model (Fig. 10). The model consists of simple dots drawn at the positions of the internal hexagonal features of the clusters in Fig. 6. Figure 10(a) shows the positions as black dots. The atoms of the Ru surface are not visible in the STM image, but the substrate lattice (blue dots) can be constructed using other observations. From the lattice constant of Ru (2.706 Å) and the periodicity of the fine structure of the clusters (3.3 Å), we know that the substrate lattice constant should be 82% of the spacing between the black dots. The rotational angle of the Ru lattice with respect to the STM image we know from previous experiments with the $\left(\sqrt{3} \times \sqrt{3}\right)R30°$-CO
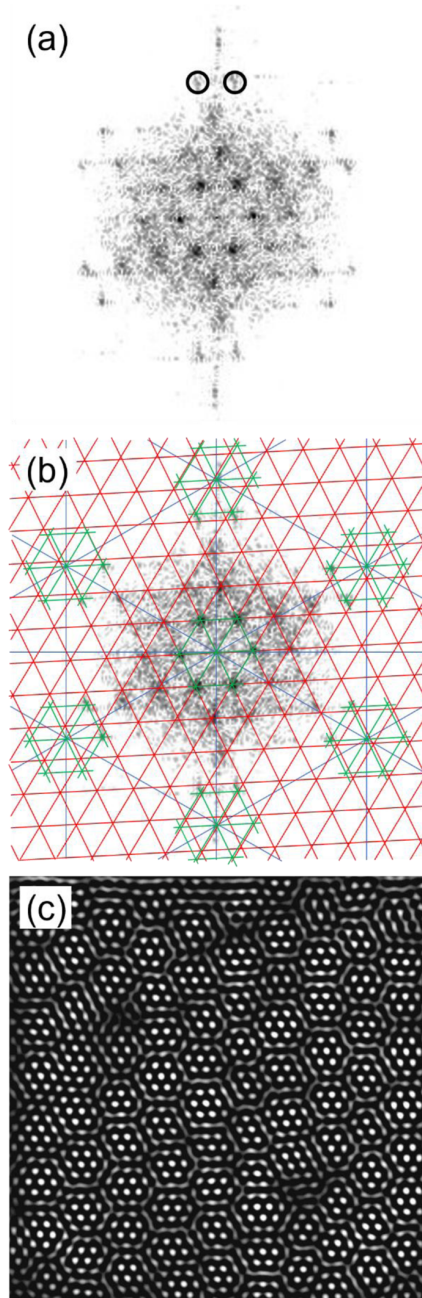
FIG. 9. Fourier analysis of the STM data. (a) Fourier transform of the constant height STM image in Fig. 6. The two marked spots are displaced from the lattice defined by the inner spots. (b) Same Fourier transform as in (a) with superimposed line grids. Red line grid: reciprocal lattice of the cluster pattern, blue line grid: reciprocal lattice of the substrate, and green hexagons: first order spots of the cluster pattern. (c) Fourier back transformation of the combined marked spots in (a) and equivalents.

17 December 2024 10:31:24
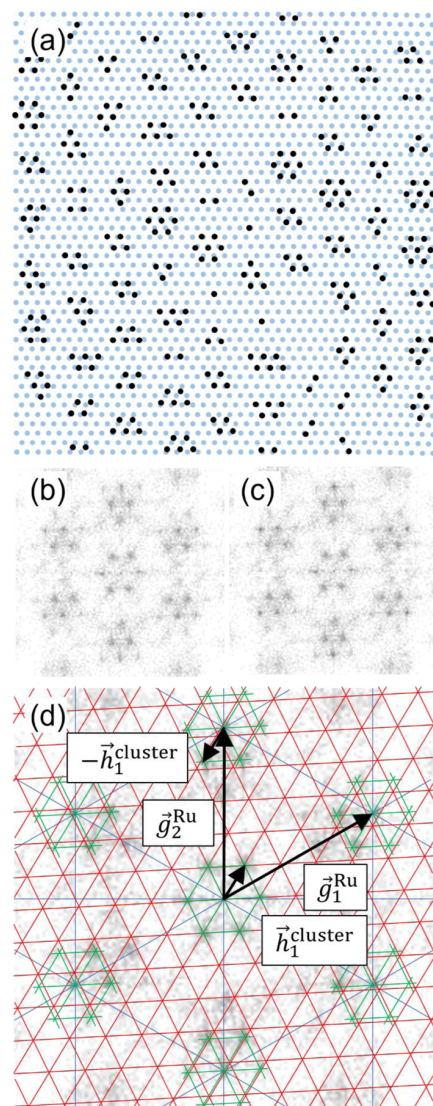
FIG. 10. Fourier analysis of a dot model. (a) Dot model of the STM image in Fig. 6. Black dots are the positions of the dots of the internal fine structure of the clusters; blue dots are the Ru atoms of the substrate. (b) Fourier transform of the black dots in (a) without the blue dots. (c) Fourier transform of the black dots together with the blue dots. (d) Same Fourier transform as (b) with a superimposed line grid. $\vec{g}_1^{Ru}$ and $\vec{g}_2^{Ru}$ are the reciprocal basis vectors of the substrate, and $\vec{h}_1^{cluster}$ is a reciprocal basis vector of the quasi-hexagonal cluster lattice. Color code as shown in Fig. 9(b).

structure and from the orientation of the internal fine structure of the clusters. The lateral relative positions of the blue and black dots we know from the fact that the centers of the clusters should be on top of the Ru atoms. As shown in Fig. 10(a), with the substrate lattice constructed in this way, the center dots of most of the clusters, in fact, pretty well fall on the positions of blue dots.

This model was then Fourier-transformed, in one case [Fig. 10(b)] by using the black dot pattern in Fig. 10(a) only, without the blue dots, which reflects the actual situation in the STM image, and in the other case [Fig. 10(c)] by using the superposition of both dot patterns in Fig. 10(a). [Note the somewhat surprising fact that the two Fourier transforms are very similar; only the spot intensities are different. This similarity can be understood by the fact that in real space, the spacings between all cluster centers are multiples of the lattice spacings of the substrate; see Fig. 10(a), so that the Fourier transform contains components of the substrate lattice even in the absence of an explicit substrate lattice.]

In both cases, the Fourier transforms show groups of spots, with a central group consisting of six spots around the origin and six groups further outside with similar internal hexagonal arrangements of spots as the central group. Figure 10(d) shows the same Fourier transform as Fig. 10(b) with superimposed reciprocal lattices and lattice vectors to identify the spots. The lattice of blue lines is constructed from the reciprocal lattice vectors $\vec{g}_1^{Ru}$ and $\vec{g}_2^{Ru}$ at the positions of the first order spots of the Ru substrate. The green hexagons around the origin and around the first order substrate spots are constructed from the reciprocal lattice vectors $\vec{h}_1^{cluster}$ (and its symmetry equivalents) of the quasi-hexagonal lattice of the clusters. The red lattice is constructed by periodically repeating the lattice points of the green hexagon at the origin. Further outside, one can see that this red lattice does not coincide with the first order substrate spots (at $\vec{g}_1^{Ru}$ and $\vec{g}_2^{Ru}$) and also not with the green hexagons around these spots. In real space, this means that the quasi-hexagonal cluster lattice is not a simple superstructure with lattice vectors given by small integer combinations of substrate vectors.

In reciprocal space, one could successively superimpose finer grids than the red one to make the outer spots finally coincide with such a grid. In real space, this would correspond to successively larger periodicities comprising several clusters. This method has been applied to construct the unit cells of CO moiré structures on the Co(0001) surface.[33] However, after applying the first two finer grids, small displacements still remain. In such a case, when small but significant displacements from periodic lattices remain after applying successively finer grids, an effect also known from moiré structures,[33] the corresponding structure is practically incommensurate. For the present system, this is actually an unexpected result. Incommensurate superstructures are usually associated with moiré structures, which are determined by intra-layer interactions, so the registry with the surface is less important. Here, CO forms an incommensurate superstructure, although all molecules are in an approximate registry with the substrate. The (average) incommensurability results from the fact that the clusters display a distribution of sizes and shapes.

We then transferred the line grids constructed in Fig. 10(d) to the Fourier transform of the experimental image [Fig. 9(b)], without any adjustments except for the overall size. Perfect matching with the spots is found, confirming that the dot pattern in Fig. 10(a) describes the order in the STM image well. The displaced green hexagons around the first order substrate spots in Fig. 9(b) fall on the outer six groups of spot pairs, showing that these spots come from the incommensurate, quasi-hexagonal arrangement of the clusters. These spot pairs contain a considerable amount of information about the structure; the Fourier back transformation of the

12 spots, with small windows around them, provides a real-space image [Fig. 9(c)] that already contains major features of the actual STM image (Fig. 6).

With this analysis, re-interpretation of the LEED pattern is straightforward. The pairs of the most intense superstructure spots close to the first order substrate spots [Fig. 1(a)] are not caused by diffraction at a periodic hexagonal CO layer, which does not exist in the cluster model. In the cluster model, these spots are caused by multiple scattering at the substrate ($\vec{g}_i^{Ru}$) and the quasi-hexagonal lattice of the clusters ($\vec{h}_j^{cluster}$); see Fig. 10(d). The six spots around the origin are caused by scattering at the cluster lattice only ($\vec{h}_j^{cluster}$). The ratio of the lengths of vectors, $\left|\vec{h}_j^{cluster}\right|/\left|\vec{g}_i^{Ru}\right|$, as extracted from the Fourier transform, varies somewhat around 0.22 depending on directions. This value is close to the value of 0.23 for a perfect $\left(5\sqrt{3}\times 5\sqrt{3}\right)R30°$ structure, the structure proposed on the basis of the LEED pattern.[13] However, the small difference is significant and a result of the fact that the actual structure is incommensurate. The reported continuous shifts of the LEED spots with varying CO coverage[13,14] can also be explained by the incommensurability. Finally, the large width of the superstructure LEED spots can be explained by the ill-defined periodicity of the structure, which leads to variations across the macroscopic surface area illuminated by the LEED beam.

CONCLUSIONS

In this study, high-coverage structures of CO on the Ru(0001) surface have been investigated by means of DFT and STM. 88 structure models of three different types, with coverages between 0.58 and 0.77 ML, have been analyzed by DFT. In all models, the CO molecules occupy on-top sites. We find that the most stable type of model consists of clusters formed by compact, small islands of 7–37 CO molecules with an internal pseudo (1×1) structure. The clusters are separated by rows of empty Ru atoms, which allow the molecules to lower their repulsive interactions through relaxations. In all structures, the clusters are arranged such that three CO molecules at the edges between three clusters form triangles with $\sqrt{3}a$ long edges. This structure element considerably contributes to the stability of the structures. The CO molecules in the centers of the clusters are exactly on top of the Ru atoms and bonded in an upright position, whereas the outer molecules are shifted from the Ru atoms by up to 0.7 Å and have molecular axes tilted by up to 16°.

STM data were recorded after saturating the surface with CO at temperatures between 60 and 70 K. The images show approximately hexagonal configurations of features with an internal hexagonal fine structure. STM images were simulated by applying the Tersoff–Hamann approximation to the most stable model,[31] and good agreement with the features observed by STM was found. The features can, therefore, be interpreted as the CO clusters predicted by DFT. The internal pseudo (1×1) fine structure can be interpreted as the innermost CO molecules and the smooth spacings between the clusters as the CO molecules at the rims. In the experiment, the clusters display a distribution of sizes ranging from 7- to 19-CO clusters, and, as a consequence, the configuration is not exactly hexagonally ordered. However, the arrangement is not random but governed by tiling rules that determine the relative orientations of the clusters,

namely, that one-atom-wide empty rows have to be left between the clusters and that the edges have to be formed by CO triangles. STM annealing experiments showed that the structure remains ordered up to 281 K.

The on-top positions of the molecules in the model agree with the results of previous HREELS and RAIRS studies.[15,16] The tilting of the molecules agrees with observations by ESDIAD,[20] and the saturation coverage of 0.66 ML agrees with the previously reported values.[13,14] The Fourier transform of the STM data shows spots at the positions of the most intense superstructure spots observed in previous LEED investigations and reproduced in the present study.[13,14] According to the cluster model, these spots are not caused by diffraction at a hexagonal CO layer forming a moiré structure but by multiple diffraction at the substrate and the quasi-hexagonal cluster lattice.

In the classification of high-coverage CO structures on hexagonally close-packed transition metal surfaces, the structure belongs to the class of cluster models. It differs from ideal cluster models by its incommensurability with the substrate lattice, which is a result of the variation in size and shape of the clusters. The fact that the CO layer does not form a mixed site or moiré structure can be explained by the relatively high energy difference of 0.3 eV between the on-top and the other adsorption sites. The fact that it does not form an antiphase domain boundary structure can be explained by the fact that in these models, the molecules can relax from their exact on-top configurations only in one dimension rather than in the two dimensions possible for compact clusters.

ACKNOWLEDGMENTS

AUTHOR DECLARATIONS
Conflict of Interest

The authors have no conflicts to disclose.

Author Contributions

Hannah Illner: Conceptualization (equal); Investigation (equal); Visualization (equal); Writing – original draft (equal); Writing – review & editing (equal). **Sung Sakong**: Conceptualization (equal); Investigation (equal); Visualization (equal); Writing – original draft (equal); Writing – review & editing (equal). **Axel Groß**: Funding acquisition (equal); Supervision (supporting); Writing – review & editing (equal). **Joost Wintterlin**: Conceptualization (equal); Supervision (lead); Writing – original draft (equal); Writing – review & editing (equal).

DATA AVAILABILITY

The data that support the findings of this study are available from the corresponding author upon reasonable request. The

optimized atomic coordinates of the DFT calculations are openly available in Zenodo at https://doi.org/10.5281/zenodo.10784616.

REFERENCES

[1] B. Böller, P. Zeller, S. Günther, and J. Wintterlin, ACS Catal. **10**, 12156–12166 (2020).

[2] S. R. Longwitz, J. Schnadt, E. K. Vestergaard, R. T. Vang, I. Stensgaard, I. Stensgaard, H. Brune, and F. Besenbacher, J. Phys. Chem. B **108**, 14497–14502 (2004).

[3] J. P. Biberian and M. A. Van Hove, Surf. Sci. **138**, 361–389 (1984).

[4] V. Sumaria, L. Nguyen, F. F. Tao, and P. Sautet, ACS Catal. **10**, 9533–9544 (2020).

[5] H. Froitzheim, H. Hopster, H. Ibach, and S. Lehwald, Appl. Phys. **13**, 147–151 (1977).

[6] W. Braun, H. P. Steinrück, and G. Held, Surf. Sci. **575**, 343–357 (2005).

[7] M. Tüshaus, W. Berndt, H. Conrad, A. M. Bradshaw, and B. Persson, Appl. Phys. A **51**, 91–98 (1990).

[8] H. J. Yang, T. Minato, M. Kawai, and Y. Kim, J. Phys. Chem. C **117**, 16429–16437 (2013).

[9] C. J. Weststrate and J. W. Niemantsverdriet, J. Catal. **408**, 142–154 (2022).

[10] K. Ueda, K. Suzuki, R. Toyoshima, Y. Monya, M. Yoshida, K. Isegawa, K. Amemiya, K. Mase, B. S. Mun, M. A. Arman, E. Grånäs, J. Knudsen, J. Schnadt, and H. Kondoh, Top. Catal. **59**, 487–496 (2016).

[11] Q. Chen, J. Liu, X. Zhou, J. Shang, Y. Zhang, X. Shao, Y. Wang, J. Li, W. Chen, G. Xu, and K. Wu, J. Phys. Chem. C **119**, 8626–8633 (2015).

[12] H. Illner, S. Sakong, A. K. Henß, A. Groß, and J. Wintterlin, J. Phys. Chem. C **127**, 7197–7210 (2023).

[13] E. D. Williams and W. H. Weinberg, Surf. Sci. **82**, 93–101 (1979).

[14] H. Pfnür and H. J. Heier, Ber. Bunsenges. Phys. Chem. **90**, 272–277 (1986).

[15] G. E. Thomas and W. H. Weinberg, J. Chem. Phys. **70**, 1437–1439 (1979).

[16] H. Pfnür, D. Menzel, F. M. Hoffmann, A. Ortega, and A. M. Bradshaw, Surf. Sci. **93**, 431–452 (1980).

[17] M. Scheffler, Surf. Sci. **81**, 562–570 (1979).

[18] P. He, H. Dietrich, and K. Jacobi, Surf. Sci. **345**, 241–246 (1996).

[19] J.-S. McEwen and A. Eichler, J. Chem. Phys. **126**, 094701 (2007).

[20] W. Riedl and D. Menzel, Surf. Sci. **163**, 39–50 (1985).

[21] B. A. J. Lechner, X. Feng, P. J. Feibelman, J. I. Cerdá, and M. Salmeron, J. Phys. Chem. B **122**, 649–656 (2018).

[22] A. K. Henß, J. Wiechers, R. Schuster, V. Platschkowski, and J. Wintterlin, Jpn. J. Appl. Phys. **59**, SN1007 (2020).

[23] D. W. Goodman and J. M. White, Surf. Sci. **90**, 201–203 (1979).

[24] M. J. van Staden and J. P. Roux, Appl. Surf. Sci. **44**, 259–262 (1990).

[25] S. Marchini, S. Günther, and J. Wintterlin, Phys. Rev. B **76**, 075429 (2007).

[26] G. Kresse and J. Furthmüller, Phys. Rev. B **54**, 11169–11186 (1996).

[27] B. Hammer, L. B. Hansen, and J. K. Nørskov, Phys. Rev. B **59**, 7413–7421 (1999).

[28] P. E. Blöchl, Phys. Rev. B **50**, 17953–17979 (1994).

[29] S. Grimme, J. Antony, S. Ehrlich, and H. Krieg, J. Chem. Phys. **132**, 154104 (2010).

[30] D. Mahlberg, S. Sakong, K. Forster-Tonigold, and A. Groß, J. Chem. Theory Comput. **15**, 3250–3259 (2019).

[31] J. Tersoff and D. R. Hamann, Phys. Rev. B **31**, 805–813 (1985).

[32] D. E. Starr and H. Bluhm, Surf. Sci. **608**, 241–248 (2013).

[33] S. Günther, P. Zeller, B. Böller, and J. Wintterlin, ChemPhysChem **22**, 870–884 (2021).

17 December 2024 10:31:24

5.3.   Walk on a flickering path: Tracer diffusion of adsorbed O atoms on a Ru(0001) surface in the limit of CO saturation

The oxygen tracer diffusion studies in a CO adlayer on the Ru(0001) surface were completed by an investigation at CO saturation coverage under UHV below 27 °C. The study addressed the question how a saturated adsorption layer impacts diffusion and mobility of tracer atoms. An open question was whether the diffusion mechanism changes or whether the diffusion slows down.

The availability of empty sites, which are required for the fluctuation-driven door-opening mechanism is obviously reduced at saturation. Surprisingly, the experimental and theoretical study revealed an enhanced diffusion of the O atoms under these conditions. The key results of the publications are:

- Two adsorption geometeries of the oxygen atoms embedded in the compact cluster structre of CO on Ru(0001) are found experimentally: O atoms adsorb on hcp sites on the Ru(0001) surface in special configurations of CO molecules at the borders between three CO clusters ("junctions"), or at, what has been called "corridors" in the publication, at the borders between two clusters.

- Trajectories of the O atoms form a honeycomb pattern that reflects the cluster structure of the CO molecules on the surface. This pattern indicates that the O atoms move along the corridors between the compact CO clusters whereas the average positions of the CO clusters remain unchanged on the timescale of several minutes. CO fluctuations are visible in the STM movies as the shapes and sizes of the clusters change.

- The trajectories reveal that the O atoms do not move on a hexagonal lattice, but their diffusion paths are restricted by the CO clusters. A simplified model with a honeycomb lattice with two types of sites (junction sites and corridor sites) was constructed that fits the experimental data well. The obtained hopping frequencies are higher than in the previous studies at lower CO coverages (0.33 ML and 0.47 ML). The mobility of the O atoms at CO saturation coverage (0.66 ML) is enhanced, and the diffusion barrier is lower compared to O tracer diffusion at lower CO coverage.

- DFT calculations show that CO displacements at the high CO coverage cost more energy than at lower coverages which is due to the increased CO-CO repulsion and the reduced availability of empty sites. However, at the same time, the

O-CO repulsion is also induces, leading to a lower hopping barrier. This effect overcompensates the reduced CO fluctuations.

- The diffusion process is similar to the door-opening mechanism: CO fluctuations between the clusters open pathways for the O atom.

- It is concluded that the flluctuation-driven diffusion mechanism still operates at saturation. The assumption of high tracer mobility does not break down.

Author contributions:
Hannah Illner: Conceptualization, Investigation, Visualization, Software, Formal analysis, Data curation, Writing – original draft, Writing – review and editing.
Sung Sakong: Conceptualization, Investigation, Visualization, Writing – original draft, Writing – review and editing.
Axel Groß: Funding acquisition, Supervision (supporting), Writing – review and editing.
Joost Wintterlin: Conceptualization, Supervision (lead), Writing – original draft, Writing – review and editing.

Article

Walk on a Flickering Path: Tracer Diffusion of Adsorbed O Atoms on a Ru(0001) Surface in the Limit of CO Saturation

Hannah Illner, Sung Sakong, Axel Gross, and Joost Wintterlin*

Cite This: *J. Phys. Chem. C* 2025, 129, 18715–18726

Read Online

ACCESS | Metrics & More | Article Recommendations | SI Supporting Information

ABSTRACT: Previous work has shown that tracer diffusion of adsorbed O atoms on a CO-covered Ru(0001) surface is driven by fluctuations of the CO clusters. Here, a study is presented on the question of whether this diffusion mechanism is suppressed at CO saturation. Experiments were performed using high-speed scanning tunneling microscopy (STM). Hopping rates of O atoms were extracted from atomic trajectories, and an activation energy was determined from temperature-dependent data. The energetics of the embedded O atoms in the CO layer was evaluated by density functional theory (DFT). DFT was also used to determine the structures occurring during the O/CO exchange process. CO at saturation forms densely packed 2D clusters on the Ru(0001) surface, which is known from previous work. The present STM data show that the trajectories of the O atoms are restricted to the narrow gaps between the CO clusters but that the atoms still move by randomly hopping between neighboring hcp sites. The molecular structures of the clusters change as the O atoms move. Surprisingly, the mobility is higher than at lower CO coverages. DFT shows that, as an O atom jumps from an hcp site to a neighboring hcp site via an intermediate fcc site, several CO molecules at the edges of the clusters are displaced, leading to low-energy hopping pathways for the O atoms. The O atoms walk on "flickering paths" driven by fluctuations of the CO clusters. CO displacements cost more energy than at the lower coverages, but this effect is overcompensated by a reduced hopping barrier of the O atoms at the high CO coverage.
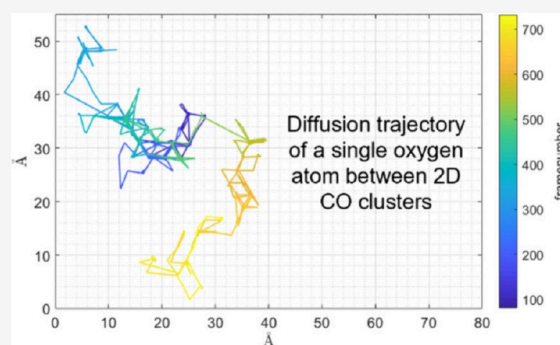
INTRODUCTION

Self-diffusion of adsorbed particles on a solid surface is a simple sequence of hopping events as long as the surface is largely empty and the particles only rarely collide with each other. In this limit, diffusion is described by a random walk of noninteracting single particles. However, in all applied surface processes, such as in heterogeneous catalysis, film growth, and electrode reactions, an adsorption layer is present and diffusion becomes complex. Even at low coverages, lateral interactions between the adsorbed particles play a role for diffusion, and at higher coverages collective site exchanges become dominant.[1]

Several scanning tunneling microscopy (STM) studies have shown how interactions between adsorbed particles may influence particle mobility on partially or fully covered surfaces. For example, at low coverages, O atoms adsorbed on a Ru(0001) surface and N atoms on an Fe(100) surface displayed hopping rates and directions that were considerably affected by interactions from single adsorbed atoms on neighboring sites.[2,3] The influence of neighboring atoms extended over several lattice constants. When adsorbed particles formed small groups or islands, collective jumps were observed. For example, chains of CO molecules on a Cu(110) surface were more mobile than individual molecules.[4]

On fully covered surfaces, diffusion of adsorbed particles is entirely mediated by collective processes. STM studies revealed several tracer diffusion mechanisms that have analogs in 3D solids.[5] For example, Pb atoms adsorbed on interstitial sites of a Ge(111) surface performed direct site exchanges with neighboring Ge atoms,[6] a mechanism discussed for 3D solids (although usually regarded as unfavorable because of the high activation barrier).[5] In and Pd atoms embedded in the top layer of a Cu(100) surface and Pb atoms in a Cu(111) surface moved by site exchanges with thermal vacancies in the terraces of the host lattices.[7−10] A vacancy mechanism is the most frequent diffusion process in 3D solids.[5] In an electrolyte solution, substitutional S atoms on a Br-covered Cu(100) surface showed exchange processes with neighboring Br atoms that resembled the so-called interstitialcy mechanism in 3D solids, and on the Cl-covered surface a ring-like exchange mechanism was observed, which is also known from 3D solids.[5,11]

In previous work, we have investigated tracer diffusion of O atoms through a CO layer on a Ru(0001) surface by means of

STM, density functional theory (DFT), and kinetic Monte Carlo (kMC) simulations.[12,13] At a coverage of $\Theta = 0.33$ monolayers (ML, defined as adsorbed particles per Ru surface atom), the CO molecules form an ordered $(\sqrt{3} \times \sqrt{3})R30°$ structure. However, the diffusion of O atoms through this 2D solid has no analog in 3D solids but proceeds by, as we called it, a door-opening mechanism. It is based on the much higher jump rates of CO molecules than of the O atoms, leading to structural fluctuations of the CO layer around a minimum energy configuration. The fluctuations frequently open low-energy paths on which an O atom can jump to a neighboring site. After the O atom has jumped, neighboring CO molecules quickly rearrange to the minimum energy configuration, completing an O/CO site exchange. The process is efficient, and the O atoms move through the CO layer almost as fast as on the empty Ru surface. Mechanisms of this type, which are based on a flexible matrix of coadsorbed particles, may be relevant for catalytic reactions as they justify the assumption of microkinetic catalysis models that surface diffusion is fast and not rate-limiting, regardless of coverage.

We further demonstrated that the O diffusion rate on the Ru(0001) surface was even higher at an increased CO coverage $(\Theta = 0.47$ ML).[14] The finding was explained by the disorder of the CO layer at this coverage, enabling yet faster fluctuations than in the ordered layer. In addition, the surface bonds of the O atoms are weakened by the stronger repulsive interactions between the O atoms and the CO molecules at the higher CO concentration. The O/CO site exchange still follows the door-opening mechanism, like in the ordered structure. In a further study, it was shown that O atoms at domain boundaries of the $(\sqrt{3} \times \sqrt{3})R30°$ structure, where the layer is disordered in narrow, fluctuating stripes along the boundaries, move faster by one order of magnitude than in the ordered domains, confirming the role of fluctuations.[15]

In all of these situations, a considerable fraction of the Ru atoms was empty, e.g., 2/3 of the sites in the $(\sqrt{3} \times \sqrt{3})R30°$ CO structure. Fluctuations happen easily, and this can explain why the diffusion mechanism is different from the known mechanisms in 3D lattices. An open question was therefore how the mechanism changes when the Ru surface is saturated with CO. Here we present a study in which we have approached this problem by increasing the CO coverage to $\Theta = 0.66$ ML, the saturation coverage under ultrahigh vacuum (UHV) below ≈300 K.

CO at saturation forms a relatively complicated structure on the Ru(0001) surface that has been solved only recently.[16] The structure consists of approximately hexagonal arrays of compact, 2D clusters that contain between 7 and 19 molecules. In the clusters, the CO molecules are densely packed, forming a pseudo (1×1) structure. Because of repulsive interactions between the CO molecules, only the CO molecules at the center of a cluster are exactly at on top sites and in upright positions, whereas the outer molecules are laterally displaced and tilted away from the center. Between the clusters, single-atom-wide rows of Ru atoms are not permanently occupied by CO because the shifted and tilted molecules at the adjacent clusters restrict the space in these "corridors". The structure remains thermally stable up to the onset of CO desorption at ≈300 K.

There appears to be hardly any free space for the fluctuation-driven diffusion of O atoms in this structure. One could, therefore, expect that the mechanism changes, possibly to one of the usual tracer diffusion mechanisms in 3D solids. Moreover, the mobility of the O atoms is expected to be reduced, possibly

even to a degree that the high mobility assumption of catalytic reaction models breaks down. However, as we show here, this is not the case. The O atoms are even more mobile than at the lower CO coverages and also on the clean surface. Experiments were performed by high-speed STM. Atomic trajectories were obtained from which hopping rates of the O atoms were extracted. From temperature-dependent measurements, activation barriers were determined. DFT calculations were used to analyze the energetics of the structures involved in the O/CO site exchanges. We propose that all findings can be explained by the door-opening mechanism that remains valid even in the restricted space of the CO-saturated surface.

■ EXPERIMENTAL SECTION

Experiments were performed in a UHV chamber (base pressure $<1 \times 10^{-10}$ mbar) on an (0001)-oriented Ru single crystal. A home-built STM setup was used that can work at imaging rates of up to 50 frames per second and can be operated at sample temperatures between 50 and 500 K.[17] The UHV chamber is additionally equipped with an Auger electron spectrometer (AES), a low-energy electron diffraction (LEED) system, an ion gun for sputtering, a quadrupole mass spectrometer (QMS), and a sample manipulator.

For surface preparation, the Ru crystal was routinely treated by cycles of Ar sputtering (1 keV Ar$^+$ ions for 10−15 min at room temperature), flash annealing to 1470 K, oxidation to remove residual carbon (by dosing 2×10^{-7} mbar O_2 for 10−15 min at 910 K or, at lower carbon coverages, by dosing 2−20 L of O_2 at 298−423 K; 1 L = 1.33×10^{-6} mbar s), and, finally, flash annealing to 1700 K. The cycles were repeated until the sample was clean according to AES. Because in AES the (strongly asymmetric) carbon KLL peak at 272 eV overlaps with the (symmetric) Ru MNN peak at 273 K, the coverage of residual C was determined indirectly, using the asymmetry of the experimental peak, which follows an established method.[18−20]

Directly before an experiment, the sample was flash-annealed to 623 K to remove any readsorbed particles. A low amount of O_2 was dosed (0.03−0.05 L) at 370 K to prepare a surface with a low coverage of adsorbed O atoms. Then 50 L of CO were dosed at 345 K which does not yet lead to CO saturation but protects the sample from adsorption of contaminants from the residual gas during cooling. The sample was then transferred to the liquid He-cooled sample holder of the STM setup, and while the sample cooled to 70 K, another 15 L of CO were dosed. This procedure led to saturation with CO $(\Theta = 0.66$ ML).[16]

For a diffusion experiment, a certain temperature was set in a range between 225 and 268 K; the range was limited by the time resolution of the experiment. When the temperature was sufficiently constant, recording by STM was started. Images were taken in the high-speed, constant height mode of the STM at 10 frames per second. Movies consisting of several thousand STM images were recorded. The data were analyzed by means of a multiscale wavelet-based algorithm that identifies and tracks the mobile O atoms.[21] O hopping rates were extracted from the obtained trajectories.

■ COMPUTATIONAL DETAILS

To determine the potential energy surfaces (PES) of the adsorbed O atoms and CO molecules, periodic DFT calculations were performed by means of the VASP software package.[22] The electronic wave functions were expanded up to 450 eV using a plane-wave basis set, and exchange-correlation

effects were computed using a revised version of the Perdew–Burke–Ernzerhof (RPBE) functional as suggested by Hammer and Nørskov.[23] The projector augmented wave (PAW) potential was employed to describe the ionic cores,[24] and Grimme's semiempirical D3 dispersion correction scheme was used for the van-der-Waals interactions between the adsorbed particles and between the adsorbates and the first layer of the Ru slab.[25−29]

The Ru(0001) surface was modeled by slabs consisting of three atomic layers with optimized Ru bulk lattice parameters a = 2.74 Å and c/a = 1.58. The slabs were separated by vacuum layers of 15 Å, and a compensating dipole field was used to correct for the surface dipole. The structures of the adsorbates and of the topmost Ru layer were fully optimized for local energy minimum configurations with a force convergence criterion of 0.01 eV/Å.

To construct the configurations of the O atoms on the CO-covered surface, information from the previous study on the CO cluster structure of the pure CO layer was used.[16] Figure 1(a)
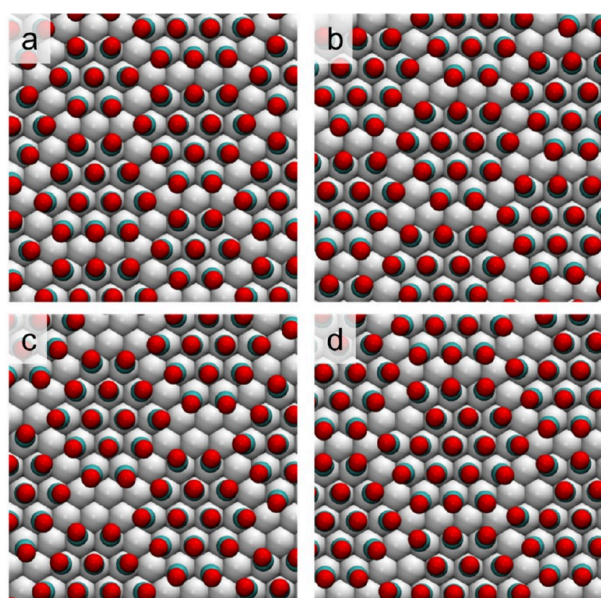
Figure 1. Four of the structure models treated by DFT. (a) Structure with two compact clusters of 12 CO molecules and one compact cluster of 7 CO molecules. (b) 12 CO cluster structure with twisted junctions. (c) 14 CO cluster structure with a vacancy block. (d) 18 CO cluster structure with a vacancy at a cluster edge. Red and turquoise spheres: CO molecules, gray spheres: Ru atoms. Further structures in Figure S1. [(a) is one of the models investigated in ref 16; coordinates available at 10.5281/zenodo.10784616].

shows, as an example, a configuration with two clusters of 12 CO molecules and one cluster of 7 CO molecules per unit cell. The model shows the on top positions of the center CO molecules, the displacements and tilts of the outer molecules, and the rows of empty Ru atoms ("corridors") between the clusters. The triangular CO configurations at the junction points of three corridors are particularly stable. Other cluster structures only differ in the number of CO molecules per cluster.[16]

For oxygen, previous work has shown that the atom occupies an hcp site and that all three Ru atoms forming the hcp site have to be free of CO molecules.[12−14] Combining this condition with the structure elements of the CO clusters leads to three types of

configurations, in which the average CO coverages are comparable to the saturation coverages of the pure CO layer. In the first configuration [Figure 1(b)], shown for a 12 CO cluster structure, one corridor junction per unit cell still has a triangular configuration, but every other junction has a "twisted", chiral configuration that provides a CO-free hcp site for an O atom. In the second configuration [Figure 1(c)], shown for a 14 CO cluster structure, both triangular configurations at the junctions are lifted, giving configurations in which vacancies with more than one hcp site are grouped together ("vacancy block"). In the third configuration [Figure 1(d)], shown for an 18 CO cluster structure, one CO molecule has been removed from an edge position of an original 19 CO cluster, providing a CO-free hcp site in a corridor.

Using these structure elements, surface unit cells consisting of 14, 18, 19, 23, 24, 27, and 30 Ru atoms in the top layer were constructed [Figure 1 and Figure S1]. In cases where single Ru atoms were bare, in addition to the corridor, triangular junction, and twisted junction sites, we also considered modified CO clusters by adding extra CO molecules. The first Brillouin zones of the unit cells were integrated using 5x5x1, 5x5x1, 5x5x1, 4x4x1, 4x4x1, 4x4x1, and 3x3x1 k-point meshes for the respective surface unit cells.

Adsorption energies of the O atoms on the bare Ru(0001) surface were between −2.55 and −2.61 eV with respect to gas phase O_2 for all unit cells. These low variations, despite the different sizes of the unit cells, indicate that the interactions between the O atoms are relatively weak. Obviously, the unit cells treated here are large enough that the O atoms are sufficiently separated, so that O coverage effects on the energies could be disregarded.

The energies of the various structures were therefore treated in terms of the respective CO adsorption energies E_{ads}. We define E_{ads} with respect to the energy of an isolated, adsorbed CO molecule on the bare Ru(0001) surface [eq 1]:

$$E_{ads} = \frac{E_{tot} - E_{slab} - n_{CO} E_{CO}^{(g)}}{n_{CO}} - E_{CO}^* \tag{1}$$

E_{tot} is the total energy of a slab with adsorbed O atoms and CO molecules, E_{slab} is the energy of an uncovered Ru(0001) or O/Ru(0001) slab depending on the presence of an O atom, $E_{CO}^{(g)}$ is the energy of a CO molecule in the gas phase, E_{CO}^* is the energy of an isolated, adsorbed CO molecule on a (6×6) lattice on the Ru(0001) surface, and n_{CO} is the number of the CO molecules in the cell. E_{CO}^* is −1.89 eV in this setup, which overestimates the experimental value by 0.3 eV.[29] However, by referring to E_{CO}^*, the adsorption energies E_{ads} only include the interactions between the adsorbed molecules; the overestimated adsorption energies of individual molecules cancel out. The activation barriers of the particle jumps were calculated by the nudged elastic band method with four images.[30]

To support the interpretation of the STM data, constant height images were simulated using the Tersoff-Hamman approximation.[31] Corresponding to the negative tunneling voltages (V_t) applied in the experiments, the densities of occupied states were integrated between the Fermi energy (0.0 eV) and energy values −0.2, −0.4, −0.5, −0.8, and −1.0 eV below E_F. Like in the previous study on the saturated, pure CO layer, the charges were calculated at distances between 1.6 and 3.6 Å above the O atoms of the CO layer in steps of 0.1 Å.[16] Images were computed by linearly interpolating the charge grids.
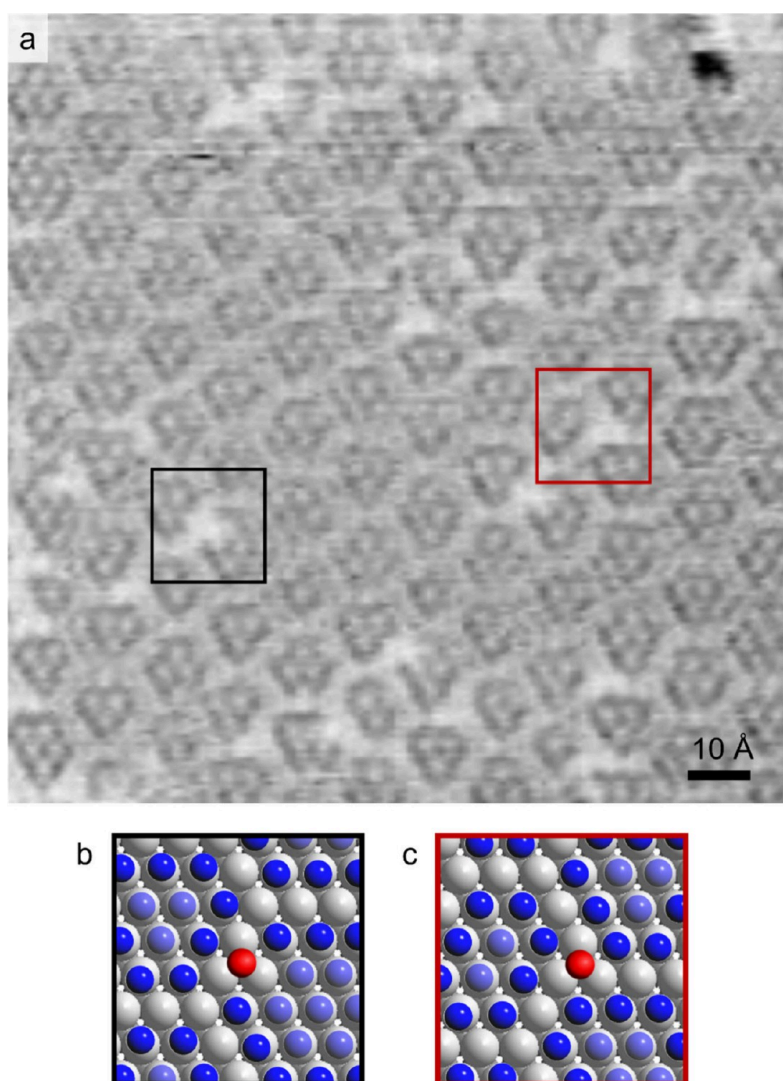
Figure 2. (a) STM image of the CO-saturated Ru(0001) surface ($\Theta = 0.66$ ML) with embedded O atoms. Features with bright dots in the interiors and dark/bright rims are CO clusters, bright dots are O atoms. (The black feature is probably some carbon species.) $T = 227$ K, tunneling voltage (V_t) = -0.2 V, tunneling current (I_t) = 10 nA, constant height mode. (b) Model of the marked area in (a) with an O atom on a corridor site. (c) Model of the marked area in (a) with an O atom on a twisted junction site. Red spheres: O atoms; blue spheres: CO molecules; lighter blue spheres are the inner CO molecules that create the fine structure in the STM image; gray spheres: Ru atoms.

For an integration range of 0.0 to -1.0 eV and at a distance of 2.5 Å, the simulated images agreed well with the experimental data.

■ RESULTS AND DISCUSSION

Configuration of the Embedded O Atoms in the Saturated CO Layer. Figure 2(a) shows one frame from an STM movie recorded at 227 K on the saturated CO layer with embedded O atoms. One can see a roughly hexagonal pattern of features of various sizes, each displaying a few units of a hexagonal inner fine structure. The periodicity of the fine structure is ≈3.3 Å, slightly larger than the lattice constant of Ru(0001) of 2.70 Å. The features represent the compact, 2D CO clusters known from the saturated, pure CO layer, and the size variations reflect the variable numbers (7−19) of the CO molecules in the clusters.[16] The fine structure reflects the inner CO molecules, and the more or less structureless space between the fine structure elements reflects the displaced and tilted outer

molecules. There is no contrast from the corridors between the clusters.

In addition to these features, several bright spots can be identified in Figure 2(a). These are absent on the pure CO layer and can therefore be interpreted as embedded O atoms. We mention that, in the constant current STM mode, adsorbed O atoms on metal surfaces usually appear dark, but in the constant height mode at negative tunneling voltages V_t the contrast is inverted.[32] Similar images have been obtained in all experiments.

Figures 2(b) and (c) show schematic models of the two marked areas in Figure 2(a). The O atoms occupy 3-fold sites, consistent with the expected hcp sites, and the surrounding CO clusters show some differences to clusters without oxygen. In one case [Figure 2(b)], one CO molecule in a corridor is missing from the edge of a cluster, and the resulting CO-free hcp site is occupied by an O atom. In the second case [Figure 2(c)], a twisted junction site between three CO clusters is CO-free and

occupied by an O atom. These cases correspond to two configurations treated by DFT [Figure 1(b) and (d)].

Simulated STM images (Figure 3), confirm the models. Figure 3(a) shows a simulated image of a structure with clusters
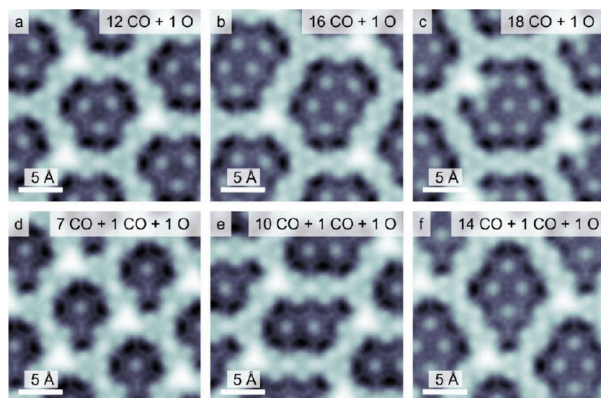
Figure 3. Simulated STM images of CO cluster structures with embedded O atoms. Inverted contrast like in the experiment; bright dots are at the positions of the inner CO molecules; bright intermediate spaces are at the positions of the outer CO molecules, and the brightest dots are at the positions of the O atoms. (a) and (c) Simulations of the models shown in Figure 1(b) and (d) with adsorbed O atoms on the CO-free hcp sites. (b) Simulation of one of the models shown in Figure S1. (d) to (f) Simulations of three of the models shown in Figure S1 with adsorbed O atoms and single additional CO molecules.

of 12 CO molecules [Figure 1(b)] and O atoms that occupy the twisted junction sites. The three central maxima in each unit of the simulated image are caused by the three inner CO molecules of the clusters, the weak modulation between the clusters is caused by the nine outer molecules, and there is no contrast

from the empty corridors. The bright spots at the corners of the unit cells are at the positions of the O atoms on the twisted junction sites. Figure 3(b) is equivalent, with 16 CO molecules per cluster and O atoms on the twisted junctions. Figure 3(c) is a simulation of a configuration with 18 CO molecules [the CO configuration of Figure 1(d)] with O atoms on the corridor sites. Figures 3(d) to (f) show configurations with embedded O atoms and single CO molecules added to sites in vacancy blocks. In all cases, the simulations are in good agreement with the experimental images.

Diffusion of the Embedded O Atoms. Movies recorded with the high-speed STM show that the embedded O atoms are mobile in the investigated temperature range (225 to 268 K). As an example, Figure 4 shows three images recorded with time intervals of 0.2 and 0.5 s on the same surface area, together with models of the marked areas (227 K). In the first frame, two O atoms (black and red arrows) occupy twisted junction sites with opposite chirality [Figure 4(a) and (d)]. In the second frame, the lower atom has moved to a corridor site, and the upper atom is still at the same position [Figure 4(b) and (e)]. At the same time, the number of CO molecules in the cluster below the displaced O atom has increased from 12 to 13. One CO molecule has left a site at the corridor (creating the CO-free hcp site for the O atom) and two originally empty Ru sites at the upper edge of the cluster are occupied by CO. There are further changes at the cluster above the displaced O atom. In the third frame, the lower O atom has jumped again, this time to a twisted junction site [Figure 4(c) and (f)] with opposite chirality to the original configuration [Figure 4(a) and (d)]. This jump is accompanied by changes in several clusters in the marked area which effectively create the CO-free hcp site for the O atom at the new twisted junction. The O atom thus moves by hopping between CO-free hcp sites, and during these jumps, the
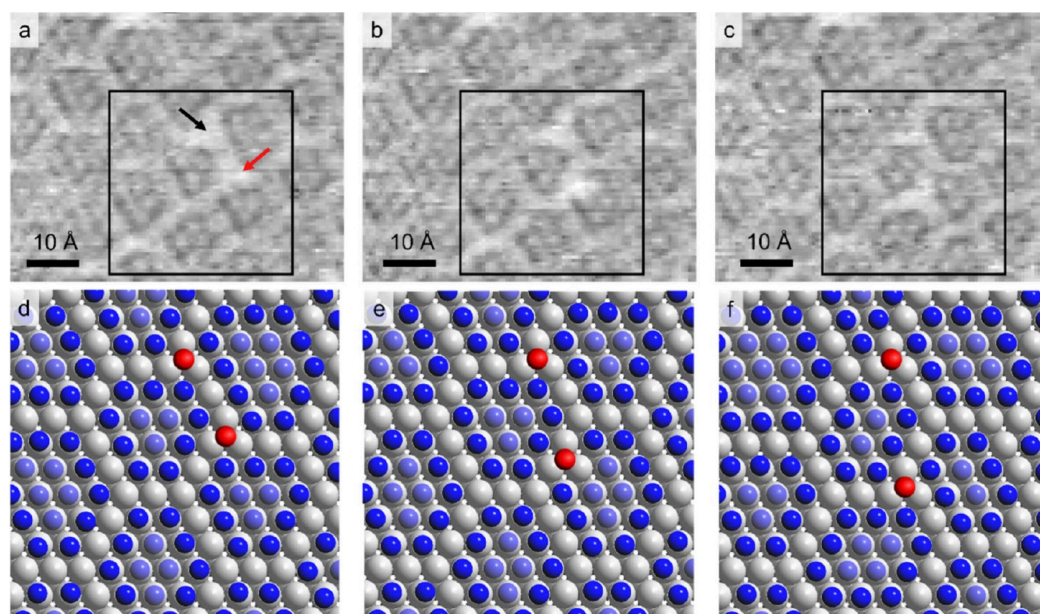
Figure 4. Series of STM images during jumps of an O atom. (a–c) STM images from a movie of the CO-saturated Ru(0001) surface (Θ = 0.66 ML) with embedded O atoms; all three images from the same area; time intervals between frames are 0.2 and 0.5 s. T = 227 K, V_t = −0.2 V, I_t = 10 nA, constant height mode, frame rate 10 s^{-1}, arrows mark two O atoms. (d–f) Models of the marked areas in (a–c). Red spheres: O atoms, blue spheres: CO molecules, gray spheres: Ru atoms.
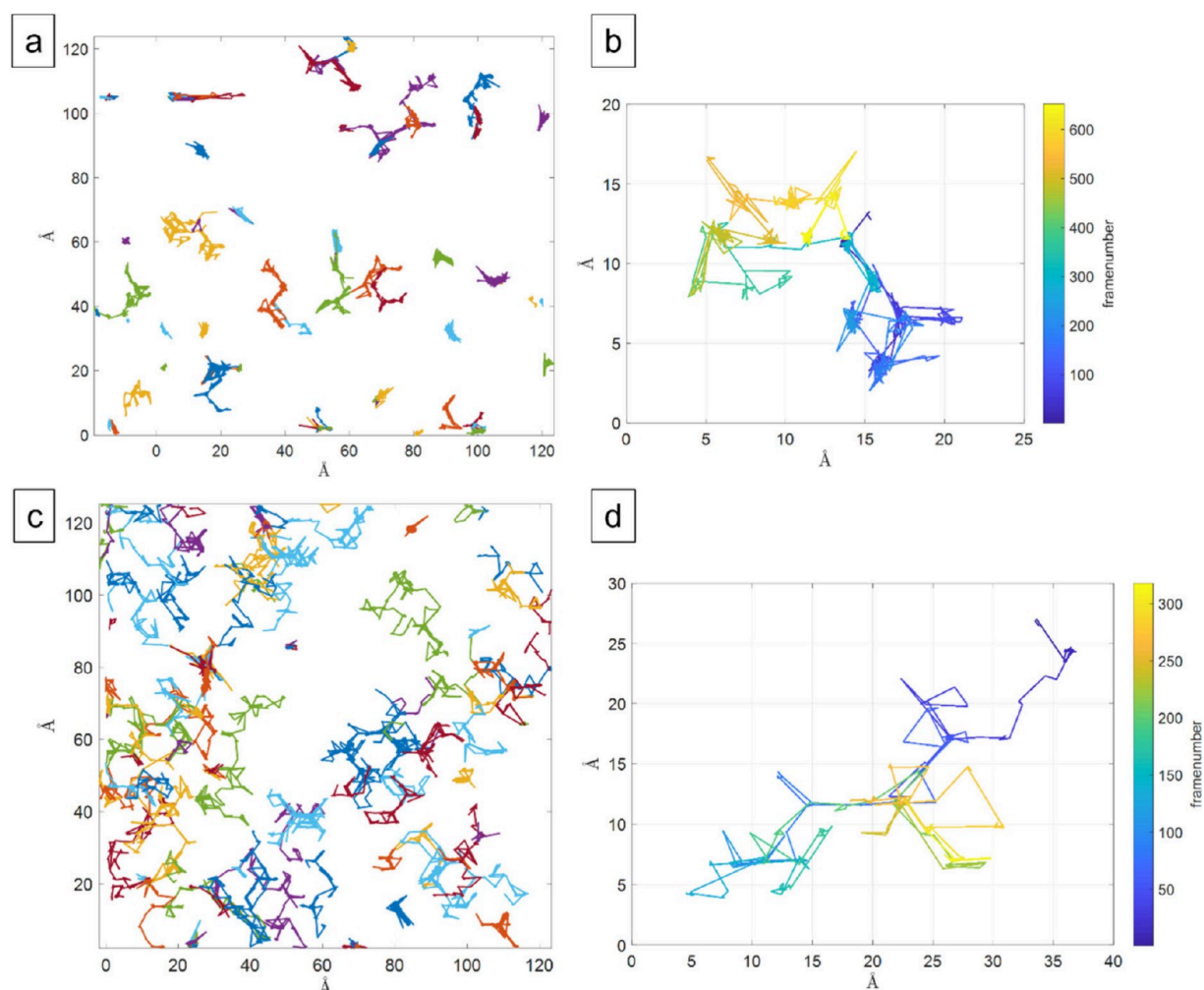
Figure 5. Trajectories of O atoms obtained with the tracking software. (a) All trajectories from an STM movie recorded at 245 K. $V_t = -0.2$ V, $I_t = 3$ nA, constant height mode, frame rate 10 s^{-1}. (b) Trajectory of a single O atom from the data set of (a). (c) All trajectories from an STM movie recorded at 259 K. $V_t = -0.2$ V, $I_t = 3$ nA, constant height mode, frame rate 10 s^{-1}. (d) Trajectory of a single O atom from the data set of (c).

molecules at the edges of several CO clusters change positions. (Movie S1 shows a full movie.)

Longer trajectories of the O atoms were recorded by means of the tracking software. Figure 5(a) and (c) shows, as examples, trajectories from a 652-frame movie at 244.5 K and from a 765-frame movie at 259 K, respectively. (The data have been drift-corrected as described before.[21]) Colors mark trajectories of different O atoms or interrupted trajectories of given atoms when the tracking software has intermittently lost the atoms. As expected, the trajectories at 259 K are longer on average than at 244.5 K (the two movies cover about equal time periods). At the higher temperature, the trajectories display a characteristic honeycomb pattern, which obviously replicates the cluster structure of the CO layer. Such trajectory patterns have also been observed in experiments in which the CO structure was not well resolved. It can be concluded that the O atoms mainly move along the corridors between the junctions of the clusters and only rarely enter the interiors of the clusters. In Figure 5(c), the honeycomb pattern partially displays two parallel lines, indicating that the O atoms can travel along the corridors on two pathways. Despite the variations in cluster sizes and shapes,

their average positions remain unchanged over the periods of the STM movies.

Figure 5(b) and (d) shows trajectories of single O atoms from the data sets of Figure 5(a) and (c). Color codes represent time. At the lower temperature, the trajectory shows "nodes" of short lines which correspond to time periods in which the atom is found on the same adsorption site, and the number of visited sites is low. At the higher temperature, the atom spends less time on an adsorption site, often just the time of one frame, and the number of visited sites is higher. Jumps are mostly one lattice constant long; occasional longer displacements at the higher temperature can be explained by successive single jumps.

For statistical analysis of the trajectories the previously described procedure was applied.[12] It includes checks that a bright feature identified by the software actually represents an O atom, and that trajectory sections in which two O atoms are more closely spaced than approximately 7 Å are removed. Data from altogether 15 temperatures in a range between 225 and 268 K were analyzed, each measurement consisting of several thousand STM images (Table S1). The results are displayed as displacement histograms between successive STM images. Figure 6(a) and (b) shows examples from two temperatures,
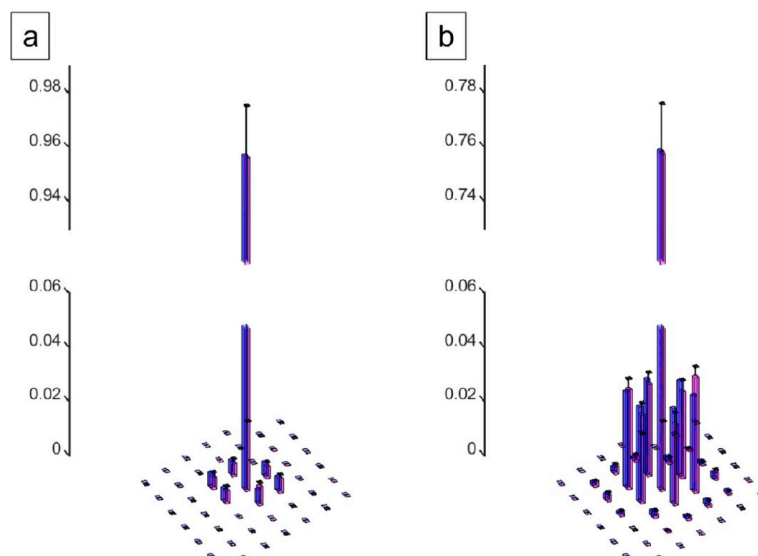
Figure 6. Displacement histograms of O atoms on the CO-saturated Ru(0001) surface. (a) and (b) from data sets at 234 and 261 K, respectively. Pink bars are from the experiments, blue bars from the fits with eq 3. Bar heights are relative counts of displacements from $(x, y) = (0.0)$ to sites with coordinates x and y between successive images; the origins in (a) and (b) are at the highest bars.
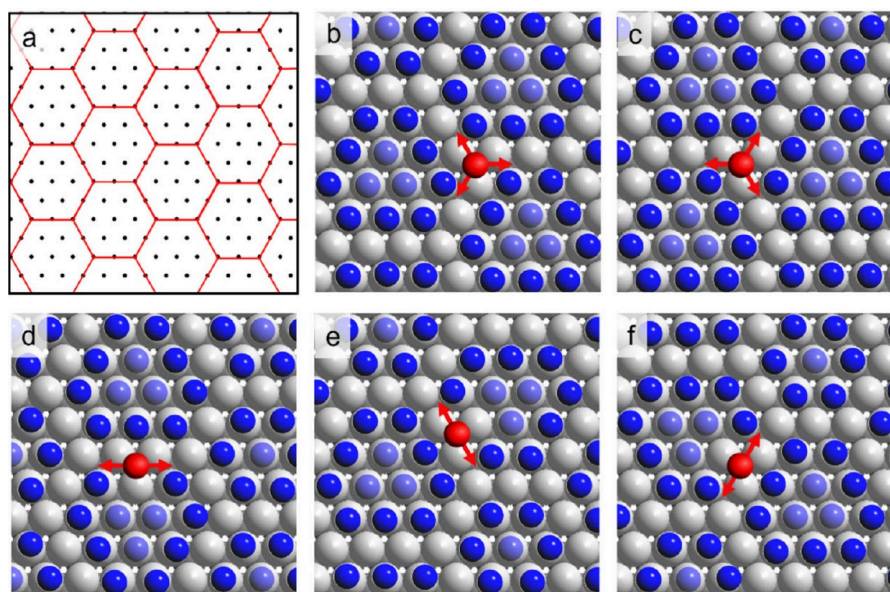
Figure 7. Diffusion model of O atoms on the CO-saturated surface. (a) Simplified lattice. Black dots are hcp sites, and the red honeycomb pattern marks hcp sites accessible to oxygen. (b−f) Structure models of the junctions and corridors of the cluster structure, respectively.

234 and 261 K (pink bars). As expected, the displacement distribution is broader and flatter at the higher temperature, but both histograms appear hexagonal.

Analysis of the Displacement Histograms. Like in the previous work,[12,14] the hopping probability of the O atoms was assumed to be given by a Poisson distribution [eq 2]

$$\tilde{P}_{t_0}(n) = \frac{(\Gamma t_0)^n}{n!} e^{-\Gamma t_0} \tag{2}$$

$\tilde{P}_{t_0}(n)$ is the probability that an O atom jumps n times in the time period t_0 between two successive STM frames (0.1 s in the present case). To obtain an experimentally accessible quantity,

$\tilde{P}_{t_0}(n)$ has to be multiplied by $w_n(x, y)$, the probability that an atom travels to a given site with coordinates (x, y) by a combination of n jumps. $w_n(x, y)$ is a geometry factor that depends on the symmetry of the lattice. It is evaluated by a recursion equation. Summing the product of $\tilde{P}_{t_0}(n)$ and $w_n(x, y)$ over all n gives $P_{t_0}(x, y)$, the probability that the O atom has moved to a site with coordinates (x, y) between two successive STM images. $P_{t_0}(x, y)$ corresponds to the experimental quantity plotted in the histograms.

For diffusion on a hexagonal lattice, $w_n(x, y)$ has a simple form.[14] In the present case, the O atoms do not move on a hexagonal lattice, but on a partially ordered honeycomb network

defined by the CO clusters [Figure 5(c)]. A further complication is that the sizes and shapes of the clusters are not uniform and change with time. Including these effects in the setup of a recursion equation $w_n(x, y)$ in a precise way is not possible, but a simplified model lattice can at least capture basic elements of the actual process. The model we chose consists of a hexagonal lattice of hcp sites [Figure 7(a), black dots] superimposed by a periodic honeycomb network that defines the hcp sites that are actually accessible to the O atoms [Figure 7(a), red lines]. The honeycomb lattice reflects the experimental observation that the O atoms only occupy sites between the clusters, whereas the interiors of the clusters are largely excluded. Structure models of the two configurations at the junctions of this model lattice and of the three configurations at the corridors are shown in Figure 7(b,c) and (d–f), respectively. Size variations of clusters and the two parallel trajectories along the corridors were not included. The hopping rate Γ was assumed to be equal for all sites. The O paths on this network are treated irrespective of the fact that CO molecules have to be displaced for each jump event, as indicated by the arrows in Figure 7(b–f). These CO displacements are implicitly contained in the obtained hopping rates.

On this simplified lattice, recursion equations $w_n(x, y)$ can be formulated (SI). Five different geometry factors are obtained, one for each starting position on one of the five different types of sites on the honeycomb lattice. A difficulty for the analysis is that one cannot decide which of these sites is the respective starting position. The irregular shapes of the individual trajectories [Figure 5(b) and (d)] illustrate this problem. An averaging method was therefore applied (SI). It was assumed that the O atoms initially either occupy, with equal probability, one of the two different junction sites, so that the two corresponding geometry factors can be averaged to give an averaged geometry factor $w_n^{jct}(x, y)$ for the junction sites. Or, the O atoms initially occupy, with equal probability, one of the three different corridor sites, and averaging the three corresponding geometry factors gives an averaged geometry factor $w_n^{crd}(x, y)$ for the corridor sites. Which fraction of atoms initially occupy junction sites or corridor sites was a priori not clear and left open. $P_{t_0}(x, y)$ is then given by eq 3:

$$P_{t_0}(x, y) = \sum_{n=0}^{\infty} \tilde{P}_{t_0}(n)[f w_n^{jct}(x, y) + (1 - f) w_n^{crd}(x, y)] \tag{3}$$

where $\tilde{P}_{t_0}(n)$ is taken from eq 2, and the expression in square brackets is the geometry factor for the honeycomb lattice. f is the fraction of atoms that initially occupy a junction site; we treat it as a second fitting parameter, in addition to the hopping frequency Γ contained in $\tilde{P}_{t_0}(n)$. Summing was performed up to $n = 10$.

Figure 6(a) and (b) shows, as examples, fits of $P_{t_0}(x, y)$ (blue bars) to the experimental histograms at 234 and 261 K (pink bars). Very good agreement is found, and the residual plots correspondingly show low values (Figure S2). The agreement confirms the assumption of the model that the O atoms move by random jumps between neighboring adsorption sites. For the hopping rates, the fits give $\Gamma = 0.3127$ s^{-1} and $\Gamma = 2.7370$ s^{-1} at 234 and 261 K, respectively, and for the fraction of atoms at the initial junction sites, the fits give $f = 0.25$ and 0.61, respectively. For comparison, we also performed fits with a recursion equation on a simple hexagonal lattice. The hopping rates, $\Gamma = 0.3112$ s^{-1} and $\Gamma = 2.6427$ s^{-1} at 234 and 261 K, respectively, are

almost identical to the values on the honeycomb lattice, indicating that the choice of the exact lattice and, thus, the simplifications of the model lattice, are uncritical. For all other measurements, application of eq 3 led to similar good fits to the experimental histograms. Table S1 lists the obtained Γ and f values. f shows no systematic trend with temperature, and the average over all measurements, $\langle f \rangle = 0.47 \pm 0.18$, indicates no significant difference between the occupation probabilities of the junction and corridor sites (the value for exact uniformity would be 2/5).

The hopping rates increase with temperature as shown in the Arrhenius plot (Figure 8). The plot contains measurements
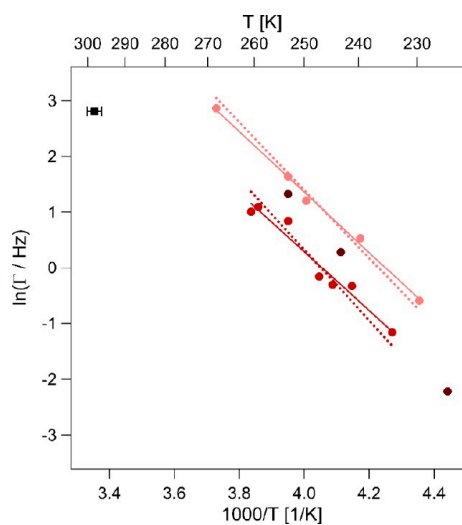
Figure 8. Arrhenius plot of hopping frequencies of O atoms on the CO-saturated Ru(0001) surface. Red and pink data points are from two separate experiments, linear regressions shown as full lines, and dark red data points are from a control experiment with a higher O coverage. Dotted lines are linear regressions with preexponential factor Γ^0 fixed at $10^{11.2}$ s^{-1}. Black square: data point from adsorbed O atoms on the bare Ru(0001) surface at room temperature, taken from ref.[2]

from two separate full experiments (red and pink data points) and three data points from a control experiment with a higher O coverage (dark red data points). That the two full data sets are displaced with respect to each other, despite nominally identical conditions, is probably caused by an error in the reference temperatures. However, both sets are well fitted by linear regressions (solid lines), giving almost identical activation energies, $E^* = 0.46 \pm 0.04$ eV and 0.47 ± 0.02 eV, respectively, and preexponential factors, $\Gamma^0 = 10^{9.3 \pm 0.9}$ s^{-1} and $10^{10.0 \pm 0.4}$ s^{-1}, respectively. The hopping rates from the control experiment are in the same range, demonstrating that the method of excluding too closely spaced O atoms works well. We additionally applied linear regressions with fixed preexponential factors at $\Gamma^0 = 10^{11.2}$ s^{-1}, the average value from previous experiments at 0.33 ML of CO where a higher number of data points was available.[12] With this constraint, the linear regressions still fit the data well (Figure 8, dotted lines), but the activation energies increase somewhat, to $E^* = 0.55$ and 0.53 eV, respectively.

Table 1 relates the Arrhenius parameters to the parameters from the previous work. At CO saturation ($\Theta = 0.66$ ML), the experimental activation energies are in the same range as at 0.47 ML, and with the fixed preexponential factor they are somewhat lower. They are distinctly lower than at 0.33 ML, independently

Table 1. Activation Energies and Preexponential Factors as Functions of CO Coverage[a]

Θ [ML]	exp. E^* [eV] for O jump	exp. Γ^0 [s^{-1}] for O jump	exp. E^* [eV] for O jump with fixed Γ^0 at $10^{11.2}$ s^{-1}	$E_{a,CO}$ [eV] for initial CO displ., DFT	$E_{d,CO}$ [eV] of config. with displ. CO, DFT	$E_{a,ox}$ [eV] for O jump after displ. CO, DFT	E_{tst} [eV], DFT	ref
0.33	0.63 ± 0.03	$10^{11.1 \pm 0.7}$	0.64	0.30	0.16	0.62	0.78	12, 13
0.47	0.44 ± 0.04	$10^{8.9 \pm 0.8}$	0.56	0.25–0.33	0.06–0.15	0.55–0.56	0.65–0.73	14
0.66/0.63	0.46 ± 0.04	$10^{9.3 \pm 0.9}$	0.55	0.26	0.24	0.45	0.69	this work
0.66/0.63	0.47 ± 0.02	$10^{10.0 \pm 0.4}$	0.53					

[a]Experimental activation energies E^*, preexponential factors Γ^0 and activation energies with fixed preexpontential factor at $\Gamma^0 = 10^{11.2}$ s^{-1}. DFT-calculated activation energies for the initial CO excitation $E_{a,CO}$ and calculated energies of the excited states $E_{d,CO}$. DFT-calculated activation energies $E_{a,ox}$ for the jump of an O atom to a CO-free fcc site after displacement of a CO molecule. Total energies E_{tst} of the transition states with respect to the minimum energy configurations. (E_{tst} is not in all cases exactly the sum of $E_{d,CO}$ and $E_{a,ox}$ when some following steps are energetically higher.) The two coverage values 0.66 and 0.63 ML in the last two rows are from the experiment and from the calculations, respectively.

of the preexponential factor. (For 0.33 ML there are two different jump processes; we here only consider the one connected with an actual O/CO site exchange.[12,13]) The preexponential factors only show small differences. Equivalently, the absolute hopping rates at CO saturation (table S1) are in the same range or somewhat higher than at 0.47 ML, and they are distinctly higher than at 0.33 ML.[12,14] When we extrapolate the regression lines in the Arrhenius plot to room temperature—here a data point exists for O atoms on the bare Ru(0001) surface (Figure 8, black data point)[2]—then we find that the hopping rate on the CO-saturated is even higher than on the CO-free surface. Quite surprisingly, the mobility of the embedded O atoms on the CO-saturated surface is not only not reduced but even enhanced compared to lower coverages and also to the bare surface.

DFT Calculations. DFT calculations were performed to explain this result. Figure 9 depicts the calculated energies [as CO adsorption energies E_{ads}, eq 1] of all considered CO cluster structures with and without coadsorbed O atoms as a function of CO coverage. All values are positive because E_{ads} is relative to an isolated adsorbed CO molecule and there are repulsive

interactions in all structures. Without O atoms, compact CO cluster structures (black dots) are the most stable configurations at a given CO coverage, as previously reported.[16] (This is except for the data at $\Theta \approx 0.7$ ML, which is beyond the experimental saturation coverage.) Cluster structures with bare hcp sites (examples are shown in Figure 1) are less stable (blue data points). This difference is explained by the fact that in order to create a bare hcp site at a given CO coverage, one has to concentrate the molecules into larger clusters, which generally lowers the adsorption energy per CO molecule.[16] Within the structures with bare hcp sites, twisted junction configurations (blue squares) are more stable than vacancy block configurations (blue diamonds). This fact suggests that one can modify the shape of a cluster by putting CO molecules on sites that are different from sites in the corridors, triangular junctions, or twisted junctions. A configuration with a bare hcp site at a cluster edge (blue star) is similarly stable as the twisted junction configuration for the same cluster size of 18 CO molecules ($\Theta = 0.67$ ML).

With O atoms on the CO-free hcp sites, all energies increase (red data points), a result of the relatively strong repulsion between O and the CO molecules. Configurations with O atoms on the twisted junctions (red squares) are more stable than configurations with O atoms in the vacancy blocks (red diamonds); the difference is more pronounced at low coverages. As shown for two 18 CO cluster structures ($\Theta = 0.67$ ML), the energy of a configuration with O atoms at corridor sites (red star) is comparable to the configuration with O atoms at twisted junction sites (red square). This fact is in agreement with the experimental finding that the occupation probabilities of the junction and corridor sites [expressed by the factor f in eq 3] are about the same.

To probe the dynamics of the O jumps, a 12 CO twisted junction structure ($\Theta = 0.63$ ML), with an O atom on the CO-free hcp site, was chosen as starting configuration (Figure 10, first model, O$_{hcp}$/12CO). It is a local energy minimum, and there are no CO-free 3-fold sites to which the O atom can jump. To create a CO-free site, one of the neighboring CO molecules is displaced to a corridor site (Figure 10, second model). The activation energy, $E_{a,CO} = 0.26$ eV, is comparable to the value at 0.47 ML and marginally lower than at 0.33 ML (Table 1). The energy $E_{d,CO}$ of the resulting O$_{hcp}$/12CO$^{(a)}$ configuration is 0.24 eV higher than the starting configuration. This increase is significantly higher than at the lower coverages (Table 1), but this is what is expected as the CO molecule has to be placed on a site in the narrow corridor where the repulsion by the neighboring CO molecules is strong. The barrier to move the CO molecule back is only 0.02 eV. It can, therefore, be assumed that the initial excitation of the CO structure is in equilibrium.
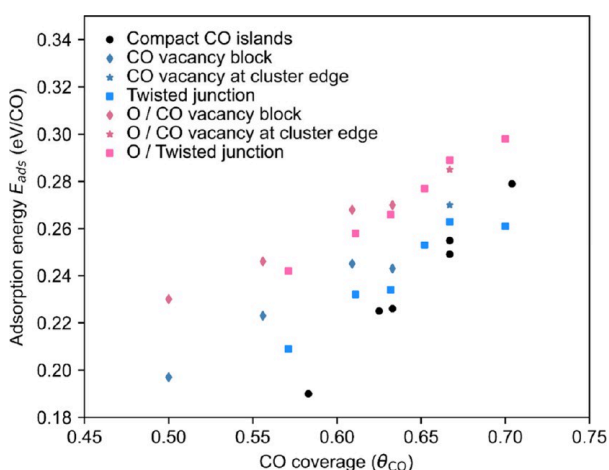
Figure 9. Energies of structures vs CO coverage from the DFT calculations. Black dots: compact, pure CO cluster structures (almost the same values as in ref 16; slight offsets are explained by a somewhat different setup of the calculations); blue squares: pure CO structures with twisted junctions; blue diamonds: pure CO structures with vacancy blocks; blue star: pure CO structure with vacancies at cluster edges; red squares: structures with O atoms on twisted junction sites; red diamonds: structures with O atoms on vacancy block sites; red star: structure with O atoms on vacancy sites at the cluster edges.
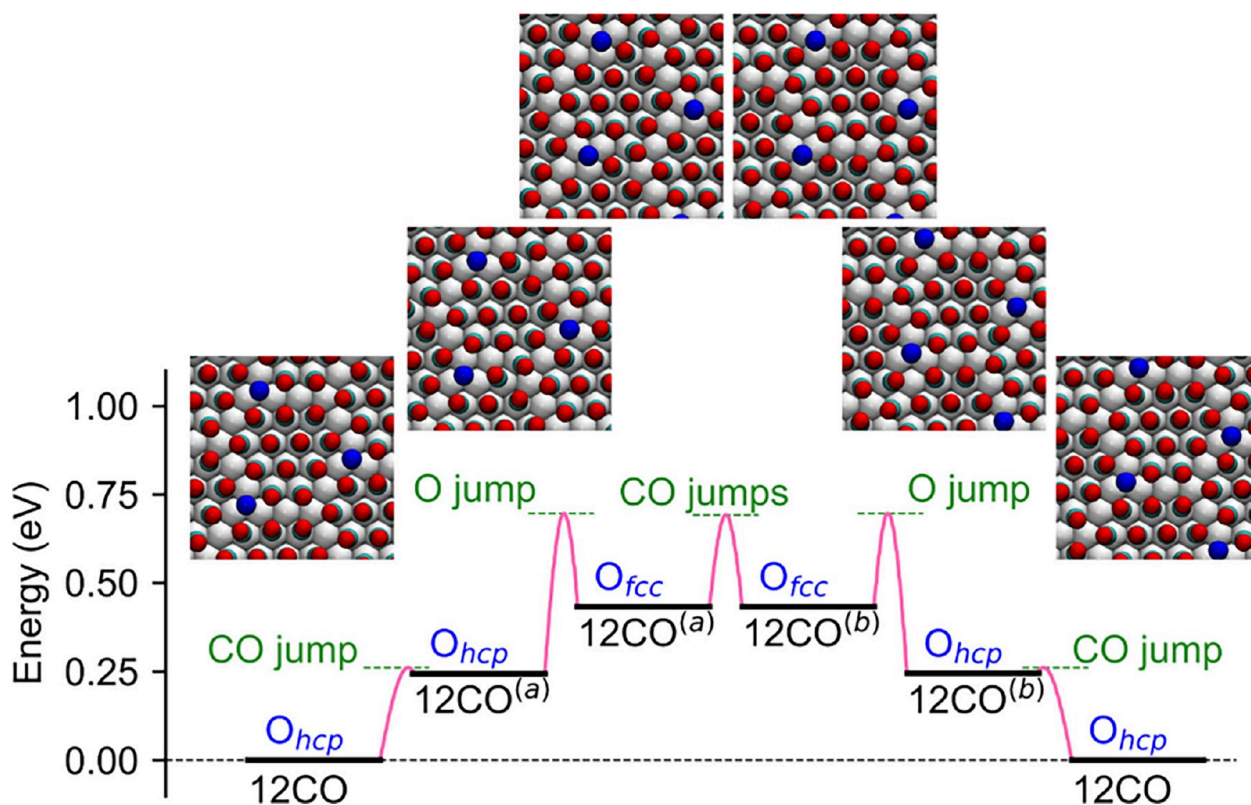
Figure 10. Energy diagram of an hcp → fcc → hcp jump of an O atom on the CO-saturated Ru(0001) surface. Models correspond to the six levels on the energy profile; oxygen atoms are indicated as blue spheres, otherwise same color code as in Figure 1.

By displacing the CO molecule, a channel to a CO-free fcc site has been opened. One could, additionally, create a CO-free hcp site, but then two CO molecules have to be displaced, which costs 0.54 eV, making this sequence less probable. More likely is that the O atom first jumps to the CO-free fcc site (Figure 10, third model, $O_{fcc}/12 CO^{(a)}$). The activation energy for this step, $E_{a,ox} = 0.45$ eV, is distinctly lower than at the lower CO coverages (Table 1). We explain this fact by the changing distances between the CO molecules and the O atom along the path of the jump. In the $O_{hcp}/12CO^{(a)}$ configuration, the distances between the CO molecules and the O atom are, on average, shorter than in the transition state (which is approximately the bridge site between the hcp and the fcc sites). Hence, as the O atom moves from the energy minimum to the transition state, the repulsion by the CO molecules and thus the activation energy decreases. Such an effect also occurred at $\Theta = 0.47$ ML,[14] but in the present case the effect is stronger because of the higher CO coverage. For the absolute energy of the transition state E_{tst}, the two effects of the high CO coverage, an increase of $E_{d,CO}$ and a decrease of $E_{a,ox}$, partially cancel out, but the decrease of $E_{a,ox}$ is higher than the increase of $E_{d,CO}$. The resulting value, 0.69 eV, is therefore lower than at the lower coverages (Table 1).

From the $O_{fcc}/12CO^{(a)}$ configuration, the O atom could then jump back to the original site, or several CO molecules rearrange in several consecutive random steps, each with a slightly lower activation energy than for the back jump, to give the configuration $O_{fcc}/12CO^{(b)}$ (Figure 10, fourth model). It has the same symmetry and optimized structure and energy as the $O_{fcc}/12CO^{(a)}$ configuration. From there, the O atom can jump to a neighboring CO-free hcp site (the $O_{hcp}/12CO^{(b)}$

configuration, Figure 10, fifth model). Finally, one CO displacement leads to a new energy minimum configuration (Figure 10, sixth model), which is equivalent to the starting configuration. As a result, the O atom has moved by one lattice constant between two hcp sites. In the intermediate states of this process, when the O atom is on the fcc site and the CO molecules rearrange quickly, the outcome can, of course, be different and lead to a different final configuration, e.g., one in which the O atom is on an hcp site in a corridor. (In the experiment, this is the more likely result as the O atoms move along the corridors.) In any case, the scenario is based on fluctuations in the CO layer and follows the door-opening mechanism known from the lower coverages; it only differs with respect to the detailed excitations of the CO layer.

The scenario is in agreement with the experimental observations. The experiments have shown that the motion of the O atoms is correlated with changes in the positions of CO molecules at the cluster edges. The fact that the experimental trajectories only show O atoms on hcp sites is consistent with the high energy of the intermediate fcc site and the corresponding short lifetime. The calculated energy of the transition state maximum E_{tst} is somewhat higher than the experimental activation energies E^*, but this has similarly been found at the lower coverages (Table 1). (Because of the pre-equilibrium of the initial CO fluctuation, the experimental E^* corresponds to E_{tst} which contains the energy to create the configuration with the displaced CO, $E_{d,CO}$.) When the experimental activation energy is corrected for a fixed preexponential factor, then the agreement is quite reasonable. Moreover, the calculations reproduce the experimentally

observed trend that the activation energies decrease with increasing CO coverage (Table 1). In sum, the increased mobility on the CO-saturated layer can be explained by two counteracting effects: Fluctuations are made more difficult by the restricted space in the saturated layer, but at the same time the jump barrier is lowered by the increased repulsive interactions between the O atoms and CO molecules, and this effect predominates.

CONCLUSIONS

Adsorbed O atoms on a Ru(0001) surface which is covered with a saturated layer of CO molecules (Θ = 0.66 ML) are highly mobile. High-speed STM movies recorded at temperatures between 225 and 268 K reveal that the O atoms perform random jumps between neighboring adsorption sites, like on the empty surface and at lower CO coverages. In contrast to these situations, the atomic trajectories are restricted to the gaps between the close-packed clusters of CO molecules that form the saturated layer. When O atoms move in these gaps, the jumps are accompanied by site changes of CO molecules at the edges of several adjacent clusters. Despite the narrow space between the clusters, the mobility is even higher than at lower CO coverages, because the activation energy for the jumps of the O atoms in the multidimensional potential energy surface is lower.

The energy profile obtained by DFT shows that a jump event of an O atom is initiated by displacing a CO molecule to an unfavorable site between the clusters. In this way, a path is opened on which the O atom can jump from its hcp site to an empty fcc site. Random rearrangements involving several successive CO jumps can then create a path to an empty neighboring hcp site. After the O atom has jumped to this site, further CO displacements restore a stable configuration. The process can be seen as a walk on a "flickering path", driven by CO fluctuations between the clusters. It is quite similar to the door-opening mechanism previously derived for lower CO coverages. At the high CO coverage, repulsions between the O atoms and the CO molecules are higher, which alters the energy landscape from that at the lower coverages, giving a lower activation energy and an increased mobility.

We can conclude that the assumption of a high, not rate-limiting diffusion of adsorbed particles, the basis of microkinetic models of catalytic reactions, is valid up to saturation of the adsorption layer. We have shown this for the specific example of tracer diffusion of O atoms on a CO-saturated Ru(0001) surface, but similar systems, such as the cluster structure formed at 0.70 ML of CO on the Ir(111) surface,[33] can be expected to show the same effect. In how far this conclusion can be generalized is not an easy question to answer. The "flickering path" process is based on the fact that even the saturated CO layer still constitutes a "soft grid" that facilitates easy fluctuations. Adsorption systems that contain sufficient numbers of empty sites may be predicted to show similar effects. When we restrict ourselves to tracer diffusion of coadsorbed particles in layers of adsorbed CO molecules, we find that the van-der-Waals diameter of CO is larger than the lattice constants of all usual low-index metal surfaces. Coverages of 1.00 ML, conditions under which molecular displacement should, in fact, be suppressed, are generally not accessible, even at high pressures. On the other hand, CO at saturation can form other types of structures than clusters, e.g., moiré structures in which the molecules form close-packed layers that display a lattice mismatch with the underlying metal surfaces. Such structures

have, e.g., been observed for CO on Pt(111) and Co(0001) surfaces.[34,35] Coverages are comparable to the cluster structures, but because of the uniform spacings between the CO molecules in such layers, there are no defined empty adsorption sites that are required for the type of fluctuation-driven mechanism described here. Fluctuations may still be possible, but these probably happen in the form of homogeneous compressions of the CO layers. It might be interesting to see how tracer diffusion of coadsorbed atoms is affected in such cases.

ASSOCIATED CONTENT

ⓢ Supporting Information

The Supporting Information is available free of charge at https://pubs.acs.org/doi/10.1021/acs.jpcc.5c04653.

> Models of CO structures with and without O atoms treated by DFT and used for the data of Figure 9. Residual plots of the displacement histograms of Figure 6. Table of STM data used for the Arrhenius plot in Figure 8. Derivation of eq 3 (PDF)
>
> STM movie of diffusing oxygen atoms on the CO-saturated Ru(0001) surface T = 247 K (AVI)

AUTHOR INFORMATION

Corresponding Author

Joost Wintterlin − *Department of Chemistry, Ludwig-Maximilians-Universität München, 81377 Munich, Germany; Center for NanoScience, 80799 Munich, Germany;* ⊙ orcid.org/0000-0002-0636-7538; Email: wintterlin@cup.uni-muenchen.de

Authors

Hannah Illner − *Department of Chemistry, Ludwig-Maximilians-Universität München, 81377 Munich, Germany;* ⊙ orcid.org/0000-0002-9559-1821

Sung Sakong − *Institute of Theoretical Chemistry, Universität Ulm, 89081 Ulm, Germany;* ⊙ orcid.org/0000-0001-9777-7489

Axel Gross − *Institute of Theoretical Chemistry, Universität Ulm, 89081 Ulm, Germany;* ⊙ orcid.org/0000-0003-4037-7331

Complete contact information is available at:
https://pubs.acs.org/10.1021/acs.jpcc.5c04653

Notes

The authors declare no competing financial interest.

REFERENCES

(1) Barth, J. V. Transport of adsorbates at metal surfaces: From thermal migration to hot precursors. *Surf. Sci. Rep.* **2000**, *40*, 75−149.

(2) Renisch, S.; Schuster, R.; Wintterlin, J.; Ertl, G. Dynamics of adatom motion under the influence of mutual interactions: O/Ru(0001). *Phys. Rev. Lett.* **1999**, *82*, 3839−3842.

(3) Pedersen, M. Ø.; Österlund, L.; Mortensen, J. J.; Mavrikakis, M.; Hansen, L. B.; Stensgaard, I.; Lægsgaard, E.; Nørskov, J. K.; Besenbacher, F. Diffusion of N adatoms on the Fe(100) surface. *Phys. Rev. Lett.* **2000**, *84*, 4898−4901.

(4) Briner, B. G.; Doering, M.; Rust, H.-P.; Bradshaw, A. M. Microscopic molecular diffusion enhanced by adsorbate interactions. *Science* **1997**, *278*, 257–260.

(5) Mehrer, H. *Diffusion in Solids*, 1st. ed.; Springer: Berlin, Heidelberg, 2007.

(6) Ganz, E.; Theiss, S. K.; Hwang, I.-S.; Golovchenko, J. Direct measurement of diffusion by hot tunneling microscopy: Activation energy, anisotropy, and long jumps. *Phys. Rev. Lett.* **1992**, *68*, 1567–1570.

(7) van Gastel, R.; Somfai, E.; van Saarloos, W.; Frenken, J. W. M. A giant atomic slide-puzzle. *Nature* **2000**, *408*, 665–665.

(8) van Gastel, R.; Somfai, E.; van Albada, S. B.; van Saarloos, W.; Frenken, J. W. M. Nothing moves a surface: Vacancy mediated surface diffusion. *Phys. Rev. Lett.* **2001**, *86*, 1562–1565.

(9) Grant, M. L.; Swartzentruber, B. S.; Bartelt, N. C.; Hannon, J. B. Diffusion kinetics in the Pd/Cu(001) surface alloy. *Phys. Rev. Lett.* **2001**, *86*, 4588–4591.

(10) Anderson, M. L.; D'Amato, M. J.; Feibelman, P. J.; Swartzentruber, B. S. Vacancy-mediated and exchange diffusion in a Pb/Cu(111) surface alloy: Concurrent diffusion on two length scales. *Phys. Rev. Lett.* **2003**, *90*, No. 126102.

(11) Rahn, B.; Wen, R.; Deuchler, L.; Stremme, J.; Franke, A.; Pehlke, E.; Magnussen, O. M. Coadsorbate-induced reversal of solid–liquid interface dynamics. *Angew. Chem., Int. Ed.* **2018**, *57*, 6065–6068.

(12) Henß, A.-K.; Sakong, S.; Messer, P. K.; Wiechers, J.; Schuster, R.; Lamb, D. C.; Groß, A.; Wintterlin, J. Density fluctuations as door-opener for diffusion on crowded surfaces. *Science* **2019**, *363*, 715–718.

(13) Sakong, S.; Henß, A.-K.; Wintterlin, J.; Groß, A. Diffusion on a crowded surface: kMC simulations. *J. Phys. Chem. C* **2020**, *124*, 15216–15224.

(14) Illner, H.; Sakong, S.; Henß, A.-K.; Groß, A.; Wintterlin, J. Diffusion of O atoms on a CO-covered Ru(0001) surface—a combined high-speed scanning tunneling microscopy and density functional theory study at an enhanced CO coverage. *J. Phys. Chem. C* **2023**, *127*, 7197–7210.

(15) Kügler, A.-K.; Illner, H.; Wintterlin, J. An STM study on the diffusion of O atoms on a CO-covered Ru(0001) surface—the role of domain boundaries. *Surf. Sci.* **2025**, *751*, No. 122597.

(16) Illner, H.; Sakong, S.; Groß, A.; Wintterlin, J. Solution of the structure of the high-coverage CO layer on the Ru(0001) surface—a combined study by density functional theory and scanning tunneling microscopy. *J. Chem. Phys.* **2024**, *161*, 014703.

(17) Henß, A. K.; Wiechers, J.; Schuster, R.; Platschkowski, V.; Wintterlin, J. A beetle-type, variable-temperature scanning tunneling microscope for video-rate imaging. *Jpn. J. Appl. Phys.* **2020**, *59*, No. SN1007.

(18) Goodman, D. W.; White, J. M. Measurement of active carbon on ruthenium (110): Relevance to catalytic methanation. *Surf. Sci.* **1979**, *90*, 201–203.

(19) van Staden, M. J.; Roux, J. P. The superposition of carbon and ruthenium auger spectra. *Appl. Surf. Sci.* **1990**, *44*, 259–262.

(20) Marchini, S.; Günther, S.; Wintterlin, J. Scanning tunneling microscopy of graphene on Ru(0001). *Phys. Rev. B* **2007**, *76*, No. 075429.

(21) Messer, P. K.; Henß, A. K.; Lamb, D. C.; Wintterlin, J. A multiscale wavelet algorithm for atom tracking in STM movies. *New J. Phys.* **2022**, *24*, No. 033016.

(22) Kresse, G.; Furthmüller, J. Efficient iterative schemes for ab initio total-energy calculations using a plane-wave basis set. *Phys. Rev. B* **1996**, *54*, 11169–11186.

(23) Hammer, B.; Hansen, L. B.; Nørskov, J. K. Improved adsorption energetics within density-functional theory using revised Perdew-Burke-Ernzerhof functionals. *Phys. Rev. B* **1999**, *59*, 7413–7421.

(24) Blöchl, P. E. Projector augmented-wave method. *Phys. Rev. B* **1994**, *50*, 17953–17979.

(25) Grimme, S.; Antony, J.; Ehrlich, S.; Krieg, H. A consistent and accurate ab initio parametrization of density functional dispersion correction (DFT-D) for the 94 elements H-Pu. *J. Chem. Phys.* **2010**, *132*, No. 154104.

(26) Grimme, S. Density functional theory with London dispersion corrections. *Wiley Interdiscip. Rev.: Comput. Mo. Sci.* **2011**, *1*, 211–228.

(27) Sakong, S.; Forster-Tonigold, K.; Groß, A. The structure of water at a Pt(111) electrode and the potential of zero charge studied from first principles. *J. Chem. Phys.* **2016**, *144*, No. 194701.

(28) Sakong, S.; Groß, A. The importance of the electrochemical environment in the electro-oxidation of methanol on Pt(111). *ACS Catal.* **2016**, *6*, 5575–5586.

(29) Mahlberg, D.; Sakong, S.; Forster-Tonigold, K.; Groß, A. Improved DFT adsorption energies with semiempirical dispersion corrections. *J. Chem. Theory Comput.* **2019**, *15*, 3250–3259.

(30) Henkelman, G.; Jónsson, H. Improved tangent estimate in the nudged elastic band method for finding minimum energy paths and saddle points. *J. Chem. Phys.* **2000**, *113*, 9978–9985.

(31) Tersoff, J.; Hamann, D. R. Theory of the scanning tunneling microscope. *Phys. Rev. B* **1985**, *31*, 805–813.

(32) Wintterlin, J.; Trost, J.; Renisch, S.; Schuster, R.; Zambelli, T.; Ertl, G. Real-time STM observations of atomic equilibrium fluctuations in an adsorbate system: O/Ru(0001). *Surf. Sci.* **1997**, *394*, 159–169.

(33) Ueda, K.; Suzuki, K.; Toyoshima, R.; Monya, Y.; Yoshida, M.; Isegawa, K.; Amemiya, K.; Mase, K.; Mun, B. S.; Arman, M. A.; et al. Adsorption and reaction of CO and NO on Ir(111) under near ambient pressure conditions. *Top. Catal.* **2016**, *59*, 487–496.

(34) Longwitz, S. R.; Schnadt, J.; Vestergaard, E. K.; Vang, R. T.; Lægsgaard, E.; Stensgaard, I.; Brune, H.; Besenbacher, F. High-coverage structures of carbon monoxide adsorbed on Pt(111) studied by high-pressure scanning tunneling microscopy. *J. Phys. Chem. B* **2004**, *108*, 14497–14502.

(35) Böller, B.; Zeller, P.; Günther, S.; Wintterlin, J. High-pressure CO phases on Co(0001) and their possible role in the Fischer–Tropsch synthesis. *ACS Catal.* **2020**, *10*, 12156–12166.

Supporting Information

Walk on a Flickering Path: Tracer Diffusion of Adsorbed O Atoms on a Ru(0001) Surface in the Limit of CO Saturation

*Hannah Illner[1], Sung Sakong[2], Axel Gross[2] and Joost Wintterlin[1, 3, *]*

[1] Department of Chemistry, Ludwig-Maximilians-Universität München, 81377 Munich, Germany

[2] Institute of Theoretical Chemistry, Universität Ulm, 89081 Ulm, Germany

[3] Center for NanoScience, Schellingstr. 4, 80799 Munich, Germany

[*] Corresponding Author: wintterlin@cup.uni-muenchen.de

Movie S1. STM movie of embedded O atoms in the CO cluster structure on Ru(0001). Θ_{CO} = 0.66 ML; T = 247 K; 903 frames; frame rate 10 s^{-1}; tunneling voltage V_t = -0.10 V; tunneling current I_t = 3 nA; frame size 126 Å x 126 Å. Most features are explained in connection with fig. 2 of the main text. Black features are probably due to minor carbon contaminants. Few immobile bright features are N atoms.
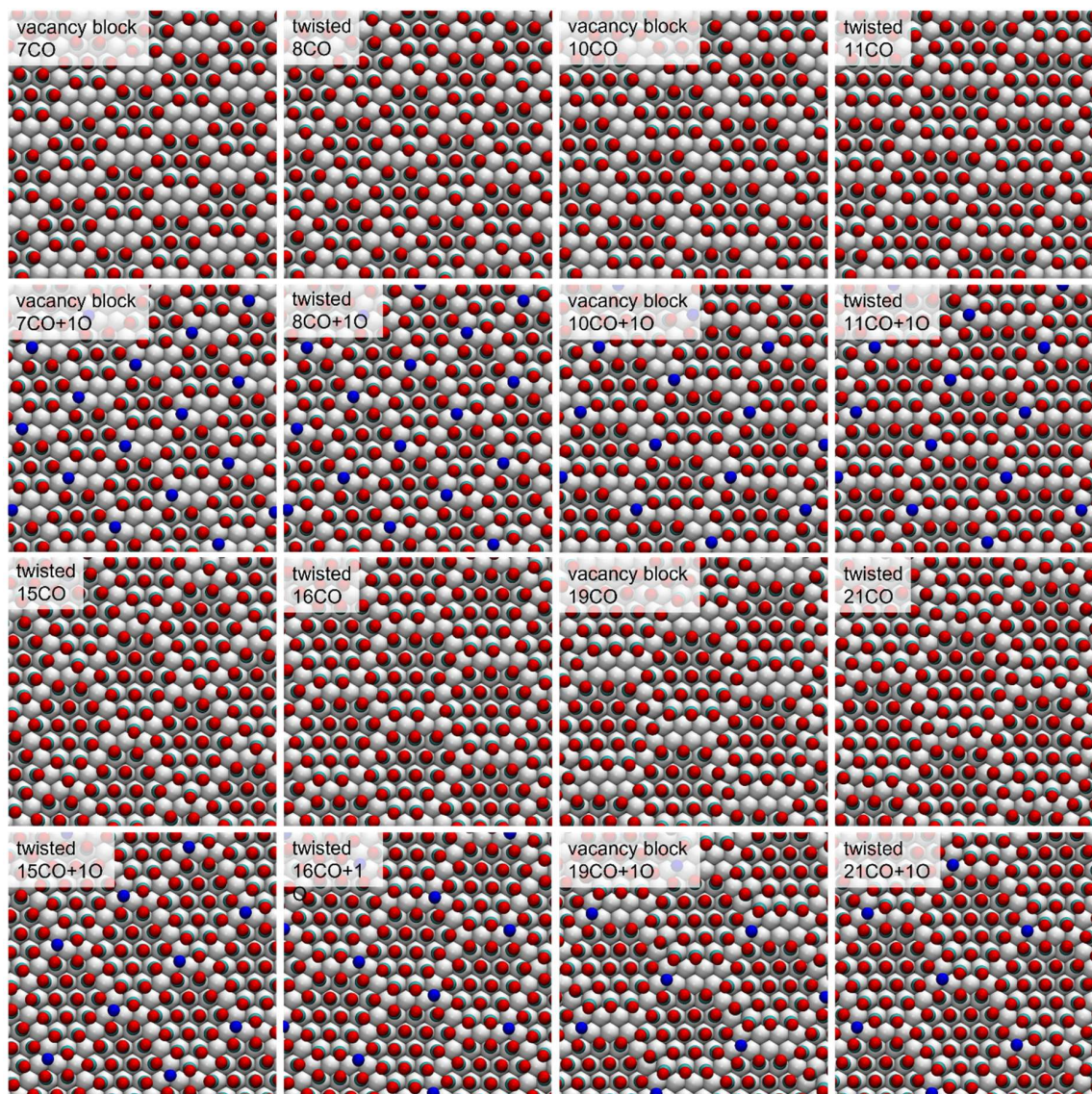
Figure S1. Model configurations used in the DFT calculation. Color code as in figs. 1 and 10 of the main text.
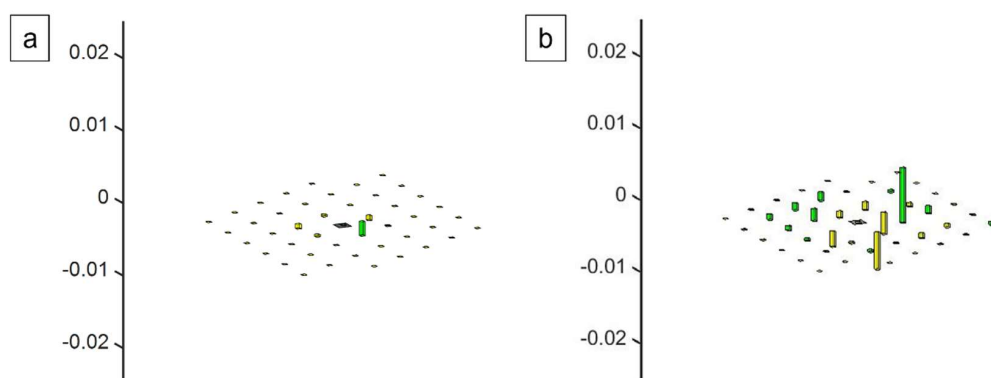
Figure S2. Residual plots. Differences between the experimental displacement histograms and the fits by eq. (3) at (a) 234 K and (b) 261 K (fig. 6 of the main text). Green bars indicate positive, yellow bars negative deviations; the position (0.0) is marked in gray.

Table S1. STM data analyzed for the Arrhenius plot of fig. 8. The list shows the respective temperatures, the numbers of evaluated STM images, the tunneling parameters V_t and I_t, the hopping frequencies Γ, and the fractions f of occupied junction sites from the fits of eq. (3) to the experimental histograms. Horizontal double lines separate the three sets of experiments that entered the Arrhenius plot of fig. 8. The first data set belongs to the pink data points, the second to the red data points, and the third to the dark red data points.

Temperature [K]	# STM images	V_t [V]	I_t [nA]	Γ [s^{-1}]	fraction f
230	4692	-0.7	3	0.5502	0.3413
240	3130	-0.7	3	1.7031	0.3689
250	2901	-0.2	3	3.3310	0.4981
253	3318	-0.2	3	5.1498	0.4227
268	1272	-0.6	3	17.5218	0.3917
234	2705	-1.0	3	0.3127	0.2508
241	3939	-0.3	3	0.7162	0.2027
245	2585	-0.2	3	0.7329	0.1994
247	4487	-0.2	3	0.8483	0.3780
253	2833	-1.0; -0.2	3	2.3222	0.4853
259	4854	-0.2	3	2.9879	0.4729
261	2338	-0.2	3	2.7370	0.6141
225	5419	-1.0	3	0.1089	0.8706
243	2461	-0.1	3	1.3245	0.3848
253	732	-0.2	3	3.7655	0.6704

Derivation of eq. (3)

The geometry factor in eq. (3) was evaluated for a 23 x 23 array of hcp sites. Figure S3 shows the inner part of this array and the honeycomb lattice that determines which of the sites can be occupied by the O atoms. The coordinates x and y of the sites are defined with respect to one of the five possible types of sites [in the case shown in fig. S3 for a junction site type (1)] at (x, y) = (0.0). With this coordination system, one can, for each site of the array, determine its type, i.e., whether it represents a junction site of type (1) or (2), a corridor site of type (1), (2), or (3), or one of the seven excluded sites inside a cluster, by two relations between the coordinates x and y. As shown in table S2, the relations $(x - y)$ and $(x + 2y)$, give, for each type of site, a different combination of two integer numbers. In this way, a lookup table can be constructed that contains the type of site for each of the 23 x 23 hcp sites of the array.

For each type of site, a specific recursion equation $w_n(x, y)$ applies (table S2). $w_n(x, y)$ is the probability that an atom, which has moved to the sites next to a given site (x, y) by a combination of $(n - 1)$ jumps, jumps to the given site by one further jump. The recursion is initialized by putting the atom on the origin, i.e., $w_0(0.0)$ = 1 and all other $w_0(x, y)$ = 0. Then n is increased in steps of one, and the recursion equations in table S2 are applied. As a result, a set of $(n + 1)$ 23 x 23 matrices are obtained, where the matrix elements $w_n^{\text{jct}(1)}(x, y)$ represent the probabilities that an O atom originally located at a junction site of type (1) at (x, y) = (0.0) has moved to a site with coordinates x and y by a combination of n jumps.

When the starting position of the atom at (x, y) = (0.0) is one of the other types of sites, the honeycomb lattice that describes the accessible O sites has to be displaced, and the identification of the site types by the relations $(x - y)$ and $(x + 2y)$ changes (not shown). Otherwise, the same procedure is applied. In this way, two matrix sets for the two types of junction sites, $w_n^{\text{jct}(1)}(x, y)$ and $w_n^{\text{jct}(2)}(x, y)$, and three matrix sets for the three types of corridor sites, $w_n^{\text{crd}(1)}(x, y)$, $w_n^{\text{crd}(2)}(x, y)$, and $w_n^{\text{crd}(3)}(x, y)$, are obtained. Finally, averages are taken because the data do not allow us to determine which site type is the respective starting position. The averaging can be justified by the fact that the two junction sites and, respectively, the three corridor sites are symmetrically equivalent to each other, and the data sets are large, so that one can assume equal occupation probabilities for the junction and the corridor sites, respectively. We obtain:

$$w_n^{\text{jct}}(x, y) = \frac{1}{2}\left[w_n^{\text{jct}(1)}(x, y) + w_n^{\text{jct}(2)}(x, y)\right]$$

$$w_n^{\text{crd}}(x, y) = \frac{1}{3}\left[w_n^{\text{crd}(1)}(x, y) + w_n^{\text{crd}(2)}(x, y) + w_n^{\text{crd}(3)}(x, y)\right]$$

$w_n^{\text{jct}}(x, y)$ and $w_n^{\text{crd}}(x, y)$ are the quantities that enter eq. (3) of the main text.
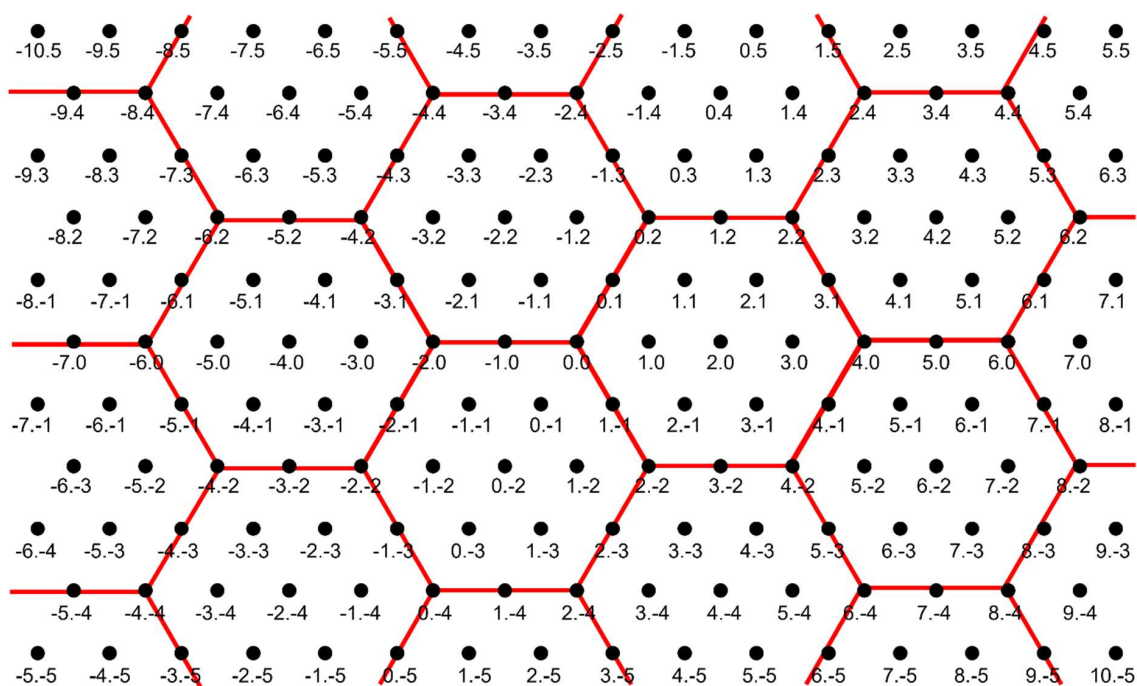
Figure S3. Inner part of the 23 x 23 array used for the geometry factor in eq. (3). Black dots are hcp sites; the red honeycomb lattice marks the hcp sites accessible to the O atoms; labels are the coordinates (x, y). In the case shown, the junction type (1) of the honeycomb lattice has been placed on the starting position of an O atom at (x, y) = (0.0). For the other starting positions, the junction type (2) or one of the three corridor sites has to be placed on (x, y) = (0.0).

Table S2. Relations $(x - y)$ and $(x + 2y)$ and corresponding types of sites and recursion equations. m_1 and m_2 are integers. The table applies to the configuration shown in fig. S3 in which a junction type (1) of the honeycomb is placed on $(x, y) = (0.0)$. For configurations in which a junction type (2) or one of the three types of corridor sites is placed on $(x, y) = (0.0)$, the types of sites and the corresponding recursion equations change.

$x - y$	$x + 2y$	Type of site	Recursion equation
$6\,m_1$	$6\,m_2$	junction site (1)	$w_n(x, y) =$ $\frac{1}{2}[w_{n-1}(x, y + 1) + w_{n-1}(x - 1, y) + w_{n-1}(x + 1, y - 1)]$
$6\,m_1 - 2$	$6\,m_2 - 2$	junction site (2)	$w_n(x, y) =$ $\frac{1}{2}[w_{n-1}(x + 1, y) + w_{n-1}(x - 1, y + 1) + w_{n-1}(x, y - 1)]$
$6\,m_1 - 1$	$6\,m_2 - 1$	corridor site (1)	$w_n(x, y) = \frac{1}{3}[w_{n-1}(x + 1, y) + w_{n-1}(x - 1, y)]$
$6\,m_1 - 1$	$6\,m_2 + 2$	corridor site (2)	$w_n(x, y) = \frac{1}{3}[w_{n-1}(x, y + 1) + w_{n-1}(x, y - 1)]$
$6\,m_1 + 2$	$6\,m_2 - 1$	corridor site (3)	$w_n(x, y) = \frac{1}{3}[w_{n-1}(x - 1, y + 1) + w_{n-1}(x + 1, y - 1)]$
$6\,m_1 + 1$	$6\,m_2 + 1$	cluster site (1)	$w_n(x, y) = 0$
$6\,m_1 + 2$	$6\,m_2 + 2$	cluster site (2)	$w_n(x, y) = 0$
$6\,m_1 + 3$	$6\,m_2 + 3$	cluster site (3)	$w_n(x, y) = 0$
$6\,m_1$	$6\,m_2 + 3$	cluster site (4)	$w_n(x, y) = 0$
$6\,m_1 + 1$	$6\,m_2 + 4$	cluster site (5)	$w_n(x, y) = 0$
$6\,m_1 + 3$	$6\,m_2$	cluster site (6)	$w_n(x, y) = 0$
$6\,m_1 + 4$	$6\,m_2 + 1$	cluster site (7)	$w_n(x, y) = 0$

6. Summary and Outlook

Surface diffusion is one of the elementary steps in heterogeneous catalytic reactions. A deeper understanding of the underlying processes and mechanisms is fundamental. Scanning tunneling spectroscopy has special advantages for investigating surface diffusion because it can combine high spatial resolution (down to the atomic level) with high temporal resolution in the high-speed mode. By additionally varying the temperature, surface processes can be slowed down or accelerated to adjust their rate to the resolution of the microscope.

In this thesis, I used a high-speed variable temperature STM setup to investigate two different systems. The focus was on single oxygen atoms and small hydrocarbon fragments on the Ru(0001) surface. Individual atoms or molecules were tracked over a wide temperature range, and the evaluation of the jump distributions revealed insights into the kinetics and mechanisms of the surface processes.

A carbon evaporator was characterized by analyzing the species evaporated on Au(111) and Ru(0001) crystal surfaces. STM measurements after evaporation on cold surfaces (< -70 °C) indicated that atomic carbon is the initial species impinging on the sample. In an activated process, larger molecules or agglomerates of carbon form. On the Au(111) surface, these species agglomerate in the elbows of the herringbone reconstruction at room temperature. On the Ru(0001) surface, the species are smaller, and two main features were identified at room temperature: an immobile round species and smaller elliptic particles. As TD spectra showed that hydrogen is also present on the surface, the observed species are interpreted as hydrocarbon derivates.

The elliptical particles (*dimers*) were not only observed after evaporation of carbon at ≈ 50 °C, but also after dosing a few Langmuirs of ethylene (0.25 - 2 L). This method was more precise and less time consuming. The *dimer* particles were the subject of a detailed diffusion study. The adsorption site of the *dimer* particles is either the hcp or the fcc site. At temperatures up to ≈ 80 °C, the particles are pinned to one Ru atom around which they perform triangular jumps. During this process, the *dimer* particles move between three hollow sites around one Ru atom and change their orientation. A second jump process was detected at temperatures

above 80 °C, which is referred to as on-site rotation. The center of rotation is the center of gravity of the *dimer* particle and during rotation the particles do not change their adsorption site. The combination of both rotations leads to lateral diffusion.

STM movies of the *dimer* particles were recorded in a temperature range from -13 °C to 124 °C, and a wavelet-based tracking algorithm was used to monitor the trajectories of the particles. By fitting the displacement histograms with a recursion model based on the two rotations, the temperature-dependent jump frequencies were extracted. The kinetic investigation of the two independent motions resulted in two very different energy barriers, 0.36 ± 0.03 eV for the triangular jumps and 1.27 ± 0.21 eV for the on-site rotations. These barriers are connected with very different preexponential factors, $10^{5.94\pm0.5}$ Hz for the triangular jumps and $10^{17.0\pm2.9}$ Hz for the on-site rotations. This finding corresponds to a compensation effect which became manifest by the fact that the two linear fits in the Arrhenius plot crossed at a finite temperature.

It was discussed how the strong difference of the activation energies might be related to the difference of the preexponential factors that contain the activation entropy. In the case of the triangular jumps, a confined transition state that rather strongly binds to the surfaces may result in a small energy barrier and a low entropy. In contrast, the high entropy in the case of the on-site rotations is explained by fewer constraints in the transition state. An alternative explanation is based on the fact that a higher number of phonons is required to bring up the higher activation energy. That these contrasting effects appear in elementary rotations of single molecules is remarkable.

Many attempts were made to determine the exact atomic composition of the *dimer* particles. It is evident that the particle consists of more than two, probably four carbon atoms and contains hydrogen atoms. The elliptic shape indicates mirror symmetry. My cooperation partner Sung Sakong investigated the stability and rotation barriers of several hydrocarbon derivates up to C_4-species. The most promising candidate was CCH-HCC, although it did not match the experimental jump barriers. The exact nature of the *dimer* particles is still open.

Suggestions for further investigations are:

- Quantitative TDS to quantify the amount of hydrogen that desorbs when the *dimer*-covered Ru(0001) surface is heated

- Vibrational spectroscopy under conditions at which the *dimer* particles were observed by STM

- XPS measurements with high resolution (probably at a synchrotron facility) to measure the exact chemical shift of the carbon atoms present in the molecule (overlap with Ruthenium signal might be problematic)

- STM or atomic force microscopy (AFM) measurements of the *dimer* particles at $-269\,°C$ (4 K) to probe the HOMO and LUMO states by scanning tunneling spectroscopy (STS) and possibly identify the positions of the H atoms by inelastic electron tunneling spectroscopy (IETS)

In the second part of this work, tracer diffusion of O atoms embedded in a CO-adlayer on a Ru(0001) surface and the high coverage structure of CO on the same surface were investigated. The investigations addressed the question how structures at high CO coverage are built on the Ru(0001) surface and whether the mobility of coadsorbates O atoms is restricted on such a surface. Crowded surfaces reflect the high coverage situation on catalysis surfaces under reaction conditions, where microkinetic models assume that surface diffusion processes are not rate-limiting. The present results confirm this assumption.

It has been known from previous studies that O atoms diffuse by the fluctuation-driven so-called door-opening mechanism in the ordered $(\sqrt{3} \times \sqrt{3})R30°$ CO structure ($\theta = 0.33$ ML). It has furthermore been known that this mechanism is still active at a CO coverage of 0.47 ML, where the CO adlayer has undergone an order-disorder transition and the mobility of the O atoms is enhanced compared to the lower coverage.

In the first project it has been observed that O atoms preferentially move along domain boundaries of two $(\sqrt{3} \times \sqrt{3})R30°$ CO domains. The diffusion constant was found to be 1 to 2 orders of magnitude enhanced compared to the diffusion within the ordered CO domains. The reasons are the enhanced CO fluctuations in the disordered configurations that enable a faster O diffusion.

In the second project of this part the structure of the saturated CO layer on the Ru(0001) surface was determine. By combining STM with DFT calculations a long-standing conflict between the interpretation of LEED diffraction patterns and findings in vibrational spectroscopy was solved. The STM measurements revealed that at 0.66 ML a structure is formed that involves compact CO islands consisting of 7 to 19 CO molecules. All CO molecules adsorb on on-top sites. The inside of the

clusters displays a pseudo (1×1) structure, while the CO molecules at the cluster rims are tilted outward. The stability of the structure was verified by DFT measurements, and Tersoff-Hamann STM simulations match the experimental results. The reflection spots in the LEED pattern were reproduced by Fourier transformations of the STM images.

In the third project of this part O atoms embedded in the CO-saturated adlayer on the Ru(0001) surface were investigated with respect to their mobility. The CO fluctuations at the high coverage of 0.66 ML are energetically more costly than at low coverages but still open diffusion pathways for the O atoms. Repulsive interactions between the CO molecules and O atoms are stronger at this high coverage as the distances are shorter. The adsorption energy of the O atoms and therefore the activation barrier for diffusion is lower. This effect is dominating in the high coverage regime. In sum, the mobility of the O atoms at saturation is higher than at lower coverages, in contrast to expectations. The door-opening diffusion mechanism stays intact over the whole coverage range of CO from 0.33 ML to saturation at 0.66 ML.

Supplementary Tables

Table 6.1 : List of abbreviations used in this work.

Abbreviation	Meaning
AES	Auger Electron Spectroscopy
AFM	Atomic Force Microscopy
CCD	Charge-Coupled Device
DFT	Density Functional Theory
fcc	face centered cubic
FEM	Field Emission Microscopy
FIM	Field Ion Microscopy
fps	frames per second
hcp	hexagonal close packed
HREELS	High-Resolution Electron Energy Loss Spectroscopy
HV	High Voltage
IETS	Inelastic Electron Tunneling Spectroscopy
IR	Infrared
L	Langmuir
LDOS	Local Density of States
LEED	Low Energy Electron Diffraction
LEEM	Low Energy Electron Microscopy
LITD	Laser-Induced Thermal Desorption
LMU	Ludwig-Maximilians-Universität
LOD	Linear Optic Diffraction
PEEM	Photoelectron Energy Microscope
px	Pixel
QMS	Quadrupole Mass Spectrometer
RAIRS	Reflection-Absorption Infrared Spectroscopy
RT	Room Temperature
SHD	Second-Harmonic Diffraction
STM	Scanning Tunneling Microscopy
STS	Scanning Tunneling Spectroscopy

TDS	Thermal Desorption Spectroscopy
UHV	Ultra-High Vacuum
VSF	Vibration Sum Frequency
VT-STM	Variable Temperature STM
XPS	X-ray Photoelectron Spectroscopy

Table 6.2 : List of symbols used in this work.

Symbol	Meaning
a	Lattice Constant
A, A_0	Preexponential Factor
C_{evap}	Amount of Evaporated Carbon (in nAs)
Γ	Jump Frequency
Γ^0	Preexponential Factor, Attempt Frequency
D	Diffusion Coefficient
D_0	Preexponential Factor
e	Elementary Charge
E_a, E^*	Activation Barrier
E_d	Energy Barrier for Diffusion
E_F	Fermi Energy
E_{kin}	Kinetic Energy
ϵ_{ph}	Energy of a Phonon
E_{vac}	Energy of the Vacuum Level
G	Gibbs Free Energy
h	Planck Constant
H	Enthalpy
$\hbar$	Reduced Planck Constant
$H^{\ddagger}$	Enthalpy of the Transition State
$h^{\ddagger}$	Enthalpy of the Transition State for a single atom/molecule
I_{emis}	Emission Current
I_{fil}	Filament Current
I_{flux}	Flux Current
I_t	Tunneling Current
κ	Decay Length

k	Rate Constant
k_{B}	Boltzmann Constant
λ	Lattice Constant
m_e	Electron Mass
N	Number of Available Phonons in Interaction Volume
n	Number of Required Phonons for Excitation
n_1	Number of triangular jumps
n_2	Number of on-site rotations
$n_{\mathrm{C}}^{\mathrm{cluster}}$	Number of C atoms in cluster particle
n_{C}^{dimer}	Number of C atoms in *dimer* particle
Φ_{eff}	Effective Tunneling Barrier
Φ_{sample}	Work Function of the Sample
Φ_{tip}	Work Function of the Tip
p	Momentum; Pressure
$\tilde{P}_{t_0}(n_1, n_2)$	Probability for the Combination of n_1 and n_2 events in time interval t_0
$P_{t_0}(x, y)$	Probability to find a Particle at Position (x,y) after t_0
$\langle r^2 \rangle$	Mean-square Displacement
R	Ideal Gas Constant
s	Tip-Sample Distance
S	Entropy
$S^{\ddagger}$	Entropy of the Transition State
$s^{\ddagger}$	Entropy of the Transition State for a single atom/molecule
θ	Coverage
t	Time
T	Absolute Temperature
t_{evap}	Evaporation Time
v	Frequency
V_{t}	Tunneling Voltage
w	Possibility
w_{n_1, n_2}	Geometric Factor for n_1 triangular jumps and n_2 on-site rotations
x	Direction/Position along the x-axis
y	Direction/Position along the y-axis

Table 6.3 : STM Data of figures in Chapter 3.

Figure	File	Frame	Pixel	Nominal Range [Å]	Scan Frequency [Hz]	V_t [V]	I_t [nA]	T
3.2 (a)	200828_12	6	512	2000	4	—1.0	1	RT
3.2 (b)	200901_7	15	512	300	4	—1.0	1	RT
3.4 (a)	201027_17	1	512	2000	2	—1.0	1	RT
3.4 (b)	201019_8	1	512	500	4	—0.2	1	RT
3.4 (c)	201019_8	17	512	500	4	—0.2	1	RT
3.5	201208_7	1	512	2000	2	—1.0	1	—155 °C
3.6	201208_15	0	512	2000	2	—1.0	1	—20 °C
3.8 (a)	210817_13	1	512	250	4	—1.0	1	RT
3.8 (b)	220125_12	1	512	500	2	—0.4	1	RT
3.10	220427_6	5	512	250	4	—1.0	1	—203 °C
3.11 (a)	220427_8	369	200	150	2000	—1.0	3	—203 °C
3.11 (b)	220427_10	1001	200	150	2000	—1.0	3	—203 °C
3.11 (c)	220428_32	560	200	150	2000	—0.2	3	—77 °C
3.11 (d)	220428_32	960	200	150	2000	—0.2	3	—77 °C
3.12 (a)	220602_26	3	512	500	4	—0.2	1	RT
3.12 (b)	220602_28	2604	200	150	2000	—1.0	3	RT

Table **6.4** : STM Data of figures in Chapter 4.

Figure	File	Frame	Pixel	Nominal Range [Å]	Scan Frequency [Hz]	V_t [V]	I_t [nA]	T
4.1 (a)	230621_8	1	512	250	4	−0.2	1	RT
4.1 (b)	230621_17	2108	200	150	2000	−0.2	3	RT
4.2 (a)	211123_15	51	200	150	2000	−0.22	3	30 °C
4.2 (b)	211123_15	54	200	150	2000	−0.22	3	30 °C
4.2 (c)	211123_15	56	200	150	2000	−0.22	3	30 °C
4.3 (a)	240227_8	935	200	150	2000	−1.5	3	30 °C
4.3 (b)	240227_8	964	200	150	2000	−1.5	3	30 °C
4.3 (c)	240227_8	980	200	150	2000	−1.5	3	30 °C
4.3 (g)	240227_8	1303	200	150	2000	−1.5	3	30 °C
4.3 (h)	240227_8	1341	200	150	2000	−1.5	3	30 °C
4.3 (i)	240227_8	1395	200	150	2000	−1.5	3	30 °C
4.4 (a)	220317_20	1336, 1337	200	150	2000	−0.8	3	112 °C
4.4 (b)	220317_20	1525, 1526	200	150	2000	−0.8	3	112 °C
4.5	220317_17	927, 928, 935, 968, 1080, 1083	200	150	2000	−0.8	3	112 °C
4.6 (a)	220623_14	4	512	500	4	−1.0	1	RT
4.6 (b)	220623_11	4	512	250	4	−0.2	1	RT
4.6 (c)	220623_7	1362	200	150	2000	−0.2	3	RT
4.6 (d)	220623_7	1638	200	150	2000	−1.2	3	RT

Figure	File	Frame	Pixel	Nominal Range [Å]	Scan Frequency [Hz]	V_t [V]	I_t [nA]	T
4.7 (a)	230828_8	1470, 1500	200	150	2000	−0.2	3	−202 °C
4.7 (b)	230828_8	1851, 1911	200	150	2000	−0.2	3	−202 °C
4.8 (a)	230828_16	3113	200	150	2000	−0.2	3	−202 °C
4.8 (b)	230828_25a1	211	200	150	2000	−0.2	3	−202 °C
4.8 (c)	230828_31a1	95	200	150	2000	−0.2	3	−202 °C
4.9	230621_23	3	512	500	4	−1.0	1	RT
4.10 (a)	240507_22	4	512	1000	4	−0.2	1	RT
4.10 (b)	240507_26	5	512	3000	4	−0.2	1	RT
4.11	240514_17	7	512	1000	4	−1.0	1	RT
4.12 (a)	240605_8	5	512	1000	4	−1.0	1	RT
4.12 (b)	240605_18	5	512	2000	4	−0.2	1	RT
4.16 (a)	220127_18	1092	200	150	2000	−0.8	3	24 °C
4.17 (a)	220127_42	2520	200	150	2000	−0.5	3	108 °C
4.17 (c)	220127_42	2466	200	150	2000	−0.5	3	108 °C
4.21 (a)	220127_18	1092	200	150	2000	−0.8	3	24 °C
4.21 (c)	220127_42	2520	200	150	2000	−0.5	3	108 °C

Table 6.5 : STM Data of figures in Chapter 5.

Figure	File	Frame	Pixel	Nominal Range [Å]	Scan Frequency [Hz]	V_t [V]	I_t [nA]	T
5.1 (table)	240514_14	1062	200	150	2000	−1.0	3	RT
	190918_27	379	200	150	2000	−0.22	3	−203 °C
	191920_14	1684	200	150	2000	−1.4	3	−203 °C

References

[1] Gomer, R. Diffusion of adsorbates on metal surfaces. *Reports on Progress in Physics* **1990**, *53*, 917–1002.

[2] Müller, E. W. Elektronenmikroskopische Beobachtungen von Feldkathoden. *Zeitschrift für Physik* **1937**, *106*, 541–550.

[3] Gomer, R., Field Emission Studies of Surface Diffusion of Adsorbates In *Surface Mobilities on Solid Materials: Fundamental Concepts and Applications*, Binh, V. T., Ed.; Springer US: Boston, MA, **1983**, 127–159.

[4] Pichaud, M.; Drechsler, M. A field emission measurement of the influence of adsorption on surface self-diffusion. *Surface Science* **1972**, *32*, 341–348.

[5] Beben, J. Investigation of Surface Diffusion by Analysis of Field Emission Current Fluctuations. *Solid State Phenomena* **1991**, *12*, 17–38.

[6] Müller, E. W. Das Feldionenmikroskop. *Zeitschrift für Physik* **1951**, *131*, 136–142.

[7] Viswanathan, R.; Burgess, D. R.; Stair, P. C.; Weitz, E. Laser-induced thermal desorption of CO from clean polycrystalline copper: Time-of-flight and surface diffusion measurements. *Journal of Electron Spectroscopy and Related Phenomena* **1983**, *29*, 111.

[8] Seebauer, E. G.; Schmidt, L. D. Surface diffusion of hydrogen on Pt(111): laser-induced thermal desorption studies. *Chemical Physics Letters* **1986**, *123*, 129–133.

[9] Engel, W.; Kordesch, M. E.; Rotermund, H. H.; Kubala, S.; von Oertzen, A. A UHV-compatible photoelectron emission microscope for applications in surface science. *Ultramicroscopy* **1991**, *36*, 148–153.

[10] Von Oertzen, A.; Rotermund, H. H.; Nettesheim, S. Diffusion of carbon monoxide and oxygen on Pt(110): experiments performed with the PEEM. *Surface Science* **1994**, *311*, 322–330.

[11] Kattwinkel, L.; Magnussen, O. M. Measurement of Surface Diffusion at the Electrochemical Interface by In Situ Linear Optical Diffraction. *ACS Measurement Science Au* **2023**, *3*, 98–102.

[12] Ellis, J.; Toennies, J. P. Observation of jump diffusion of isolated sodium atoms on a Cu(001) surface by helium atom scattering. *Physical Review Letters* **1993**, *70*, 2118–2121.

[13]   Graham, A. P.; Hofmann, F.; Toennies, J. P.; Chen, L. Y.; Ying, S. C. Experimental and theoretical investigation of the microscopic vibrational and diffusional dynamics of sodium atoms on a Cu(001) surface. *Physical Review B* **1997**, *56*, 10567–10578.

[14]   Binnig, G.; Rohrer, H. Scanning tunneling microscopy. *Helv. Phys. Acta* **1982**, *55*, 726–735.

[15]   Binnig, G.; Rohrer, H. Scanning tunneling microscopy. *Surface Science* **1983**, *126*, 236–244.

[16]   Binnig, G.; Fuchs, H.; Stoll, E. Surface diffusion of oxygen atoms individually observed by STM. *Surface Science Letters* **1986**, *169*, L295–L300.

[17]   Lozano, M. L.; Tringides, M. C. Surface Diffusion Measurements from STM Tunneling Current Fluctuations. *Europhysics Letters* **1995**, *30*, 537.

[18]   Swartzentruber, B. S. Direct Measurement of Surface Diffusion Using Atom-Tracking Scanning Tunneling Microscopy. *Physical Review Letters* **1996**, *76*, 459–462.

[19]   Wang, K.; Ming, F.; Huang, Q.; Zhang, X.; Xiao, X. Study of CO diffusion on stepped Pt(111) surface by scanning tunneling microscopy. *Surface Science* **2010**, *604*, 322–326.

[20]   Gómez-Rodríguez, J. M.; Sáenz, J. J.; Baró, A. M.; Veuillen, J. Y.; Cinti, R. C. Real-Time Observation of the Dynamics of Single Pb Atoms on Si(111)-(7 × 7) by Scanning Tunneling Microscopy. *Physical Review Letters* **1996**, *76*, 799–802.

[21]   Zambelli, T.; Trost, J.; Wintterlin, J.; Ertl, G. Diffusion and Atomic Hopping of N Atoms on Ru(0001) Studied by Scanning Tunneling Microscopy. *Physical Review Letters* **1996**, *76*, 795–798.

[22]   Henß, A. K.; Wiechers, J.; Schuster, R.; Platschkowski, V.; Wintterlin, J. A beetle-type, variable-temperature scanning tunneling microscope for video-rate imaging. *Japanese Journal of Applied Physics* **2020**, *59*, SN1007.

[23]   Messer, P. K.; Henß, A. K.; Lamb, D. C.; Wintterlin, J. A multiscale wavelet algorithm for atom tracking in STM movies. *New Journal of Physics* **2022**, *24*, 033016.

[24]   Henß, A.-K. Diffusion in a Crowded Adsorbate Layer - A Video-Rate Scanning Tunneling Microscopy Study, Thesis, **2019**.

[25]   Henß, A.-K.; Sakong, S.; Messer, P. K.; Wiechers, J.; Schuster, R.; Lamb, D. C.; Groß, A.; Wintterlin, J. Density fluctuations as door-opener for diffusion on crowded surfaces. *Science* **2019**, *363*, 715–718.

[26]   Gritsch, T. Oberflächenstrukturen, Strukturumwandlungsprozesse und Adsorbate auf Pt(110) und Au(110) – Eine STM Untersuchung, Thesis, **1990**.

[27]   Ertl, G.; Küppers, J. Low Energy Electrons and Surface Chemistry. *Zeitschrift für Chemie* **1975**, *15*, 499–500.

[28] Seah, M. P.; Dench, W. A. Quantitative electron spectroscopy of surfaces: A standard data base for electron inelastic mean free paths in solids. *Surface and Interface Analysis* **1979**, *1*, 2–11.

[29] Tersoff, J.; Hamann, D. R. Theory and Application for the Scanning Tunneling Microscope. *Physical Review Letters* **1983**, *50*, 1998–2001.

[30] Tersoff, J.; Hamann, D. R. Theory of the scanning tunneling microscope. *Physical Review B* **1985**, *31*, 805–813.

[31] Besocke, K. An easily operable scanning tunneling microscope. *Surface Science* **1987**, *181*, 145–153.

[32] Frohn, J.; Wolf, J. F.; Besocke, K.; Teske, M. Coarse tip distance adjustment and positioner for a scanning tunneling microscope. *Review of Scientific Instruments* **1989**, *60*, 1200–1201.

[33] Goodman, D. W.; White, J. M. Measurement of active carbon on ruthenium (110): Relevance to catalytic methanation. *Surface Science* **1979**, *90*, 201–203.

[34] Van Staden, M. J.; Roux, J. P. The superposition of carbon and ruthenium auger spectra. *Applied Surface Science* **1990**, *44*, 259–262.

[35] Marchini, S.; Günther, S.; Wintterlin, J. Scanning tunneling microscopy of graphene on Ru(0001). *Physical Review B* **2007**, *76*, 075429.

[36] Davis, L.; MacDonald, N.; Palmberg, P.; Riach, G.; Weber, R., Handbook of Auger electron spectroscopy; Physical Electronics Industries, Inc.: **1976**; *1*.

[37] Klink, C.; Stensgaard, I.; Besenbacher, F.; Lægsgaard, E. An STM study of carbon-induced structures on Ni(111): evidence for a carbidic-phase clock reconstruction. *Surface Science* **1995**, *342*, 250–260.

[38] Klink, C.; Stensgaard, I.; Besenbacher, F.; Lægsgaard, E. Carbidic carbon on Ni(110): an STM study. *Surface Science* **1996**, *360*, 171–179.

[39] Land, T. A.; Michely, T.; Behm, R. J.; Hemminger, J. C.; Comsa, G. STM investigation of single layer graphite structures produced on Pt(111) by hydrocarbon decomposition. *Surface Science* **1992**, *264*, 261–270.

[40] Weststrate, C. J.; Kızılkaya, A. C.; Rossen, E. T. R.; Verhoeven, M. W. G. M.; Ciobîcă, I. M.; Saib, A. M.; Niemantsverdriet, J. W. Atomic and Polymeric Carbon on Co(0001): Surface Reconstruction, Graphene Formation, and Catalyst Poisoning. *The Journal of Physical Chemistry C* **2012**, *116*, 11575–11583.

[41] Günther, S.; Dänhardt, S.; Ehrensperger, M.; Zeller, P.; Schmitt, S.; Wintterlin, J. High-Temperature Scanning Tunneling Microscopy Study of the Ordering Transition of an Amorphous Carbon Layer into Graphene on Ruthenium(0001). *ACS Nano* **2012**, *7*, 154–164.

[42] Shimizu, T. K.; Mugarza, A.; Cerda, J. I.; Salmeron, M. Structure and reactions of carbon and hydrogen on Ru(0001): a scanning tunneling microscopy study. *J Chem Phys* **2008**, *129*, 244103.

[43] McCarty, K. F.; Feibelman, P. J.; Loginova, E.; Bartelt, N. C. Kinetics and thermodynamics of carbon segregation and graphene growth on Ru(0001). *Carbon* **2009**, *47*, 1806–1813.

[44] Schelz, S.; Richmond, T.; Kania, P.; Oelhafen, P.; Güntherodt, H. J. Electronic and atomic structure of evaporated carbon films. *Surface Science* **1996**, *359*, 227–236.

[45] Loginova, E.; Bartelt, N. C.; Feibelman, P. J.; McCarty, K. F. Evidence for graphene growth by C cluster attachment. *New Journal of Physics* **2008**, *10*, 093026.

[46] GmbH, F., Electron beam evaporator with Flux Monitor; EFM Series for Ultra-Pure Submonolayer and Multilayer Thin Film Growth; Focus GmbH: **2023**.

[47] GmbH, O. N., Instruction Manual UHV Evaporator EFM 2/3/3s/4, **2008**.

[48] De Mongeot, F. B.; Toma, A.; Molle, A.; Lizzit, S.; Petaccia, L.; Baraldi, A. Carbon Monoxide Dissociation on Rh Nanopyramids. *Phys. Rev. Lett.* **2006**, *97*, 056103.

[49] Grüneis, A.; Kummer, K.; Vyalikh, D. V. Dynamics of graphene growth on a metal surface: a time-dependent photoemission study. *New Journal of Physics* **2009**, *11*, 073050.

[50] Barth, J. V. Zur Struktur von reinen und Alkalimetall-bedeckten Goldoberflächen, Thesis, **1992**.

[51] Shimizu, T. K.; Mugarza, A.; Cerdá, J. I.; Heyde, M.; Qi, Y.; Schwarz, U. D.; Ogletree, D. F.; Salmeron, M. Surface Species Formed by the Adsorption and Dissociation of Water Molecules on a Ru(0001) Surface Containing a Small Coverage of Carbon Atoms Studied by Scanning Tunneling Microscopy. *The Journal of Physical Chemistry C* **2008**, *112*, 7445–7454.

[52] Mak, C. H.; Koehler, B. G.; Brand, J. L.; George, S. M. Surface diffusion of hydrogen on carbon-covered Ru(001) surfaces studied using laser-induced thermal desorption. *The Journal of Chemical Physics* **1987**, *87*, 2340–2345.

[53] Brand, J. L.; Deckert, A. A.; George, S. M. Surface diffusion of hydrogen on sulfur-covered Ru(001) surfaces studied using laser-induced thermal desorption. *Surface Science* **1988**, *194*, 457–474.

[54] Westre, E. D.; Brown, D. E.; Kutzner, J.; George, S. M. Surface diffusion of carbon monoxide and potassium coadsorbed on Ru(001): Confirmation of a 1:1 CO:K trapping interaction. *The Journal of Chemical Physics* **1996**, *104*, 7313–7324.

[55] Zhao, W.; Asscher, M. Coverage grating template for the study of surface diffusion: K coadsorbed with CO on Re(001). *Surface Science* **1999**, *429*, 1–13.

[56] Song, Y.; Gomer, R. Diffusion of CO on the Mo(110) plane. *Surface Science* **1993**, *295*, 174–182.

[57] Xiao, X.-D.; Xie, Y.; Jakobsen, C.; Galloway, H.; Salmeron, M.; Shen, Y. R. Impurity Effect on Surface Diffusion: CO/S/Ni(110). *Physical Review Letters* **1995**, *74*, 3860–3863.

[58] Mak, C. H.; Deckert, A. A.; George, S. M. Effects of coadsorbed carbon monoxide on the surface diffusion of hydrogen on Ru(001). *The Journal of Chemical Physics* **1988**, *89*, 5242–5250.

[59] Magnussen, O. M. Atomic-Scale Insights into Electrode Surface Dynamics by High-Speed Scanning Probe Microscopy. *Chemistry – A European Journal* **2019**, *25*, 12865–12883.

[60] Rahn, B.; Wen, R.; Deuchler, L.; Stremme, J.; Franke, A.; Pehlke, E.; Magnussen, O. M. Coadsorbate-Induced Reversal of Solid-Liquid Interface Dynamics. *Angewandte Chemie International Edition* **2018**, *57*, 6065–6068.

[61] Hsieh, M.-F.; Lin, D.-S.; Tsay, S.-F. Possibility of direct exchange diffusion of hydrogen on the Cl/Si(100)-2×1 surface. *Physical Review B* **2009**, *80*, 045304.

[62] Kolsbjerg, E. L.; Goubert, G.; McBreen, P. H.; Hammer, B. Rotation and diffusion of naphthalene on Pt(111). *The Journal of Chemical Physics* **2018**, *148*, 124703.

[63] Weckesser, J.; Barth, J. V.; Kern, K. Direct observation of surface diffusion of large organic molecules at metal surfaces: PVBA on Pd(110). *The Journal of Chemical Physics* **1999**, *110*, 5351–5354.

[64] Stipe, B. C.; Rezaei, M. A.; Ho, W. Coupling of Vibrational Excitation to the Rotational Motion of a Single Adsorbed Molecule. *Physical Review Letters* **1998**, *81*, 1263–1266.

[65] Matsumoto, C.; Kim, Y.; Okawa, T.; Sainoo, Y.; Kawai, M. Low-temperature STM investigation of acetylene on Pd(111). *Surface Science* **2005**, *587*, 19–24.

[66] Stipe, B. C.; Rezaei, M. A.; Ho, W. Inducing and Viewing the Rotational Motion of a Single Molecule. *Science* **1998**, *279*, 1907–1909.

[67] Shchadilova, Y. E.; Tikhodeev, S. G.; Paulsson, M.; Ueba, H. Rotation of a Single Acetylene Molecule on Cu(001) by Tunneling Electrons in STM. *Physical Review Letters* **2013**, *111*, 186102.

[68] Rosei, F.; Schunack, M.; Naitoh, Y.; Jiang, P.; Gourdon, A.; Laegsgaard, E.; Stensgaard, I.; Joachim, C.; Besenbacher, F. Properties of large organic molecules on metal surfaces. *Progress in Surface Science* **2003**, *71*, 95–146.

[69] Gimzewski, J. K.; Joachim, C.; Schlittler, R. R.; Langlais, V.; Tang, H.; Johannsen, I. Rotation of a Single Molecule Within a Supramolecular Bearing. *Science* **1998**, *281*, 531–533.

[70] Baber, A. E.; Tierney, H. L.; Sykes, E. C. H. A Quantitative Single-Molecule Study of Thioether Molecular Rotors. *ACS Nano* **2008**, *2*, 2385–2391.

[71] Tierney, H. L.; Han, J. W.; Jewell, A. D.; Iski, E. V.; Baber, A. E.; Sholl, D. S.; Sykes, E. C. H. Chirality and Rotation of Asymmetric Surface-Bound Thioethers. *The Journal of Physical Chemistry C* **2011**, *115*, 897–901.

[72] Tierney, H. L.; Murphy, C. J.; Jewell, A. D.; Baber, A. E.; Iski, E. V.; Khodaverdian, H. Y.; McGuire, A. F.; Klebanov, N.; Sykes, E. C. H. Experimental demonstration of a single-molecule electric motor. *Nature Nanotechnology* **2011**, *6*, 625–629.

[73] Jewell, A. D.; Tierney, H. L.; Baber, A. E.; Iski, E. V.; Laha, M. M.; Sykes, E. C. H. Time-resolved studies of individual molecular rotors. *Journal of Physics: Condensed Matter* **2010**, *22*, 264006.

[74] Barragán, A.; Nicolás-García, T.; Lauwaet, K.; Sánchez-Grande, A.; Urgel, J. I.; Björk, J.; Pérez, E. M.; Écija, D. Design and Manipulation of a Minimalistic Hydrocarbon Nanocar on Au(111). *Angewandte Chemie International Edition* **2023**, *62*, e202212395.

[75] Shimizu, H.; Christmann, K.; Ertl, G. Model studies on bimetallic Cu/Ru catalysts: II. Adsorption of hydrogen. *Journal of Catalysis* **1980**, *61*, 412–429.

[76] Martoccia, D.; Willmott, P. R.; Brugger, T.; Björck, M.; Günther, S.; Schlepütz, C. M.; Cervellino, A.; Pauli, S. A.; Patterson, B. D.; Marchini, S.; Wintterlin, J.; Moritz, W.; Greber, T. Graphene on Ru(0001): A 25×25 Supercell. *Physical Review Letters* **2008**, *101*, 126102.

[77] Hills, M. M.; Parmeter, J. E.; Mullins, C. B.; Weinberg, W. H. Interaction of ethylene with the ruthenium(001) surface. *Journal of the American Chemical Society* **1986**, *108*, 3554–3562.

[78] Barteau, M. A.; Broughton, J. Q.; Menzel, D. Vibrational spectroscopy of hydrocarbon intermediates on Ru(001). *Applications of Surface Science* **1984**, *19*, 92–115.

[79] Parlett, P. M.; Chesters, M. A. The surface reactions of ethene on Ru(001) studied by reflection-absorption infrared spectroscopy. *Surface Science* **1996**, *357-358*, 791–795.

[80] Ren, Y.; Waluyo, I.; Beale, E.; Trenary, M. Hydrogenation and dehydrogenation reactions of C2Hx moieties on the Ru(001) surface. *Surface Science* **2016**, *650*, 144–148.

[81] Kirsch, H.; Tong, Y.; Campen, R. K. Experimental Characterization of CCH(ads) and CCH_2(ads) during the Thermal Decomposition of Methane and Ethylene on Ru(0001). *ChemCatChem* **2016**, *8*, 728–735.

[82] Jakob, P.; Cassuto, A.; Menzel, D. Adsorption and reaction of acetylene on Ru(001): Vibrational spectroscopy and thermal desorption. *Surface Science* **1987**, *187*, 407–433.

[83] Parmeter, J.; Hills, M.; Weinberg, W. Interaction of acetylene with the ruthenium (001) surface. *Journal of the American Chemical Society* **1986**, *108*, 3563–3569.

[84] Kirsch, H.; Zhao, X.; Ren, Z.; Levchenko, S. V.; Wolf, M.; Campen, R. K. Controlling CH_2 dissociation on Ru(0001) through surface site blocking by adsorbed hydrogen. *Journal of Catalysis* **2014**, *320*, 89–96.

[85] Ande, C. K.; Elliott, S. D.; Kessels, W. M. M. First-Principles Investigation of C–H Bond Scission and Formation Reactions in Ethane, Ethene, and Ethyne Adsorbed on Ru(0001). *The Journal of Physical Chemistry C* **2014**, *118*, 26683–26694.

[86] Chiu, C.-c.; Genest, A.; Rösch, N. Decomposition of Ethanol Over Ru(0001): A DFT Study. *Topics in Catalysis* **2013**, *56*, 874–884.

[87] Ibach, H., Physics of Surfaces and Interfaces; Springer-Verlag: Berlin Heidelberg, **2006**; *1*.

[88] Kim, H.; Saiz, E.; Chhowalla, M.; Mattevi, C. Modeling of the self-limited growth in catalytic chemical vapor deposition of graphene. *New Journal of Physics* **2013**, *15*, 053012.

[89] Illner, H.; Sakong, S.; Henß, A.-K.; Groß, A.; Wintterlin, J. Diffusion of O Atoms on a CO-Covered Ru(0001) Surface - A Combined High-Speed Scanning Tunneling Microscopy and Density Functional Theory Study at an Enhanced CO Coverage. *The Journal of Physical Chemistry C* **2023**, *127*, 7197–7210.

[90] Illner, H.; Sakong, S.; Groß, A.; Wintterlin, J. Solution of the structure of the high-coverage CO layer on the Ru(0001) surface - A combined study by density functional theory and scanning tunneling microscopy. *The Journal of Chemical Physics* **2024**, *161*, 014703.

[91] Gao, M.; Zhang, Y.-F.; Huang, L.; Pan, Y.; Wang, Y.; Ding, F.; Lin, Y.; Du, S.-X.; Gao, H.-J. Unveiling carbon dimers and their chains as precursor of graphene growth on Ru(0001). *Applied Physics Letters* **2016**, *109*, 131604.

[92] Chen, H.; Zhu, W.; Zhang, Z. Contrasting Behavior of Carbon Nucleation in the Initial Stages of Graphene Epitaxial Growth on Stepped Metal Surfaces. *Physical Review Letters* **2010**, *104*, 186101.

[93] Mahlberg, D.; Groß, A. Vacancy assisted diffusion on single-atom surface alloys. *ChemPhysChem* **2021**, *22*, 29–39.

[94] Xu, L.; Mavrikakis, M. Adsorbate-Induced Adatom Formation on Lithium, Iron, Cobalt, Ruthenium, and Rhenium Surfaces. *JACS Au* **2023**, *3*, 2216–2225.

[95] Cui, Y.; Fu, Q.; Tan, D.; Bao, X. Temperature Dependence of the Formation of Graphene and Subsurface Carbon on Ru(0001) and Its Effect on Surface Reactivity. *ChemPhysChem* **2010**, *11*, 995–998.

[96] Conner, W. C. A general explanation for the compensation effect: The relationship between $\Delta S^{\ddagger}$ and activation energy. *Journal of Catalysis* **1982**, *78*, 238–246.

[97] Bligaard, T.; Honkala, K.; Logadottir, A.; Nørskov, J. K.; Dahl, S.; Jacobsen, C. J. H. On the Compensation Effect in Heterogeneous Catalysis. *The Journal of Physical Chemistry B* **2003**, *107*, 9325–9331.

[98] Patterson, W. R.; Rooney, J. J. An explanation of the compensation effect in catalysis. *Journal of Catalysis* **1994**, *146*, 310–312.

[99] Cremer, E.; Marschall, E. Heterogener Zerfall von N_2O an Katalysatoren mit variabler Aktivität. *Monatshefte für Chemie und verwandte Teile anderer Wissenschaften* **1951**, *82*, 840–846.

[100] Bond, G. C.; Hooper, A. D.; Slaa, J. C.; Taylor, A. O. Kinetics of Metal-Catalyzed Reactions of Alkanes and the Compensation Effect. *Journal of Catalysis* **1996**, *163*, 319–327.

[101] Cremer, E., The Compensation Effect in Heterogeneous Catalysis In *Advances in Catalysis*, Frankenburg, W. G., Komarewsky, V. I., Rideal, E. K., Eds.; Academic Press: **1955**, 75–91.

[102] Agrawal, R. K. On the compensation effect. *Journal of Thermal Analysis* **1986**, *31*, 73–86.

[103] Galwey, A. K., Compensation Effect in Heterogeneous Catalysis In *Advances in Catalysis*, Eley, D. D., Pines, H., Weisz, P. B., Eds.; Academic Press: **1977**, 247–322.

[104] Koga, N.; Šesták, J. Kinetic compensation effect as a mathematical consequence of the exponential rate constant. *Thermochimica Acta* **1991**, *182*, 201–208.

[105] Eyring, H. The Activated Complex in Chemical Reactions. *The Journal of Chemical Physics* **1935**, *3*, 107–115.

[106] Meyer, W.; Neldel, H. Über die Beziehungen zwischen der Energiekonstante e und der Mengenkonstate a in der Leitwerts-Temperaturformel bei oxydischen Halbleitern. *Z. Tech. Phys.* **1937**, *18*, 588–593.

[107] Yelon, A.; Movaghar, B. Microscopic explanation of the compensation (Meyer-Neldel) rule. *Physical Review Letters* **1990**, *65*, 618–620.

[108] Yelon, A.; Movaghar, B.; Branz, H. M. Origin and consequences of the compensation (Meyer-Neldel) law. *Physical Review B* **1992**, *46*, 12244–12250.

[109] Nilekar, A. U.; Greeley, J.; Mavrikakis, M. A Simple Rule of Thumb for Diffusion on Transition-Metal Surfaces. *Angewandte Chemie International Edition* **2006**, *45*, 7046–7049.

[110] Fuggle, J. C.; Madey, T. E.; Steinkilberg, M.; Menzel, D. Photoelectron spectroscopic studies of adsorption of CO and oxygen on Ru(001). *Surface Science* **1975**, *52*, 521–541.

[111] Madey, T. E.; Albert Engelhardt, H.; Menzel, D. Adsorption of oxygen and oxidation of CO on the ruthenium (001) surface. *Surface Science* **1975**, *48*, 304–328.

[112] Kostov, K. L.; Rauscher, H.; Menzel, D. Adsorption of CO on oxygen-covered Ru(001). *Surface Science* **1992**, *278*, 62–86.

[113] Narloch, B.; Held, G.; Menzel, D. A LEED-IV determination of the Ru(001)-p(2×2)(O+CO) structure: A coadsorbate-induced molecular tilt. *Surface Science* **1995**, *340*, 159–171.

[114] Stampfl, C.; Scheffler, M. Energy barriers and chemical properties in the coadsorption of carbon monoxide and oxygen on Ru(0001). *Physical Review B* **2002**, *65*, 155417.

[115] McEwen, J.-S.; Eichler, A. Phase diagram and adsorption-desorption kinetics of CO on Ru(0001) from first principles. *The Journal of Chemical Physics* **2007**, *126*, 094701.

[116] Lindroos, M.; Pfnür, H.; Held, G.; Menzel, D. Adsorbate induced reconstruction by strong chemisorption: Ru(001)p(2 × 2)-O. *Surface Science* **1989**, *222*, 451–463.

[117] Stampfl, C.; Scheffler, M. Theoretical study of O adlayers on Ru(0001). *Physical Review B* **1996**, *54*, 2868–2872.

[118] Williams, E. D.; Weinberg, W. H. The geometric structure of carbon monoxide chemisorbed on the ruthenium (001) surface at low temperatures. *Surface Science* **1979**, *82*, 93–101.

[119] Pfnür, H.; Menzel, D.; Hoffmann, F. M.; Ortega, A.; Bradshaw, A. M. High resolution vibrational spectroscopy of CO on Ru(001): The importance of lateral interactions. *Surface Science* **1980**, *93*, 431–452.

[120] Kaur, Y.; Gust, W., Fundamentals of Grain and Interface Boundary Diffusion; Wiley: Chichester, **1995**.

[121] Kaur, Y.; Gust, W.; Kozma, I., Handbook of Grain and Interphase Boundary Diffusion Data; Ziegler: Stuttgart, **1989**.

[122] Kügler, A.-K.; Illner, H.; Wintterlin, J. An STM study on the diffusion of O atoms on a CO-covered Ru(0001) surface - The role of domain boundaries. *Surface Science* **2025**, *751*, 122597.

[123] Biberian, J. P.; Van Hove, M. A. A new model for CO ordering at high coverages on low index metal surfaces: A correlation between LEED, HREELS and IRS: II. CO adsorbed on fcc (111) and hcp (0001) surfaces. *Surface Science* **1984**, *138*, 361–389.

[124] Böller, B.; Zeller, P.; Günther, S.; Wintterlin, J. High-Pressure CO Phases on Co(0001) and Their Possible Role in the Fischer–Tropsch Synthesis. *ACS Catalysis* **2020**, *10*, 12156–12166.

[125] Longwitz, S. R.; Schnadt, J.; Vestergaard, E. K.; Vang, R. T.; Stensgaard, I.; Brune, H.; Besenbacher, F. High-Coverage Structures of Carbon Monoxide Adsorbed on Pt(111) Studied by High-Pressure Scanning Tunneling Microscopy. *The Journal of Physical Chemistry B* **2004**, *108*, 14497–14502.

[126] Pfnür, H.; Heier, H. J. Order-Disorder Phenomena in the System CO/Ru(001). *Berichte der Bunsengesellschaft für physikalische Chemie* **1986**, *90*, 272–277.

[127] Thomas, G. E.; Weinberg, W. H. The vibrational spectrum and adsorption site of CO on the Ru(001) surface. *The Journal of Chemical Physics* **1979**, *70*, 1437–1439.

[128] He, P.; Dietrich, H.; Jacobi, K. Lateral interaction of CO chemisorbed on Ru(0001). *Surface Science* **1996**, *345*, 241–246.

[129] Illner, H.; Sakong, S.; Groß, A.; Wintterlin, J. Walk on a Flickering Path: Tracer Diffusion of Adsorbed O Atoms on a Ru(0001) Surface in the Limit of CO Saturation. *The Journal of Physical Chemistry C* **2025**, *129*, 18715–18726.

Danksagung

Am Ende meiner Dissertation möchte ich die Gelegenheit nutzen, mich bei allen, die mich während dieser Zeit begleitet haben, zu bedanken. Ohne eure Unterstützung und motivierenden Worte wäre das Gelingen dieser Arbeit nicht möglich gewesen.

Mein herzlicher Dank gilt:

Prof. Dr. Joost Wintterlin für die Möglichkeit meine Doktorarbeit in seinem Arbeitskreis durchführen zu können, die fachliche Expertise und wertvollen Ratschläge, das Vertrauen in meine Fähigkeiten und meine Daten, sowie die tatkräftige Unterstützung, die maßgeblich zum Gelingen der Arbeit beigetragen haben.

Prof. Dr. Sebastian Günther für die Übernahme des Zweitgutachtens und dem gesamten AK Günther (**Dr. Paul Leidinger** und **Tim Kratky**) für die bereichernde Erweiterung unseres Arbeitskreises und die immer gute Stimmung bei jeglichen gemeinsamen Events.

Dr. Ann-Kathrin Kügler (Henß) für die exzellente Betreuung während meiner Masterarbeit, für das Anvertrauen der VT-STM Kammer mit dem einzigartigen high-speed modus und das damit verbundene Entfachen meiner Begeisterung für hüpfende Atome und Teilchen auf Oberflächen, und für die stete Erreichbarkeit und Unterstützung auch über die Zeit der Masterarbeit hinaus.

meinem Kollegen **Sebastian Kläger (Daszko)** für die immer gute Gesellschaft im Büro, und nicht nur fürs Teilen der verschiedensten Snacks in unseren gemeinsamen Pausen, sondern auch der so manchen Herausforderungen sowie vielen Freuden des Promotionsalltags.

all meinen ehemalige Kolleg:innen: **Dr. Katharina Golder (Durner)**, **Dr. Paul Leidinger**, **Dr. Bernhard Böller**, **Dr. Ann-Kathrin Kügler (Henß)**, **Dr. Regina Wyrwich** und **Dr. Patrick Zeller** für die freundschaftliche und hilfsbereite Atmosphäre im Arbeitskreis und für den weiterhin bestehenden tollen Zusammenhalt. Außerdem habe ich an euch gesehen, dass eine Promotion abgeschlossen werden kann und sich danach viele verschiedene Wege eröffnen.